Experimental and numerical dynamic analysis of press-formed viscoelastic sandwich structures

Manex Martinez Agirre

Mondragon Goi Eskola Politeknikoa
Mechanical and Manufacturing Department

November 11, 2011

Experimental and numerical dynamic analysis of press-formed viscoelastic sandwich structures

Manex Martinez Agirre

dirigida por:

Dra. María Jesús Elejabarrieta Olabarri
Mechanical and Manufacturing Department
Mondragon Unibertsitatea

para la obtención del grado de Doctor
bajo el programa de doctorado de la Universidad de Mondragon:
Comportamiento Mecánico y Materiales.

Tribunal de Tesis:
Presidente: Dr. D. José María Goicolea Ruigómez (Universidad Politécnica de Madrid)
Vocal: Dr. D. José Dias Rodrigues (Faculdade de Engenharia da Universidade do Porto)
Vocal: Dra. Dña. Silvia Illescas Fernández (Universitat Politècnica de Catalunya)
Vocal: Dr. D. Fernando Cortés Martínez (Universidad de Deusto)
Secretario: Dr. D. José Manuel Abete Huici (Mondragon Unibertsitatea)

November 11, 2011

Acta de Grado de doctor
Acta de defensa de Tesis Doctoral

Doctorando: D. Manex Martinez Agirre

Título de la Tesis: "**Experimental and numerical dynamic analysis of press-formed viscoelastic sandwich structures.**"

El tribunal nombrado por el Excmo. y Magfco. Sr. Rector para calificar la Tesis Doctoral arriba indicada y constituido en el día de la fecha por los miembros que suscriben la presente Acta, una vez efectuada la defensa por el doctorando y contestadas las objeciones y/o sugerencias que se han formulado ha otorgado por _____ la calificación de:

El Presidente:	Fdo:_____
El Secretario:	Fdo:_____
Vocal:	Fdo:_____
Vocal:	Fdo:_____
Vocal:	Fdo:_____

Doctorando: ..... Fdo:_____

En _____, a _____ de _____ de 20___

Agustinari

Abstract

This dissertation presents the experimental and numerical dynamic analysis of press-formed viscoelastic sandwich structures composed by two thin metallic face layers and a constrained viscoelastic film. Such structures can be formed by classical sheet metal forming processes, but the relative displacement given between the elastic face layers subjects the viscoelastic core to a static prestrain. Besides the temperature and the frequency, the dynamic properties of the viscoelastic core also depend on such static prestrain, which must be taken into consideration to properly determine the dynamic response of formed sandwich parts.

The viscoelastic core is characterized in function of the frequency, temperature and static prestrain by two different experimental techniques. The frequency dependence is characterized by a new analysis method developed for identifying the dynamic properties of high damping and strong frequency-dependent viscoelastic materials from the dynamic response measured by the *forced vibration test with resonance* technique. By contrast, the temperature and the static prestrain dependence is characterized by conducting *dynamic mechanical analysis* (DMA) tests. The dynamic properties characterized by both experimental techniques are compared and discussed.

Different material constitutive models are considered to characterize the dynamic properties of the viscoelastic core in function of the three variables. The frequency dependence is described by a four-parameter fractional derivative model, the influence of the temperature is included by the frequency-temperature superposition principle making use of the Arrhenius equation, and a new material constitutive model to describe the frequency-prestrain dependence is proposed.

In addition, a higher order eigensensitivities-based numerical method is presented for the dynamic analysis in frequency domain of viscoelastically damped systems characterized by a structural damping matrix. Two different schemes are proposed, an iterative algorithm for determining the complex modal parameters, and an incremental algorithm for computing the dynamic response by the complex mode superposition method. The developed numerical method is applied for the dynamic analysis of flat and formed sandwich parts, proving its effectiveness and efficiency by comparing it with classical methods.

Finally, the influence of the static prestrain on the dynamic behavior of formed sandwich beams is assessed by experimental tests. To this end, several beams are bent with different angles, the induced static prestrain distribution is measured, and its influence on the modal parameters and the dynamic response is analyzed. From this study, the relevance of the static prestrain on the dynamic behavior of formed sandwich parts is stated.

Laburpena

Doktorego tesi honetan konformatuak izan diren bi azal metalikoz eta film biskoelastiko batez eraturiko sandwich egituren portaera dinamikoa aztertzen da bai esperimentalki, baita zenbakizko metodoen bidez ere. Egitura hauek ohiko prozesuen bidez konformatu badaitezke ere, bi azalen artean ematen den desplazamentu erlatiboa dela eta nukleo biskoelastikoa era iraunkorrean deformaturik geratzen da. Tenperatura eta maiztasunaz gain, aurre-deformazio honek material biskoelastikoaren propietate mekanikoetan eragina aintzat hartu beharreko aldagaia da, konformatuak izan diren sandwich egituren portaera dinamikoa egoki aurreikusteko.

Nukleo biskoelastikoaren propietate dinamikoak maiztasuna, tenperatura eta aurre-deformazioaren arabera karakterizatu dira bi teknika esperimental ezberdinekin. Maiztasunari dagokionez, moteltze-maila altuko eta maiztasunarekiko menpekotasun nabaria duten material biskoelastikoen propietate dinamikoak egoki zehazteko, habe erako laginen erantzun dinamikoan oinarritutako metodo berri bat garatu da. Tenperaturaren eta aurre-deformazioaren menpekotasuna, aldiz, erresonantzia gabeko saiakuntza dinamikoen bidez aztertu da. Era berean, bi tekniken bidez karakterizatutako propietate dinamikoak alderatu eta bateratu dira.

Nukleo biskoelastikoaren propietate dinamikoek hiru aldagaiekiko duten menpekotasuna deskribatzeko material-eredu ezberdinak erabili dira. Maiztasunaren eragina lau parametroko deribatu frakzionarioen ereduaz deskribatu da. Tenperaturaren efektua, tenperatura-maiztasuna gainezarpen printzipioaz barneratu da Arrhenius-en ekuazioa erabiliz. Azkenik, aurre-deformazioaren eragina eredu berri baten bidez zehaztu da.

Bestalde, autobalio eta autobektoreen goi mailako deribatuetan oinarritzen den zenbakizko metodo berri bat proposatu da material biskoelastikoen bidez moteldutako egituren portaera dinamikoa kalkulatzeko. Bi eskema ezberdin proposatu dira, batetik egituraren parametro-modal konplexuak zehazteko eskema iteratiboa, eta bestetik, modu konplexuen gainezarpenez erantzun dinamikoa lortzeko eskema inkrementala. Garatutako zenbakizko eskemak, sandwich egitura lauen eta konformatuen portaera dinamikoa aztertzeko erabili dira, eta hauen eraginkortasuna ohiko metodoek eskeinitako emaitzekin alderatuz frogatu da.

Azkenik, nukleo biskoelastikoak jasandako aurre-deformazioak konformatutako sandwich egituren portaera dinamikoan duen eragina aztertu da saiakuntza esperimentalen bidez. Horretarako, hainbat habe angelu ezberdinekin tolestu dira, luzeran zehar nukleoak jasandako aurre-deformazioaren banaketa neurtu da, eta honek portaera dinamikoan duen eragina frogatu da. Ikerketa honetatik ondorioztatu denez, nukleoaren aurre-deformazioa kontuan hartu beharreko aldagaia da konformatutako sandwich egituren portaera dinamikoa egoki zehazteko.

Resumen

Las estructuras sándwich de núcleo viscoelástico son una alternativa efectiva para la atenuación de las vibraciones y así, mejorar el confort vibro-acústico, la seguridad o al ciclo de vida de los productos. La utilización de un film viscoelástico situado entre dos capas metálicas permite obtener laminados que pueden ser conformados mediante los procesos convencionales de transformación de chapa. El diseño de piezas con estas estructuras sándwich conlleva determinar correctamente su respuesta dinámica, por lo que es necesario conocer la dependencia de las propiedades dinámicas del núcleo viscoelástico con la frecuencia, la temperatura y la predeformación que se induce por el desplazamiento relativo de las dos capas metálicas al ser conformadas. Además, esta dependencia se debe incluir en un modelo constitutivo del material, que junto con los métodos numéricos adecuados permitan predecir la atenuación vibratoria que aportan estos laminados en componentes industriales.

Así, en esta tesis doctoral se ha analizado el comportamiento dinámico de estructuras sándwich conformadas, tanto de forma experimental como numérica.

El núcleo viscoelástico se ha caracterizado en función de la frecuencia, la temperatura y la predeformación mediante dos técnicas experimentales. La dependencia con la frecuencia se ha establecido mediante un nuevo método de análisis a partir de la respuesta dinámica obtenida con la técnica de vibraciones forzadas con resonancia. El método desarrollado permite identificar las propiedades dinámicas de materiales viscoelásticos con alto amortiguamiento y fuerte dependencia en frecuencia. Por otro lado, la influencia de la temperatura y la predeformación se ha determinado mediante ensayos de vibraciones forzadas sin resonancia. Así, empleando ambas técnicas experimentales, se han identificado las propiedades dinámicas en un amplio ancho de banda. La influencia de cada variable se ha descrito mediante diferentes modelos constitutivos de material. La dependencia con la frecuencia se ha determinado mediante un modelo fraccionario de cuatro parámetros, la temperatura se ha incluido aplicando el principio de superposición frecuencia-temperatura con la ecuación de Arrhenius; y por último, la influencia de la predeformación se ha definido con un nuevo modelo constitutivo de material que actualiza la dependencia con la frecuencia en función del nivel de deformación inducida por el conformado.

Además, se han doblado vigas con diferentes ángulos, se ha establecido la distribución de la predeformación originada en el núcleo y se ha estudiado su efecto en los parámetros modales, así como en la respuesta dinámica. Con este estudio se ha demostrado la relevancia de la predeformación del núcleo viscoelástico en el comportamiento dinámico de estructuras sándwich conformadas.

En el análisis teórico, se presenta un nuevo método numérico basado en las derivadas de orden superior de los autovalores y autovectores para el análisis dinámico de estructuras con amortiguamiento viscoelástico en el dominio de la frecuencia. Se proponen dos esquemas, uno iterativo para determinar los parámetros modales complejos, y otro incremental para el cálculo de la respuesta dinámica mediante la superposición de modos complejos. Los algorítmos propuestos se han aplicado en el análisis dinámico de estructuras sándwich tanto planas como conformadas, demostrando su eficacia y eficiencia.

Eskertzak

Lerro hauen bitartez eskerrak eman nahi dizkiet era batera edo bestera lau urteko lan hau gauzatzen lagundu nauten guztiei.

Nire eskerrik beroenak tesi honen zuzendaria izan den Maria Jesus Elejabarrietari eskeinitako denbora eta arreta guztiagatik. Gauzak behar bezala eta biribil egiteko xedez izan ditugun eztabaida guztiengatik, bere aldarte, malgutasun, gardentasun eta besteen azalean jartzeko gaitasunagatik.

Amaiari, orain zazpi bat urte, gaur lerro hauekin ixten dudan zikloaren hasiera ahalbidetu izanagatik. Fernandori, harekin elkarlanean aritutako urteak benetan aberasgarriak izan zirelako, eskeinitako denboragatik, eta gauzak ondo egiteko aukera izanda ere, hobeto egiteko grina kutsatzeagatik. Unairi, saiakuntza esperimentalak egiterakoan eskeinitako laguntzagatik eta beharrezko izan ditudan tresna guztiak behar zuten tokian eta moduan mantentzeagatik.

Tailerreko hirukoteari, Gotzon, Harkaitz eta Iñakiri probeta eta beharrezko piezak egiteagatik, eta azken hilabete honetan ostatu eskeintzeagatik. Larraitzi, laborategian eiginiko saiakuntza eta neurketetan eskeinitako laguntzagatik. Javiri, prentsa mekanikoaren erabileraren inguruko argibideak emateagatik eta gauzak behar bezela egiten nituela ziurtatzeko hartutako denboragatik.

Silviari, saiakuntzetan eskeinitako denbora eta bitartekoengatik, gertutasunagatik, eta Terrassako egonaldietan suertatutako behar guztiei gogo onez erantzuteagatik. Mariari, berarekin izandako elkarlanagatik, Silviarekin harremanetan jartzeagatik eta orohar Kataluiniako egonaldietan eskeinitako arretagatik. Mila esker Bartzelonako gainontzeko lagun guztiei, bereziki Joan, Helena eta Sergiori, egonaldi guztietan momentu atseginak eta dibertigarriak igaro ditugulako.

Replasa enpresako Yolandari, izandako elkarlanagatik, lan honetan jarritako interesagatik eta tesi honetan aztertu den materiala helarazteagatik.

Eguneroko jardunean lankide izan ditudan guztiei, kalkulu zentrotik hasi, mila ta hamahirutik jarraitu, eta hiru mila eta hamabostarte, nire eskerrik beroenak giro jator

eta atseginean aritu garelako. Bakoitza bere harri eta haizeekin, lagun talde xelebre zein alaia osatu dugulako, momentu onenak eta txarrenak elkarrekin igaro ditugulako, laino ilunak agertutakoan elkar lagundu eta animatu garelako, eta uxatutakoan afari eta parranda earrak ein ditteulako. Segi horrela!

Datozen urteetan lankide izango ditudan fluidoen taldeko kideei, ofiziala egin aurretik ere beti taldekotzat hartu nauzuelako.

Era batera edo bestera lagundu nauten Mondragon Goi Eskola Politeknikoko lankideei, batez ere liburutegiko, informatikako, mantenketako, erosketa saileko eta idazkaritzako lankideei, sortutako beharrei gogo onez, garaiz eta zuzen erantzuteagatik.

Halaber, eskerrak eman nahi dizkiot Eusko Jaurlaritzari, Hezkuntza Sailak eskeinitako bekari esker gauzatu delako honako tesia.

Esker berezia ere urte guzti hauetan pixukide izan ditudan lagunei. Uribetarrei, Aratz, Haritz, Iker eta Iñigo anaiei, etxetik kanpo igarotako gure lehen bi urteak ahaztezinak eta errepikaezinak izan zirelako, ohiko biltzarretan oraindik ere pasarteak oroituz parrez lehertzen garelako. Hurrengo urtean aterpea eman zidaten eta lanerako nahiz bizitzarako eredu izan ditudan Tibur eta Agustinari. Erdiko kaleko Haritz, Mattin eta Madari, urte erdia soilik elkar banatu bagenuen ere giro alai eta bizia izan genuelako. Usaetxeko Haritz eta Nuriari, beti zeozi punta atera behar hortan inoiz aspertzen ez ginelako, elkar zirikatuz eguna joan eguna etorri earki pasatzen genuelako. Pasealekuko Nuria, Iñigo, Xabier, Jon eta Iñakiri, elkarbizitza atsegina eta istorio xelebrez betea lantzen ari garelako, eta lan egun astunen ondoren antidotorik onena zaretelako. Mila esker guztioi!

Eskerrik beroenak ere ikasle garaian egindako lagun guztiei. Bereziki batxilergokoei, txabola xume batzutan ezagutu ginenetik hamarkada bat atzean utzia dugun hontan, urtean bizpahiru aldiz elkartzearekin konformatu ez eta pasarte zoro eta ahaztezinez biribiltzen ditugulako gure afariak. Goierriko ingeniaritzako ikaslagun guztiei, inguruko herri bakoitzetik ordezkaririk xelebreenak elkartu eta urte apartak pasa genituelako. Arrasateko ikaslagunei, berriz ere hizkera ezberdineko aurpegi berrietara moldatu behar izan bagenuen ere konturatzerako talde bikaina sortu genuelako, klaseak arin eta parrandak fin egin genituelako, ta egipziarren artean urte pare hori borobildu genuelako. Geroztik ere harremanetan jarraitu dugun Irati, Leire, Jurgi eta Amaiari, ea laixter Oñatiko pintxo-poteoan bixita gidatua noiz eskeintzen didazuen.

Nola ez, kuadrilako lagun guztiei. Mila esker kolore bakarreko uda honi egun batzuetan bederen tankera aldatu diozuelako. Nitaz gogoratu zaretenoi eta hitz hauek idatzi beharko nituen eguna laixter iritsiko zela esanez animatu nauzuen guztioi. Eskerrik asko Mikel, azken hilabeteetako apaiz bizitza hau arintze aldera antolatu dizkidazun afari eta tertuliengatik. Hau ospatu beharren gare!

Eskerrak ere munduko txoko ezberdinetan bidailagun izan ditudanei, bizitzako unerik gogoangarrienak partekatu ditugulako lagun moduan joan eta anai itzuliz. Halaber, eskerrak munduko bazter ezberdin horietan ezagutu ditudan hainbat eta hainbat gizabanakoei, apaltasunez unibertsitatean ere ikas ezin daitezkeen ikasgai baliotsuak eskeintzeagatik. Eskerrak ere mendian, erreketan, arroiletan, urpean zein gainean, ZG AG igarobideetan,... lagun izan ditudanei, zuei esker lau urteko lan hau eramangarriagoa izan delako eta aparteko momentuak bizi izan ditugulako. Paperak alde batera utzi eta oraindik beste oroitzapen mordoa metatzeko grinaz eta ilusioz, laixter berriz martxan izango garelakoan... Inshallah!

Azkenik, nire bizitzan lehenak direnei eskertu nahi diet mugagabe eskeinitako laguntza eta animoa, guztion buru den Agustinari, aitari eta amari, Eider, Maialen eta Edurneri, igandeak alaitzen dizkiguten Garazi eta Galderri, osaba-izebei, postizoei eta lehengusuei. Bereziki Izarori, gure artean betiko umore eta irriparrez ikustea pozgarria delako.

Aupa zuek!!!

Contents

List of Tables

List of Figures

Nomenclature

Symbols

A	area.
A_r	amplitude of the rth resonance.
$\mathbf{A}_{r,n}$	matrix of coefficients for computing the nth eigenvector derivatives.
b	width of the beam.
$\mathbf{b}_{r,n}$	vector used for computing the nth eigenvector derivatives.
B_r	modal constant.
$\mathbf{B}_m$	membrane strain operator.
$\mathbf{B}_f$	bending strain operator.
$\mathbf{B}_c$	shear strain operator.
c	center of the arc.
c_i, c_r	coefficients of the frequency-prestrain material constitutive model.
$c_{r,n}$	scalar of the Nelson's method related to the nth eigenvector derivative.
C_1, C_2	coefficients of the William-Landel-Ferry equation.
C_r	coefficient for the rth mode related to the applied boundary conditions.
D	density ratio.
$e_{\max}$	total number of finite elements.
$E(t)$	relaxation modulus.
E_0	relaxed or static modulus.
E_∞	asymptotic modulus.
E_a	activation energy of the reaction.
E^*	complex modulus.
E', E	storage modulus.
E''	loss modulus.
f	frequency.

f_i	function for describing the frequency dependence of f_I.
f_r	rth resonance frequency, function for describing the frequency dependence of f_R.
f_R	function that relates the storage modulus of the prestrained viscoelastic material with the storage modulus of the not prestrained one.
f_I	function that relates the loss modulus of the prestrained viscoelastic material with the loss modulus of the not prestrained one.
$\mathbf{f}(t)$	force vector.
F	force.
F_0	static preload.
$\mathbf{F}^*$	complex vector of applied force amplitudes.
g	shear parameter.
$g(t)$	relaxation function.
G^*	shear complex modulus.
G'	shear modulus.
G''	shear loss modulus.
G_0	static shear modulus.
G_∞	asymptotic shear modulus.
$h(t)$	harmonic displacement excitation.
h_0	preload induced displacement.
H	thickness.
$H(\omega)$	frequency response function.
${}_rH(\omega)$	contribution of the rth mode to the total frequency response function.
$\mathrm{H}(t)$	Heaviside function.
$\mathbf{H}$	structural damping matrix.
$\mathbf{H}_{\mathrm{v},\gamma_0}$	stiffness matrix to account for the variation of the dissipative properties of the viscoelastic material due to the static prestrain.
i	imaginary unit.
I	second moment of area.
$j_{\max}$	total number of response points.
$k_{\max}$	total number of control frequencies.
$\mathbf{K}$	stiffness matrix.
$\mathbf{K}^e$	stiffness matrix of the element.
$\mathbf{K}_{\mathrm{v},\gamma_0}$	stiffness matrix to account for the variation of the elastic properties of the

$\mathbf{K}_{\text{fictitious}}$	fictitious stiffness matrix for stabilizing the assembly.
	viscoelastic material due to the static prestrain.
l	overlap.
l_{clamp}	distance between clamps.
l_e	length of the element.
L	length.
m_r	modal mass.
$\mathbf{M}$	mass matrix.
$\mathbf{M}^e$	mass matrix of the finite element.
n	decay in dBs of the n dB bandwidth method,
	size of a matricial system,
	number of superposed modes,
	nth order of differentiation,
	number of considered derivatives.
n_i, n_r	coefficients of the frequency-prestrain material constitutive model.
N	interpolation function.
$\mathbf{N}$	interpolation matrix.
$\mathbf{N}_x$	interpolation vectors related to the axial displacements.
$\mathbf{N}_r$	interpolation vectors related to the rotation.
$\mathbf{N}_y$	interpolation vectors related to the transverse displacements.
p	wave number.
q_r	generalized modal displacement.
$\mathbf{q}$	vector of elementary degrees of freedom.
$\mathbf{Q}$	transformation matrix.
r	radius of the arc.
R	ideal gas constant.
$\mathbf{R}^*$	complex amplitude vector of the reaction forces on the base.
$\mathcal{R}_n$	error after n terms related to the truncation of the Taylor's series.
$s_{\max}$	total number of tested specimens.
$s(t)$	base motion.
$\mathbf{S}^*$	complex amplitude vector of the applied base motion.
t	time.
t_0	time for solving the undamped real eigenproblem.
Δt	time lag.

T	temperature,
	thickness ratio.
T_0	reference temperature.
T_g	glass transition temperature.
$T^*(\omega)$	transfer function.
${}_rT^*(\omega)$	contribution of the rth mode to the total transfer function.
$\mathbf{T}$	matrices comprising transfer functions measured at several points,
	coordinate transformation matrix.
Tol	tolerance.
$u(t)$	longitudinal displacement.
$\mathbf{u}$	displacements vector.
	vector of generalized displacements.
$\dot{u}(t)$	velocity.
$\ddot{\mathbf{u}}$	acceleration vector.
$\mathbf{U}^*$	complex amplitude vector of the displacements.
${}_r\mathbf{U}^*$	contribution of the rth mode to the total complex displacements vector.
$v(t)$	transversal displacement.
x	spatial coordinate.
y	spatial coordinate,
	distance from the midplane.
z	spatial coordinate.
α	fractional parameter,
	coefficient of the Rayleigh model.
	scaling factor.
α_T	shift factor related to the temperature.
α_{γ_0}	shift factor related to the static prestrain.
β	coefficient of the Rayleigh model.
β_{xi}	membrane strain of the ith layer.
γ	shear strain.
γ_0	static prestrain.
$\gamma_{\max}$	amplitude of the harmonic shear strain.
$\dot{\gamma}$	shear strain rate.
δ	phase lag.
δ_{rs}	Kronecker delta function.

ϵ_0	amplitude of the applied strain step.
ϵ_r	tolerance for the rth mode.
$\epsilon_{xx,i}$	axial strain of the ith layer.
$\epsilon(t)$	strain.
η	loss factor.
η_r	modal loss factor.
θ	bending angle.
$\theta(t)$	rotation.
κ	reduction factor.
λ_r	rth eigenvalue.
ν	Poisson's ratio.
$\boldsymbol{\nu}_r$	vector of the Nelson's method related to the nth eigenvector derivative.
ξ_r	coefficient for the rth mode related to the applied boundary conditions.
π	number pi.
ρ	density.
$\sigma(t)$	stress.
τ	relaxation time, shear stress.
τ_0	static prestress.
$\tau_{\max}$	amplitude of the harmonic shear stress.
${}_r\phi_i$	ith element of the rth eigenvector.
$\boldsymbol{\phi}_r$	rth eigenvector.
χ_k	weighting coefficient for the kth control frequency.
χ_{xi}	curvature strain of the ith layer.
$\psi(t)$	shear strain of the core.
ω	angular frequency.
ω_0	frequency for the reference temperature T_0.
ω_f	final frequency,
ω_i	initial frequency,
ω_k	kth control frequency, computational frequency.
ω_r	natural frequency.
$\Delta\omega$	half power bandwidth.

Subscripts

$(\bullet)_0$	referring to the undamped system.
$(\bullet)_{\mathrm{e}}$	referring to the elastic layer.
$(\bullet)_{\mathrm{exp}}$	referring to the experimental data.
$(\bullet)_i$	referring to the ith degree of freedom,
	referring to the ith layer.
$(\bullet)_{\mathrm{Im}}$	referring to the imaginary part.
$(\bullet)_j$	referring to the jth degree of freedom,
	referring to the jth iteration.
$(\bullet)_n$	relative to the nth derivative.
$(\bullet)_r$	relative to the rth mode.
$(\bullet)_{\mathrm{Re}}$	referring to the real part.
$(\bullet)_s$	relative to the base displacement.
	relative to sth specimen.
$(\bullet)_u$	relative to the unknown displacements.
$(\bullet)_{\mathrm{v}}$	referring to the viscoelastic layer.

Operators

$\mathrm{Im}(\bullet)$	imaginary part of a complex number.
$\mathrm{Re}(\bullet)$	real part of a complex number.
$\Delta(\bullet)$	increment.
$(\bullet)^{\mathrm{H}}$	Hermitian operator.
$(\bullet)^{\mathrm{T}}$	transposition operator.
$(\bullet)^*$	complex number
$(\bullet)'$	real part of a complex number.
	differentiation with respect to an arbitrary parameter.
$(\bullet)''$	imaginary part of a complex number.
$(\dot{\bullet})$	first derivative with respect to time.
$(\ddot{\bullet})$	second derivative with respect to time.
$(\tilde{\bullet})$	Fourier transform.
$(\bullet)!$	factorial.

Acronyms

ADF	anelastic displacement fields damping model.
ATF	augmenting thermodynamic fields damping model.
CL	constrained layer
CLD	constrained layer damping
DMA	dynamic mechanical analysis
DMTA	dynamic mechanical thermal analysis
DOF	degree of freedom
EPDM	ethylene-propylene-diene monomer.
FEM	finite element method.
FFT	fast Fourier transform.
FLD	free layer damping
FRF	frequency response function.
GAC	global amplitude correlation.
GHM	Golla-Hughes-McTavish damping model.
GSC	global shape correlation.
HPB	half power bandwidth method.
ICE	iterative complex eigensolution.
IMSE	iterative modal strain energy.
IR	infrared spectroscopy.
IRAM	implicitly restarted Arnoldi method.
MAC	modal assurance criterion.
MDOF	multiple degree of freedom.
MSE	modal strain energy.
RKU	Ross-Kerwin-Ungar CLD homogenization model.
SDOF	single degree of freedom.
TVD	tuned viscoelastic damper
WLF	William-Landel-Ferry equation.
WEDM	wire electrical discharge machining.

Chapter 1

Introduction

The structural vibration control is a fundamental concern in several industries to reduce the sound radiation and to improve the performance of the designed mechanical systems. The passive damping treatments using viscoelastic materials, are one of the most widely applied structural vibration control techniques as they provide high damping capability over wide temperature and frequency ranges [87, 115, 46, 30]. In addition, they are simpler to implement and more cost-effective than active, semi-active, or adaptive damping treatments [119], being also possible to combine them with active techniques leading to hybrid damping treatments [121]. Viscoelastic damping materials have been used to enhance the damping within a structure in three different configurations: *free layer damping* (FLD), *constrained layer damping* (CLD), and *tuned viscoelastic damper* (TVD) [45]. The FLD treatment consists on attaching the viscoelastic damping material to the surface of the structure. The damping material is subjected to extensional loads and it must be sufficiently stiff to provide a reliable damping level. By contrast, adding an elastic constraining layer to the former configuration, a CLD treatment is obtained where the shearing of the viscoelastic material is enhanced improving the damping capacity of the treatment. This latter configuration is more effective than the FLD configuration for a given added weight [105], and provides a high damping capability with soft viscoelastic materials [72].

The CLD configuration is of special interest for applications where the mass of the components is critical, such as the aeronautical and the automotive industries [105], since it provides a high damping capability even with very thin viscoelastic layers [66, 69]. Nowadays, adhesive films of few microns in thickness are being used for manufacturing high damping performance laminates. Moreover, this laminates can be formed by classical sheet metal forming processes to obtain damped parts with complex geometries. Thus, components classically manufactured by transforming homogeneous solid sheets, can be obtained using CLD laminates in a similar way. This feature is specially interesting since the final damped part can be obtained with less manufacturing steps saving time and costs.

The use of the finite element method is a common practice to aid the design of effective damping treatments and to analyze real-life engineering problems. For the numerical analysis of viscoelastically damped structural systems, the dynamic properties must be experimentally characterized and proper mathematical models defined. In addition, suitable numerical solution methodologies are demanded to consider the dependencies exhibited by the dynamic properties of viscoelastic materials on several environmental factors, such as the temperature, the frequency or the static prestrain [87, 46].

The influence of the temperature on the dynamic properties of viscoelastic materials has been extensively analyzed and the procedure to include the effect of such factor is well-stablished [132, 35, 16]. The influence of the frequency has also been widely studied, being the forced vibration test with resonance technique one of the most commonly applied experimental procedure for identifying the dynamic properties of viscoelastic materials in FLD and CLD configurations. However, the classical analysis methods employed for determining the elastic and dissipative properties from the measured dynamic response, are not suitable for the dynamic characterization of high damping and strong frequency-dependent viscoelastic materials. When analyzing the dynamic behavior of press-formed CLD parts, besides the temperature and the frequency, the static prestrain induced during the forming process due to the relative displacement between both face layers must be taken into consideration. The influence of such static prestrain on the elastic and dissipative properties of viscoelastic films has been barely analyzed to date [48], and no works have been published dealing with the effect of the static prestrain on the dynamic behavior of press-formed CLD parts.

Thus, the goal of this thesis has been to analyze the influence of the static prestrain on the dynamic behavior of press-formed CLD parts.

To meet this main objective, the following partial objectives have been defined.

- Characterize the viscoelastic core in function of the frequency, the temperature and the static prestrain. To this end is necessary to:
  - establish the experimental techniques.
  - propose material constitutive models for characterizing such dependencies.
  - develop an analysis method for the dynamic characterization of high damping and strong frequency-dependent viscoelastic materials from vibration test data.

- Develop efficient numerical methods for the dynamic analysis in frequency domain of viscoelastically damped systems characterized by a frequency-dependent structural damping matrix, for determining:

  - the complex modal parameters.
  - the total dynamic response by the complex mode superposition method.

- Establish the relevance of the static prestrain on the dynamic behavior of press-formed CLD parts. This requires to:
  - define an experimental technique for forming CLD beams.
  - establish an experimental procedure for measuring the induced static prestrain in the core.
  - develop suitable numerical methods for including the influence of the static prestrain on the dynamic analysis of press-formed CLD parts.

The work carried out to meet the defined objectives is presented in the next four chapters.

In Chapter 2, the dynamic characterization of the viscoelastic core is addressed. The linear viscoelastic constitutive behavior, the mathematical models for describing the frequency dependence of viscoelastic materials, and the different characterization techniques are reviewed. The employed *forced vibration test with resonance* experimental technique is described, the different analysis methods are reviewed, and their applicability for characterizing high damping and strong frequency-dependent viscoelastic materials is discussed. Motivated by the limitations exhibited by the reviewed analysis methods, a new inverse method is proposed. The procedure to be followed is detailed and it is applied for characterizing the viscoelastic core from the dynamic response of the tested CLD beams. The identified dynamic properties are validated, and finally they are compared with those determined by classical analysis methods in order to better reflect the advantages of the proposed inverse method.

After that, in Chapter 3 *dynamic mechanical analysis* (DMA) technique is considered for characterizing the influence of the temperature and the static prestrain on the dynamic properties of the viscoelastic core. The experimental set-up is established, and the material parameter extraction procedure is detailed. First, the temperature influence is analyzed, the master curve is obtained, and the identified dynamic properties are compared with those determined by the forced vibration test with resonance method. From this analysis, the advantages and the limitations of both used experimental techniques are outlined, and the dynamic properties are identified in a wider frequency bandwidth. After that, the effect of the static prestrain on the elastic and dissipative properties of the core is included with other set of experimental tests. A new material constitutive model for including the influence of the static prestrain on the dynamic properties of the core by combining it with the material model already used in Chapter 2 for characterizing the frequency dependence,

is proposed and validated. Finally, a comparative analysis is presented where the influence of the frequency, the temperature and the static prestrain on the dynamic properties of the viscoelastic core, is compared for the range of variables analyzed.

Once the viscoelastic material has been characterized, in Chapter 4 a new higher order eigensensitivities-based numerical method is proposed for the dynamic analysis in frequency domain of viscoelastically damped systems characterized by a frequency-dependent structural damping matrix. The bases of the method are detailed and the fundamental updating procedure is described. The latter is then implemented into an iterative and an incremental schemes with different purposes. The iterative algorithm aims to determine the complex modal parameters, whereas the incremental one computes the complex and frequency-dependent modal parameters within the defined frequency bandwidth in order to compute the frequency response by the complex mode superposition method. A practical example is presented to prove the effectiveness of the presented algorithms, and an analysis is performed in order to prove the efficiency of the new algorithms with respect to classical ones.

Finally, in Chapter 5 the dynamic analysis of press-formed CLD beams is presented and all the contributions made in previous chapters are applied. Several CLD beams are bent into different angles and the static prestrain induced in the viscoelastic core is measured. First, the experimental frequency response is compared with that computed using the nominal dynamic properties determined without including the influence of the static prestrain in Chapter 2, from where the relevance of the static prestrain effect is verified. After that, the nominal dynamic properties identified in Chapter 2 are combined with the frequency-prestrain material model proposed in Chapter 3 in order to correct the deviations observed in the frequency response. Furthermore, the higher order eigensensitivities-based numerical method developed in Chapter 4 is extended for the dynamic analysis of press-formed CLD parts, proving its effectiveness with a practical example. From the presented study is concluded that the static prestrain is a factor to be taken into consideration for properly analyzing the dynamic behavior of press-formed CLD parts.

The conclusions of each chapter show that the established objectives have been met.

Chapter 2

Dynamic characterization: forced vibration test with resonance

The work summarized in the present chapter was motivated by the need to characterize high damping and strong frequency-dependent viscoelastic materials from the frequency response measured by the forced vibration test with resonance.

First, the linear viscoelastic constitutive behavior and the mathematical models for describing the frequency dependence of the dynamic properties of such materials are reviewed. After that, the different experimental techniques are described and the forced vibration test with resonance considered for characterizing the viscoelastic core, as well as the tested specimens, are detailed.

Then, the existing modal parameter-based and dynamic response-based analysis methods for identifying the dynamic properties from the measured dynamic response are reviewed, and their limitations for characterizing high damping and strong frequency-dependent viscoelastic materials are discussed. Motivated by the limitations exhibited by the reviewed methods, a new inverse method is proposed and the procedure to be followed is detailed.

The proposed inverse method is applied to characterize the complex shear modulus of the viscoelastic film sandwiched in CLD configuration. The identified dynamic properties are validated and compared with those determined by classical methods, in order to demonstrate the advantages of the proposed method. The presented method proves to be effective for identifying the dynamic properties in a relatively broad frequency bandwidth not being affected by the damping level nor by the strong frequency dependence of the viscoelastic material to be characterized. Furthermore, the suggested procedure simplifies the overall characterization process drastically reducing the amount of required experimental tests.

2.1 Introduction

The design of structural systems involving viscoelastic damping materials require knowledge of material properties and proper mathematical models to describe them. The frequency is one of the most influential environmental factor that affects to the elastic and dissipative properties of viscoelastic materials, being necessary to determine such dependency by means of experimental tests.

Viscoelastic damping is exhibited by many polymeric and glassy materials showing both viscous and elastic characteristics. The damping arises from the interaction of the polymer network during the cyclic deformation transforming the mechanical energy into heat [87, 46]. In addition, when subjected to a constant load, the induced deformation increases over a period of time, whereas the force required to maintain a given deformation decreases. Both phenomenons are referred to as creep and relaxation [21], respectively.

As the Boltzmann superposition principle states [15], the actual response of a viscoelastic material depends on the complete past history of the applied load. Assuming that the stress and strain history can be represented by continuous and differentiable functions, the one-dimensional stress-strain constitutive relationship for small strains, is given by a convolution integral according to the theory of linear viscoelasticity [21, 17]. Being $\sigma(t) = \epsilon(t) = 0$ for $t < 0$, and applying a strain step at $t = 0$, such that $\epsilon(t) = \epsilon_0 \mathrm{H}(t)$, where ϵ_0 and $\mathrm{H}(t)$ are the amplitude of the applied strain step and the Heaviside function, respectively, the stress-strain relationship is written as

$$\sigma(t) = \int_0^t E(t-\tau)\frac{\partial \epsilon(\tau)}{\partial \tau}\mathrm{d}\tau, \tag{2.1}$$

where $\sigma(t)$ is the time dependent stress, τ is the retardation time, and $E(t)$ is the relaxation modulus. The latter may be determined by means of relaxation tests relating the stress history with the applied step strain, so that

$$E(t) = \frac{\sigma(t)}{\epsilon_0} = E_0 + g(t), \tag{2.2}$$

where $E_0 = \lim_{t\to\infty} E(t)$ and $g(t)$ are the relaxed or static modulus and the relaxation function, which represent the elastic behavior and the dissipation effects, respectively.

Additionally, an appropriate mathematical function for describing the measured material properties must be defined. An arbitrary stress-strain relationship can be represented by classical or differential damping models defined by the combination of discrete spring and dashpot elements. Basic models, such as those of Maxwell and Kelvin-Voigt may be defined. The generalized Maxwell or the generalized Kelvin-Voigt models may be also ob-

tained combining several Maxwell or Kelvin-Voigt models, respectively, whose time-domain material function is expressed by a series of decaying exponentials, often referred to as a Prony series [131]. Similarly, the Maxwell and Kelvin-Voigt models may be combined in series or parallel to define the Zener or the Burger models. A complete revision of the classical or differential models is given by Bert [13], Sun and Lu [115], and Jones [46], among others. Although is possible to obtain accurate representations of the measured properties, large amount of parameters are commonly required when classical models are considered. By contrast, fractional derivative models allow describing the stress-strain constitutive relationship with a low number of parameters considering a non-integer order derivatives. The fractional derivative models have been satisfactorily applied by several authors for characterizing the dynamic properties of viscoelastic materials [46, 92, 79, 64, 70]. Bagley and Torvik [7, 9] analyzes the fractional derivatives from a molecular and thermodynamical point of view. Pritz [99, 101, 102] analyzes the four- and five-parameter fractional derivative models in frequency domain, whereas the use of fractional derivatives for transient analysis is addressed by Bagley and Torvik [8], Padovan [93], Schmidt and Gaul [111], Galucio *et al.* [39], and Cortés and Elejabarrieta [25], among others.

As well, several authors have proposed different mathematical representations for the relaxation function $g(t)$ in the last decades. Recent compilations of different mathematical models are given by Adhikari and Woodhouse [3], and Vasques *et al.* [127], for example. Most of those models are basically variants of the general exponential model proposed by Biot [14]. Among these, the most widely used models are the double exponential or GHM (*Golla-Hughes-McTavish*) model proposed by Golla and Hughes [40] and further developed by McTavish and Hughes [78], and the ADF (*anelastic displacement fields*) developed by Lesieutre and Bianchini [58], which is based on the ATF (*augmenting thermodynamic fields*) model previously developed by Lesieutre and Mingori [59]. These methods use additional internal dissipation coordinates to account for the frequency dependence of the viscoelastic material, simplifying and linearizing the motion equation. These methods have been widely used for the transient response analysis as they can be easily incorporated into finite element models. However, due to the addition of internal variables the problem size increases, these models not resulting attractive for the analysis in frequency domain. Nevertheless, in order to avoid the drawback of increasing the model size, model reduction techniques have been also proposed by Friswell and Inman [38], Park *et al.* [94], and Trindade [120], for example.

For the dynamic analysis in frequency domain, the complex modulus approach is commonly adopted for describing the steady-state oscillatory conditions. The complex modulus may be defined from the Fourier transform of Equation (2.1), given by

$$\tilde{\sigma}(\omega) = \mathrm{i}\omega\tilde{E}(\omega)\tilde{\epsilon}(\omega), \tag{2.3}$$

where $(\tilde{\bullet})$ denotes the Fourier transform. Thus, the complex modulus $E^*(\omega) = \tilde{\sigma}(\omega)/\tilde{\epsilon}(\omega)$, is written as

$$E^*(\omega) = \mathrm{i}\omega\tilde{E}(\omega) = \mathrm{i}\omega \int_0^\infty E(t)\mathrm{e}^{-\mathrm{i}\omega t}\ \mathrm{d}t, \tag{2.4}$$

where $(\bullet)^*$ denotes a complex quantity. The real and the imaginary parts of the complex modulus can be computed separating the two components of the relaxation modulus as described by Equation (2.2), yielding to

$$E'(\omega) = E_0 + \omega \int_0^\infty g(t)\sin\omega t\ \mathrm{d}t \tag{2.5}$$

and

$$E''(\omega) = \omega \int_0^\infty g(t)\cos\omega t\ \mathrm{d}t, \tag{2.6}$$

where the real $E'(\omega)$ and the imaginary $E''(\omega)$ parts of the complex modulus are referred to as the storage and loss modulus, respectively. Therefore, the stress-strain relationship is expressed in frequency domain in a complex form, such as

$$E^*(\omega) = E'(\omega) + \mathrm{i}E''(\omega). \tag{2.7}$$

The loss factor, $\eta(\omega)$, may be defined as the non-dimensional quantity relating the imaginary and the real part of the complex modulus as

$$\eta(\omega) = \frac{E''(\omega)}{E'(\omega)}. \tag{2.8}$$

The loss factor measures the average ratio of energy dissipated to the maximum stored energy per cycle, under a harmonic excitation.

After reviewing the linear viscoelastic constitutive representations in time and frequency domains and the most commonly employed damping models, next the experimental techniques for characterizing the frequency dependence of the viscoelastic materials are reviewed and that used in the present dissertation is further described.

2.2 Experimental technique

There exist several experimental techniques for characterizing the frequency dependence of viscoelastic materials. The election of the most suitable technique depends on several factors, such as the nature of the viscoelastic material and the possibility to preform appropriate samples, the frequency bandwidth of interest, and so on. A survey on experimental techniques for characterizing the dynamic properties of viscoelastic materials is given by Lakes [55] and, by Ward and Sweeney [130]. The experimental techniques may be classified according to the frequency range where the material properties are determined.

The quasi-static properties ($<$1 Hz) are characterized by creep and relaxation tests. The creep test consists on measuring the evolution of the deformation when a constant stress is applied, whereas the relaxation test consists on measuring the evolution of the stress induced by a constant deformation. Both phenomenons are described by the Boltzmann principle [16]. The time dependent relaxation modulus measured by relaxation tests, $E(t)$, may be transformed into frequency domain by the Fourier transform using Equation (2.3), and vice versa. A complete description of interconversion methodologies are described by Park and Schapery [95], Emri *et al.* [33], and Brinson and Brinson [17], among others.

For the low frequencies (up to the first resonance frequency), the dynamic properties may be determined by the free vibration decay method [87]. This method consists on measuring the decay rate of the transient response of the structure caused by either impulsive excitation or interrupted steady-state excitation, from where the storage modulus and the loss factor for the fundamental resonance frequency are identified. This method is best suited for lightly damped structures.

For the low-medium frequency range, the dynamic properties may be determined by direct techniques such as the *dynamic mechanical analysis* (DMA) [80]. The DMA tests are commonly performed using commercial equipments with the test procedure and configuration recommended by the manufacturer. A harmonic force or displacement excitation in extension, bending, torsion or shear is applied to the sample, and the induced harmonic strain or stress is measured. From the stress-strain relationship, the elastic and dissipative properties of the material are identified for each discrete excitation frequency. Performing several tests at different temperatures under isothermal conditions, and making use of the temperature–frequency superposition principle, the master curve of the viscoelastic material can be identified [132]. This experimental technique is employed in Chapter 3 for characterizing the frequency, temperature and static prestrain dependence exhibited by the dynamic properties of the viscoelastic core.

Other authors proposes direct identification procedures based on the frequency response of specially designed discrete experimental set-ups. For example, Moreira *et al.* [84] use a

two degrees of freedom system for the dynamic characterization of cork compounds up to 400 Hz, whereas de Espindola *et al.* [31] consider a single degree of freedom configuration for identifying the dynamic properties of a viscoelastic material up to 3 kHz.

Another technique for characterizing the dynamic properties in the low-medium frequency range is the dynamic nanoindentation. The method originally used for measuring the static elastic and quasi-static viscoelastic properties of polymers, has been recently developed for measuring the dynamic viscoelastic properties of such materials. The dynamic nanoindentation, which was conceived for measuring the localized properties of nanostructured polymer composite materials, is applied by Odegard *et al.* [91] for characterizing homogeneous polymers, showing a good agreement with the properties identified by DMA tests.

The forced vibration test with resonance is an indirect technique for characterizing viscoelastic materials in the medium frequency range (from 1 Hz up to several kHz). This method consists on exciting the flexural vibration modes of beams within the frequency bandwidth of interest. Employing the classical analysis method, the storage modulus and the loss factor are determined from the resonances, identifying discrete complex modulus values at each resonance frequency. The forced vibration test with resonance allows determining the dynamic properties of homogeneous viscoelastic materials, as well as of those attached to elastic beams in FLD and CLD configurations. In those cases, the characterization of the viscoelastic material is completed in two stages. First the homogenized complex modulus of the whole structure is identified, and then, the complex modulus of the viscoelastic material is determined. The extensional complex modulus of viscoelastic materials in FLD configuration is calculated according to the homogenization theory of Oberst and Frankenfeld [90, 45, 29]; whereas the complex shear modulus of viscoelastic materials in CLD configuration is determined according to the homogenization theory of Ross, Ungar, and Kerwin [107] (see Refs. [1, 87, 46, 28] for further details about this method).

Finally, for high excitation frequencies (from some kHz to MHz), viscoelastic properties can be characterized by wave propagation and ultrasonic methods [55].

In the present chapter, the viscoelastic core of the CLD structure under analysis is characterized up to 1 kHz at room temperature (20 °C), by the forced vibration test with resonance technique. The experimental set-up employed for measuring the frequency response of cantilever beams and the considered specimens, are described. As well, the linearity analysis conducted for assuring that the deformations induced in the core were within the linear viscoelastic range, is presented.

2.2.1 Experimental set-up

The standard ASTM E756-05 [1] establishes the experimental procedure for measuring the frequency response functions (FRF) of beam-like specimens. It states that non-contacting transducers should be used for the excitation and the response measurement to minimize all sources of damping except that of the material to be investigated. In order to avoid the use of non-contacting transducers and simplify the experimental set-up, Cortés and Elejabarrieta [26] propose to replace the forced excitation by a seismic excitation at the clamp. They prove that the procedure established by the standard ASTM E756-05 to determine the complex modulus is applicable with transfer functions in the same way.

For the dynamic characterization transfer functions were measured, so the study is focused on the analysis of this type of functions. The experimental set-up employed for measuring the transfer functions of cantilever beams is schematized in Figure 2.1.

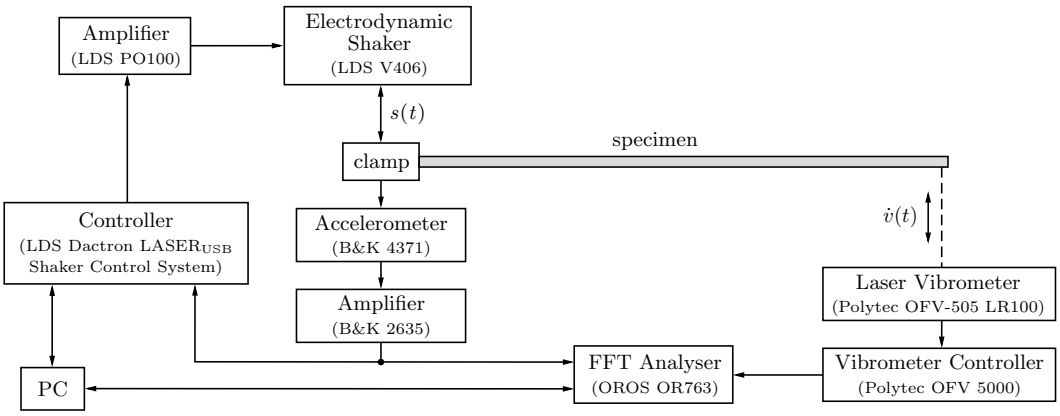

Figure 2.1: Experimental set-up.

The beam was excited in the thickness direction avoiding any rotation of the clamped end. The base motion, $s(t)$, consisted of a white noise which acceleration amplitude was loopback controlled. The velocity of the selected response point, $\dot{v}(t)$, was measured by means of a laser vibrometer. The transfer functions were measured up to 1 kHz frequency bandwidth with a 0.3125 Hz constant resolution, and the test temperature was 20 ± 1 °C.

The experimental transfer function, ${}_{\text{exp}}T^*(\omega)$, was determined relating the transverse displacement of the response point with that applied at the base, so that

$$ {}_{\text{exp}}T^*(\omega) = \frac{\tilde{v}(\omega)}{\tilde{s}(\omega)}, \tag{2.9} $$

where $\tilde{v}(\omega)$ and $\tilde{s}(\omega)$ are the Fourier transforms of the transverse displacement measured at the response point, $v(t)$, and of that applied at the base, $s(t)$, respectively.

2.2.2 Specimens

The tested CLD beams were symmetrical, i.e., the material and thickness of the constraining layers (CL) were equal, being composed of two cold rolled DC04 steel layers and a constrained thin viscoelastic film. The viscoelastic core was identified by *infrared spectroscopy* (IR) [112], resulting in a ethylene-propylene-diene (EPDM) adhesive.

For characterizing the dynamic properties of the viscoelastic core, first the storage modulus of the constraining layers must be determined. Therefore, to completely characterize the CLD beams under analysis two specimen types were tested; CL specimens, from where the storage modulus of the metallic layers, E_{e}, was identified; and CLD specimens, from where the dynamic shear complex modulus of the viscoelastic core, $G^*_{\mathrm{v}}(\omega)$, was determined. From now on, the subindices $(\bullet)_{\mathrm{e}}$ and $(\bullet)_{\mathrm{v}}$ will be used for referring to the elastic and viscoelastic layers, respectively.

Three CL specimens were tested each with a different free length, so that three experimental transfer functions were considered for characterizing the storage modulus of the metallic constraining layers. The specimens were $b = 10$ mm width, and the considered free lengths were $L_1 = 150$ mm, $L_2 = 175$ mm and $L_3 = 200$ mm. The thickness, H_{e}, was measured by means of a micrometer whereas the density, ρ_{e}, was measured by the Archimedes' principle after weighting the specimens in air and under water. In Table 2.1 the thickness and the density of the CL specimens are summarized.

Once the storage modulus of the constraining layers, E_{e}, was determined, CLD beams were tested to characterize the dynamic properties of the viscoelastic core, $G^*_{\mathrm{v}}(\omega)$. Three CLD specimens were tested with three different free lengths for each specimen, so that nine experimental tests were performed. The specimens were 10 mm width and the considered free lengths were $L_1 = 170$ mm, $L_2 = 210$ mm and $L_3 = 250$ mm. The thickness, H_{v}, was measured by means of a Wild® *M420* optical macroscope equipped with a Kappa® *CF 11 DSP* camera, whereas the values for the density, ρ_{v}, and the Poisson's ratio, ν_{v}, were taken from bibliography [65]. The geometrical and physical properties of the elastic and viscoelastic layers of the tested CLD specimens are summarized in Table 2.1.

Table 2.1: Geometrical and physical properties of the tested specimens.

metallic layers			viscoelastic core		
H_{e} ($\pm$ 0.005 mm)	ρ_{e} ($\pm$ 12 kg/m^3)	ν_{e}	H_{v} ($\pm$ 0.005 mm)	ρ_{v}(kg/m^3)	ν_{v}
0.587	7869	0.3	0.025	990	0.49

2.2.3 Linearity analysis

The mechanical properties of viscoelastic materials also depend on the applied strain level. The effect of the strain amplitude on the dynamic properties of viscoelastic materials is reported by Nashif [87] among others, showing that the stiffness decreases and the loss factor increases when the deformations get over the linear viscoelastic range.

The amplitude of the induced deformations in the viscoelastic core is directly related with the applied excitation amplitude at the base, so that the control of the excitation level is of special concern when measuring the frequency response of this type of laminates. The high damping capacity shown by the analyzed CLD specimens, demands a reasonable excitation level in order to obtain measurements with good signal-to-noise ratio. However, special attention is required since too large excitation levels may induce deformations over the linear viscoelastic range in the core, resulting in a non-linear behavior of the tested specimen. Therefore, before testing the specimens a linearity analysis was performed to define the maximum excitation amplitude to be applied.

For the linearity analysis, the frequency response of a 270 mm long CLD cantilever beam under different excitation levels was analyzed. The excitation consisted of a white noise which acceleration magnitude was loopback controlled. In a first instance, the attention was focused on the fundamental resonance (first bending mode) since the largest deformations are given at this resonance, resulting the most sensitive mode to manifest a non-linear behavior. In Figure 2.2, the modulus and the phase of the first resonance are plotted. The transfer functions of the 270 mm long CLD beam were measured at the free end under different excitation levels. From Figure 2.2, the non-linear behavior of the first bending mode was evidenced.

As can be seen, the resonance frequency of the first bending mode was shifted to the left whereas its amplitude was reduced as the excitation level increased. This fact revealed that the strain levels induced in the viscoelastic core exceeded the limit of the linear viscoelastic range. The core exhibited a lower stiffness and a higher damping capacity as the excitation level was increased, according with that described in the open literature [87]. From this analysis, the maximum excitation level that should be applied to the first bending mode was determined, resulting 0.1 m/s^2.

Nevertheless, as this excitation amplitude resulted insufficient to properly measure the frequency response at higher frequencies, the same procedure was repeated with the higher order modes. The excitation amplitude for the first mode was fixed (0.1 m/s^2) and the excitation amplitude for the higher order modes was increased in order to improve the signal-to-noise ratio. Again, the maximum amplitude level to induce deformations within the linear viscoelastic range was determined being 2.5 m/s^2 up to 1 kHz. Note

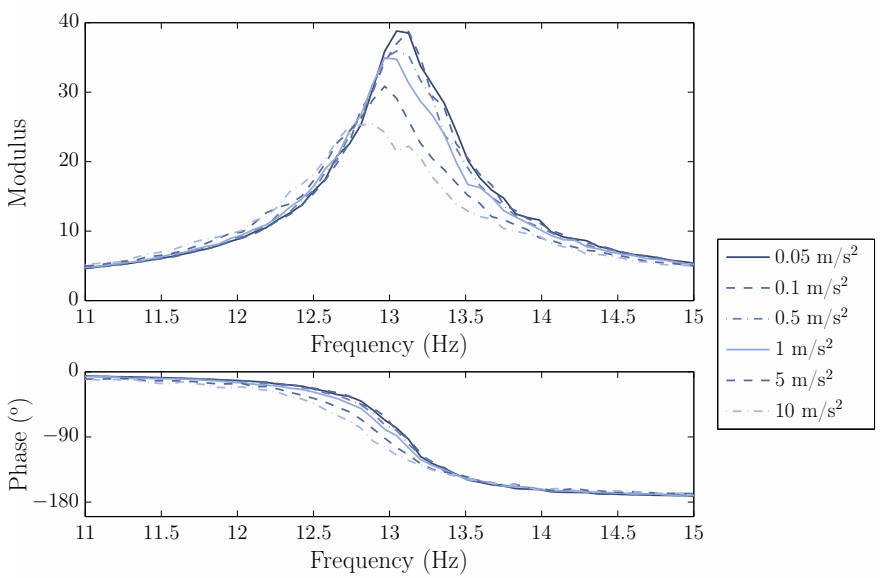

Figure 2.2: Modulus and phase of the transfer functions measured at the free end under different excitation levels.

that the presented analysis is conservative because the free length of the specimen used for the linearity analysis (270 mm) was larger than that of the specimens used for the characterization. So that, all the experimental tests were performed assuring that the deformations given in the viscoelastic core were within the linear viscoelastic range.

2.3 Review of material parameter identification methods

In this section, the classical and other recently proposed methods for identifying the dynamic properties of viscoelastic materials from vibration test data are reviewed and discussed. Special emphasis is placed on the high damping and strong frequency dependence of the material to be characterized, providing a critical review of the discussed procedures.

There exist many different methodologies for the characterization of the complex modulus from vibration test data. Most of them are based on the extraction of the modal parameters (natural frequency ω_r and modal loss factor η_r) of the tested specimen, from where the complex modulus of the material is determined. By contrast, other methods consider the frequency response instead of the modal parameters of the specimen under analysis. In Figure 2.3, the stages to be completed by the procedures based on modal parameters and frequency responses, are schematized.

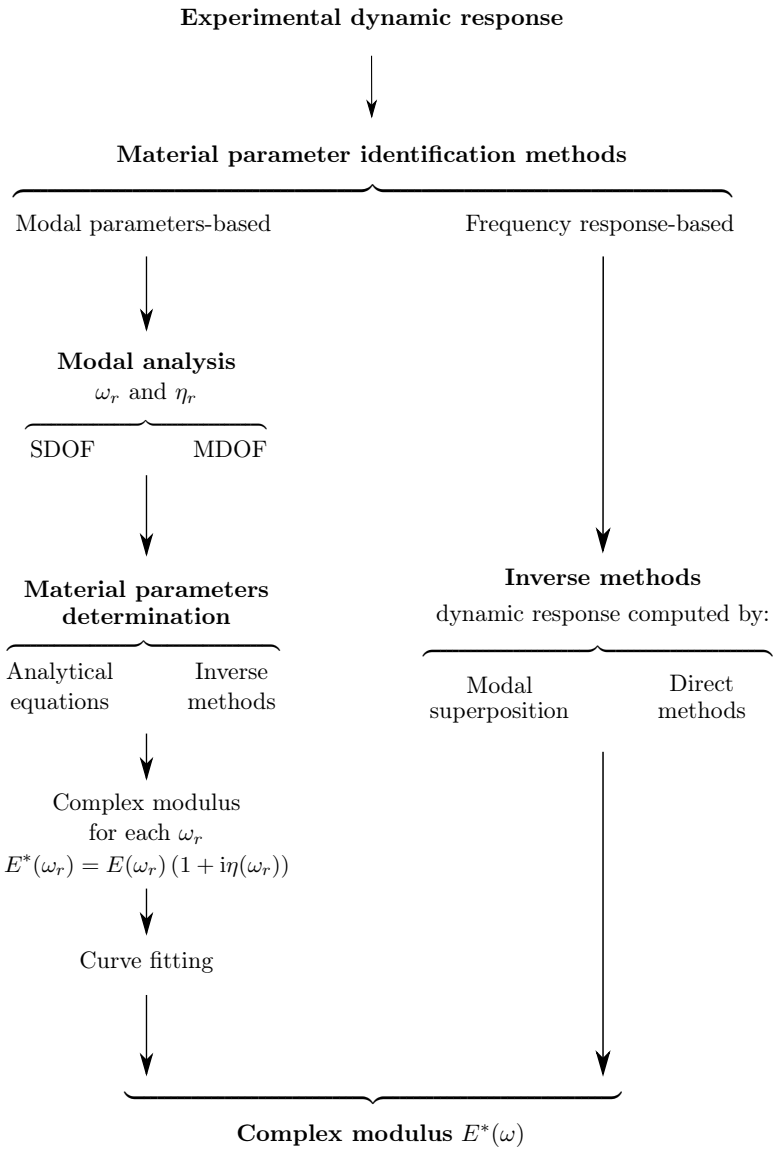

Figure 2.3: Different procedures for the dynamic characterization from vibration test data.

2.3.1 Modal parameter-based methods

Modal analysis methods may be classified in two subgroups depending on whether the influence of a single or several modes is considered when determining the modal parameters from a given resonance. The former are referred to as single degree of freedom (SDOF) methods, whereas the latter are referred to as multiple degree of freedom (MDOF) methods. A revision of the different modal analysis methods is presented by Ewins [34]. From the identified modal parameters, the material properties for each resonance frequency may be determined by analytic expressions or inverse methodologies.

SDOF modal analysis methods

The SDOF modal analysis methods are widely applied in modal testing due to their simplicity. These methods identify the modal parameters (ω_r and η_r) of each mode assuming the fact that the response in the vicinity of a resonance is given exclusively by a single mode. Therefore, due to this assumption, these methods are sensitive to the influence of the contribution of the neighboring modes. This effect is specially important when the modes are closely spaced or the system presents high damping. Furthermore, the accuracy of the identified modal parameters by SDOF modal analysis methods, is not only related to the non-negligible influence of the neighboring modes. Some of the most widely used SDOF modal analysis methods do not provide reliable results even from the frequency response of highly damped SDOF systems. So that, these methods are reviewed and their accuracy for determining the modal loss factor of highly damped SDOF systems is discussed next.

The *half power bandwidth* (HPB) method, also considered by the standard ASTM E756–05, is one of the most widely used SDOF method for determining the modal loss factor. The latter is determined relating the bandwidth $\Delta\omega$ at which the amplitude of the resonance decreases 3.01 dB, with the resonance frequency ω_r, such as

$$\eta_r = \frac{\Delta\omega}{\omega_r}. \tag{2.10}$$

The analytic definition of the modal loss factor deduced by the HPB method from the response of a SDOF system subjected to a base motion is given by [87]

$$\eta_r = \frac{2\eta}{\sqrt{1+\eta} + \sqrt{1-\eta}}, \tag{2.11}$$

where η_r is the modal loss factor identified by the HPB method, whereas η is the loss factor of the material. The modal loss factor identified with the HPB method coincides with the loss factor of the material only when the latter is small ($\eta < 0.1$), but discrepancies grow exponentially as the loss factor of the material increases. These errors can be reduced considering the n dB *bandwidth* method [34, 67], which can be considered as the generalization of the HPB method. In this case, the frequencies above and below the resonance frequency are measured where the value of the amplitude is n dB less than the value at the resonance, n being the value specified by the user. Typical values are those comprised between 3 and 0.5 dB. When considering the n dB bandwidth method, the modal loss factor is given by

$$\eta_r = \left(\frac{1}{\sqrt{x^2-1}}\right)\frac{\Delta\omega}{\omega_r}, \tag{2.12}$$

where $x = 10^{(n/20)}$.

Although the n dB bandwidth method provides more accurate results than the HPB method, it also fails to accurately determine the modal loss factor from the frequency response of highly damped SDOF systems. In Figure 2.4, the errors committed by the HPB and the n dB bandwidth methods when evaluating the modal loss factor η_r from the frequency response of a SDOF system subjected to a seismic excitation, are plotted in function of the loss factor of the material η.

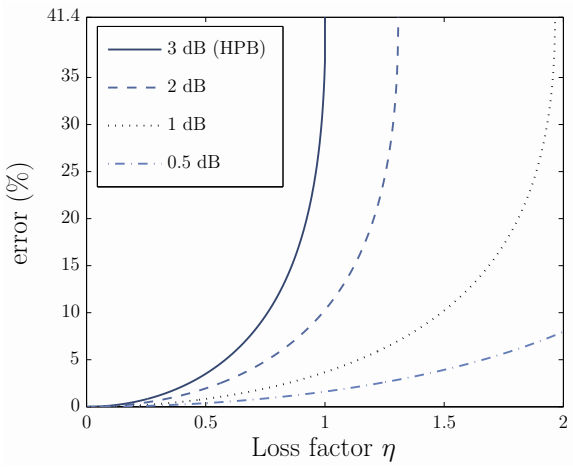

Figure 2.4: Error in function of the loss factor of the material, η, when determining the modal loss factor from the frequency response of a SDOF system subjected to a seismic excitation by the HPB and n dB bandwidth method with 2, 1, and 0.5 dB decays.

As is concluded from Figure 2.4, the error committed by the HPB method can be significantly reduced by considering the n dB bandwidth method. Nevertheless, both methods are limited for identifying the modal loss factor of highly damped SDOF systems.

Another widely accepted SDOF modal analysis method is the so called *circle-fit* method [34]. This method consists on fitting the transfer function of a SDOF system to the resonances of the experimental transfer function, from where the resonance frequencies and the modal loss factors are determined. The analytic expression of the modal transfer function $T_r^*(\omega)$, is given by

$$T_r^*(\omega) = \frac{B_r(1+\mathrm{i}\eta_r)}{1+\mathrm{i}\eta_r-(\omega/\omega_r)^2}, \tag{2.13}$$

where B_r is the modal constant; for SDOF systems $B_r = 1$, whereas B_r is complex for a given mode of a MDOF system. The modal parameters can be also identified applying the geometrical properties of the fitted modal transfer function which produces a circle-like curve in the complex plane (see Ewins [34] for further details). The circle-fit SDOF modal analysis method identifies the exact modal loss factor of SDOF systems with constant damping being applicable for all damping levels.

From the analysis of the different SDOF modal analysis methods for determining the modal loss factor of highly damped SDOF systems, the following conclusions are derived. The HPB method does not offer accurate results when the damping becomes high, but the error can be reduced considering the n dB bandwidth method. By contrast, the circle-fit method identifies the exact modal loss factor from the frequency response of a SDOF system with constant damping, not being conditioned by the damping level.

Anyway, as stated before, the major limitation of the SDOF modal analysis methods for determining the modal parameters of highly damped MDOF systems, is that the single mode approach is no longer acceptable as the modal coupling becomes non-negligible. Due to the influence of the neighboring modes, the proper identification of the modal parameters by SDOF modal analysis methods is conditioned, and thus also the material properties determination. The influence of the modal coupling on the frequency response of a cantilever beam subjected to a base motion is shown with a numerical example. The beam considered was made of a homogeneous material and the dynamic properties were assumed to be constant in frequency. The transfer function of the free end was computed by superposition of normal modes, the modal contributions and the total response being plotted in Figure 2.5.

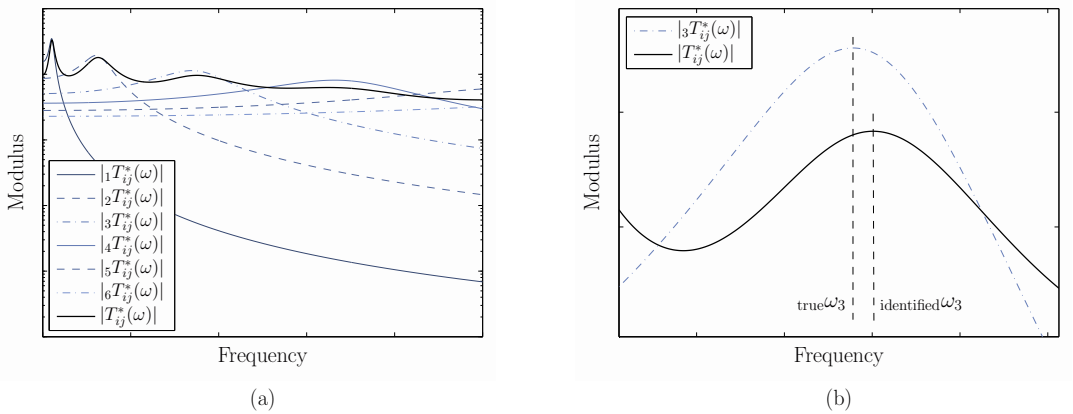

Figure 2.5: (a) Total transfer function, $T^*_{ij}(\omega)$, and first six modal transfer functions, ${}_rT^*_{ij}(\omega)$, relating the transverse displacement of the free end with that applied at the clamped end; (b) zoom of the third resonance.

Figure 2.5(a) shows the modulus of the modal transfer functions concerning to the first six bending modes and the total transfer function, all relating the transverse displacement of the free end with that applied at the base. In Figure 2.5(a) the relevance of the modal coupling is evidenced, being more significant for the higher order modes. As is better appreciated in the zoom of the third resonance shown in Figure 2.5(b), the modal coupling affects both the resonance frequency and the amplitude of the resonances. The identified

resonance frequency is higher than that of the mode under consideration, resulting in an overestimation of the determined storage modulus. Moreover, due to the contribution of the neighboring modes, the measured resonance (——) results wider and with lower amplitude than that of the mode to be identified (– · –). This fact, together with the improper determination of the natural frequency, results in an incorrect estimation of the modal loss factor.

Due to the modal coupling originated by the high damping level, SDOF modal analysis methods may provide reliable results only from the lower order resonances, considerably reducing the frequency bandwidth where the modal parameters are accurately identified. Therefore, for taking into account the influence of the neighboring modes and for properly identifying the modal parameters of highly damped systems, MDOF modal analysis methods may be applied.

MDOF modal analysis methods

The MDOF modal analysis methods consist on generating the frequency response of the system under study by superposition of normal modes. The difference between the measured and the computed frequency responses is determined and the modal parameters of the superposed modes are modified in order to obtain improved estimates. This procedure is repeated iteratively until the regenerated frequency response fits the experimental one and the modal parameters of all the modes converge.

Although the modal parameters are identified with higher accuracy because the influence of the neighboring modes is taken into account, the underlying hypothesis may be limiting since the frequency response is computed assuming real and non-frequency-dependent modal parameters. For the particular case of the analyzed CLD beams, this assumption is not acceptable as their modal parameters are complex and depend on frequency due to the non-uniform damping distribution and the frequency-dependent properties of the viscoelastic core.

Material parameters determination

After determining the modal parameters of the modes within the bandwidth under analysis, the material properties may be determined by analytical equations or inverse methodologies, as is schematized in Figure 2.3.

The procedure stablished by the standard ASTM E756-05 for identifying the complex shear modulus of the viscoelastic core, $G_{\mathrm{v}}^{*}(\omega)$, is based on analytic expressions. Assuming the Euler-Bernoulli hypothesis, the homogenized storage modulus of the CLD beam is determined from the resonance frequencies as follows:

$$E(\omega_r) = \frac{12\rho L^4 \omega_r^2}{H^2 C_r^2}, \tag{2.14}$$

where ρ is the homogenized volumetric density, L is the free length, H is the total thickness, and C_r is a coefficient for the rth mode related to the applied boundary conditions. According to the standard, the homogenized loss factor η is evaluated by the HPB method, given by Equation (2.10). With this procedure the homogenized complex modulus, $E^*(\omega_r) = E(\omega_r)\,(1 + \mathrm{i}\eta(\omega_r))$, is determined for each resonance frequency. After that, the complex shear modulus of the viscoelastic core $G_{\mathrm{v}}^*(\omega_r) = G_{\mathrm{v}}(\omega_r)\,(1 + \mathrm{i}\eta_{\mathrm{v}}(\omega_r))$ is determined according to the homogenization theory of Ross, Ungar, and Kerwin [107], detailed in Appendix A; where $G_{\mathrm{v}}(\omega_r)$ and $\eta_{\mathrm{v}}(\omega_r)$ are the shear modulus and the loss factor of the viscoelastic core for the ω_r resonance frequency, respectively.

Instead of considering analytical expressions for determining the dynamic properties from the identified modal parameters, several authors have proposed inverse methods based on numerical models defined by the finite element method (FEM). These iterative procedures minimize the differences between the experimental and numerical modal parameters computed by the defined FEM model in order to identify the dynamic properties of the material at the resonance frequencies. This type of procedures are applied by Shi *et al.* [113] and Barkanov *et al.* [11] for characterizing the shear complex modulus of viscoelastic layers of sandwich beams. A very similar methodology is applied by Jahani and Nobari [42] for identifying the storage modulus and the shear modulus of a structural adhesive, and by Qian *et al.* [103] for determining the elastic and dissipative properties of composite laminates. All these methods identifies the material properties just at the resonance frequencies.

In fact, the major drawback of the modal parameter-based procedures is that they offer discrete data for the dynamic properties at the resonance frequencies. Therefore, a large number of tests with different free lengths are commonly required for obtaining a sufficient data to fit the considered material constitutive model with certainty. The application of modal parameter-based procedures for characterizing strong frequency-dependent materials is a lengthy and time consuming process and it requires a relatively high level of operator interaction, even more when high damping materials are characterized. Finally, remark that a new approximation is made at the final stage of the characterization process when fitting the selected constitutive model to the identified discrete data.

2.3.2 Frequency response-based methods

The inverse methods based on the minimization of the experimental and numerical frequency responses are quite similar to those that minimizes the difference between the

experimental and numerical modal parameters. They also need to define a suitable numerical model, commonly by the finite element method, to be updated at each iteration. The main advantage of these methods is that they are not conditioned by the modal coupling originated by the high damping level of the material to be characterized. As well, instead of determining the material properties at the resonance frequencies, these methods directly identify the parameters of the considered constitutive model. Therefore, the dynamic properties of the material under analysis are determined within the frequency bandwidth under analysis and not just at resonances. Nevertheless, the hypotheses assumed when defining the FEM model, the election of the material constitutive model, and the way on how the numerical frequency response is computed, directly affects to the accuracy of the identified material properties.

Moreira and de-Carvalho [83] propose an inverse method for identifying the non-frequency-dependent elastic and dissipative properties of cork compounds. They consider beam type sandwich finite elements for defining the numerical model and they compute the theoretical frequency response by the direct frequency method.

Kim and Lee [53] present an inverse method for identifying the parameters of the four-parameter fractional derivative model considered to represent the complex modulus of viscoelastic materials in FLD configuration. Their method minimizes the difference between the experimental and theoretical magnitude of the frequency response function (FRF) experimentally measured and theoretically computed. However, they obtain the theoretical frequency response by modal superposition considering real and non-frequency-dependent modal parameters determined from the solution of the real eigenvalue problem. Thereby, the method may lose precision in the characterization of high damping and strong frequency-dependent materials.

A similar inverse method was recently proposed by Ren *et al.* [106] for characterizing the dynamic properties of the viscoelastic core of CLD beams in free-free configuration. Departing from FRFs measured at different temperatures, the proposed optimization procedure identifies the four parameters of the fractional derivative model in conjunction with the three parameters of the Williams–Landel–Ferry equation obtaining the master curve of the viscoelastic material. They consider an analytic sandwich model based on the RKU equations, and they compute the theoretical frequency response by normal mode superposition method showing the same drawback as the method proposed by Kim and Lee.

To overcome the limitations shown by the revised modal parameter-based and frequency response-based methods, a new inverse method is proposed. The features of the method and the stages to be completed for determining the dynamic properties of the viscoelastic material to be characterized, are detailed in the next section.

2.4 Proposed inverse method

The development of the present inverse method is motivated by the need to characterize the dynamic properties of high damping and strong frequency-dependent viscoelastic materials in a broad frequency bandwidth. As well, the other main reason that has led to develop the present method, is the need to reduce the huge amount of experimental tests demanded by the classical methodology stated by the standard ASTM E756–05. The objective is to provide a systematic procedure that simplifies the overall characterization process, carrying it out faster and more accurately. This method has been recently published in the *Journal of Sound and Vibration* [71], and presented in the *8th International Conference on Structural Dynamics* [74].

The proposed inverse method minimizes the residue between the experimental and theoretical frequency response at certain discrete frequencies in order to identify the parameters of the considered material constitutive model. The method departs from the experimental frequency response measured by the forced vibration test with resonance. First of all, the geometrical and physical properties of the tested specimen are specified in order to define the FEM model required to compute the theoretical frequency response. As well, a suitable material constitutive model to describe the frequency dependence of the dynamic properties of the viscoelastic material to be characterized is defined, and an initial guess for the parameters is provided. Then, the discrete frequencies, referred to as control frequencies, where the residue between the experimental and numerical transfer functions is computed, are selected following some provided criteria. Finally, suitable numerical methods for computing the theoretical frequency response and a minimization algorithm are required.

The parameters of the material constitutive model are modified at each iteration; the FEM model is updated and the numerical transfer function is computed at the selected control frequencies; the error is evaluated at such frequencies and the iterative process is repeated until the error becomes smaller than a certain specified tolerance or a maximum number of iterations is exceeded. Finally, the theoretical frequency response computed with the converged parameters is correlated with the experimental one for validating the identified dynamic properties. In Figure 2.6, the proposed inverse method is schematized.

Next, the required input data, the FEM model, the material constitutive model, the control frequencies selection criteria, the numerical procedure for computing the theoretical frequency response, and the minimization algorithm to completely characterize the dynamic complex shear modulus, $G_{\mathrm{v}}^{*}(\omega)$, of the tested CLD specimens by the proposed inverse method, are detailed. To conclude, some considerations concerning the selection of the response point, are provided.

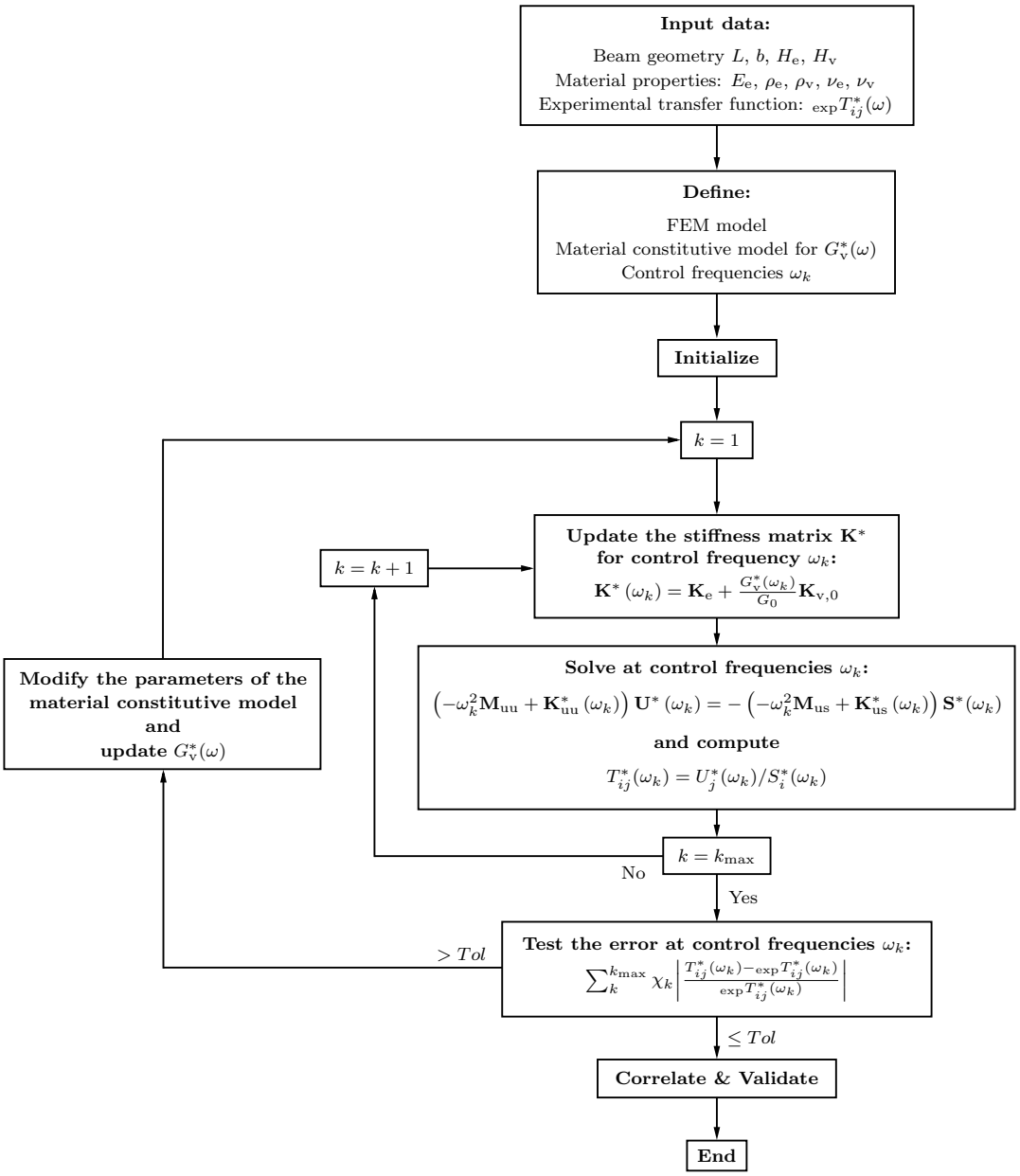

Figure 2.6: Scheme of the proposed inverse method for the dynamic characterization of viscoelastic materials in CLD configuration from the experimental transfer function of a single point.

2.4.1 Input data

The geometrical (L, b, H_{e} and H_{v}) and physical (E_{e}, ρ_{e}, ρ_{v}, ν_{e} and ν_{v}) properties of the beam under analysis must be specified in order to define the FEM model. Those properties are summarized in Section 2.2.2 except the storage modulus of the constraining layers E_{e}, which must be previously identified from the frequency response of CL specimens. Additionally, the experimental transfer function, ${}_{\mathrm{exp}}T^{*}_{ij}(\omega)$, must be provided.

2.4.2 Finite element model

The finite element model of a viscoelastically damped sandwich structure must adequately describe the high shear deformation given in the viscoelastic core, and may be defined in several different ways. The most straightforward alternative when working with commercial FEM codes is to define layered models using brick elements or combining plate and brick elements [44, 98, 82, 70]. These models effectively describe the dynamic behavior of CLD structures, but in general yield to large model sizes and the redefinition of the model may result a laborious task. In order to avoid those major limitations, several authors have proposed discrete layer finite element formulations for sandwich beams and plates.

In the present dissertation, a three-layer sandwich beam finite element was considered. This finite element is defined by two nodes with four degrees of freedom per node: longitudinal displacement u, transverse displacement v, rotation θ_z, and rotation due to the shear strain of the core ψ_z. All layers are assumed incompressible through the thickness, perfectly bonded and in plane stress state. Euler-Bernoulli theory is assumed for the elastic face layers and Timoshenko thory for the viscoelastic core. The element combines linear shape functions for the longitudinal displacement and for rotation due to the transverse shear of the core, and cubic shape functions for the transverse displacement, which avoids shear locking effects in the element. The displacement fields considered by this element have already been used by several authors, see References [109, 123, 39, 4] for more details. The formulation of this finite element is detailed in Appendix B.

The present finite element is formulated for thin soft core sandwich beams, and neglects the shear stress in the constraining layers. This is an acceptable approximation for the analyzed CLD beam, since the stiffness of the viscoelastic core is five orders of magnitude lower than the stiffness of the constraining layers. Nevertheless, when this assumption is no longer acceptable, a more general finite element formulation should be considered, e.g., that proposed by Plagianakos and Saravanos [96] for beams, or that proposed by Plagianakos and Saravanos [97] and/or by Moreira et al. [85] for plates, to account for the interlaminar shear stress continuity through the thickness.

2.4.3 Material constitutive model

Another prerequisite of the method is to define a material constitutive model that will satisfactorily reproduce the frequency dependence of the viscoelastic material to be characterized. Making use of the proposed inverse method, the parameters of the considered material model are identified.

A four-parameter fractional derivative model was considered for describing the frequency dependence of the complex shear modulus of the viscoelastic core $G_{\mathrm{v}}^{*}(\omega)$. The most remarkable feature of the fractional derivative models, is their ability for describing the frequency dependence of viscoelastic materials with a low number of parameters. The four-parameter fractional derivative model, also known as the generalized Zener model, is given by the fractional differential equation [6]

$$\sigma(t) + \tau^{\alpha} \frac{\partial^{\alpha} \sigma(t)}{\partial t^{\alpha}} = E_0 \epsilon(t) + E_{\infty} \tau^{\alpha} \frac{\partial^{\alpha} \epsilon(t)}{\partial t^{\alpha}}, \tag{2.15}$$

where E_0 is the static modulus, E_{∞} is the asymptotic modulus, τ is the relaxation time, and α is the fractional parameter, all to be identified from experimental data. Assuming that the Poisson's ratio ν_{v} is real and constant within the analyzed frequency bandwidth [100, 125], the complex shear modulus yields

$$G_{\mathrm{v}}^{*}(\omega) = \frac{G_0 + G_{\infty} (\mathrm{i}\omega\tau)^{\alpha}}{1 + (\mathrm{i}\omega\tau)^{\alpha}}, \tag{2.16}$$

where G_0 and G_{∞} are the static and asymptotic shear modulus, respectively.

In addition, for initializing the iterative process, an initial guess for the parameters of the material constitutive model must be specified, for example taking approximate values from bibliography [46].

2.4.4 Control frequencies

The so-called control frequencies, are discrete frequencies selected by the user where the residue between the experimental and the computed frequency responses is evaluated at each iteration. The use of control frequencies is proposed since they offer two main advantages. On the one hand, the experimental noise and the poor signal-to-noise ratio present on certain frequency bandwidths of an experimental frequency response are avoided. On the other hand, the efficiency of the method is significantly improved since the theoretical transfer function is determined just at the control frequencies.

The criteria for the selection of the control frequencies are those detailed next:

1. The control frequencies should be located at the resonances since they are characteristic of the dynamic response of the system under analysis, and a good signal-to-noise ratio is guaranteed.

2. A systematic procedure to select the control frequencies at each resonance consists on selecting the frequencies at the minimum and maximum of the real part, and at the maximum absolute value of the imaginary part.

3. The selection of three points at each resonance may be sufficient, but a greater number of control frequencies may provide a better fit of the theoretical response to the experimental one.

In Figure 2.7, a given resonance is plotted both in frequency domain and in the complex plane, where the control frequencies are selected following the provided criteria.

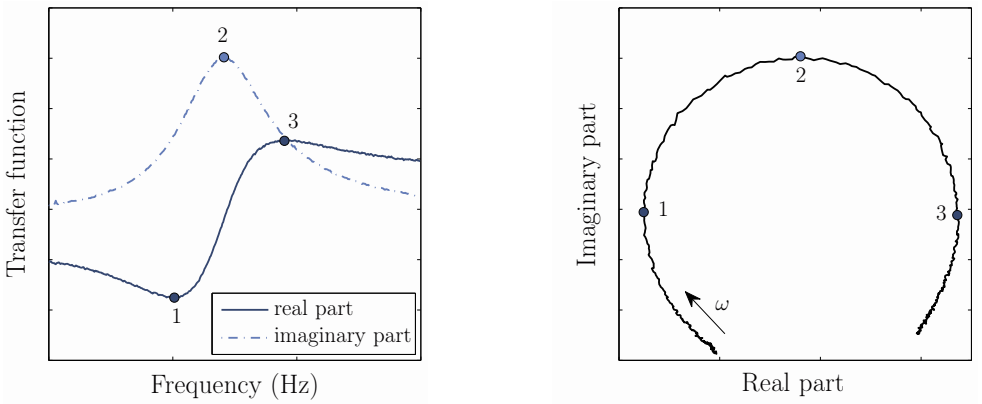

Figure 2.7: Example of the control frequencies selection (•) on a given resonance; (a) real and imaginary parts plotted in the frequency domain, and (b) in the complex plane.

This criteria was applied on the experimental examples except when the resonances were affected by the experimental noise. In those cases the control frequencies were selected manually as close as possible to the resonance frequency.

Furthermore, preference may be given to a certain frequency bandwidth considered of major relevance by the user. As stated in the third criterion, this can be done selecting more than three control frequencies at the resonances located within the bandwidth of interest, or conversely weighting coefficients may be defined for the three control frequencies selected within such bandwidth. The use of weighting coefficients was considered when experimentally characterizing the complex shear modulus of the viscoelastic core. Further details on how these weighting coefficients should be defined are provided when presenting the minimization algorithm in Section 2.4.6.

2.4.5 Theoretical frequency response

After selecting the control frequencies, a proper numerical method for computing the theoretical dynamic response of the CLD beams under analysis is required. The motion equation of a viscoelastically damped discrete system characterized by a structural damping model is governed by a set of ordinary, second-order non-linear differential equations, written as

$$\mathbf{M}\ddot{\mathbf{u}}(t) + \mathbf{K}^*(\omega)\mathbf{u}(t) = \mathbf{f}(t), \tag{2.17}$$

where $\mathbf{f}(t)$, $\ddot{\mathbf{u}}(t)$ and $\mathbf{u}(t)$ are the force, acceleration and displacement vectors, respectively, and the dot denotes differentiation with respect to time. $\mathbf{M}$ and $\mathbf{K}^*(\omega)$ are the mass and the frequency-dependent complex stiffness matrices, respectively. The complex stiffness matrix can be decomposed in a constant stiffness matrix, $\mathbf{K}_\mathrm{e}$, related to the elastic components, and another complex and frequency-dependent stiffness matrix, $\mathbf{K}^*_\mathrm{v}(\omega)$, related to the viscoelastic material, as follows:

$$\mathbf{K}^*(\omega) = \mathbf{K}_\mathrm{e} + \mathbf{K}^*_\mathrm{v}(\omega), \tag{2.18}$$

where

$$\mathbf{K}^*_\mathrm{v}(\omega) = \mathbf{K}_\mathrm{v}(\omega) + \mathrm{i}\mathbf{H}_\mathrm{v}(\omega), \tag{2.19}$$

being $\mathbf{K}_\mathrm{v}(\omega)$ and $\mathbf{H}_\mathrm{v}(\omega)$ the frequency-dependent stiffness and structural damping matrices, respectively.

If a harmonic mechanical excitation is considered, $\mathbf{f}(t) = \mathbf{F}^*\mathrm{e}^{\mathrm{i}\omega t}$, $\mathbf{F}^*$ being the complex vector of applied force amplitudes, the resultant steady-state response is also harmonic, $\mathbf{u}(t) = \mathbf{U}^*\mathrm{e}^{\mathrm{i}\omega t}$, $\mathbf{U}^*$ being the complex response (displacement) vector. Thus, the motion equation in frequency domain is written as,

$$\left(-\omega^2\mathbf{M} + \mathbf{K}^*(\omega)\right)\mathbf{U}^* = \mathbf{F}^*. \tag{2.20}$$

By contrast, the motion equation in frequency domain of a cantilever beam subjected to a steady-state harmonic base motion, $\mathbf{s}(t) = \mathbf{S}^*\mathrm{e}^{\mathrm{i}\omega t}$, may be written differentiating the degrees of freedom relative to the base displacement and the unknown displacements, indicated by $(\bullet)_\mathrm{s}$ and $(\bullet)_\mathrm{u}$ respectively, as

$$\left(-\omega^2 \begin{bmatrix} \mathbf{M}_{\mathrm{ss}} & \mathbf{M}_{\mathrm{su}} \\ \mathbf{M}_{\mathrm{us}} & \mathbf{M}_{\mathrm{uu}} \end{bmatrix} + \begin{bmatrix} \mathbf{K}^*_{\mathrm{ss}}(\omega) & \mathbf{K}^*_{\mathrm{su}}(\omega) \\ \mathbf{K}^*_{\mathrm{us}}(\omega) & \mathbf{K}^*_{\mathrm{uu}}(\omega) \end{bmatrix}\right) \begin{Bmatrix} \mathbf{S}^* \\ \mathbf{U}^* \end{Bmatrix} = \begin{Bmatrix} \mathbf{R}^* \\ \mathbf{0} \end{Bmatrix}, \tag{2.21}$$

where $\mathbf{S}^*$, $\mathbf{U}^*$ and $\mathbf{R}^*$ are the complex amplitude vectors of the applied base motion, unknown displacements, and reaction forces on the base, respectively.

The displacement amplitude vector $\mathbf{U}^*$, may be determined by modal superposition or direct frequency methods. Modal superposition method can be efficiently applied when the system is proportionally (classically) damped since the undamped modal matrix uncouples the equations of motion; therefore the computation of the undamped eigenvectors is sufficient for the damped response analysis. By contrast, if the system is non-proportionally (non-classically) damped, as is the case of the present CLD specimens, the undamped modal matrix is not orthogonal with respect to the damping matrix and the equations of motion in terms of the principal co-ordinates contain coupling terms. The eigenvectors that uncouples the equations of motion of non-proportionally damped systems are in general complex, and moreover, as viscoelastic materials present frequency-dependent properties, the complex modal parameters also depend on frequency. Although the complex mode superposition method may be applied for computing the dynamic response, the direct frequency method is considered for simplicity and efficiency.

As is schematized in Figure 2.6, the material parameters are modified at each iteration, the complex stiffness matrix related to the viscoelastic core is updated for each control frequency ω_k, as

$$\mathbf{K}^*_{\mathrm{v}}(\omega_k) = \frac{G^*_{\mathrm{v}}(\omega_k)}{G_0}\mathbf{K}_{\mathrm{v},0}, \tag{2.22}$$

where $\mathbf{K}_{\mathrm{v},0}$ is the static stiffness matrix related to the viscoelastic material; and the total complex stiffness matrix $\mathbf{K}^*(\omega_k)$ is obtained by Equation (2.18). The theoretical frequency response is computed for each control frequency ω_k solving the next equation derived from Equation (2.21)

$$\left(-\omega_k^2\mathbf{M}_{\mathrm{uu}} + \mathbf{K}^*_{\mathrm{uu}}(\omega_k)\right)\mathbf{U}^*(\omega_k) = -\left(-\omega_k^2\mathbf{M}_{\mathrm{us}} + \mathbf{K}^*_{\mathrm{us}}(\omega_k)\right)\mathbf{S}^*(\omega_k). \tag{2.23}$$

Finally, the theoretical transfer function for the control frequency ω_k, $T^*_{ij}(\omega_k)$, is determined as the experimental one given by Equation (2.9), relating the transverse displacement of the response point (jth DOF) with the transverse displacement applied at the excitation point (ith DOF), as

$$T^*_{ij}(\omega_k) = \frac{U^*_j(\omega_k)}{S^*_i(\omega_k)}. \tag{2.24}$$

2.4.6 Minimization algorithm

After determining the theoretical transfer function for each control frequency ω_k, a minimization algorithm is required for identifying the parameters of the material constitutive model. The minimization procedure was carried out by the Nelder-Mead algorithm [88] implemented in the *fminsearch* command of MATLAB® [77]. The residue between the experimental and theoretical transfer functions was minimized both in real and imaginary parts. Finally, since the Nelder-Mead simplex algorithm is an unconstrained optimization method, it must be verified whether the thermodynamic constraints are satisfied [9] ($G_\infty > G_0 > 0$, $\tau > 0$ and $0 < \alpha < 1$) at the end of the minimization process.

The minimization may be performed in several different ways. The simplest alternative is to consider a single experimental transfer function measured on a certain response point, so that the minimization function is given by

$$\sum_{k}^{k_{\max}} \chi_k \left| \frac{T_{ij}^*(\omega_k) - {}_{\exp}T_{ij}^*(\omega_k)}{{}_{\exp}T_{ij}^*(\omega_k)} \right|, \tag{2.25}$$

where χ_k is the weighting coefficient defined for the control frequency ω_k, and $k_{\max}$ is the total number of control frequencies. This routine may provide consistent results, nevertheless more sophisticated minimization procedures can be easily implemented in order to ensure the robustness of the identified material parameters. For instance, the residue between the theoretical and experimental transfer functions of several response DOFs can be simultaneously minimized. This way, the errors that may arise due to an imprecise laser vibrometer positioning may be compensated. In this case, the minimization function results

$$\sum_{j}^{j_{\max}} \sum_{k}^{k_{\max}} \chi_k \left| \frac{T_{ij}^*(\omega_k) - {}_{\exp}T_{ij}^*(\omega_k)}{{}_{\exp}T_{ij}^*(\omega_k)} \right|, \tag{2.26}$$

where $j_{\max}$ is the total number of considered response DOFs.

Furthermore, a more consistent minimization routine may be defined to also account for the variability of the results when testing several specimens. The alternative is to minimize the residue between the theoretical and experimental transfer functions of several response DOFs measured on different specimens simultaneously. This way, robust results can be obtained with a single minimization procedure simplifying the overall process. The minimization function is given by,

$$\sum_{s}^{s_{\max}} \sum_{j}^{j_{\max}} \sum_{k}^{k_{\max}} \chi_k \left| \frac{T^*_{s,ij}(\omega_k) - {}_{\exp}T^*_{s,ij}(\omega_k)}{{}_{\exp}T^*_{s,ij}(\omega_k)} \right|, \tag{2.27}$$

where $s_{\max}$ is the number of tested specimens; whereas $T^*_{s,ij}(\omega_k)$ and ${}_{\exp}T^*_{s,ij}(\omega_k)$ are the theoretical and experimental transfer functions relating DOF j and i of the sth specimen for the control frequency ω_k. This last minimization procedure is considered in the practical application.

During the minimization procedure preference may be given to certain control frequencies in order to improve the fit within a given frequency bandwidth considered of major relevance. To this end, weighting coefficients χ_k are applied to those control frequencies located within such frequency bandwidth. To define those values, first the minimization procedure is carried out without defining any weighting coefficient and then, if necessary, values are assigned to such coefficients in order to improve the global and/or the local fit.

2.4.7 Response DOF selection

Ideally, the proposed inverse method can be applied whatever the selected response DOF is, but in practice the election is conditioned by the quality of the measured frequency response at such DOF. The response DOFs located close to the free end are preferred since all the modes contribute significantly. By contrast, the points located close to the clamping device should be avoided since the transfer functions show a poor signal-to-noise ratio. As well, although the material parameters may be identified satisfactorily from the transfer functions measured close to the nodal points of the bending modes, special attention is required. When considering a response DOF close to a nodal point of a given mode, the influence of the laser vibrometer positioning error is magnified, so that no control frequencies should be selected at the resonance of such mode.

2.5 Results

The dynamic characterization of the CLD beams is carried out in two stages. First, the storage modulus of the elastic layers, E_{e}, is determined from the CL specimens and then, the dynamic shear complex modulus of the viscoelastic core, $G^*_{\mathrm{v}}(\omega)$, is characterized from the CLD specimens. After that, the identified dynamic properties are validated, and finally, the properties identified by classical procedures and by the present method are compared and discussed.

2.5.1 Elastic layers

The objective of testing the CL specimens was to identify the storage modulus of the metallic face layers, E_e, in order to define the FEM models of the CLD specimens. The dissipative properties of the metallic layers were neglected when defining the FEM model of the CLD beams since the nominal loss factor, $\eta_e = 1 \times 10^{-3}$ [1], is three orders of magnitude smaller than that of the viscoelastic core. Nevertheless, it was identified since it is an useful indicator to check if the amount of damping introduced by the clamping device is really negligible.

Three CL specimens were tested each with a different free length (150, 175 and 200 mm). In all cases, the transfer function of the response DOF located 5 mm from the free end was measured up to 1 kHz with a 0.3125 Hz resolution. The first four bending modes were detected for the 150 mm long CL beam, and the first five bending modes for the 175 and 200 mm long CL beams. The storage modulus values, E_e, were computed from the identified resonance frequencies by Equation (2.14), whereas the modal loss factor values, η_e, where determined by the HPB method using Equation (2.10). In Table 2.2, the mean values and the standard deviations of the storage modulus and the loss factor identified from all the detected resonances are summarized for the three tested specimens.

Table 2.2: Identified material parameters of the elastic layers.

Free length	E_e (Pa)	η_e
150 mm	$201.8 \pm 1.3 \times 10^9$	$3.9 \pm 1.5 \times 10^{-3}$
175 mm	$200.9 \pm 1.3 \times 10^9$	$3.4 \pm 1.7 \times 10^{-3}$
200 mm	$202.6 \pm 1.4 \times 10^9$	$3.1 \pm 1.6 \times 10^{-3}$

The readings in Table 2.2 showed little deviation between the results obtained from the three specimens. The final value for the storage modulus was determined as the mean value of the three results. Nevertheless, due to the uncertainty involved in the measurement of the geometrical and physical magnitudes detailed in Table 2.1, the final value for the storage modulus was $202 \pm 6 \times 10^9$ Pa.

By contrast, the identified loss factor was slightly larger than the nominal one as a consequence of the clamped boundary condition employed in the experimental test. Anyway, this source of damping was small enough, so that it was neglected when characterizing the viscoelastic core from the dynamic response of the CLD specimens. When the accurate determination of the loss factor of lightly damped structures is required, the clamped boundary condition shown in Figure 2.1 should be replaced by a free-free boundary condition in order to avoid all sources of damping except that of the material under study.

2.5.2 Viscoelastic core

For characterizing the dynamic complex shear modulus of the viscoelastic core, $G_{\mathrm{v}}^{*}(\omega)$, three CLD specimens were tested each with three different free lengths (170, 210 and 250 mm), so that in total nine tests were carried out. In order to compensate the errors that may arise from an imprecise laser vibrometer positioning, in each test two response points located at 5 and 10 mm from the free end were considered. So in total, eighteen transfer functions were measured up to 1 kHz frequency bandwidth with a 0.3125 Hz resolution.

For each free length a minimization procedure was carried out. As three specimens were tested with each free length, and two transfer functions measured per specimen, six transfer functions were considered for each minimization procedure. The minimized function was that given by Equation (2.27), and for each free length, a set of material parameters (G_0, G_∞, τ and α) was identified. Finally, a single set of parameters that describes the mean of the real and imaginary parts of the complex shear modulus was identified. The dynamic properties described by these latter parameters were considered the final results, and are employed on all the subsequent analyses.

In the transfer functions measured on the 170, 210 and 250 mm long CLD beams, the first four, five and six bending modes were detected, respectively. For the 170 and 210 mm long CLD beams, three control frequencies were selected at each resonance following the stablished criteria. For the 250 mm long one, the fourth resonance was disregarded as was affected by the experimental noise. As well, the three control frequencies of the second, fifth and sixth resonances were manually selected in order to avoid the negative influence of the experimental noise. Three numerical models were defined for each free length using 5 mm long sandwich beam-type finite elements described in Section 2.4.2. The three beams were discretized into 34, 42 and 50 finite elements defined by 35, 43 and 51 nodes, yielding to 136, 168 and 200 DOFs, respectively. The considered minimization function was that given by Equation (2.27), i.e., the residue between the six theoretical and experimental transfer functions measured at two different DOFs on the three specimens with the same free length, was minimized. The initial guesses for the four parameters were $G_0 = 1 \times 10^5$ Pa, $G_\infty = 1 \times 10^8$ Pa, $\tau = 1 \times 10^{-6}$ s and $\alpha = 0.5$ [70]. As well, weighting coefficients were defined in order to improve the fit at certain frequencies guaranteeing a proper overall fit. In Table 2.3 the used weighting coefficients are summarized.

In Figure 2.8, the modulus and the phase of the experimental and identified transfer functions regarding the transverse displacement of the DOF located 5 mm from the free end when a transverse displacement is applied on the base, can be seen for the three tested beam lengths.

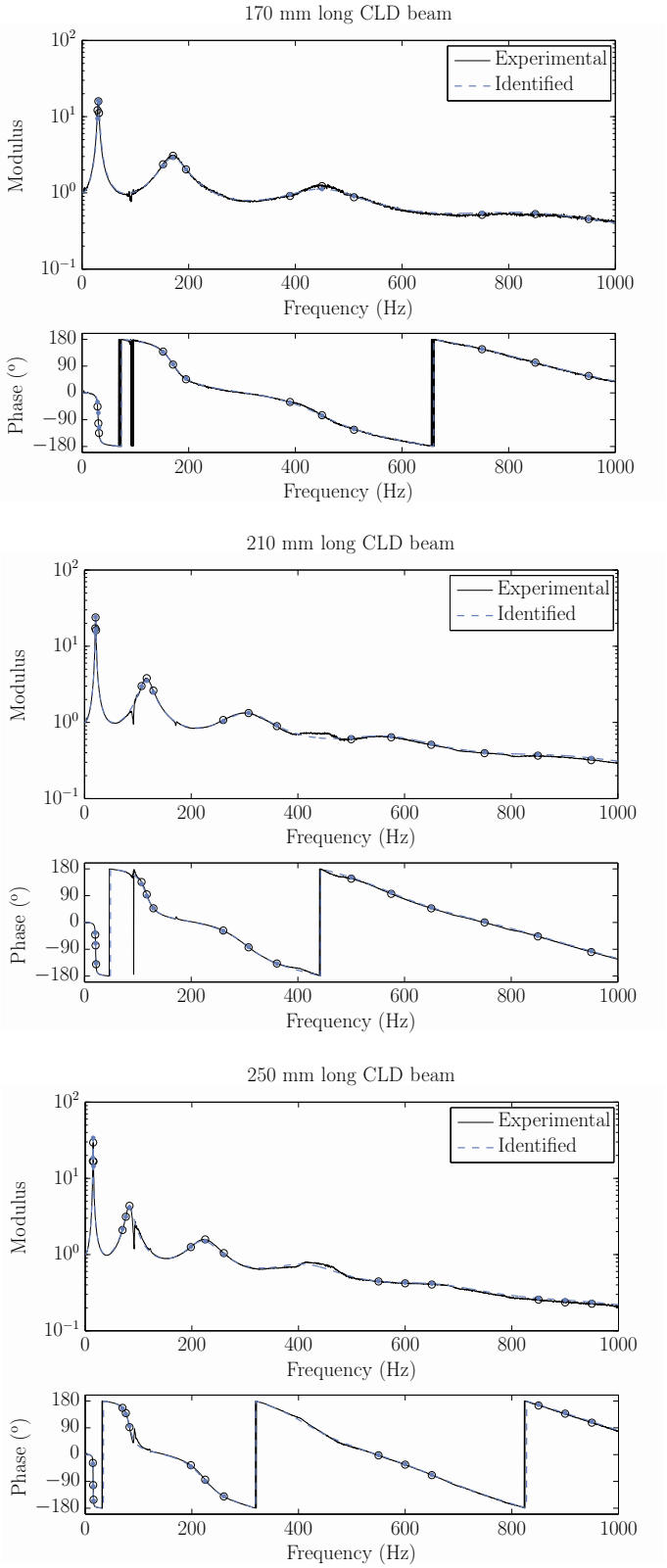

Figure 2.8: Modulus and phase of the experimental and identified transfer functions of the 170, 210 and 250 mm long CLD beams regarding the transverse displacement of the DOF located 5 mm from the free end when a base motion is applied; (∘) experimental values and (•) identified values at the selected control frequencies.

Table 2.3: Defined weighting coefficients.

Free length	Resonances					
	1st	2nd	3rd	4th	5th	6th
170 mm	1	5/2	1	3/2	—	—
210 mm	3/4	7/4	9/4	9/4	1	—
250 mm	1	1	3/2	—	2	1

Good correlation was observed between the experimental and the identified transfer functions for all the tested free lengths. For the 170 mm long CLD beam, the major deviations were localized at the third resonance, but these discrepancies were due to the experimental noise manifested in all the transfer functions between 400 and 500 Hz. Apart from that, the larger deviations were localized at the first resonance, the identified resonance frequency and the amplitude resulting 2.8 % and 7.8 % larger, respectively. For the 210 mm long one, the major discrepancies were localized at the second resonance, the identified resonance frequency and the amplitude being 1.5 % and 6.8 % underestimated, respectively. For the 250 mm long CLD beam, the greatest differences were localized at the first resonance, although the identified resonance frequency matched with the experimental one, the amplitude of the identified transfer function was 11.3 % larger. By contrast, the deviations observed in the second and the fourth resonances were originated by the experimental noise.

The material parameters identified from the transfer functions measured at 5 and 10 mm from the free end, on the three specimens with the same free length, are gathered in each of the rows of Table 2.4. As well, the parameters that describe the mean of the real and imaginary parts of the complex shear modulus are given in the fourth row. From now on, these latter parameters are considered the final results and are used in all the following analyses.

Table 2.4: Identified parameters of the four-parameter fractional derivative model from the 170, 210 and 250 mm long CLD specimens, and computed mean values.

Free length	Identified parameters			
	G_0 (Pa)	G_∞ (Pa)	τ (s)	α
170 mm	3.462×10^5	3.179×10^9	8.791×10^{-9}	0.682
210 mm	3.488×10^5	2.865×10^9	7.950×10^{-9}	0.667
250 mm	3.558×10^5	3.030×10^9	8.425×10^{-9}	0.676
mean values	3.504×10^5	3.062×10^9	8.230×10^{-9}	0.675

In Figure 2.9, the complex shear modulus described by the parameters identified from each free length (the first three rows of Table 2.4), and the mean complex shear modulus described by the final parameters (fourth row of Table 2.4), are plotted.

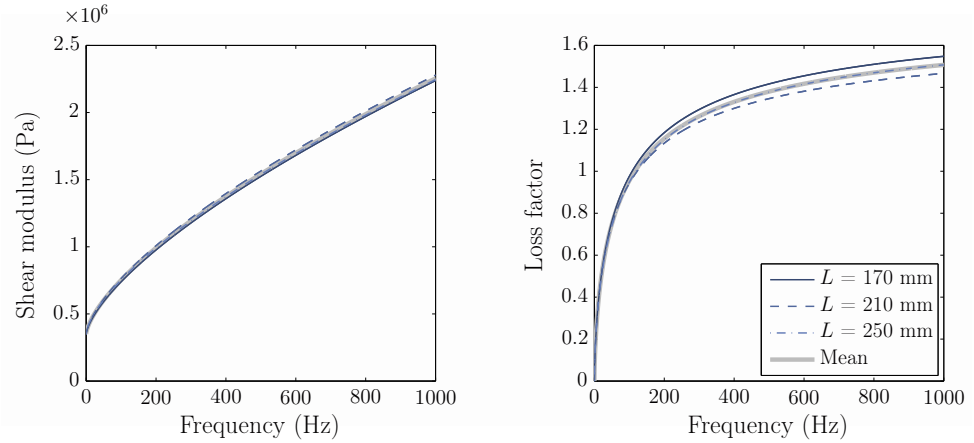

Figure 2.9: Identified complex shear modulus of the viscoelastic core from the 170, 210 and 250 mm long CLD specimens, and the computed mean complex shear modulus.

From Figure 2.9, the low dispersion of the three identified complex shear modulus was remarkable, being the deviations greater for the loss factor. The differences at 1 kHz were inferior to 1.8 % and 5.4 % for the shear modulus and the loss factor, respectively. As well, the high damping capacity and strong frequency dependence of the elastic and dissipative properties of the viscoelastic material were observed, in which the end of the rubbery zone and the beginning of the transition zone were evidenced [46].

2.5.3 Validation

In order to validate the identified final material properties, the dynamic response of the whole beam was correlated. To this end, transfer functions of 10 mm equi-spaced response DOFs were measured along the length on one of the three tested specimens for each of the free lengths. Therefore 17, 21 and 25 frequency responses were measured on the 170, 210 and 250 mm long beams, respectively.

The correspondence degree of the experimental and theoretical frequency responses was analyzed by two global correlation indices proposed by Zang *et al.* [133]. These indicators correlate the experimental and theoretical spatial deflection exhibited by the structure at each excitation frequency both in shape and in amplitude. The first indicator is the *Global Shape Correlation* (GSC) function, which is sensitive to shape differences, being defined as

$$\mathrm{GSC}(\omega_k) = \frac{\left|{}_{\mathrm{exp}}\mathbf{T}^{*\mathrm{H}}(\omega_k)\mathbf{T}^{*}(\omega_k)\right|^2}{\left({}_{\mathrm{exp}}\mathbf{T}^{*\mathrm{H}}(\omega_k){}_{\mathrm{exp}}\mathbf{T}^{*}(\omega_k)\right)\left(\mathbf{T}^{*\mathrm{H}}(\omega_k)\mathbf{T}^{*}(\omega_k)\right)}, \tag{2.28}$$

where $(\bullet)^{\mathrm{H}}$ denotes the conjugate transpose and, ${}_{\mathrm{exp}}\mathbf{T}^{*}(\omega)$ and $\mathbf{T}^{*}(\omega)$ are the matrices that comprise the experimental and theoretical transfer functions measured at all the response DOFs, respectively. Note that this correlation indicator is similar to the *Modal Assurance Criterion* (MAC) indicator, except that the GSC is evaluated at each excitation frequency ω_k. As the MAC indicator, GSC assumes values between [0,1] where 1 means perfect correlation and 0 means no correlation at all. Nevertheless, as the MAC indicator, the GSC indicator is unable to detect scaling errors being only sensitive to discrepancies in the overall deflection shape. The authors [133] also propose a supplementary indicator, the *Global Amplitude Correlation* (GAC), to detect the discrepancies in amplitude at each excitation frequency. The GAC indicator is given by

$$\mathrm{GAC}(\omega_k) = \frac{2\left|{}_{\mathrm{exp}}\mathbf{T}^{*\mathrm{H}}(\omega_k)\mathbf{T}^{*}(\omega_k)\right|}{{}_{\mathrm{exp}}\mathbf{T}^{*\mathrm{H}}(\omega_k){}_{\mathrm{exp}}\mathbf{T}^{*}(\omega_k) + \mathbf{T}^{*\mathrm{H}}(\omega_k)\mathbf{T}^{*}(\omega_k)}. \tag{2.29}$$

As the GSC indicator, the GAC offers values limited between 0 and 1, where 0 mean no correlation at all and 1 means perfect correlation. The simultaneous use of both correlation criteria offers a global quantification of the closeness of two vibration data sets, both in shape and amplitude.

Next, the correlation degree between the experimental dynamic response and that computed with the final material properties is analyzed for the three tested free lengths. In Figure 2.10 the GSC and GAC global correlation indicators for the three tested free lengths are shown.

As concluded from Figure 2.10, the global correlation in shape and in amplitude was good for the analyzed frequency bandwidth, being both the GSC and GAC indicator values very close to the unity for the three free lengths. The discrepancies mainly observed at 100 Hz and within 400 and 500 Hz were originated by the experimental noise.

With the presented analysis the robustness of the identified final dynamic properties was proved. The dynamic response of the 170, 210 and 250 mm long specimens was satisfactorily reproduced showing a good global correlation degree both in shape and amplitude. Therefore, from now on, these material properties will be considered for all the subsequent analyses.

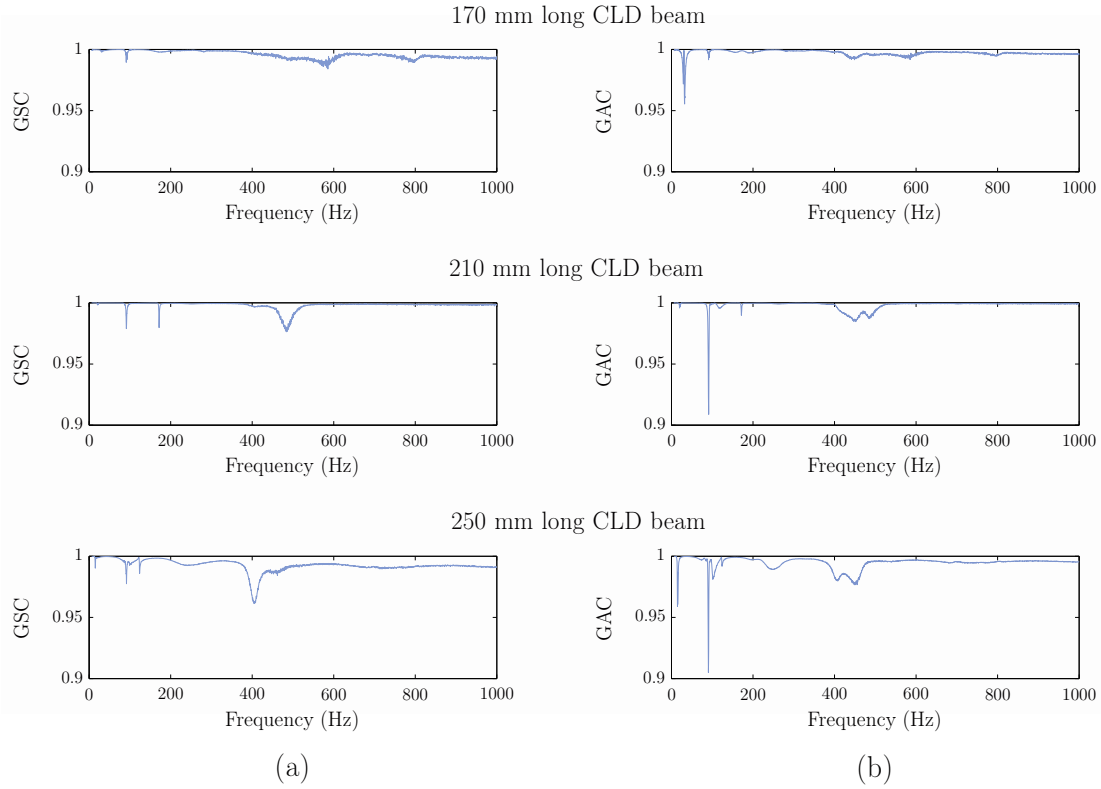

Figure 2.10: GSC (a) and GAC (b) indicators for the three analyzed free lengths.

2.5.4 Discussion

The objective of this discussion is to compare the dynamic properties identified by the proposed inverse method, with those determined by the classical procedure stated by the standard ASTM E756–05, and with other widely used SDOF methods, such as the n dB bandwidth and circle-fit methods. To this end, a single specimen was considered with the three different free lengths already mentioned (170, 210 and 250 mm). In the three cases, the transfer functions were measured at 5 mm from the free end.

First, the HPB, n dB bandwidth (with $n = 1$), and circle-fit SDOF modal analysis methods were applied to the transfer function measured on the 210 mm long CLD beam in order to show the accuracy of each method. The HPB and n dB methods only were applicable on the first three resonances and the circle-fit method on the first four resonances. In Figure 2.11, the complex shear modulus identified by the proposed inverse method and the discrete values identified by the SDOF modal analysis methods are shown.

As can be seen in Figure 2.11, the three SDOF modal analysis methods offered similar results for the first two resonances, but large differences were noticed on the results obtained from the third resonance. This discrepancies were mainly originated by the non

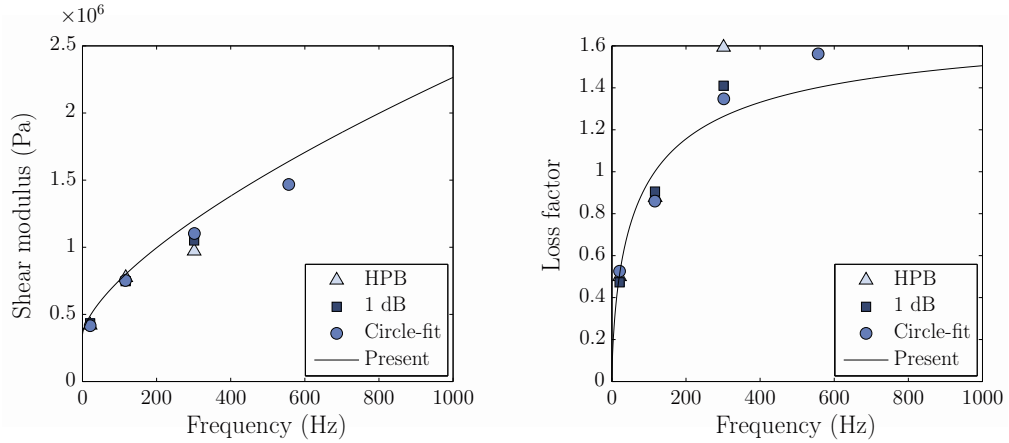

Figure 2.11: Complex shear modulus of the viscoelastic core identified by the present method and by the SDOF modal analysis methods from the transfer function measured on the 210 mm long beam at the DOF located 5 mm from the free end.

negligible modal coupling. The HPB was the most sensitive method to the modal coupling, but this influence was reduced by using the n dB bandwidth method or even more, by the circle-fit method. Nevertheless, the differences observed on the results obtained from the fourth resonance revealed that the circle-fit method was also affected by the modal coupling, which is more important for the higher order modes. Therefore, from this analysis was proved that the main limitation when using SDOF modal analysis methods for identifying the modal parameters of highly damped MDOF systems is the modal coupling, which reduces drastically the frequency bandwidth where the material properties can be accurately determined. In the present example, similar results were obtained up to 100 Hz with the proposed inverse method and with the procedure stablished by the standard ASTM E756–05, i.e., with the HPB method; and up to 300 Hz making use of the n dB bandwidth and circle-fit methods.

After analyzing the ability of the different SDOF modal analysis methods, the complex shear modulus was also identified from the transfer functions measured on the 170 and 250 mm long beams, but now only by the circle-fit method. The circle-fit method was applied to the resonances that were not negatively affected by the experimental noise. Therefore, the method was applied to the first two, and to the first four resonances of the 170 and 210 mm long CLD beams, respectively; and to the first and third resonances of the 250 mm long beam. In Figure 2.12, the discrete values identified from the three transfer functions are shown.

As evidenced from Figure 2.12, the results obtained by the circle-fit method presented a noticeable scatter being the deviations larger for the loss factor. As well, the deviations were larger for the higher frequencies because the modal coupling effect is more significant

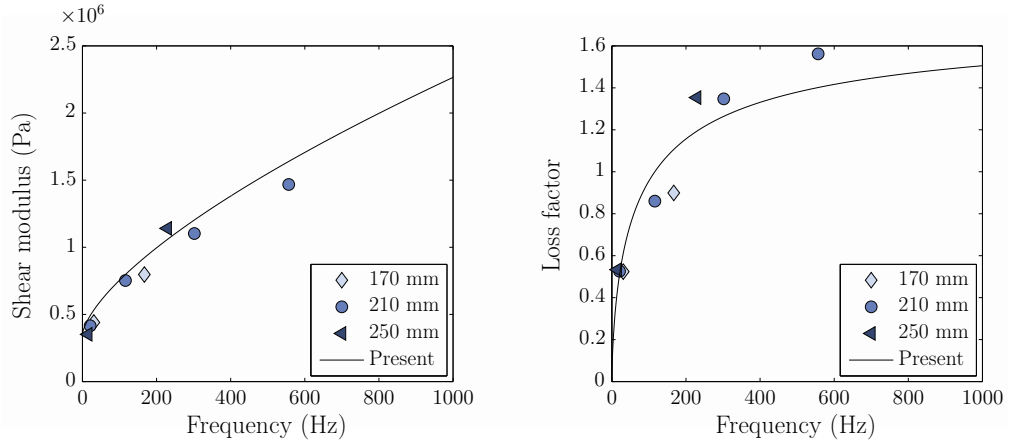

Figure 2.12: Complex shear modulus of the viscoelastic core identified by the present method and by the circle-fit method from transfer functions measured on the 170, 210 and 250 mm long beams at the DOF located 5 mm from the free end.

for the higher order modes. The dispersion of the results highlighted the difficulty to accurately determine the modal parameters of the tested CLD specimens. Moreover, while SDOF methods only provided discrete data at the resonance frequencies, the proposed inverse method identified the parameters of the four-parameter fractional derivative model, the complex shear modulus being determined up to 1 kHz.

As the SDOF modal analysis methods provide discrete results, specimens with several free lengths must be tested in order to fit the fractional derivative model with certainty, resulting in a cumbersome and time consuming process. Moreover, another approximation is made when the fractional derivative model is fitted to the experimental discrete data. By contrast, the proposed inverse method allowed characterizing high damping and strong frequency-dependent viscoelastic materials from few experimental tests, saving the required time for testing and data processing.

2.6 Conclusions

In this chapter, the dynamic characterization of high damping and strong frequency-dependent viscoelastic materials, has been addressed. Different analysis methods for determining the dynamic properties of viscoelastic materials from vibration test data measured by the forced vibration test with resonance have been reviewed. The limitations of such methods for characterizing high damping materials have been discussed, and a new inverse method has been proposed. The main conclusions derived from this analysis are summarized next.

When applied on the dynamic response of SDOF systems, the HPB and n dB bandwidth methods only provide reliable results for lightly damped systems with non-frequency-dependent properties. By contrast, the circle-fit method offers accurate results not being conditioned by the damping level. Nevertheless, all these methods are not suitable for the analysis of highly damped MDOF systems due to the modal coupling.

The MDOF analysis methods provide more precise modal parameter estimates, but are not suitable for characterizing the tested CLD specimens since the theoretical frequency response is computed by normal mode superposition method.

Modal parameter-based methods determine the material properties at the resonance frequencies, demanding a large amount of experimental tests and a final curve fitting procedure, resulting in a laborious and lengthy process.

The frequency response-based characterization methods identify the parameters of the material constitutive model reducing the required number of tests. However, the accuracy of these methods depends on the hypotheses assumed when defining the numerical model and the considered numerical method for determining the theoretical frequency response.

A new frequency response-based inverse method has been proposed for identifying the parameters of the considered material constitutive model. The novel use of the control frequencies makes the method insensitive to the experimental noise and the efficiency is notably improved. The direct frequency method has been considered for computing the theoretical frequency response, so the applicability of the method is neither affected by the damping level nor by the frequency dependence of the material. The effectiveness of the method has been proved with the experimental dynamic characterization of the viscoelastic core of CLD cantilever beams.

The proposed inverse method has allowed characterizing high damping and strong frequency-dependent viscoelastic materials in a broad frequency bandwidth from few experimental tests, saving the time required for testing and data processing.

This method has been published in the *Journal of Sound and Vibration* [71] and presented in the *8th International Conference on Structural Dynamics* [74].

Chapter 3

Frequency-Temperature-Prestrain characterization

To predict the dynamic response of formed CLD specimens, the influence of the static prestrain on the dynamic properties of the viscoelastic core must be taken into consideration. So that, the main objective of the present chapter is to characterize such dependency by means of experimental tests. To this end, *dynamic mechanical analysis* (DMA) technique is considered, as it allows precisely controlling the frequency, the temperature and the static prestrain level.

First, tests to verify that similar dynamic properties are identified by DMA and by the forced vibration test with resonance, are completed. Frequency sweeps are conducted at several temperatures under isothermal conditions, the master curve of the viscoelastic material is constructed, and the determined dynamic properties are compared with those identified in Chapter 2 for the same temperature. The results obtained by both experimental techniques are compared, and the dynamic properties are identified in a wider bandwidth.

After checking that both methods yield to comparable dynamic properties, the influence of the static prestrain on the complex shear modulus of the viscoelastic core, is analyzed. Several frequency sweeps are executed under different static prestrain levels while the temperature is hold constant. With these tests, the frequency-prestrain dependency of the viscoelastic core is determined, and a new material model to describe such dependency is proposed and validated. The use of the DMA technique for characterizing the static prestrain dependence of constrained viscoelastic films is novel, and the presented results proves that is a suitable technique. The proposed material model is applied later for the dynamic analysis of formed CLD beams in Chapter 5.

Finally, the influence of the frequency, temperature and the static prestrain on the elastic and dissipative properties of the viscoelastic core is compared and discussed.

3.1 Introduction

Dynamic mechanical analysis (DMA) technique can be used for measuring the dynamic properties of viscoelastic materials either by transient (creep and relaxation tests) or oscillatory tests. The oscillatory tests are commonly employed to characterize the frequency dependence of the elastic and dissipative properties of such materials. Nevertheless, time-frequency interconversion methods can also be applied to obtain the dynamic properties in frequency domain from transient tests, see for example the works of Park and Schapery [95], Schapery and Park [110] or Emri *et al.* [33], for more details.

The oscillatory test consists on applying a harmonic strain (or stress) in extension, bending, torsion or shear and measuring the induced stress (or strain) under steady-state oscillatory conditions. Linearity implies that the induced stress (or strain) is also harmonic, with an amplitude proportional to that of the strain (or stress), but with a time or phase lag between both. The ideal elastic samples exhibit a 0° phase lag, whereas the ideal viscous samples show a 90° phase difference. Since a viscoelastic material has properties intermediate between those of an ideal elastic and an ideal viscous material, the exhibited phase lag is between 0° and 90°. This latter parameter measures the relative degree of viscous to elastic character of the tested material. For further details about the dynamic mechanical analysis and the more general *dynamic mechanical thermal analysis* (DMTA) techniques, see for example the handbooks of Menard [80], Ward and Sweeney [130] or, Menczel and Prime [81].

In the present work, oscillatory tests were considered, and the applied strain was the controlled parameter. In Figure 3.1, the steady-state response of a harmonically excited viscoelastic sample can be seen, where the time lag Δt between the stress and the strain, is evidenced.

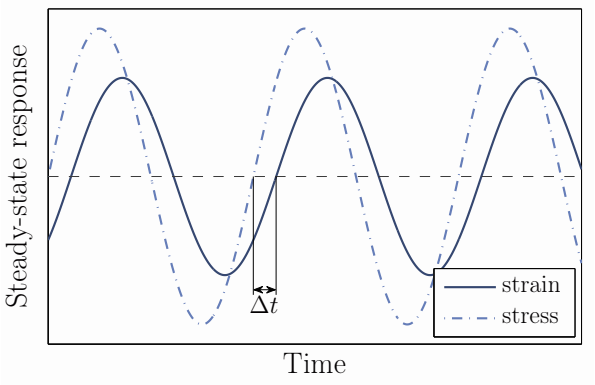

Figure 3.1: Steady-state response of a viscoelastic material under harmonic excitation.

From the amplitudes relation and the time lag between the stress and strain histories, the complex modulus of the material is characterized for the test excitation frequency and temperature. The procedure to determine the dynamic properties from the measured force and displacement data is detailed in Section 3.2.2.

To characterized the frequency, temperature and prestrain dependence exhibited by the dynamic properties of the viscoelastic core, three sets of DMA oscillatory tests are considered with different purposes:

The first set of tests aims to determine the linear viscoelastic range of the tested material. To this end, several amplitude sweeps are executed under the extreme excitation frequency and temperature conditions, in order to determine the maximum applicable strain level.

With the second set of tests the frequency and the temperature dependence of the viscoelastic core is characterized. For such purpose, several frequency sweeps are conducted at different temperatures under isothermal conditions. The master curve of the viscoelastic core is obtained making use of the *frequency–temperature superposition* principle [35]. Another major objective of these tests is to verify that similar results are obtained for a given test temperature by the DMA and by the forced vibration test with resonance technique already applied in Chapter 2.

Once proved that both experimental techniques lead to comparable dynamic properties, a third set of tests to characterize the static prestrain dependence is executed. To this end, frequency sweeps are executed under different static prestrain levels and isothermal conditions. The influence of the static prestrain in the elastic and dissipative properties of the viscoelastic core is analyzed, and a new material model to characterize such dependency is proposed and validated. The use of DMA tests for characterizing the frequency-prestrain dependence of constrained viscoelastic films is novel, and the suitability of this technique is proved with the presented results.

To conclude, the influence of the frequency, the temperature, and the static prestrain on the elastic and dissipative properties of the viscoelastic material is compared and discussed.

3.2 Experimental technique

In this section the employed experimental set-up, the specimens and the test configuration, are described. Then, the procedure for determining the complex shear modulus of the viscoelastic core, G_v^*, from the measured force and displacement data, is reviewed. Finally, the linearity analysis performed before conducting the tests for characterizing the temperature and the static prestrain influences, is presented.

3.2.1 Experimental set-up and specimens

The DMA tests were undertaken by a *Q800* DMTA machine of *TA Instruments* [41] in the *Centre Català del Plàstic* (CCP). The specimens were tested in tension configuration placing the samples between a fixed and moveable clamp as shown in Figure 3.2.

Figure 3.2: Tension test configuration (*Q800* DMTA machine of *TA Instruments*).

The upper clamp is fixed, whereas the excitation force or displacement, is applied to the sample with the lower movable clamp. The samples were positioned vertically and the dynamic loads were applied in the longitudinal direction. To induce pure shear deformation in the viscoelastic core, both constraining layers were cut leaving a certain distance between the cuts, thus defining samples similar to single lap joints. The employed test configuration permitted to conduct frequency sweeps under different static preload levels, allowing to characterize the influence of the static prestrain level on the dynamic properties of the viscoelastic core. In Figure 3.3, a photograph of the tested specimens and the schematized test configuration, can be seen.

Regarding Figure 3.3(b), F_0 is the static preload, $h(t)$ is the applied harmonic displacement excitation, $b = 5$ mm is the width, H is the total thickness of the specimen, $l = 5$ mm is the overlap or distance between cuts, and $l_{\text{clamp}} = 8$ mm is the distance between clamps. All the geometrical and test parameters were defined following the indications of the DMTA machine manufacturer [41].

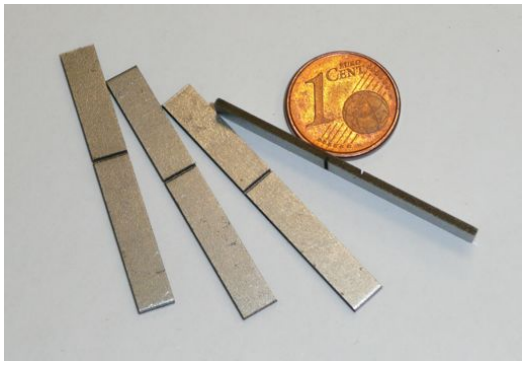

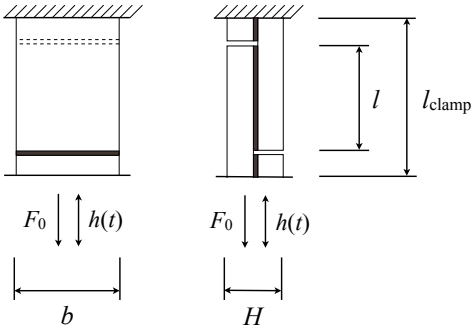

(a) (b)

Figure 3.3: (a) Tested specimens, and (b) scheme of the test configuration.

3.2.2 Material parameter extraction

When performing DMA oscillatory tests the applied force or displacement may be the controlled variable. In all the conducted tests, the applied displacement was the controlled parameter, which maximum amplitude was determined after carrying out a linearity analysis detailed in the next section. From the force and position measurements, the complex shear modulus of the viscoelastic core, $G_{\mathrm{v}}^{*}(\omega)$, was identified.

In Figure 3.4, the applied displacement h, the corresponding shear strain γ, and the shear stress τ induced in the viscoelastic core, are represented.

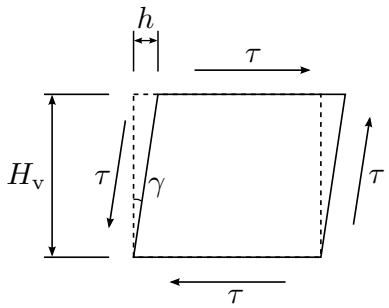

Figure 3.4: Shear deformation of the viscoelastic core.

The shear strain γ, is determined from the applied displacement h, as follows:

$$\gamma = \arctan\left(\frac{h}{H_{\mathrm{v}}}\right), \tag{3.1}$$

where H_{v} is the thickness of the viscoelastic core. The induced shear stress τ, is determined relating the measured dynamic force F, with the overlap area A, so that

$$\tau = \frac{F}{A}, \tag{3.2}$$

the overlap area being $A = bl$, as deduced from Figure 3.3(b).

After calculating the shear strain and stress from the displacement and force data, the next step consists on determining the shear complex modulus of the viscoelastic core, G_{v}^{*} [80]. The harmonic shear strain related to the applied harmonic displacement for the angular frequency ω, is given by

$$\gamma(t) = \gamma_{\max} \mathrm{e}^{\mathrm{i}\omega t}, \tag{3.3}$$

where $\gamma_{\max}$ is the amplitude of the shear strain. Assuming linearity between the stress and the strain, a harmonic shear stress is induced with a time or phase lag, so that

$$\tau(t) = \tau_{\max} \mathrm{e}^{\mathrm{i}(\omega t + \delta)}, \tag{3.4}$$

where $\tau_{\max}$ is the amplitude of the shear stress, and $\delta = \omega \Delta t$ is the phase lag between the shear strain and stress. The complex shear modulus G_{v}^{*}, is determined by

$$G_{\mathrm{v}}^{*} = \frac{\tau(t)}{\gamma(t)} = \frac{\tau_{\max}}{\gamma_{\max}} \mathrm{e}^{\mathrm{i}\delta} = \frac{\tau_{\max}}{\gamma_{\max}} \left(\cos\delta + \mathrm{i}\sin\delta\right). \tag{3.5}$$

Therefore, the shear modulus G_{v}' and the shear loss modulus G_{v}'' result

$$G_{\mathrm{v}}' = \frac{\tau_{\max}}{\gamma_{\max}} \cos\delta \tag{3.6}$$

and

$$G_{\mathrm{v}}'' = \frac{\tau_{\max}}{\gamma_{\max}} \sin\delta, \tag{3.7}$$

respectively. From where the loss factor η_{v} is defined relating the imaginary and the real part of the complex shear modulus as,

$$\eta_{\mathrm{v}} = \frac{G_{\mathrm{v}}''}{G_{\mathrm{v}}'} = \tan\delta. \tag{3.8}$$

Following the described procedure, the complex shear modulus of the viscoelastic core is identified for the considered discrete excitation frequency. Remark that this procedure is valid only if the specimens are tested within the linear viscoelastic range. Thus, before performing the oscillatory tests for characterizing the temperature and static prestrain dependence of the core, a linearity analysis was conducted to determine the maximum applicable strain level, i.e., to identify the limit of the linear viscoelastic range of the viscoelastic material under study.

3.2.3 Linearity analysis

The linear viscoelasticity assumes that the elastic and dissipative properties of the viscoelastic material do not depend on the applied strain level. In practice, the real polymeric materials behave linearly only within a certain range, so that the limit of the linear viscoelastic range must be experimentally determined before performing any oscillatory test.

To this end, amplitude sweeps were executed on four different specimens under different excitation frequencies and temperatures. To ensure that all the tests conducted for the frequency-temperature characterization where carried out within the linear viscoelastic range, four linearity tests were carried out considering the extreme environmental conditions and the maximum excitation amplitude was determined for each of the test conditions. The first linearity test was conducted with $T = 30$ °C and $f = 0.5$ Hz, the second one with $T = 30$ °C and $f = 200$ Hz, the third one with $T = 70$ °C and $f = 0.5$ Hz, and the fourth one with $T = 70$ °C and $f = 200$ Hz.

In Figure 3.5, the shear modulus G'_{v}, and the loss factor η_{v}, in function of the applied shear strain level γ, are plotted for the four linearity test conditions.

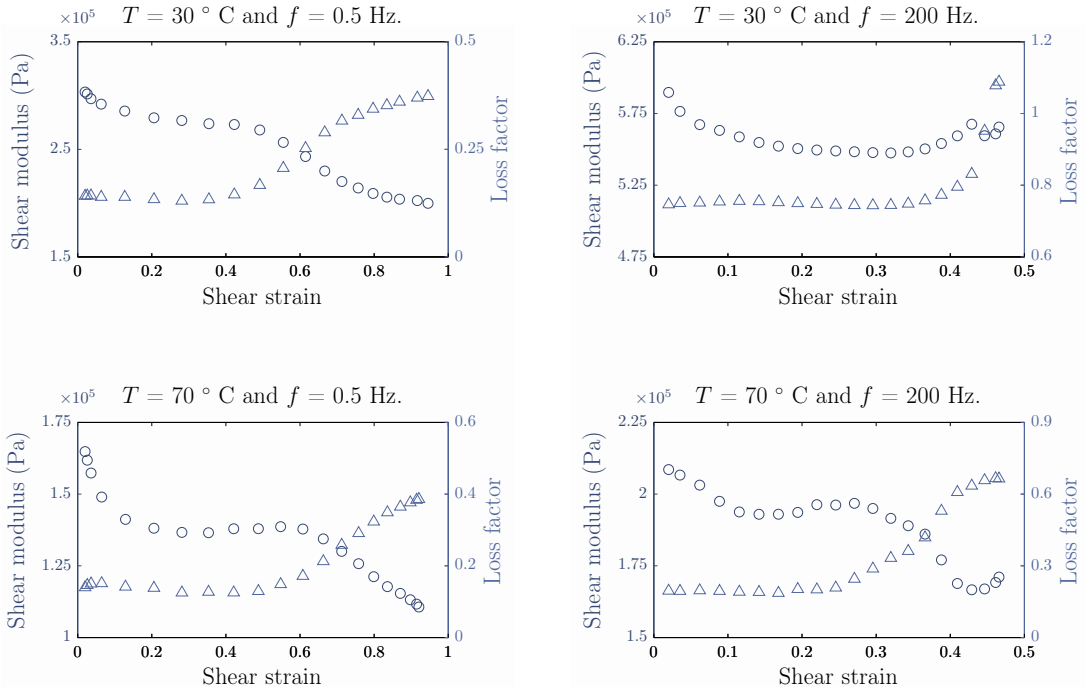

Figure 3.5: Shear modulus (○) and loss factor (△) in function of the applied shear strain level for the four linearity test conditions.

From the amplitude sweeps, the limit of the linear viscoelastic range was determined as the strain level where the shear modulus started to decrease and the loss factor to increase.

From all the executed tests, the fourth test conditions were the limiting ones since presented the narrowest linear range, the maximum shear strain being $\gamma_{\max} = 0.25$. After determining the maximum applicable strain level to ensure linearity between the applied strain and the induced stress, a strain value of $\gamma = 0.2$ ($h = 5$ μm in amplitude) was considered for all the subsequent tests.

3.3 Frequency–Temperature characterization

In this section, the frequency-temperature characterization of the viscoelastic core is presented with two main objectives. The first one is to include the effect of the temperature on the dynamic properties of the viscoelastic core, and the second one, to compare the dynamic properties determined by DMA tests and by the forced vibration tests with resonance.

First, the frequency–temperature superposition principle is reviewed. Then, the experimental tests are described, the results are presented, and the master curve of the viscoelastic core is constructed. Finally, the dynamic properties identified by both experimental techniques are compared and discussed.

3.3.1 Superposition principle

The commercial DMTA equipments offer a precise control of the test temperature allowing to characterize the viscoelastic material both in frequency and temperature. To this end, frequency sweeps are conducted under several test temperatures under isothermal conditions. Then, the temperature dependence is included into the dynamic properties of the viscoelastic material making use of the frequency–temperature superposition principle [35]. This well-established principle relates the complex shear modulus measured for the frequency ω at a temperature T, with that measured for the frequency ω_0 at the reference temperature T_0, expressed as

$$G_{\mathrm{v}}^{*}\left(\omega, T\right) = G_{\mathrm{v}}^{*}\left(\omega \times \alpha_T, T_0\right), \tag{3.9}$$

where the shift factor $\alpha_T = \alpha(T)$, depends on temperature and is a characteristic of each polymer. The shift factor is defined as follows:

$$\alpha_T = \frac{\omega_0}{\omega}, \tag{3.10}$$

where ω_0 is the frequency at which the complex shear modulus exhibits a particular value at the reference temperature T_0, and ω is the frequency at which the complex shear modulus

shows the same value at another temperature T. The master curve can be constructed only if the shift factor is constant within the analyzed frequency range, which is fulfilled if a single relaxation process is manifested [16].

The temperature dependence of the shift factor can be described by the equation of Williams–Landel–Ferry (WLF) [132] and that of Arrhenius [46]. The WLF equation is applied for temperatures above the glass transition temperature T_g, commonly ranging from T_g to $T_g + 100$ °C. This model assumes a nonlinear relationship between the shift factro α_T and $1/T$ in the logarithmic scale, and is given by

$$\log \alpha_T = \frac{C_1 \left(T - T_0\right)}{C_2 + T - T_0}, \tag{3.11}$$

where C_1 and C_2 are characteristic coefficients of each polymer to be identified from the experimental tests, and T_0 is the reference temperature. By contrast, the Arrhenius model, which is based on the molecular kinetic theory of chemical reactions, describes a linear relationship between the shift factor α_T and $1/T$ in the logarithmic scale, being given by

$$\log \alpha_T = \frac{E_a}{R}\left(\frac{1}{T} - \frac{1}{T_0}\right), \tag{3.12}$$

where T is the temperature in Kelvins, $R = 8.314$ Jmol^{-1}K^{-1} is the gas constant, and E_a is the activation energy of the reaction. The Arrhenius model is usually better suited than the WLF model when $T > T_g + 100$ °C, or when $T < T_g$ [16].

Making use of the frequency–temperature superposition principle, the complex modulus curves measured at different temperatures, are superposed by horizontal shifts along the frequency scale to give a single master curve covering a larger range of frequencies.

3.3.2 Master curve

For characterizing the viscoelastic core in frequency and temperature, three specimens were tested within 0.5–200 Hz frequency bandwidth, under temperatures comprised between 30 and 70 °C with 5 °C temperature steps. The specimens were tested from the lowest temperature to the highest one under isothermal conditions, and the excitation amplitude was $h = 5$ μm, as was determined from the linearity analysis. Three frequency sweeps were executed continuously for each test temperature in order to stabilize the response of the sample and guarantee the repeatability of the results. Although very similar results were obtained from the second and the third sweeps, the results obtained from the first one were noisy and dissimilar respect to the results obtained from the two latter sweeps. Therefore, the results obtained from the first one were omitted and all the presented results are the mean values obtained from the last two frequency sweeps.

In Figure 3.6, the shear modulus and the loss factor measured on the three specimens under different test temperatures, are plotted.

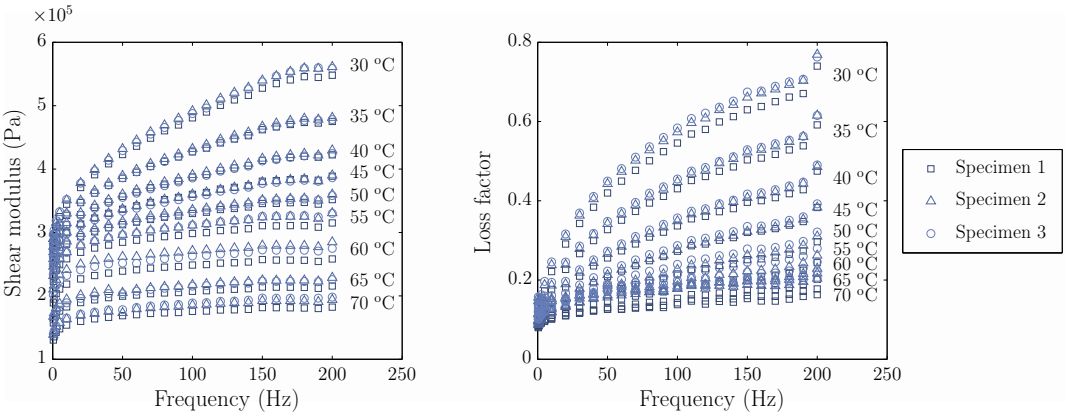

Figure 3.6: Shear modulus and loss factor determined from three specimens tested under temperatures comprised between 30 and 70 °C.

The dynamic properties measured on the second and third specimens agreed, whereas those obtained from the first specimen slightly differed. The dynamic properties measured on the three specimens showed a significant scatter over 50 °C, being the deviations more accused for the loss factor. In addition, the results obtained at higher frequencies over 180 Hz seemed to be unreliable since the trend of the shear modulus and the loss factor changed significantly. For these reasons, the dynamic properties measured over 50 °C and 180 Hz were omitted before calculating the mean values of the shear modulus and the loss factor determined from the three specimens. With the mean values, the frequency–temperature superposition principle was applied and the master curve of the viscoelastic core obtained. The mean dynamic properties measured between 30 and 50 °C are plotted in Figure 3.7.

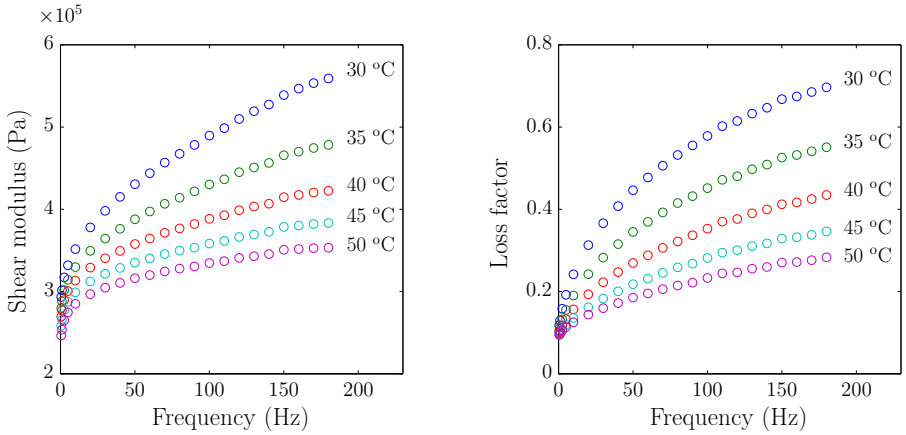

Figure 3.7: Mean dynamic properties measured between 30 and 50 °C.

The strong frequency and temperature dependence of the viscoelastic material was evidenced from Figure 3.7. The frequency dependence of the shear modulus and the loss factor was notably larger for the lowest test temperature, whereas the temperature dependence was more significant for the higher excitation frequencies. Both the shear modulus and the loss factor decreased with the temperature, evidencing that the tests were conducted over the glass transition temperature.

To construct the master curve of the viscoelastic core, the reference temperature was set to $T_0 = 30$ °C and the mean value of the shift factor α_T was determined for each test temperature. Attending to the glass transition temperature T_g of the EPDM viscoelastic core, which is comprised between -60 and -33 °C (depending on the exact composition) [65], the Arrhenius model would be better suited than the WLF model as the test temperatures are close or maybe over $T_g + 100$ °C temperature. Both equations were fitted to the mean values of the identified shift factor α_T, the result being that plotted in Figure 3.8.

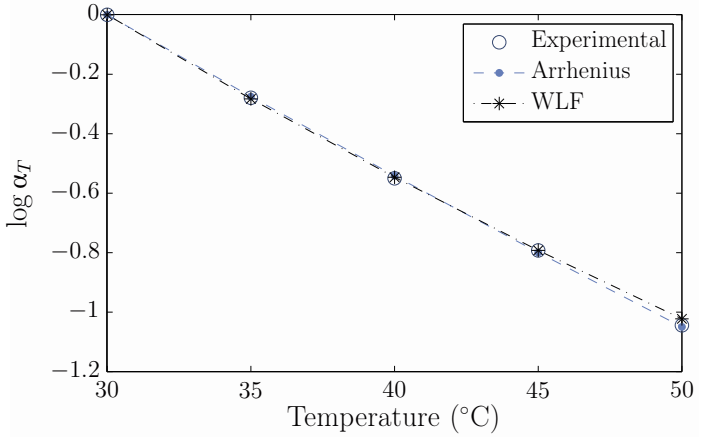

Figure 3.8: Shift factor α_T and fitted WLF ($C_1 = 7.98$ and $C_2 = 136.06$) and Arrhenius ($E_a/R = 5163$ K) equations in function of the temperature.

Both, the Arrhenius and the Williams-Landel-Ferry equations fitted satisfactorily to the experimental data, but a better result was obtained with the former. Therefore, it was considered to construct the master curve, the parameter of the Arrhenius model being $E_a/R = 5163$ K after fitting.

The master curve of the viscoelastic material was constructed for the reference temperature $T_0 = 30$ °C, the result being that shown in Figure 3.9.

As concluded from Figure 3.9, all the shear modulus and loss factor curves overlapped satisfactorily after applying the frequency–temperature superposition principle using the Arrhenius equation.

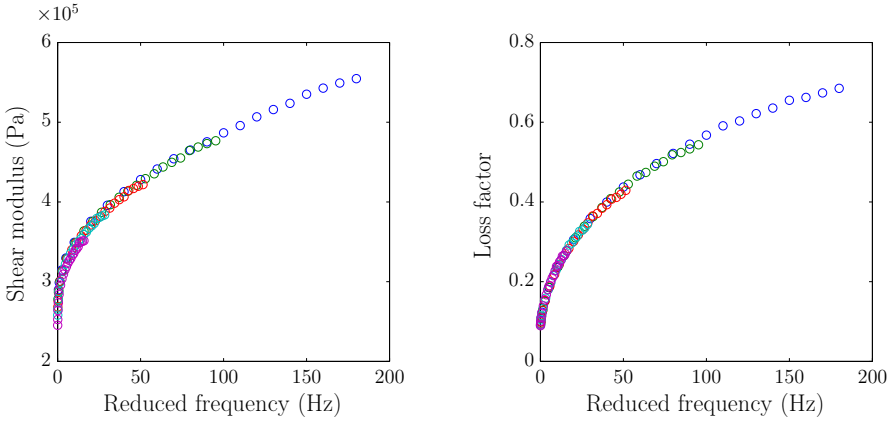

Figure 3.9: Master curve for the shear modulus and the loss factor, for the reference temperature $T_0 = 30$ °C.

3.3.3 DMA vs. forced vibration test with resonance

Besides characterizing the temperature dependence of the viscoelastic core, another major objective of these tests was to compare the dynamic properties identified by the DMA technique, with those already identified by the forced vibration test with resonance in Chapter 2. In order to compare the dynamic properties determined by both experimental techniques, the complex shear modulus described by the master curve for 30 °C, was extrapolated to the test temperature of the latter technique, i.e., to 20 °C.

In Figure 3.10, the dynamic properties obtained by extrapolating the master curve to 20 °C, and those identified by the proposed inverse method making use of the forced vibration test with resonance, can be seen.

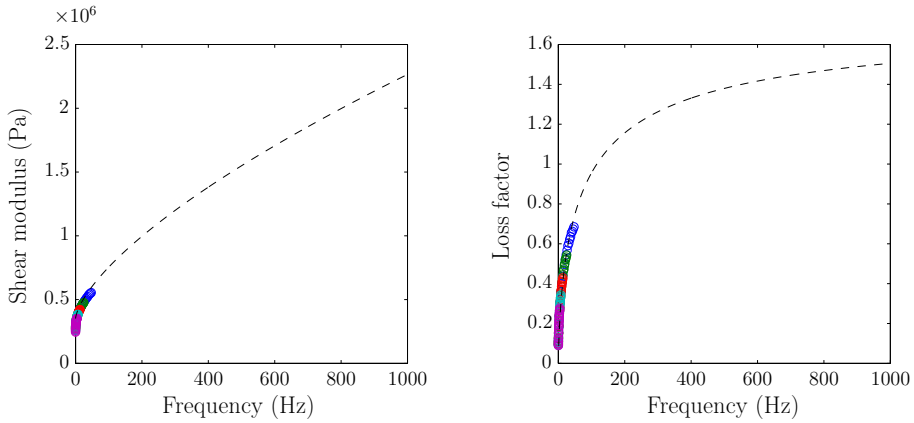

Figure 3.10: Complex shear modulus identified by the proposed inverse method (- - - -), and master curve (∘) extrapolated to $T = 20$ °C making use of the frequency–temperature superposition method using the Arrhenius equation.

The complex shear modulus $G_v^*(\omega)$ identified by DMA tests and by the proposed inverse method showed a good agreement. Nevertheless, the frequency bandwidth (0–180 Hz) where the master curve was determined for the reference temperature $T_0 = 30$ °C, was reduced to nearby 40 Hz after extrapolating it to 20 °C. This fact considerably limited the range of frequencies where both results were comparable. To compare them in a broader frequency bandwidth for the 20 °C temperature, additional frequency sweeps would be necessary with temperatures comprised between $T_g \leq T \leq 20$ °C. Anyway, some important conclusions were drawn from the presented results. For convenience, the same data shown in Figure 3.10 is again represented in Figure 3.11, but with the abscissas in logarithmic scale to better appreciate the differences at low frequencies.

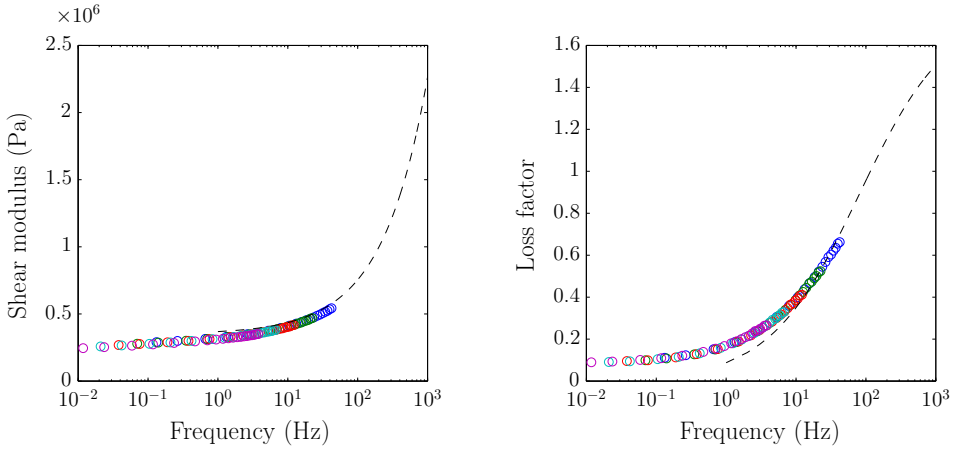

Figure 3.11: Complex shear modulus identified by the proposed inverse method (- - - -), and master curve (∘) extrapolated to $T = 20$ °C making use of the frequency–temperature superposition method using the Arrhenius equation, with abscissas in logarithmic scale.

Limited by the instrumentation involved in the forced vibration test with resonance, in special by the accelerometers, the dynamic response can not be properly measured for frequencies below 1 Hz, that is why the results provided by this method were plotted from this frequency on. The major discrepancies between both results were observed at low frequencies, concretely the shear modulus and the loss factor identified by DMA tests were 15 % lower and 47 % larger for $f = 1$ Hz, respectively. However, both results tend to converge between 10 and 20 Hz, the differences of the shear modulus and the loss factor reducing below 5 %. It should be remarked that the identification of the dynamic properties by the forced vibration test with resonance, is based on the resonances of the tested beam. The first resonance frequency of all the tested free lengths in Chapter 2, were 15, 20.5 and 30 Hz for the 250, 210 and 170 mm long CLD beams, respectively. With this, it may be concluded that the forced vibration test with resonance is not well-suited for characterizing the dynamic properties of viscoelastic materials for frequencies below

the first resonance frequency. By contrast, the main advantage of the DMA tests and the use of the frequency–temperature superposition principle, consists on that the long term behavior of viscoelastic materials can be determined.

Summarizing, two different experimental techniques were compared. The main advantage of the forced vibration test with resonance used in conjunction with the proposed inverse method, is that viscoelastic materials are characterized in a broad frequency bandwidth from tests performed at a single temperature. By contrast, several DMA tests must be conducted under different test temperatures below the temperature of interest, and the frequency–temperature principle applied to identify the dynamic properties for the same frequency bandwidth. However, the DMA technique allows characterizing the long term properties of viscoelastic materials, whereas the forced vibration test with resonance provides reliable results from the first resonance frequency. The main advantage of the DMA technique is that the tests can be executed within a wide temperature range with an accurate temperature control. By contrast, conducting forded vibration tests with resonance under different temperatures presents more technical difficulties. To include the influence of the temperature, an environmental chamber to precisely control and homogenize the temperature along the specimen under test, and specific temperature insensitive devices for exciting the beams and measuring their response, should be necessary.

3.4 Frequency–Prestrain characterization

Next, the frequency-prestrain characterization of the viscoelastic core is addressed. The influence of the static prestrain on the dynamic properties is measured, and a material model to describe such dependency, is proposed. The frequency-prestrain characterization presented next, has been submitted to the journal *International Journal of Adhesion and Adhesives* [75] for publication.

When a flat CLD panel is press formed, a relative displacement between both metallic face sheets appears subjecting the viscoelastic core to a static prestrain. This initial predeformation affects to the elastic and dissipative properties of the viscoelastic core. However, such influence is vaguely described in bibliography and has been studied to a limited extent.

Nashif *et al.* [87] qualitatively describes the influence of the static prestress on the dynamic properties of a viscoelastic material, showing an increment of the storage modulus and a decrement of the loss factor as the static prestress level increases. To date, only Kergourlay *et al.* [49] have experimentally analyzed the effect of the static prestrain on the dynamic properties of a sandwiched viscoelastic film. As the present thesis, their work was motivated by the need to properly determine the theoretical frequency response of press-

formed CLD parts [10]. They use a specially designed test rig to measure the dynamic properties of viscoelastic films under different temperatures and prestrain conditions. They characterize the effect of the prestrain for different temperatures, and they investigate the same superposition methodology employed for the frequency–temperature characterization concluding that the frequency–prestrain superposition hypothesis is not applicable. The authors do not provide an alternative material model to describe the prestrain dependence of the analyzed viscoelastic material.

The present tests aims to analyze the influence of the static prestrain on the elastic and dissipative properties of the viscoelastic core. A material model to characterize the frequency-prestrain dependence of the dynamic properties is presented, and the parameters of the model are identified by curve fitting. Finally, the proposed material model is validated with the dynamic properties measured under different preload levels.

3.4.1 Experimental tests

Three specimens were tested under several static preload levels to characterize the static prestrain influence on the dynamic properties of the viscoelastic core. First, a static preload F_0 was applied inducing an initial relative displacement between the face layers h_0, and the corresponding static prestrain γ_0 in the viscoelastic core. After the material was prestrained, the frequency sweep was conducted by applying an excitation of amplitude h. From the force and displacement data, the induced shear stress τ and strain γ were calculated, and the complex shear modulus of the prestrained viscoelastic material determined following the procedure described in Section 3.2.2. In Figure 3.12, the shear deformation of the viscoelastic material during the test, is represented.

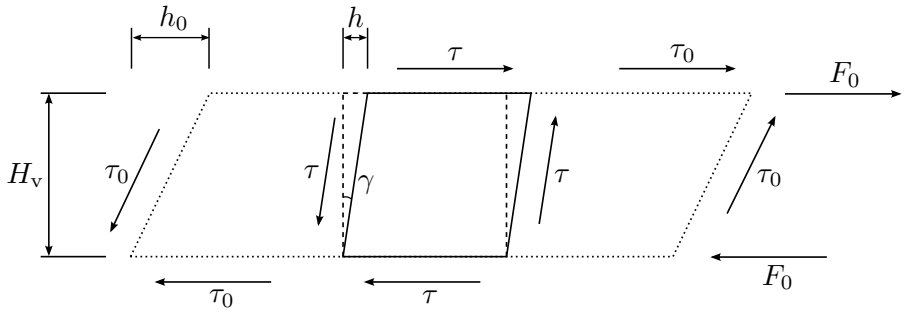

Figure 3.12: Shear deformation of the preloaded viscoelastic core.

The static prestress τ_0 induced by a certain static preload value F_0, is computed by

$$\tau_0 = \frac{F_0}{A}, \tag{3.13}$$

whereas, the induced static prestrain γ_0 is defined relating the induced displacement h_0 with the thickness of the viscoelastic layer, such that

$$\gamma_0 = \frac{h_0}{H_\mathrm{v}}. \tag{3.14}$$

Remark that γ_0 does not represent the shear strain due to the static preload F_0, but quantifies the degree of predeformation exhibited by the core in relation to the thickness.

The frequency sweeps were performed between 0.5 and 200 Hz, and the static preload F_0 was progressively increased from 0 to 18 N by 1 N step increments from test to test. The relative displacement h_0 induced by the static preload F_0 was almost constant during each test, being the variation due to the relaxation phenomena inferior to 0.5 % for all the static preload levels. The maximum applied preload value ($F_0 = 18$ N), induced a static prestrain of $\gamma_0 = 4.1$. The excitation amplitude was $h = 5$ μm, and the test temperature was 30 °C. Three frequency sweeps were executed continuously for each static preload level in order to stabilize the response of the specimen and guarantee the repeatability. Similar results were obtained from the second and the third sweeps but not from the first one. Therefore, the results obtained from the first sweep were omitted, all the presented results being the mean values calculated from the last two frequency sweeps.

Regarding the analysis of formed CLD beams, is difficult to measure the induced static prestress distribution in the viscoelastic core after the forming operation. By contrast, the induced static prestrain may be measured marking the two constraining layers before being formed. So that, working with the static prestrain results more convenient, and therefore the dependency of the viscoelastic material is described in function of the static prestrain instead of the static prestress. Anyway, the results obtained from these tests evidenced that for this particular viscoelastic material both alternatives are equivalent. A linear relationship was observed between the static prestress τ_0 and the static prestrain γ_0, as the induced relative displacement between the face layers h_0 was proportional to the applied static preload level F_0.

3.4.2 Results

Next, the dynamic properties of the viscoelastic core determined from the tests performed under different static preload levels are presented. In Figure 3.13 the shear modulus and the loss factor measured on the three specimens are plotted as a function of the prestrain. For example, three different excitation frequencies are selected, concretelly 5, 50 and 150 Hz.

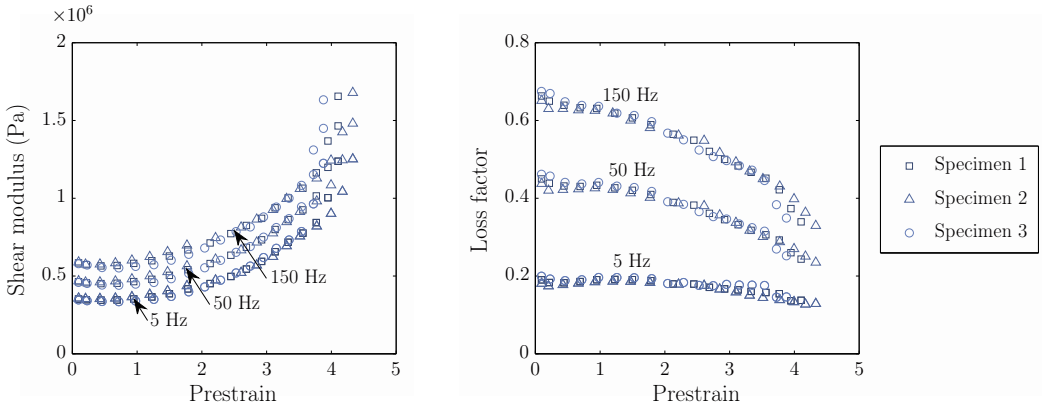

Figure 3.13: Shear modulus and loss factor as a function of the static prestrain for 5, 50 and 150 Hz excitation frequencies, at 30 °C.

The dynamic properties determined from the three specimens showed little dispersion, the only remarkable differences being manifested in the results obtained from the tests conducted with $F_0 = 16$ to 18 N. Before continuing with the analysis, the results obtained from these last three tests were omitted since they did not appear to be reliable. As is qualitatively described by Nashif *et al.* [87], the static prestrain leaded to an increment of the shear modulus and a decrement of the loss factor. Although the influence of the static prestrain was not remarkable for low prestrain values, $\gamma_0 \leq 1$, its effect grew exponentially with the static prestrain level.

The variations of the elastic and the dissipative properties when applying the retained maximum prestrain level ($\gamma_0 = 3.8$) for the considered three excitation frequencies, were those summarized next. The shear modulus increased by 140, 110 and 100 %, and the loss factor decreased by 22, 34 and 36 %, for the 5, 50 and 150 Hz excitation frequencies, respectively. As was concluded, the variation of the shear modulus due to the static prestrain was larger for the low excitation frequencies, whereas the variation of the loss factor was greater for the higher ones.

Next, the shear modulus and the loss factor of the viscoelastic material measured under different static preload values ranging from 0 to 15 N with 1 N increments, are plotted in function of the excitation frequency. In Figure 3.14, only the results of the first specimen are plotted for clarity.

From Figure 3.14 the strong static prestrain dependence of the dynamic properties was evidenced again. The increment of the shear modulus and the decrement of the loss factor was observed as the prestrain level increased. As concluded from Figure 3.14, the dynamic properties measured at the highest excitation frequencies did not seem reliable, so that the results obtained over 170 Hz were omitted.

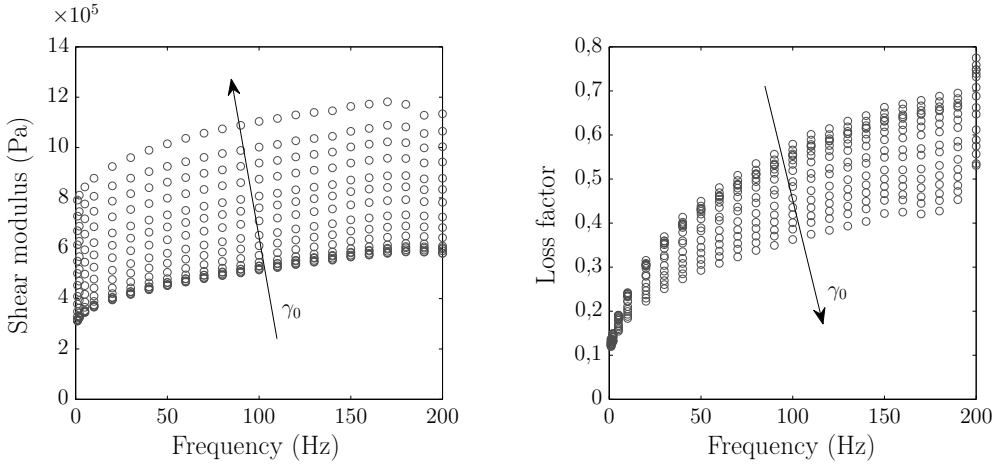

Figure 3.14: Shear modulus and loss factor measured on the first specimen within $0.5 - 200$ Hz, under static preload levels comprised between 0 and 15 N, at 30 °C.

After removing the unreliable data, the mean values of the shear modulus and the loss factor measured on the three specimens were calculated. These final results are used in the next section for defining the material model to characterize the frequency and static prestrain dependence of the viscoelastic material.

3.4.3 Proposed material model

As is described by Ferry [35], besides the temperature dependence, the influence of other variables may be described by reduced variables procedure. This suggests that the prestrain dependence may be included in a similar way to that of the temperature by considering the frequency–prestrain superposition principle. This means that the complex shear modulus of the prestrained viscoelastic core for a given temperature T, may be obtained from the not prestrained one, given by

$$G_{\mathrm{v}}^{*}(\omega, \gamma_0, T) = G_{\mathrm{v}}^{*}(\omega \times \alpha_{\gamma_0}, T), \tag{3.15}$$

where $\alpha_{\gamma_0} = \alpha(\gamma_0)$ is the shift factor related to the static prestrain defined as

$$\alpha_{\gamma_0} = \frac{\omega_0}{\omega}, \tag{3.16}$$

where ω_0 is the frequency at which the not prestrained complex shear modulus exhibits a particular value at temperature T, and ω is the frequency at which the prestrained complex shear modulus shows the same value at the same temperature. Remark that the reduced

variables procedure is only applicable if the shift factor is constant within the frequency bandwidth under analysis.

The frequency–prestrain superposition principle is considered by Kergourlay *et al.* [49] to construct the master curve of a thin viscoelastic film. Although the shear modulus curves measured under different static preloads overlap after shifting them in the frequency axis, the loss factor data do not collapse into a single curve. Therefore, they conclude that this procedure is not applicable to describe the frequency–prestrain dependence of the tested viscoelastic material.

From the present results similar conclusions were drawn. On the one hand, there is not a common shift factor that overlaps the shear modulus and loss factor curves simultaneously. The shift factor must be $\alpha_{\gamma_0} > 1$ to collapse all the shear modulus curves, whereas the shift factor to overlap the loss factor curves must be $\alpha_{\gamma_0} < 1$. On the other hand, the shift factors computed from the shear modulus and loss factor curves were not constant within the analyzed frequency. Thus, the frequency–prestrain superposition principle was discarded and an alternative material model to characterize the frequency-prestrain dependence of the viscoelastic material proposed. This material model relates the dynamic properties of the prestrained viscoelastic core with those of the not prestrained one.

As concluded from the results, the elastic and dissipative properties of the viscoelastic material do not change to the same extent for a given static prestrain level. Therefore, two different functions were defined to relate the shear modulus and the shear loss modulus of the prestrained viscoelastic core with those of the not prestrained one. Moreover, it was concluded that the properties variation due to a certain prestrain level also depends on frequency. Thus, such relations were defined as a function of the frequency and the static prestrain, the complex shear modulus $G^*_{\mathrm{v}}(\omega, \gamma_0)$ of the prestrained viscoelastic core being defined as follows:

$$G^*_{\mathrm{v}}(\omega, \gamma_0) = f_R(\omega, \gamma_0) G'_{\mathrm{v}}(\omega) + \mathrm{i} f_I(\omega, \gamma_0) G''_{\mathrm{v}}(\omega), \tag{3.17}$$

where $G'_{\mathrm{v}}(\omega)$ and $G''_{\mathrm{v}}(\omega)$ are the shear modulus and the shear loss modulus measured without applying any static prestrain ($F_0 = 0$ N), respectively; and where $f_R(\omega, \gamma_0)$ and $f_I(\omega, \gamma_0)$ are the functions that relate the shear modulus and the shear loss modulus of the prestrained viscoelastic material with those of the not prestrained one, respectively.

To define a suitable mathematical model that properly describes the frequency and static prestrain dependence of $f_R(\omega, \gamma_0)$ and $f_I(\omega, \gamma_0)$, the relations represented by those functions were computed from the experimental results, both being plotted in Figure 3.15 in function of the static prestrain.

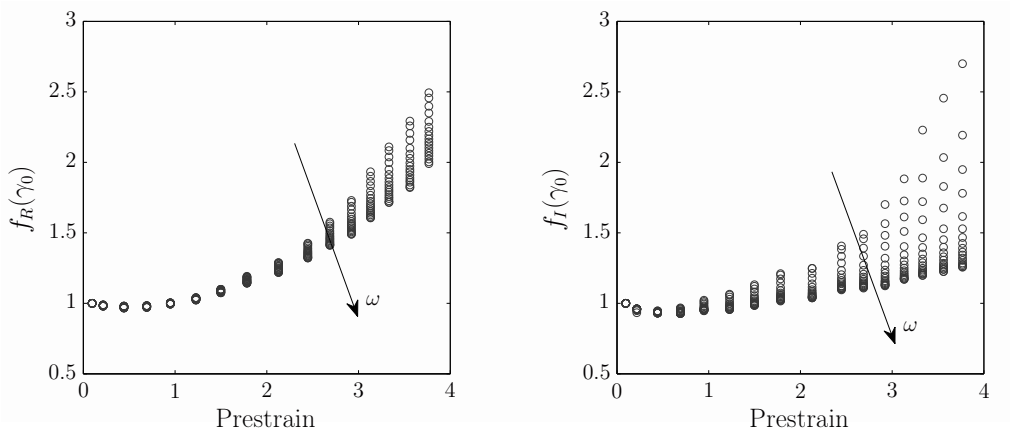

Figure 3.15: Functions $f_R(\omega, \gamma_0)$ and $f_I(\omega, \gamma_0)$ plotted in function of the static prestrain.

From Figure 3.15 it was deduced that the $f_R(\omega, \gamma_0)$ and $f_I(\omega, \gamma_0)$ functions may be described by a power law model, given by

$$f_R(\omega, \gamma_0) = 1 + f_r(\omega)\gamma_0^{n_r} \tag{3.18}$$

and

$$f_I(\omega, \gamma_0) = 1 + f_i(\omega)\gamma_0^{n_i}, \tag{3.19}$$

respectively. Similarly, in Figure 3.16, the functions $f_R(\omega, \gamma_0)$ and $f_I(\omega, \gamma_0)$ are represented in function of the excitation frequency.

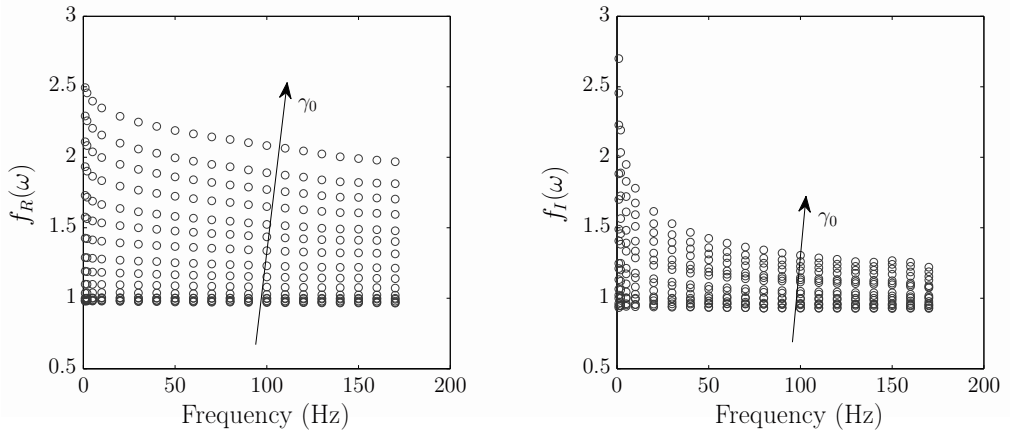

Figure 3.16: Functions $f_R(\omega, \gamma_0)$ and $f_I(\omega, \gamma_0)$ plotted in function of the frequency.

As was concluded from Figures 3.15 and 3.16, low prestrain levels ($\gamma_0 < 1$) did not significantly affect to the dynamic properties of the viscoelastic core, but this influence became remarkable as the prestrain level increased. The shear modulus was affected to a larger extent than the loss modulus, this influence being more significant for the low excitation frequencies in both cases. As well, the loss modulus resulted more sensitive to the excitation frequency, and this sensitiveness became more noticeable as the prestrain level increased. After analyzing Figure 3.16, an exponential model was considered to describe the frequency dependence of $f_r(\omega)$ and $f_i(\omega)$ functions, being defined as follows:

$$f_r(\omega) = c_{r1} + c_{r2}\mathrm{e}^{-\omega c_{r3}} \tag{3.20}$$

and

$$f_i(\omega) = c_{i1} + c_{i2}\mathrm{e}^{-\omega c_{i3}}, \tag{3.21}$$

respectively. Therefore, the final expressions for the functions that relate the real and imaginary parts of the dynamic complex shear modulus of the prestrained and not prestrained viscoelastic material yielded to,

$$f_R(\omega, \gamma_0) = 1 + \left(c_{r1} + c_{r2}\mathrm{e}^{-\omega c_{r3}}\right)\gamma_0^{n_r} \tag{3.22}$$

and

$$f_I(\omega, \gamma_0) = 1 + \left(c_{i1} + c_{i2}\mathrm{e}^{-\omega c_{i3}}\right)\gamma_0^{n_i}, \tag{3.23}$$

respectively. After defining the mathematical model to describe the frequency and static prestrain dependence of $f_R(\omega, \gamma_0)$ and $f_I(\omega, \gamma_0)$, the four parameters of each function were identified by curve fitting to experimental data. The minimization procedure was carried out by the Nelder-Mead algorithm [88], the minimized functions being given by

$$\sum_{k=1}^{k_{\max}} \chi_k \left|\left| f_R(\omega_k, \gamma_0) -_{\exp} f_R(\omega_k, \gamma_0) \right|\right| \tag{3.24}$$

and

$$\sum_{k=1}^{k_{\max}} \chi_k \left|\left| f_I(\omega_k, \gamma_0) -_{\exp} f_I(\omega_k, \gamma_0) \right|\right|, \tag{3.25}$$

where $f_R(\omega, \gamma_0)$ and $f_I(\omega, \gamma_0)$ are the functions given by Equations 3.22 and 3.23, respectively; and where ${}_{\exp}f_R(\omega, \gamma_0)$ and ${}_{\exp}f_I(\omega, \gamma_0)$ represent the data shown in Figures 3.15 and 3.16. A weighting coefficient of $\chi_k = 1/2$ was only applied to the first three frequencies (0.5, 1 and 5 Hz) to improve the overall fit. The identified parameters are gathered in Tables 3.1 and 3.2.

Table 3.1: Parameters of the $f_R(\omega, \gamma_0)$ function.

c_{r1}	c_{r2}	c_{r3}	n_r
2.226×10^{-2}	1.397×10^{-2}	1.485×10^{-3}	2.754

Table 3.2: Parameters of the $f_I(\omega, \gamma_0)$ function.

c_{i1}	c_{i2}	c_{i3}	n_i
5.918×10^{-3}	1.913×10^{-2}	3.621×10^{-3}	2.761

The proposed material model is combined with the four-parameter fractional derivative model used for characterizing the dynamic properties of the not prestrained viscoelastic material. In Table 3.3 the parameters of the fractional derivative model that describes the complex shear modulus of the not prestrained viscoelastic core at 30 °C, are summarized.

Table 3.3: Parameters of the four-parameter fractional derivative model for describing the complex shear modulus of the not prestrained viscoelastic material $G^*_{\mathrm{v}}(\omega)$, at 30 °C.

G_0 (Pa)	G_∞ (Pa)	τ (s)	α
3.103×10^5	3.141×10^8	2.153×10^{-8}	0.6

With the data gathered in Tables 3.1-3.3, the dynamic complex shear modulus for different prestrain levels $G^*_{\mathrm{v}}(\omega, \gamma_0)$, was computed by Equation (3.17) and compared with that experimentally measured in order to validate the proposed material model. In Figure 3.17 the shear modulus and the loss factor of the viscoelastic core measured with DMA tests under different prestrain levels, and that predicted by the proposed material model can be seen.

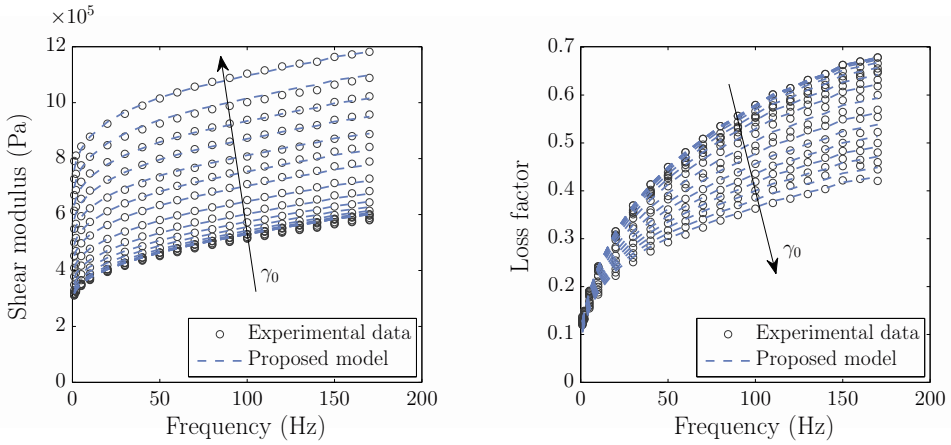

Figure 3.17: Shear modulus and loss factor of the prestrained viscoelastic core experimentally measured and predicted by the proposed material model.

From Figure 3.17 the good correlation between the measured and predicted complex modulus was evidenced. The proposed material model satisfactorily described the frequency and static prestrain dependence of the dynamic complex shear modulus of the analyzed viscoelastic material under different static prestrain levels.

3.5 Comparative analysis: frequency, temperature and static prestrain influence

Finally, the influence of the frequency, the temperature and the static prestrain on the dynamic properties of the characterized viscoelastic material is compared in order to better reflect the influence of each of the analyzed variables.

From the presented results, the strong frequency dependence of the elastic and dissipative properties was evidenced. As well, the frequency-temperature and the frequency-prestrain characterizations highlighted that such dependency also depends on temperature and static prestrain level. For example, in Figure 3.18 the shear modulus and loss factor determined without applying any prestrain level, are plotted in function of the frequency and the test temperature.

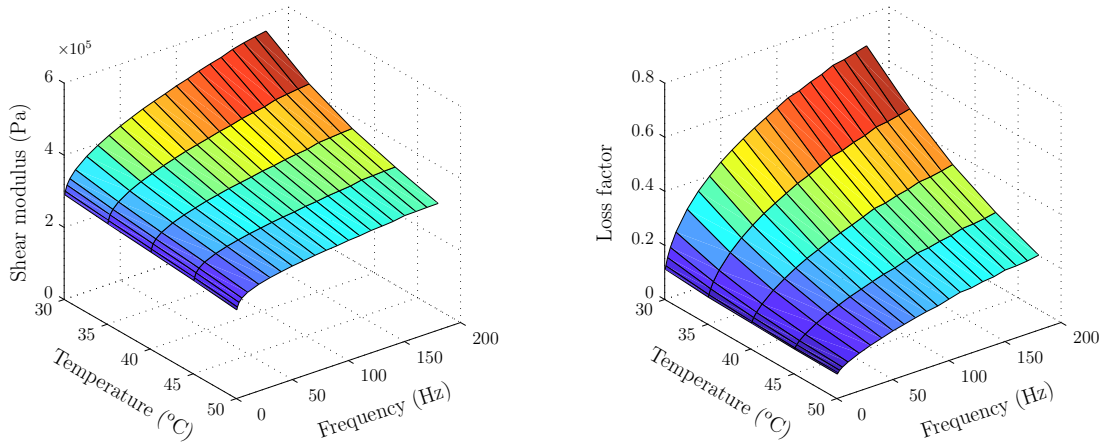

Figure 3.18: Shear modulus and loss factor in function of the frequency ($f : 0.5 - 180$ Hz) and the temperature ($T : 30 - 50$ °C).

As concluded from Figure 3.18, the frequency dependence of the dynamic properties was more pronounced for the lower test temperatures. At 30 °C, when the frequency was increased from 0.5 to 180 Hz, the shear modulus and the loss factor increased by 91 % and 517 %, respectively; whereas at 50 °C both properties varied by 43 % and 209 %, respectively.

As well, in Figure 3.19 the shear modulus and loss factor measured under different prestrain levels for 30 °C, are plotted in function of the frequency and the static prestrain.

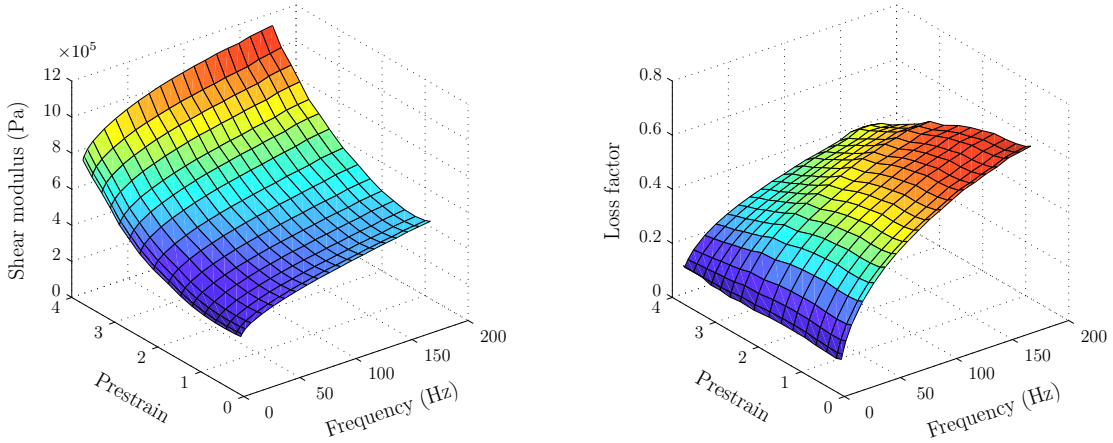

Figure 3.19: Shear modulus and loss factor in function of the frequency ($f : 0.5 - 170$ Hz) and the static prestrain ($\gamma_0 : 0 - 3.8$)

As shown in Figure 3.19, the frequency dependence exhibited by the properties of the core also depends on the static prestrain level. Without applying any prestrain, the shear modulus and the loss factor increased by 89 % and 506 %, respectively; whereas with a $\gamma_0 = 3.8$ prestrain level, both properties varied by 49 % and 206 %, respectively when the frequency was increased from 0.5 to 170 Hz. As evidenced, the frequency dependence exhibited by the dynamic properties decreased with the static prestrain level.

As was concluded from Figures 3.18 and 3.19, the excitation frequency is one of the most influential factors on the dynamic properties of the analyzed viscoelastic material, and its influence depends both in temperature and static prestrain. These two figures also showed the important influence of the temperature and the static prestrain on the dynamic properties of the analyzed viscoelastic material. The effect of these two variables is analyzed next.

In Table 3.4, the variations of the shear modulus and the loss factor due to static prestrain and temperature changes are gathered for the limiting excitation frequencies (0.5 and 170 Hz). The first column reflects the variations due to the static prestrain changes measured at 30 °C; the second column shows the variation between the results measured at the lower (30 °C) and upper (50 °C) temperatures used to construct the master curve without applying any prestrain; and the third one presents the variations given between the reference temperature (30 °C) and the temperature at which the forced vibration tests with resonance were performed (20 °C), without any prestrain.

Table 3.4: Variation of the shear modulus and the loss factor due to temperature and static prestrain changes.

Frequency (Hz)	$\gamma_0: 0 \rightarrow 3.8$		$T: 30 \rightarrow 50$ °C		$T: 30 \rightarrow 20$ °C	
	ΔG_v	$\Delta \eta_v$	ΔG_v	$\Delta \eta_v$	ΔG_v	$\Delta \eta_v$
0.5	149 %	−8 %	−16 %	−24 %	5 %	36 %
170	97 %	−38 %	−36 %	−60 %	69 %	64 %

From Table 3.4, the relevance of each of the analyzed variables was verified. The comparative analysis showed that the static prestrain and the temperature affected in a different way to the dynamic properties of the viscoelastic core. The shear modulus experimented the largest variations due to the static prestrain, whereas in general the temperature affected more significantly to the loss factor within the analyzed range. As well, the temperature affected to a greater extent at higher frequencies, whereas the static prestrain originated a larger shear modulus and loss factor variations at the lower and higher frequencies, respectively.

Although the temperature changes originated smaller shear modulus variations than the static prestrain changes for the range of variables analyzed, the influence of the former is expected to be considerably larger at temperatures below 20 °C, closer to the glass transition temperature T_g. The results gathered in the second and third columns also support this statement. Although the absolute percentile variation of the loss factor is roughly equivalent when increasing the temperature 20 °C or decreaing it 10 °C, the shear modulus varied significantly more when decreasing the temperature 10 °C. This is because the results identified at 20 °C, corresponded with the end of the rubbery zone and the beginning of the transition zone, as is evidenced in Figure 3.20. This figure aims to reflect the three characteristic regions of an amorphous polymer. It should be remarked that over 1 kHz the shear modulus and loss factor functions have been extrapolated with the material parameters identified in Chapter 2 up to 1 kHz frequency bandwidth.

Figure 3.20 describes the frequency and temperature dependences of an amorphous polymer, showing that both variables have opposite effects. As is observed, decreasing the temperature even more, a significant increment of the shear modulus is expected as the identified properties corresponded with the beginning of the transition zone. By contrast, the loss factor is already close to its maximum value, so no a relevant variation is expected when decreasing the temperature. This figure also justifies why the frequency dependence of the dynamic properties is more pronounced for the lower test temperatures, as was concluded from Figure 3.18.

From this analysis, the relevance of the frequency, the temperature and the static prestrain influence on the dynamic properties of the analyzed viscoelastic material has been

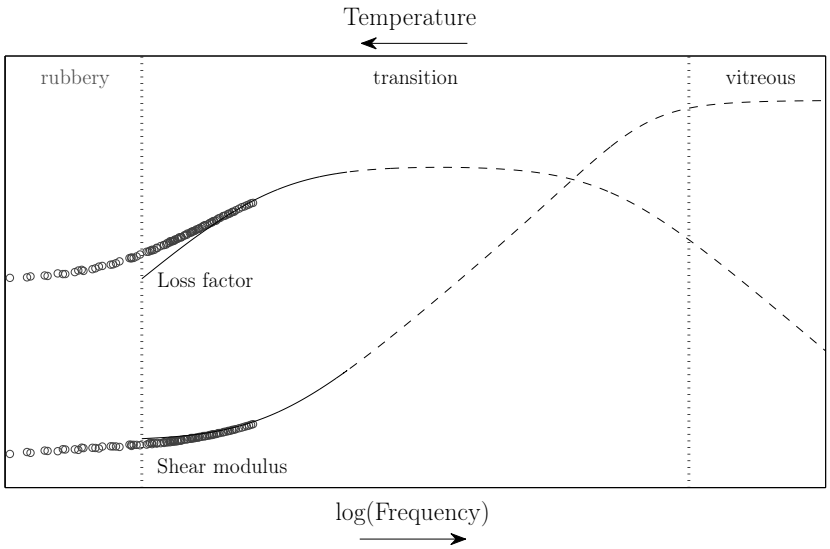

Figure 3.20: Evolution of the complex shear modulus with the frequency for 20 °C, and the three characteristic regions of an amorphous polymer. (∘) DMA tests $f : 0.01 - 40$ Hz, (——) forced vibration test with resonance up to 1 kHz, and (- - -) extrapolated data.

proved, and how each of the variables affect to the elastic and dissipative properties of the viscoelastic core has been described. The presented frequency-prestrain characterization has proved that the influence of the static prestrain on the elastic and dissipative properties of the tested viscoelastic material is important, and comparable to the influence of the temperature and the frequency.

3.6 Conclusions

In this chapter the influence of the frequency, the temperature, and the static prestrain on the elastic and dissipative properties of the viscoelastic core, has been analyzed. To this end, dynamic mechanical analysis (DMA) technique has been considered proving that is a suitable technique for characterizing constrained viscoelastic films in function of the three studied variables.

First of all, a linearity analysis has been carried out showing that the analyzed viscoelastic material presents a relatively broad linear viscoelastic range.

The frequency-temperature dependence has been characterized by conducting frequency sweeps under several test temperatures under isothermal conditions. The results has evidenced the high temperature dependence of the dynamic properties. From these tests the master curve has been constructed making use of the frequency–temperature superposition principle using the Arrhenius equation.

The dynamic properties measured by the DMA technique have been extrapolated to 20 °C, and compared with those measured by the forced vibration test with resonance. The results have reflected that the forced vibration test with resonance does not provide reliable data below the first resonance frequency, the DMA method resulting better suited for determining the long term properties. The forced vibration test with resonance has identified the dynamic properties in a broader frequency bandwidth than the DMA technique from tests conducted at a single temperature. The dynamic properties identified by both experimental techniques have showed to be consistent and complementary.

In addition, frequency sweeps under several static preloads have been performed to characterize the frequency-prestrain dependence of the viscoelastic core. With these tests, the significance of the static prestrain influence on the dynamic properties of the viscoelastic material has been verified. Both, the shear modulus and the loss modulus have increased and the loss factor has decreased, showing that the shear modulus is more sensitive to the static prestrain influence. The influence of the static prestrain on the dynamic properties of the core has grown exponentially. As well, it has been shown that the effect of the static prestrain depends on the excitation frequency, being this influence for the shear and the loss modulus more significant for the lower frequencies. For a given static prestrain level, the loss modulus has manifested larger variations than the shear modulus with the excitation frequency, this sensitiveness becoming more important as the prestrain level increases.

A new material model has been proposed for characterizing the frequency-prestrain dependence of the viscoelastic core. Two four-parameter functions have been defined and combined with the four-parameter fractional derivative model used for characterizing the dynamic properties of the not prestrained viscoelastic core. The proposed model has been validated by comparing the experimentally measured dynamic complex shear modulus for different prestrain levels with that described by the model.

Finally, the influence of the frequency, the temperature and the static prestrain on the dynamic properties of the analyzed viscoelastic material has been compared. For the range of variables analyzed, the influence of the frequency has decreased by increasing the temperature and the static prestrain. The temperature has affected more to the loss factor than to the shear modulus, and its influence has been more pronounced at higher frequencies. The static prestrain has varied more the shear modulus than the loss factor, and its influence has been more important at low frequencies. The comparative analysis have proved the relevant influence of the static prestrain on the dynamic properties of the analyzed viscoelastic material.

The presented frequency-prestrain characterization has been submitted to the journal *International Journal of Adhesion and Adhesives* [75] for publication.

Chapter 4

Higher order eigensensitivities-based numerical method

The dynamic analysis of viscoelastically damped structural systems demand specific solution methods due to the non-proportional nature of the damping and the frequency dependence of the properties of the viscoelastic materials.

In this chapter, a new higher order eigensensitivities-based numerical method is presented for the dynamic analysis in the frequency domain of viscoelastically damped structural systems characterized by a structural damping matrix. The higher order eigenderivatives are defined and the proposed fundamental updating procedure is described and implemented into two different schemes. An iterative algorithm is presented for determining the complex modal parameters, and an incremental algorithm for computing the complex and frequency-dependent modal parameters in order to determine the dynamic response by the complex mode superposition method. The effectiveness and the efficiency of both schemes is verified with a practical example.

The iterative scheme is validated by comparing the computed modal parameters with the exact ones determined by the *iterative complex eigensoluion* method. Similarly, the incremental scheme is applied and the dynamic response obtained by the complex mode superposition method. The approximated dynamic response is validated by correlating it with the exact one computed by the direct frequency method, and with the experimental one.

Finally, the efficiency of the proposed higher order eigensensitivities-based numerical method is verified by comparing the computation time required by the proposed iterative and incremental algorithms, with that demanded by the classical methods.

4.1 Introduction

The motion equation of a viscoelastically damped discrete system characterized by a structural damping matrix, as already presented in Chapter 2, is governed by a set of second-order non-linear differential equations, given by

$$\mathbf{M}\ddot{\mathbf{u}}(t) + \mathbf{K}^*(\omega)\mathbf{u}(t) = \mathbf{f}(t), \tag{4.1}$$

where $\mathbf{f}(t)$, $\ddot{\mathbf{u}}(t)$ and $\mathbf{u}(t)$ are the force, acceleration and displacement vectors, respectively, $\mathbf{M}$ and $\mathbf{K}^*(\omega)$ are the mass and the frequency-dependent complex stiffness matrices, respectively, and the dot denotes differentiation with respect to time. The frequency dependence of the viscoelastic materials introduces a non linearity in the motion equation as the coefficients of the complex stiffness matrix are not constant. Specific damping models that consider additional internal dissipation coordinates, such as the GHM [40, 78] and ADF [58] models, were developed in order to simplify and linearize the governing equations. These models have been extensively applied for the transient analysis of structural systems involving viscoelastic materials, but they are not attractive for the analysis in frequency domain since the addition of internal variables considerably increases the problem size. Anyway, model reduction techniques have been also developed in the last decade to minimize this limitation (see for example Friswell and Inman [38], Park *et al.* [94], and Trindade [120]).

For the dynamic analysis in frequency domain the complex modulus approach is the most commonly adopted alternative. For systems subjected to steady-state oscillatory conditions where the mechanical excitation and the resultant response are both harmonic, such that $\mathbf{f}(t) = \mathbf{F}^* \mathrm{e}^{\mathrm{i}\omega t}$ and $\mathbf{u}(t) = \mathbf{U}^* \mathrm{e}^{\mathrm{i}\omega t}$, the motion equation in frequency domain is written as

$$\left(-\omega^2\mathbf{M} + \mathbf{K}^*(\omega)\right)\mathbf{U}^* = \mathbf{F}^*, \tag{4.2}$$

where $\mathbf{F}^*$ and $\mathbf{U}^*$ are the complex vectors of applied force and response amplitudes. The mass $\mathbf{M}$ and the frequency dependent complex stiffness $\mathbf{K}^*(\omega)$ matrices are decomposed into the counterparts related to the elastic and viscoelastic components as follows:

$$\mathbf{M} = \mathbf{M}_\mathrm{e} + \mathbf{M}_\mathrm{v} \tag{4.3}$$

and

$$\mathbf{K}^*(\omega) = \mathbf{K}_\mathrm{e} + \mathbf{K}_\mathrm{v}^*(\omega) = \mathbf{K}_\mathrm{e} + \mathbf{K}_\mathrm{v}(\omega) + \mathrm{i}\mathbf{H}_\mathrm{v}(\omega), \tag{4.4}$$

respectively. The structural damping matrix of the system $\mathbf{H}$ is not proportional to the mass $\mathbf{M}$ and/or the stiffness $\mathbf{K}$ matrices. In such cases, the damping is referred to as non-proportional or non-classical, and in general the equations of motion are not uncoupled by the undamped normal modes. A condition that should be satisfied by the mass, stiffness and damping matrices of a proportionally damped system is given by Caughey and O'Kelly [18]. If the damping matrix is a linear combination of the mass and stiffness matrices, such as

$$\mathbf{H} = \alpha\mathbf{M} + \beta\mathbf{K}, \tag{4.5}$$

where α and β are proportionality constants, the damping is referred to as Rayleigh damping, proportional damping or classical damping. In such cases, normal modes can be used to describe the dynamic behavior of the damped system. The proportionality condition in the most general case, may be expressed as

$$\mathbf{K}\mathbf{M}^{-1}\mathbf{H} = \mathbf{H}\mathbf{M}^{-1}\mathbf{K}. \tag{4.6}$$

By contrast, if the mass, stiffness and damping matrices do not satisfy the condition given by Equation (4.6), the damping is referred to as non-proportional or non-classical, and the eigenvectors that uncouples the equations of motion are in general complex. Moreover, due to the frequency dependence of the coefficients of the stiffness $\mathbf{K}_{\mathrm{v}}$ and the structural damping $\mathbf{H}_{\mathrm{v}}$ matrices related to the viscoelastic material, the complex eigenvalues and eigenvectors also become frequency-dependent. This fact demands specific solution strategies for determining the complex modal parameters and the frequency response of viscoelastically damped structural systems.

Next, the classical numerical methods for determining the modal parameters and the frequency response of structural systems with viscoelastic damping, are reviewed and discussed.

4.1.1 Modal analysis

The modal analysis is the process whereby the system under study is described in terms of its dynamic properties, such as the natural frequencies, modal loss factors and mode shapes, referred to as modal parameters. For determining the modal parameters of a viscoelastically damped structural system, a non-linear complex eigenproblem must be solved, which is given by

$$\mathbf{K}^*(\omega_r)\phi_r^* = \lambda_r^*\mathbf{M}\phi_r^*, \tag{4.7}$$

where λ_r^* and ϕ_r^* are the rth complex eigenvalue and eigenvector, respectively. A complete survey on numerical methods for the complex eigensolution is given by Sorensen [114] or Saad [108], for example. The complex eigenproblem given by Equation (4.7) needs to be solved iteratively for each mode, requiring the solution of a complex eigenproblem per iteration. This methods is referred to as the *iterative complex eigensolution* (ICE) method and converges to the exact modal parameters. The convergence criterion is commonly defined with the resonance frequencies of consecutive iterations, such that

$$\epsilon_r \geq \left| \frac{\omega_{r,j} - \omega_{r,j-1}}{\omega_{r,j}} \right|, \tag{4.8}$$

where ϵ_r is the tolerance defined for the rth mode, whereas j refers to the current iteration. For the solution of the complex eigenproblem classical algorithms may be considered, such as the techniques of Lanczos [56] or Arnoldi [5]. Currently, efficient iterative methods are also available for large ordered systems, such as the *implicitly restarted Arnoldi method* (IRAM), a variant of the Arnoldi's method. This method is implemented in the free software ARPACK [57] and in the *eigs* function of MATLAB®. The results provided by IRAM are used as a reference in the different examples of the practical application for validation. In Table 4.1, the ICE algorithm for computing the complex eigenvalues and eigenvectors is summarized.

Table 4.1: Iterative complex eigensolution (ICE) procedure.

1. Solve the undamped real eigenproblem: $\mathbf{K}(0)\phi_{r,0} = \lambda_{r,0}\mathbf{M}\phi_{r,0}$

  1.1. Compute the rth undamped natural frequency: $\omega_{r,0} = \sqrt{\lambda_{r,0}}$

2. **while** $\epsilon_r < \left| \frac{\omega_{r,j} - \omega_{r,j-1}}{\omega_{r,j}} \right|$, initialize $j = 0$

  2.1. Update $j = j + 1$

  2.2. Update the complex stiffness matrix: $\mathbf{K}^*(\omega_{r,j-1})$

  2.3. Solve the updated complex eigenproblem: $\mathbf{K}^*(\omega_{r,j-1})\phi_{r,j}^* = \lambda_{r,j}^*\mathbf{M}\phi_{r,j}^*$

  2.4. Compute: $\omega_{r,j} = \sqrt{\mathrm{Re}(\lambda_{r,j}^*)}$, and test the convergence.

3. Store the computed rth complex eigenpair (λ_r^*, ϕ_r^*).

From the computed complex eigenvalues the modal loss factor is determined by

$$\eta_r = \frac{\mathrm{Im}\,(\lambda_r^*)}{\mathrm{Re}\,(\lambda_r^*)}. \tag{4.9}$$

Although the described procedure converges to the exact complex modal parameters, the solution of a complex eigenproblem per iteration demands relatively large computational requirements as the problem size increases. Therefore, the use of approximated methods has constituted a common practice during the last decades in order to avoid the complex eigensolution.

The *Modal Strain Energy* (MSE) approach has been one of the most widely used method for determining the modal loss factor of viscoelastically damped structural systems. This approach was suggested by Ungar and Kerwin [126], and first implemented in a commercial finite element software package by Johnson and Kienholz [43]. The MSE method, in conjunction with the finite element method, aided the design of damping treatments of parts with complex geometries. The method, constitutes a powerful alternative to the analytical formulations which are applicable only to simple geometries such as beams and plates. The analytical formulations for viscoelastically damped CLD beams and plates, were first derived by Kerwin [50] and Ross *et al.* [107], and after them, several authors contributed to the development of those models. For a complete revision on the evolution of the analytic models of CLD laminates, the readers are referred to the work of Li and Crocker [60], or that of Teng and Hu [118], for example.

When applying the MSE approach, it is assumed that the damped structure can be represented in terms of the normal modes of the associated undamped system. The modal loss factor of the rth mode, is determined relating the dissipated energy by the viscoelastic material to the total strain energy stored by the whole system, given by

$$\eta_r = \frac{\phi_r^{\mathrm{T}} \operatorname{Im}\left(\mathbf{K}^*(\omega_r)\right) \phi_r}{\phi_r^{\mathrm{T}} \operatorname{Re}\left(\mathbf{K}^*(\omega_r)\right) \phi_r}, \tag{4.10}$$

where $\phi_r = \phi_{r,0}$ is the rth undamped eigenvector, and $(\bullet)^{\mathrm{T}}$ denotes the transposition operator. However, assuming that the damped system can be represented in terms of the undamped normal modes is only valid for lightly damped systems.

Another limitation of the MSE method is related with the analysis of systems involving strong frequency-dependent viscoelastic materials. As it does not consider the frequency dependence of the elastic and dissipative properties of the viscoelastic materials, the MSE method might yield to precise modal parameter values. Nevertheless, the method can be applied under an iterative scheme (IMSE) to account for the frequency dependency of the elastic properties of the viscoelastic material and obtain more accurate estimates. As is detailed in Table 4.2, at each iteration the real stiffness matrix is updated and the real eigenproblem solved until the natural frequency converges.

Table 4.2: Iterative modal strain energy (IMSE) algorithm.

1. Solve the undamped real eigenproblem: $\mathbf{K}(0)\phi_{r,0} = \lambda_{r,0}\mathbf{M}\phi_{r,0}$

1.1. Compute the rth undamped natural frequency: $\omega_{r,0} = \sqrt{\lambda_{r,0}}$

2. while $\epsilon_r < \left|\frac{\omega_{r,j}-\omega_{r,j-1}}{\omega_{r,j}}\right|$, initialize $j = 0$

2.1. Update $j = j + 1$

2.2. Update the real stiffness matrix: $\mathbf{K}(\omega_{r,j-1})$

2.3. Solve the updated real eigenproblem: $\mathbf{K}(\omega_{r,j-1})\phi_{r,j} = \lambda_{r,j}\mathbf{M}\phi_{r,j}$

2.4. Compute: $\omega_{r,j} = \sqrt{\lambda_{r,j}}$, and test the convergence.

3. Store the computed rth real eigenpair (λ_r, ϕ_r).

From the computed modal parameters, the modal loss factor η_r is determined by Equation (4.10). The IMSE algorithm provides more realistic eigenvectors as the frequency dependence of the elastic properties is taken into account, which in turn allow computing more precise modal loss factor values. Trindade *et al.* [122] compares the modal parameters obtained by the IMSE procedure and the ADF and GHM models, showing that both ADF and GHM models are superior to the IMSE method for highly damped systems. Similarly, Vasques *et al.* [128] analyzes the ADF and the GHM models, and the IMSE and the ICE methods for computing the modal parameters and the dynamic response of sandwich plates. The ADF and GHM models and the ICE method provide precise results, the IMSE method being the less accurate approach.

From this review is concluded that the MSE method is only applicable for those cases where the damped system can be described in terms of the real undamped eigenvectors. More accurate results may be obtained considering the iterative version of the latter method (IMSE), as the frequency dependence of the elastic properties is taken into consideration when computing the real modal parameters. However, as the IMSE method does not consider the complexity of the eigenvectors, it may be limited for determining the modal parameters of highly and non-proportionally damped systems. By contrast, although the ICE method provides the exact complex eigenparameters (λ_r^*, ϕ_r^*), demands large computational requirements since a complex eigenproblem must be solved per each iteration. For this reasons, a new algorithm based on the use of the higher order eigensensitivities is developed for computing the complex modal parameters of viscoelastically damped structural systems characterized by a structural damping matrix.

4.1.2 Frequency response

Unlike the proportionally damped systems, the frequency response of non-proportionally damped systems can not be determined by the classical normal mode superposition method. Although the approximated dynamic response is greatly improved when superposing the complex modes computed by the algorithm summarized in Table 4.1, this procedure does not provide the exact solution as the complex eigenvalues and eigenvectors are also frequency dependent $(\lambda_r^*(\omega), \phi_r^*(\omega))$. The superposition of complex modes accounting for the frequency dependency of the modal parameters is applied by Cortés and Elejabarrieta [23, 27] for determining the forced response of a rod with a viscoelastic damper. As well, Cortés [22] and, Martinez-Agirre and Elejabarrieta [68], applies this procedure for computing the frequency response of FLD and CLD beams, respectively. Next, the basis of the complex mode superposition method are reviewed.

Complex mode superposition method

Although the most straightforward strategy for approximating the dynamic response is to superpose the complex modes determined by the ICE method, the exact solution is not achieved. To compute the exact dynamic response, is necessary to account for the variation of the complex eigenvalues and eigenvectors within the frequency bandwidth under analysis. The complex eigenpair may be computed for each computational frequency ω_k, by solving the complex eigenproblem given by

$$\mathbf{K}^*(\omega_k)\phi_r^*(\omega_k) = \lambda_r^*(\omega_k)\mathbf{M}\phi_r^*(\omega_k). \tag{4.11}$$

From the complex and frequency-dependent eigenpair, the individual contribution of a given mode may be determined. For a force excited structural system governed by Equation (4.2), the modal contribution of the rth mode ${}_rH_{ij}^*(\omega)$ to the total frequency response function $H_{ij}^*(\omega)$ relating the ith and jth DOFs, is defined as follows [34, 23]:

$${}_rH_{ij}^*(\omega) = \frac{{}_r\phi_i^*(\omega){}_r\phi_j^*(\omega)}{m_r^*(\omega)\left(\lambda_r^*(\omega) - \omega^2\right)}, \tag{4.12}$$

where the rth modal mass $m_r^*(\omega)$, is expressed as

$$m_r^*(\omega) = \phi_r^{*\mathrm{T}}(\omega)\mathbf{M}\phi_r^*(\omega), \tag{4.13}$$

In experimental modal analysis and finite element method, the eigenvectors are commonly normalized with respect to the unit modal mass, so that $m_r^* = 1$.

The exact frequency response function relating the ith and jth DOF $H_{ij}^*(\omega)$, is then approximated by superposing the contribution of each mode ${}_rH_{ij}^*(\omega)$, as follows:

$$H_{ij}^*(\omega) \simeq \sum_{r=1}^{n} {}_rH_{ij}^*(\omega), \tag{4.14}$$

where n is the number of modes superposed.

By contrast, for systems subjected to a harmonic base motion, $\mathbf{s}(t) = \mathbf{S}^* \mathrm{e}^{\mathrm{i}\omega t}$, $\mathbf{S}^*$ being the complex amplitude vector of the applied displacement, the motion equation may be expressed distinguishing the degrees of freedom relative to the base displacement and the unknown displacements, indicated by $(\bullet)_\mathrm{s}$ and $(\bullet)_\mathrm{u}$ respectively, such that

$$\left(-\omega^2 \begin{bmatrix} \mathbf{M}_{\mathrm{ss}} & \mathbf{M}_{\mathrm{su}} \\ \mathbf{M}_{\mathrm{us}} & \mathbf{M}_{\mathrm{uu}} \end{bmatrix} + \begin{bmatrix} \mathbf{K}_{\mathrm{ss}}^*(\omega) & \mathbf{K}_{\mathrm{su}}^*(\omega) \\ \mathbf{K}_{\mathrm{us}}^*(\omega) & \mathbf{K}_{\mathrm{uu}}^*(\omega) \end{bmatrix} \right) \begin{Bmatrix} \mathbf{S}^* \\ \mathbf{U}^* \end{Bmatrix} = \begin{Bmatrix} \mathbf{R}^* \\ 0 \end{Bmatrix}, \tag{4.15}$$

where $\mathbf{R}^*$ denotes the complex amplitude vector of the reaction forces on the base. Similarly, for determining the displacement vector $\mathbf{U}^*(\omega)$ by the complex mode superposition method, first the complex and frequency-dependent modal parameters must be determined within the frequency bandwidth of interest, for example by solving Equation (4.11) with $\mathbf{M} = \mathbf{M}_{\mathrm{uu}}$ and $\mathbf{K}^* = \mathbf{K}_{\mathrm{uu}}^*$. After that, the vector of modal contributions to the total displacement vector ${}_r\mathbf{U}^*(\omega)$, is determined as

$${}_r\mathbf{U}^*(\omega) = q_r^*(\omega)\boldsymbol{\phi}_r^*(\omega), \tag{4.16}$$

where $q_r^*(\omega)$ is the generalized modal displacement, given by

$$q_r^*(\omega) = \frac{\boldsymbol{\phi}_r^{*\mathrm{T}}(\omega)\left(-\omega^2\mathbf{M}_{\mathrm{us}} + \mathbf{K}_{\mathrm{us}}^*(\omega)\right)\mathbf{S}^*(\omega)}{\boldsymbol{\phi}_r^{*\mathrm{T}}(\omega)\left(-\omega^2\mathbf{M}_{\mathrm{uu}} + \mathbf{K}_{\mathrm{uu}}^*(\omega)\right)\boldsymbol{\phi}_r^*(\omega)}. \tag{4.17}$$

Finally, the total displacement vector is approximated by the superposition of the individual contributions of each mode as

$$\mathbf{U}^*(\omega) \simeq \sum_{r=1}^{n} {}_r\mathbf{U}^*(\omega), \tag{4.18}$$

n being the number of superposed modes. Similarly, the modal contribution ${}_rT_{ij}^*(\omega)$ to the total transfer function $T_{ij}^*(\omega)$, relating the jth DOF and the ith DOF where a base motion is applied, may be defined as

$${}_rT_{ij}^*(\omega) = \frac{{}_rU_j^*(\omega)}{S_i^*(\omega)}. \tag{4.19}$$

and the total transfer function may be approximated by the superposition of the individual contributions, such that

$$T_{ij}^{*}(\omega) \simeq \sum_{r=1}^{n} {}_{r}T_{ij}^{*}(\omega). \tag{4.20}$$

The superposition of the modal contributions computed with the complex and frequency-dependent eigenpair converges to the exact harmonic response. The complex mode superposition method proves to be of special interest for engineers concerned with the design of effective damping treatments, since the information regarding to the contribution of each mode to the total response is retained. Nevertheless, the major inconvenience of this procedure is that it requires the computation of the complex and frequency dependent modal parameters of several modes within a given bandwidth, which demands large computational requirements when classical algorithms are used. Due to this fact, the complex mode superposition method has been relegated for the analysis of small systems, being common to resort to direct solution methods when the problem size increases. The direct frequency method consists on updating the complex stiffness matrix $\mathbf{K}^{*}(\omega_k)$ for each computational frequency ω_k, and solving Equation (4.2) when the system is excited by a force, or solving the equation derived from Equation (4.15)

$$\left(-\omega^2\mathbf{M}_{\mathrm{uu}} + \mathbf{K}_{\mathrm{uu}}^{*}(\omega_k)\right)\mathbf{U}^{*}(\omega_k) = -\left(-\omega^2\mathbf{M}_{\mathrm{us}} + \mathbf{K}_{\mathrm{us}}^{*}(\omega_k)\right)\mathbf{S}^{*}(\omega_k), \tag{4.21}$$

if the system is excited by a base motion. However, although the exact frequency response is obtained, this method fails to provide information on the individual participation of each mode to the total response.

Motivated by the large computational requirements demanded by the iterative complex eigensolution (ICE) method for determining the complex modal parameters, and by the complex mode superposition method for approximating the frequency response when classical algorithms are considered, new algorithms based on the use of the higher order eigenderivatives are proposed. The developed numerical method is inspired by the earlier work of Cortés and Elejabarrieta [23, 24], who suggested a numerical procedure for approximating the complex eigenpair for a certain computational frequency ω_k, from the undamped one. Therefore, their method only requires the solution of the undamped real eigenproblem, the complex eigenvectors are approximated by finite increments, and the eigenvalues are determined by the Rayleigh quotient. This procedure proves to be an efficient alternative as the solution of a complex eigenproblem for each computational frequency ω_k is avoided. For the particular case of highly damped systems, they also suggest an incremental updating procedure [24] where the eigenvectors are updated in several smaller increments. Nevertheless, the method presents a shortcoming since the choice of the number of increments for approximating the eigenpair with a given tolerance results uncertain.

The proposed numerical method is based on the same fundamental updating idea but several differences are remarkable. Instead of approximating the first order derivatives as finite increments, the present method considers the first and higher order exact eigenderivatives. The fundamental updating procedure updates the complex eigenvectors by the Taylor's series using the first and higher order eigenvector derivatives, and the complex eigenvalues are then computed by the Rayleigh quotient. The contributions of the higher order eigenvector derivatives to the total eigenvector increment, are used to establish a criteria for updating the complex eigenpair with the desired accuracy. In this context, an adaptive step-size control scheme is implemented for computing the complex eigenpair preserving the accuracy defined by the user. The fundamental updating procedure is implemented in two schemes with different purposes: an iterative scheme for computing the complex modal parameters of the system; and an incremental scheme for updating the complex eigenpair within a given frequency bandwidth in order to compute the dynamic response by the complex mode superposition method. With these algorithms, it is intended to provide efficient tools for the dynamic analysis of real-life engineering problems involving strong frequency-dependent viscoelastic materials.

4.2 Higher order eigensensitivities-based updating method

In this section, the higher order eigensensitivities-based numerical method is presented. First, the higher order eigenvalue and eigenvector derivatives respect to the excitation frequency are deduced. After that, the fundamental updating procedure is detailed, the convergence and the accuracy conditions are defined, and the implemented adaptive step-size control scheme is described. Finally, the fundamental updating procedure is implemented into an iterative scheme for computing the complex modal parameters, and into an incremental scheme for determining the complex and frequency-dependent eigenpair within the defined bandwidth.

The developed numerical method has been published in the *International Journal for Numerical Methods in Engineering* [73].

4.2.1 Eigenvalue and eigenvector derivatives

The eigenvalue and eigenvector derivatives with respect to design parameters are commonly employed in structural optimization, sensitivity analysis and finite element model updating algorithms [37, 19, 124]. Extensive surveys of the applications and the methods to compute the eigenderivatives with respect to arbitrary parameters are presented by Adelman and Haftka [2] and, Murthy and Haftka [86].

Although eigenderivatives have several applications, the objective of this dissertation is to develop numerical algorithms for the dynamic analysis in frequency domain. Therefore, all the presented derivatives are computed with respect to the excitation frequency ω.

For deducing the first and higher order eigenderivatives the generalized eigenproblem is considered with real and symmetric mass $\mathbf{M}$ and stiffness $\mathbf{K}$ matrices, given by

$$\left(-\lambda_r \mathbf{M} + \mathbf{K}\right) \phi_r = 0, \tag{4.22}$$

where the mass $\mathbf{M}$ and stiffness $\mathbf{K}$ matrices have dimension $n \times n$ and are considered to be positive definite, so that the system posses n real and positive distinct eigenvalues. The eigenvectors may be arbitrarily normalized being common in practice to normalize them with respect to the unit modal mass. The mass normalized eigenvectors satisfy an orthogonality relationship over the mass and stiffness matrices, such that

$$\phi_r^{\mathrm{T}} \mathbf{M} \phi_s = \delta_{rs} \tag{4.23}$$

$$\text{and} \quad \phi_r^{\mathrm{T}} \mathbf{K} \phi_s = \lambda_r \delta_{rs}, \qquad \forall\ r, s = 1, \cdots, n \tag{4.24}$$

where δ_{rs} is the Kronecker delta function.

The first order eigenderivatives of the rth mode are obtained differentiating Equation (4.22) with respect to the excitation frequency ω, resulting in

$$\left(-\frac{\partial \lambda_r}{\partial \omega}\mathbf{M} - \lambda_r \frac{\partial \mathbf{M}}{\partial \omega} + \frac{\partial \mathbf{K}}{\partial \omega}\right) \phi_r + \left(-\lambda_r \mathbf{M} + \mathbf{K}\right) \frac{\partial \phi_r}{\partial \omega} = 0. \tag{4.25}$$

The terms containing $\partial \mathbf{M}/\partial \omega$ are omitted since the mass of the system remains invariable. Premultiplying by ϕ_r^{T}, Equation (4.25) may be rewritten as

$$\phi_r^{\mathrm{T}} \left(-\frac{\partial \lambda_r}{\partial \omega}\mathbf{M} + \frac{\partial \mathbf{K}}{\partial \omega}\right) \phi_r + \phi_r^{\mathrm{T}} \left(-\lambda_r \mathbf{M} + \mathbf{K}\right) \frac{\partial \phi_r}{\partial \omega} = 0. \tag{4.26}$$

The term $\phi_r^{\mathrm{T}} \left(-\lambda_r \mathbf{M} + \mathbf{K}\right)$ is invariably equal to zero according to Equation (4.22) as $\mathbf{M}$ and $\mathbf{K}$ are both symmetric. Noting that the eigenvectors are mass normalized, the derivative of the rth eigenvalue respect to the excitation frequency ω, yields

$$\frac{\partial \lambda_r}{\partial \omega} = \phi_r^{\mathrm{T}} \frac{\partial \mathbf{K}}{\partial \omega} \phi_r. \tag{4.27}$$

While rearranging Equation (4.25) to reflect the eigenvector derivative, it leads to

$$\mathbf{A}_{r,\mathrm{I}} \frac{\partial \phi_r}{\partial \omega} = \mathbf{b}_{r,\mathrm{I}}, \tag{4.28}$$

where

$$\mathbf{A}_{r,\mathrm{I}} = \left(-\lambda_r \mathbf{M} + \mathbf{K}\right), \tag{4.29}$$

and

$$\mathbf{b}_{r,\mathrm{I}} = \left(\frac{\partial \lambda_r}{\partial \omega}\mathbf{M} - \frac{\partial \mathbf{K}}{\partial \omega}\right)\phi_r, \tag{4.30}$$

where subindex $(\bullet)_{\mathrm{I}}$ refers to the first-order derivative. From Equation (4.28), the eigenvector derivative $\partial\phi_r/\partial\omega$ cannot be explicitly solved since the matrix of coefficients $\mathbf{A}_{r,\mathrm{I}}$ is singular as λ_r is an eigenvalue of the system.

The classical methods to compute the eigenvector derivatives of non-repeating eigenvalues are those proposed by Fox and Kapoor [36] and that of Nelson's [89]. The former defines the rth eigenvector derivative as a linear combination of all the modes of the system, whereas the latter considers a pivoting procedure only requiring the rth eigenpair for computing the exact eigenvector derivative of such mode. Some authors have proposed alternative methods to that of Fox and Kapoors for truncated problems, e.g., Wang [129], Liu *et al.* [63] and, Zhang and Zerva [134] uses a residual static correction. The efficiency of different methods to evaluate the eigenvector derivatives of full and truncated problems is analyzed by Cortés and Elejabarrieta [24]. The authors verifies that the Nelson modality is the most efficient method for truncated problems since only the corresponding eigenvalue and eigenvector are required for calculating the exact eigenvector derivative. This feature makes this method suitable for large-ordered structural systems where working with the complete modal base becomes impracticable. In addition, the Nelson's method constitutes a specially powerful alternative since allows computing the higher order derivatives efficiently, as is evidenced when dealing with the second and higher order derivatives. For those reasons the Nelson's method is considered for computing the eigenvector derivatives.

The solutions of Equation (4.28) takes the general form given by

$$\frac{\partial \phi_r}{\partial \omega} = \nu_{r,\mathrm{I}} + c_{r,\mathrm{I}}\phi_r, \tag{4.31}$$

where ν_r is an arbitrary particular solution of

$$\mathbf{A}_{r,\mathrm{I}}\nu_{r,\mathrm{I}} = \mathbf{b}_{r,\mathrm{I}}. \tag{4.32}$$

Since the matrix of coefficients $\mathbf{A}_{r,\mathrm{I}}$ is singular, the vector $\nu_{r,\mathrm{I}}$ is computed by a pivoting procedure. At this stage, the matrix of coefficients $\mathbf{A}_{r,\mathrm{I}}$ is factorized and the system of linear equations given by Equation (4.32) solved.

The scalar $c_{r,\mathrm{I}}$ of the homogeneous solution $c_{r,\mathrm{I}}\phi_r$, is calculated differentiating the mass normalization equation, leading to

$$2\phi_r^{\mathrm{T}}\mathbf{M}\frac{\partial\phi_r}{\partial\omega}+\phi_r^{\mathrm{T}}\frac{\partial\mathbf{M}}{\partial\omega}\phi_r=0. \tag{4.33}$$

Substituting Equation (4.31) into Equation (4.33), using mass normalization, and being $\partial\mathbf{M}/\partial\omega=0$, yields

$$c_{r,\mathrm{I}}=-\phi_r^{\mathrm{T}}\mathbf{M}\nu_{r,\mathrm{I}}. \tag{4.34}$$

This way, assuming that the stiffness matrix $\mathbf{K}$ is differentiable with respect to the excitation frequency, the exact eigenvector derivative $\partial\phi_r/\partial\omega$ is computed by applying the Nelson's method.

The first order eigenvector derivative computed for the frequency ω_k, may be used for approximating the eigenvector for ω_{k+1}, such that

$$\phi_r^*\left(\omega_{k+1}\right)\approx\phi_r^*\left(\omega_k\right)+\frac{\partial\phi_r^*\left(\omega_k\right)}{\partial\omega}\left(\omega_{k+1}-\omega_k\right), \tag{4.35}$$

thus accounting for the variations of the dynamic properties exhibited by the viscoelastic material when varying the excitation frequency. Nevertheless, the linear approximation inherent in the use of the first order derivatives might be adequate when large variations are manifested with respect to the excitation frequency. This is common on viscoelastically damped structures since the mechanical properties of such materials strongly vary with frequency. Similarly, the use of the first order derivatives considerably limits the maximum frequency increment $\Delta\omega$ that can be considered to approximate the eigenvectors precisely. This limitation can be minimized if the second and higher order eigenderivatives are considered.

The higher order derivatives are calculated following a similar procedure described for the first order derivatives. Differentiating Equation (4.22) twice with respect to the excitation frequency, and omitting the terms $\partial^n\mathbf{M}/\partial\omega^n$, yields

$$\left(-\frac{\partial^2\lambda_r}{\partial\omega^2}\mathbf{M}+\frac{\partial^2\mathbf{K}}{\partial\omega^2}\right)\phi_r+2\left(-\frac{\partial\lambda_r}{\partial\omega}\mathbf{M}+\frac{\partial\mathbf{K}}{\partial\omega}\right)\frac{\partial\phi_r}{\partial\omega}+\left(-\lambda_r\mathbf{M}+\mathbf{K}\right)\frac{\partial^2\phi_r}{\partial\omega^2}=0. \tag{4.36}$$

Premultiplying by ϕ_r^{T} and using mass normalization condition, the second derivative of the rth eigenvalue yields

$$\frac{\partial^2\lambda_r}{\partial\omega^2}=\phi_r^{\mathrm{T}}\frac{\partial^2\mathbf{K}}{\partial\omega^2}\phi_r-2\phi_r^{\mathrm{T}}\left(\frac{\partial\lambda_r}{\partial\omega}\mathbf{M}-\frac{\partial\mathbf{K}}{\partial\omega}\right)\frac{\partial\phi_r}{\partial\omega}. \tag{4.37}$$

By rearranging Equation (4.36), the second order eigenvector derivative may be determined from

$$\mathbf{A}_{r,\mathrm{II}}\frac{\partial^2\phi_r}{\partial\omega^2} = \mathbf{b}_{r,\mathrm{II}}, \tag{4.38}$$

where the matrix of coefficients $\mathbf{A}_{r,\mathrm{II}} = \mathbf{A}_{r,\mathrm{I}}$. The vector $\mathbf{b}_{r,\mathrm{II}}$ is obtained rearranging Equation (4.36), yielding to

$$\mathbf{b}_{r,\mathrm{II}} = \left(\frac{\partial^2\lambda_r}{\partial\omega^2}\mathbf{M} - \frac{\partial^2\mathbf{K}}{\partial\omega^2}\right)\phi_r + 2\left(\frac{\partial\lambda_r}{\partial\omega}\mathbf{M} - \frac{\partial\mathbf{K}}{\partial\omega}\right)\frac{\partial\phi_r}{\partial\omega}. \tag{4.39}$$

Again, the solution of Equation (4.38) is obtained following the same procedure described for solving Equation (4.28), where the solution of the second order eigenvector derivative is written as in Equation (4.31), so that

$$\frac{\partial^2\phi_r}{\partial\omega^2} = \nu_{r,\mathrm{II}} + c_{r,\mathrm{II}}\phi_r. \tag{4.40}$$

The procedure to be performed is the same as the one described for the first-order derivatives. The particular solution $\nu_{r,\mathrm{II}}$ may be calculated from

$$\mathbf{A}_{r,\mathrm{II}}\nu_{r,\mathrm{II}} = \mathbf{b}_{r,\mathrm{II}}. \tag{4.41}$$

To solve 4.41, the pivoting procedure is again applied yielding to a non-singular set of equations from where the particular solution $\nu_{r,\mathrm{II}}$ can be solved. At this point, the major advantage of the Nelson's method for computing the higher order eigenvector derivatives is manifested. Since the matrix of coefficients does not change, being $\mathbf{A}_{r,\mathrm{II}} = \mathbf{A}_{r,\mathrm{I}}$, the factorization of $\mathbf{A}_{r,\mathrm{II}}$ is not necessary, thus avoiding the most time demanding operation when solving Equation (4.41). This way, the particular solution $\nu_{r,\mathrm{II}}$ is efficiently computed, and as a result, also the second order eigenvector derivative.

The scalar $c_{r,\mathrm{II}}$ is obtained by differentiating the mass normalization condition for a second time with respect to the excitation frequency. Differentiating twice Equation (4.23), yields

$$\frac{\partial\phi_r^{\mathrm{T}}}{\partial\omega}\mathbf{M}\frac{\partial\phi_r}{\partial\omega} + \phi_r^{\mathrm{T}}\mathbf{M}\frac{\partial^2\phi_r^{\mathrm{T}}}{\partial\omega^2} = 0. \tag{4.42}$$

Substituting Equation (4.40) into Equation (4.42) and using mass normalization condition, leads to

$$c_{r,\mathrm{II}} = -\phi_r^{\mathrm{T}}\mathbf{M}\nu_{r,\mathrm{II}} - \frac{\partial\phi_r^{\mathrm{T}}}{\partial\omega}\mathbf{M}\frac{\partial\phi_r}{\partial\omega}. \tag{4.43}$$

This way, the exact second order eigenvector derivative is determined.

Following the same procedure as that described by Equations (4.25-4.34) for the first order eigenderivatives, or by Equations (4.36-4.43) for the second order ones, the higher order eigenderivatives may be computed. The expression for the nth eigenvalue derivative, with $n \geq 2$, $\partial\mathbf{M}/\partial\omega = 0$, and being $\mathbf{M}$ and $\mathbf{K}$ both symmetric, is written as

$$\frac{\partial^n \lambda_r}{\partial \omega^n} = \phi_r^{\mathrm{T}} \frac{\partial^n \mathbf{K}}{\partial \omega^n} \phi_r - \phi_r^{\mathrm{T}} \left[\sum_{p=1}^{n-1} \binom{n}{p} \left(\frac{\partial^p \lambda_r}{\partial \omega^p} \mathbf{M} - \frac{\partial^p \mathbf{K}}{\partial \omega^p} \right) \frac{\partial^{n-p} \phi_r}{\partial \omega^{n-p}} \right]. \tag{4.44}$$

Following the steps described by Equations (4.31-4.34) or Equations (4.40-4.43), the nth eigenvector derivative may be solved from

$$\mathbf{A}_{r,n} \frac{\partial^n \phi_r}{\partial \omega^n} = \mathbf{b}_{r,n}, \tag{4.45}$$

where the matrix of coefficients $\mathbf{A}_{r,n} = (-\lambda_r \mathbf{M} + \mathbf{K})$ remains invariable. The vector $\mathbf{b}_{r,n}$, is written as

$$\mathbf{b}_{r,n} = \left(\frac{\partial^n \lambda_r}{\partial \omega^n} \mathbf{M} - \frac{\partial^n \mathbf{K}}{\partial \omega^n} \right) \phi_r + \sum_{p=1}^{n-1} \binom{n}{p} \left(\frac{\partial^p \lambda_r}{\partial \omega^p} \mathbf{M} - \frac{\partial^p \mathbf{K}}{\partial \omega^p} \right) \frac{\partial^{n-p} \phi_r}{\partial \omega^{n-p}}, \tag{4.46}$$

the solution of Equation (4.45) takes the form

$$\frac{\partial^n \phi_r}{\partial \omega^n} = \nu_{r,n} + c_{r,n} \phi_r. \tag{4.47}$$

The particular solution $\nu_{r,n}$ is again solved by a pivoting procedure from

$$\mathbf{A}_{r,n} \nu_{r,n} = \mathbf{b}_{r,n}, \tag{4.48}$$

whereas the scalar $c_{r,n}$ of the homogeneous solution $c_{r,n}\phi_r$, is given by

$$c_{r,n} = -\phi_r^{\mathrm{T}} \mathbf{M} \nu_{r,n} - \sum_{p=1}^{n-1} \frac{1}{2} \binom{n}{p} \frac{\partial^p \phi_r^{\mathrm{T}}}{\partial \omega^p} \mathbf{M} \frac{\partial^{n-p} \phi_r}{\partial \omega^{n-p}}. \tag{4.49}$$

For computing the eigenderivatives, the stiffness matrix derivatives are also required. The stiffness matrix of a viscoelastically damped structure is decomposed into a constant stiffness matrix related to the elastic components and another complex and frequency dependent stiffness matrix related to the viscoelastic material. Thus, the nth derivative of the stiffness matrix is written as

$$\frac{\partial^n \mathbf{K}^*(\omega)}{\partial \omega^n} = \frac{\partial^n \mathbf{K}_{\mathrm{v}}^*(\omega)}{\partial \omega^n}, \tag{4.50}$$

where as given by Equation (2.22), the complex and frequency-dependent stiffness matrix related to the viscoelastic material is defined as

$$\mathbf{K}_{\mathrm{v}}^{*}(\omega) = \frac{G_{\mathrm{v}}^{*}(\omega)}{G_0}\mathbf{K}_{\mathrm{v},0}, \tag{4.51}$$

where $G_{\mathrm{v}}^{*}(\omega)$ is the complex shear modulus of the viscoelastic material, G_0 is the static shear modulus and $\mathbf{K}_{\mathrm{v},0}$ is the static stiffness matrix related to the viscoelastic material. Thus, assuming that the material constitutive model that characterizes the complex shear modulus $G_{\mathrm{v}}^{*}(\omega)$ is continuous and differentiable within the frequency bandwidth under analysis, Equation (4.51) is rewritten as

$$\frac{\partial^n \mathbf{K}^{*}(\omega)}{\partial \omega^n} = \frac{1}{G_0}\frac{\partial^n G_{\mathrm{v}}^{*}(\omega)}{\partial \omega^n}\mathbf{K}_{\mathrm{v},0}. \tag{4.52}$$

Nelson's method constitutes an efficient way for computing the higher order eigenderivatives since the matrix of coefficients $\mathbf{A}_r$ does not change for a given mode and computational frequency and thus, $\mathbf{A}_r$ is once factorized when computing the first order eigenvector derivative. As the major computation efforts when solving Equation (4.32) are related to the factorization of $\mathbf{A}_{r,\mathrm{I}}$, the higher order eigenvector derivatives are computed considerably faster than the first order one.

4.2.2 Fundamental updating procedure

Next, the fundamental updating procedure from where the iterative and the incremental schemes are derived, is described. This procedure considers the Taylor's series to approximate the rth eigenvector for the frequency ω_{k+1}, from the known eigenvector for the frequency ω_k, making use of the first and the higher order eigenvector derivatives computed for the latter frequency. Thus, the eigenvector $\phi_r^{*}(\omega_{k+1})$ can be approximated by the Taylor's series as

$$\phi_r^{*}\left(\omega_{k+1}\right) = \sum_{p=0}^{n} \frac{\partial^p \phi_r^{*}\left(\omega_k\right)}{\partial \omega^p}\frac{\left(\omega_{k+1}-\omega_k\right)^p}{p!} + \mathcal{R}_n, \tag{4.53}$$

where $\mathcal{R}_n$ is the error after n terms, given by

$$\mathcal{R}_n = \int_{\omega_k}^{\omega_{k+1}} \frac{\partial^{n+1}\phi_r^{*}(\omega)}{\partial \omega^{n+1}}\frac{\left(\omega_{k+1}-\omega\right)^n}{n!}\mathrm{d}\omega, \tag{4.54}$$

using the mean-value theorem, the residue term can be rewritten in the Lagrange form as

$$\mathcal{R}_n = \frac{\partial^{n+1}\phi_r^*(\omega_c)}{\partial\omega^{n+1}}\frac{(\omega_{k+1}-\omega_k)^{n+1}}{(n+1)!}, \tag{4.55}$$

being $\omega_c \in [\omega_k, \omega_{k+1}]$. When a truncated series is considered, the accuracy of the approximated eigenvector for the frequency ω_{k+1} depends on the considered step size $\Delta\omega = \omega_{k+1} - \omega_k$. Therefore, some conditions must be defined for selecting a proper step size that will ensure the accuracy of the approximated eigenvector $\phi_r^*(\omega_{k+1})$. The first established condition ensures the convergence of the function approximated by the Taylor's series for the frequency ω_{k+1}, and states that the norm of a given term must be greater than the norm of the next term, such that

$$\left\|\frac{\partial\phi_r^*(\omega_k)}{\partial\omega}\Delta\omega\right\| > \left\|\frac{\partial^2\phi_r^*(\omega_k)}{\partial\omega^2}\frac{\Delta\omega^2}{2!}\right\| > \ldots > \left\|\frac{\partial^n\phi_r^*(\omega_k)}{\partial\omega^n}\frac{\Delta\omega^n}{n!}\right\|, \tag{4.56}$$

This condition ensures that the contribution of the term $n+1$ is smaller than the contribution of the last term n, but it does not guarantee the precision of the approximated eigenvector. Therefore, a second condition related to the error due to the Taylor's series truncation results necessary. The second established condition states that the norm of the last term with respect to the norm of the total increment, must be smaller than a user defined tolerance, such that

$$\frac{\left\|\frac{\partial^n\phi_r^*(\omega_k)}{\partial\omega^n}\frac{\Delta\omega^n}{n!}\right\|}{\left\|\sum_{p=1}^{n}\frac{\partial^p\phi_r^*(\omega_k)}{\partial\omega^p}\frac{\Delta\omega^p}{p!}\right\|} \leq \text{Tol.} \tag{4.57}$$

This second condition, in conjunction with the first one, guarantees the accuracy of the approximated eigenvector $\phi_r^*(\omega_{k+1})$.

To better understand how the method is applied, the process is outlined in Figure 4.1, where the frequency dependence of the jth element of the rth eigenvector ${}_r\phi_j^*(\omega)$, is represented. Lets consider that from the known eigenpair $(\lambda_r^*(\omega_i),\ \phi_r^*(\omega_i))$ for the initial frequency ω_i, the eigenpair $(\lambda_r^*(\omega_f),\ \phi_r^*(\omega_f))$ for the final frequency ω_f must be computed.

The first step consists on defining the number of eigenvector derivatives that are going to be considered, and the tolerance for the accuracy condition given by Equation (4.57). After that, the considered n eigenvector derivatives are computed for the initial frequency ω_i and is tried to update the complex eigenpair for the final frequency ω_f, so that the frequency increment $\Delta\omega = \omega_f - \omega_i$, is assumed. The conditions given by Equations (4.56) and (4.57) may be violated if the frequency increment $\Delta\omega$ results too large. In such case, the frequency step must be reduced until both conditions are met. The frequency increment may be adapted in several different ways, the simplest form consisting on the use of a constant reduction factor, so that the new frequency increment is defined as

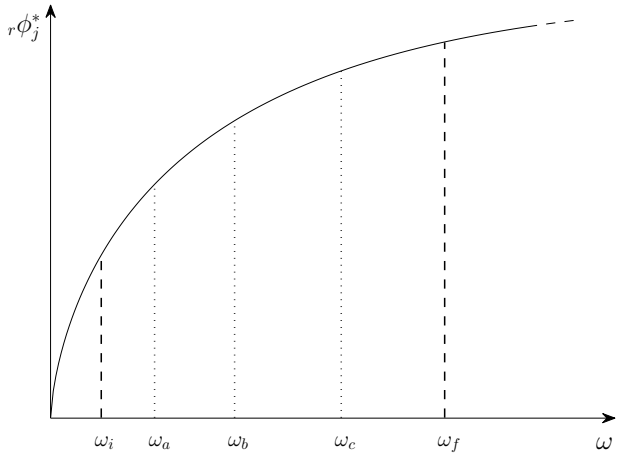

Figure 4.1: Scheme of the fundamental updating procedure.

$$\Delta\omega = \kappa\Delta\omega_0, \tag{4.58}$$

where κ is the reduction factor commonly defined between $3/4 \leq \kappa < 1$ and, $\Delta\omega$ and $\Delta\omega_0$ are the adapted and the initial frequency increments, respectively. If the accuracy conditions are not satisfied after the first reduction, the already adapted frequency increment $\Delta\omega$ is declared as the initial one $\Delta\omega_0$, and Equation (4.58) is again applied until Equations (4.56) and (4.57) are satisfied. With the adapted frequency step $\Delta\omega$ the eigenvector for the frequency $\omega_a = \omega_i + \Delta\omega$ is updated, the n eigenvector derivatives are again computed for ω_a, and the eigenvector for the frequency ω_f is tried to be computed considering the frequency increment $\Delta\omega = \omega_f - \omega_a$. If such frequency step does not satisfies the accuracy conditions, the frequency increment is adapted by Equation (4.58), the eigenvector for the intermediate frequency $\omega_b = \omega_a + \Delta\omega$ is updated, the n eigenvector derivatives for ω_b computed, and is attempted to compute ω_f with $\Delta\omega = \omega_f - \omega_b$. This process is repeated until reaching to the final frequency ω_f. The adaptive step-size control scheme guarantees the accuracy of the approximated eigenvectors for the frequency ω_f, and forces to recalculate the eigenvector derivatives if the convergence and the accuracy conditions given by Equations (4.56) and (4.57), respectively, are not satisfied.

After updating the complex eigenvector for the frequency ω_f, the complex eigenvalue $\lambda_r^*(\omega_f)$ is determined by the Rayleigh quotient, as follows:

$$\lambda_r^*\left(\omega_f\right) = \frac{\phi_r^{*\mathrm{T}}\left(\omega_f\right)\mathbf{K}^*\left(\omega_f\right)\phi_r^*\left(\omega_f\right)}{\phi_r^{*\mathrm{T}}\left(\omega_f\right)\mathbf{M}\,\phi_r^*\left(\omega_f\right)}. \tag{4.59}$$

This way, the complex eigenpair for the desired frequency ω_f is approximated with the

established tolerance. The presented fundamental updating procedure allows determining the complex eigenpair for any frequency avoiding the solution of a complex eigenproblem. The only requisite is to know the complex eigenpair for a reference frequency ω_i, commonly the undamped eigenpair is used as the initial data, so that $\omega_i = 0$. Nevertheless, although some difficulties emerge when departing from the undamped solution, they can be avoided with the procedure detailed next.

The proposed updating procedure can be applied only if the derivatives of the material model considered for describing the frequency dependence of the complex shear modulus $G^*_{\mathrm{v}}(\omega)$ are defined within the frequency bandwidth under analysis. In the particular case of the four-parameter fractional derivative model considered to characterize the viscoelastic core in Chapter 2, the first and the higher order derivatives are not defined for $\omega_i = 0$. To avoid this singularity, the Nelson's method may be applied in the way suggested by Cortés and Elejabarrieta [24], so that the first order derivatives are approximated as finite increments. With this procedure, the complex eigenpair $(\lambda^*_r(\omega_a),\ \phi^*_r(\omega_a))$ for the frequency ω_a from where the proposed method will depart, may be approximated from the undamped eigenpair $(\lambda_{r,0},\ \phi_{r,0})$ as detailed next.

First the eigenvalue increment is deduced from Equation (4.27), such as

$$\Delta\lambda^*_r = \phi^{\mathrm{T}}_{r,0}\Delta\mathbf{K}^*\phi_{r,0}, \tag{4.60}$$

where

$$\Delta\mathbf{K}^* = \frac{1}{G_0}\left(G^*_{\mathrm{v}}(\omega_a) - G_0\right)\mathbf{K}_{\mathrm{v},0}, \tag{4.61}$$

is the increment exhibited by the complex stiffness matrix due to the frequency increment $\Delta\omega = \omega_a$. The eigenvector increment is defined from Equations (4.28-4.30), resulting in

$$\left(-\lambda_{r,0}\mathbf{M} + \mathbf{K}_0\right)\Delta\phi^*_r = \left(\Delta\lambda^*_r\mathbf{M} - \Delta\mathbf{K}^*\right)\phi_{r,0}, \tag{4.62}$$

where $\mathbf{K}_0 = \mathbf{K}_{\mathrm{e}} + \mathbf{K}_{\mathrm{v},0}$ is the static global stiffness matrix. The solution of Equation (4.62) takes the form

$$\Delta\phi^*_r = \nu_r + c_r\phi_{r,0}, \tag{4.63}$$

where the particular solution ν_r is solved by the pivoting procedure from

$$\left(-\lambda_{r,0}\mathbf{M} + \mathbf{K}_0\right)\nu_r = \left(\Delta\lambda^*_r\mathbf{M} - \Delta\mathbf{K}^*\right)\phi_{r,0}, \tag{4.64}$$

and where the scalar c_r of the homogenous solution $c_r\phi_{r,0}$ is analogous to that given by Equation (4.34), so that

$$c_r = -\phi^{\mathrm{T}}_{r,0}\mathbf{M}\nu_r. \tag{4.65}$$

Substituting Equation (4.65) into (4.63), the eigenvector increment $\Delta\phi_r^*$ is computed, and the eigenvector for the frequency ω_a approximated as

$$\phi_r^*(\omega_a) \approx \phi_{r,0} + \Delta\phi_r^*. \tag{4.66}$$

Finally, the complex eigenvalue $\lambda_r^*(\omega_a)$ for the same frequency is determined by the Rayleigh quotient by Equation (4.59).

With this procedure the singularity given at the initial frequency $\omega_i = 0$ is avoided, and the updating procedure based on the use of the first and the higher order eigensensitivities can be applied departing from the eigenpair $\lambda_r^*(\omega_a),\ \phi_r^*(\omega_a)$. This alternative is computationally much cheaper than solving the complex eigenproblem for the frequency ω_a by classical algorithms. The only aspect to consider is that small frequency increments may only be considered in order to preserve the accuracy.

Next, an iterative and an incremental scheme are presented both being derived from this fundamental updating procedure. The iterative algorithm is applied for determining the complex modal parameters of the system, whereas the incremental algorithm aims to compute the complex eigenpair within the frequency bandwidth of interest with a given frequency resolution. From the complex and frequency-dependent eigenpair, the contribution of each mode to the total dynamic response is determined, and the total response computed by superposition of such modal contributions.

4.2.3 Iterative scheme

The iterative process departs from the undamped real eigensolution $(\lambda_{r,0},\ \phi_{r,0})$ from where an initial estimate for the natural frequency is obtained $\omega_{r,0} = \sqrt{\lambda_{r,0}}$. The complex eigenpair for the frequency $\omega_{r,0}$ may be determined by the fundamental updating procedure. However, this first iteration is the most time consuming one since the eigenderivatives must be computed several times, even more when the higher order modes are analyzed. Therefore, depending on the specific system under analysis, considering the solution of the complex eigenproblem for computing the complex eigenpair for the frequency $\omega_{r,0}$ may be a more convenient alternative.

The advantage of the proposed iterative method is that the complex eigensolution is avoided for the subsequent iterations. In general, after the complex eigenpair have been obtained for the frequency $\omega_{r,0}$, computing the eigenderivatives at $\omega_{r,0}$ is sufficient to determine the complex eigenpair for all the $\omega_{r,j}$ resonance frequencies of the next jth iterations until reaching to the converged solution. The iterative algorithm employed on all the presented practical examples is schematized in Table 4.3, where the complex eigensolution is considered for the first iteration.

Table 4.3: Proposed iterative scheme.

1. Solve the undamped real eigenproblem: $\mathbf{K}(0)\phi_{r,0} = \lambda_{r,0}\mathbf{M}\phi_{r,0}$

1.1. Compute the rth undamped natural frequency: $\omega_{r,0} = \sqrt{\lambda_{r,0}}$

2. Initialize $j = 1$; solve the complex eigenproblem: $\mathbf{K}^*(\omega_{r,0})\phi^*_{r,j} = \lambda^*_{r,j}\mathbf{M}\phi^*_{r,j}$, and obtain the new estimate for the natural frequency: $\omega_{r,1} = \sqrt{\mathrm{Re}(\lambda^*_{r,1})}$

3. Compute n eigenderivatives at $\omega_{r,0}$

4. while $\epsilon_r < \left|\frac{\omega_{r,j}-\omega_{r,j-1}}{\omega_{r,j}}\right|$

4.1. Update j = j +1

4.2. Update the complex eigenvector $\phi^*_{r,j}$ from $\phi^*_{r,1}$ by Taylor series

4.3. Compute the complex eigenvalue $\lambda^*_{r,j}$ by Rayleigh

4.4. Compute: $\omega_j = \sqrt{\mathrm{Re}(\lambda^*_{r,j})}$, and test the convergence

5. Store the computed rth complex eigenpair (λ^*_r, ϕ^*_r)

This alternative is specially interesting for large-ordered structural systems, since the complex eigenproblem is solved only in the first iteration, and in general the complex eigenderivatives needs to be computed only once at $\omega_{r,0}$. If during the iterative process the accuracy conditions described by Equations 4.56 and 4.57 are not fulfilled, the step size must be adapted and the eigenderivatives recalculated somewhere between $\omega_{r,0}$ and the converged resonance frequency. However, in the practical application some criteria for the proper choice of the number of eigenderivatives is provided in order to avoid having to recalculate them.

4.2.4 Incremental scheme

Another interesting feature of the proposed higher order eigensensitivities-based numerical method, is related to the computation of the complex eigenvalues and eigenvectors within a given frequency bandwidth. The computation of the complex and frequency-dependent modal parameters aims to determine the steady-state dynamic response by the complex mode superposition method.

The proposed fundamental updating procedure is implemented in an incremental scheme for updating the complex eigenparameters within an initial frequency ω_i and a final one ω_f, with a certain frequency resolution $\Delta\omega_{\mathrm{res}}$. The major advantage of the proposed incremental scheme is that the computation of the eigenderivatives is not re-

quired for each frequency step. The n eigenvector derivatives computed for the initial frequency ω_i, are employed to approximate the eigenvectors of the next m steps, $\phi_r^*(\omega_{i+1})$, $\phi_r^*(\omega_{i+2}), \ldots, \phi_r^*(\omega_{i+m})$, until one of the two defined accuracy conditions described by Equations (4.56) and (4.57) is not satisfied because $\Delta\omega = (m+1)\Delta\omega_{\text{res}}$ becomes too large. Therefore, the n eigenderivatives are recalculated at the last updated computational frequency ω_{i+m}, and again, the next p eigenvectors are updated until one of the accuracy conditions is infringed with the frequency increment $\Delta\omega = (p+1)\Delta\omega_{\text{res}}$. In Table 4.4 the proposed incremental algorithm for updating the rth eigenpair is schematized assuming that it is departed from the undamped solution, so that $\omega_i = 0$.

Commonly, when computing the frequency response of a system within a given frequency bandwidth, hundreds or even thousands computational frequencies used to be considered. The solution of a complex eigenproblem for each computational frequency by classical algorithms becomes very time consuming, specially when the size of the system increases. By contrast, the proposed incremental scheme only requires the computation of the eigenderivatives at relatively few frequencies, and as the major computational effort is related to the calculation of such derivatives, the eigenparameters are efficiently updated within the frequency bandwidth under analysis, even if a small frequency resolution is required.

4.3 Practical application

Next, a practical application to validate the proposed iterative and incremental algorithms is presented. Concretely, the 210 mm long CLD beam already analyzed in Chapter 2 is considered. The same finite element model described in Section 2.5.2 is employed, the beam being discretized into 5 mm long 42 finite elements defined by 43 nodes, yielding to 168 degrees of freedom after applying the clamped boundary condition. The geometrical and physical properties of each layer are summarized in Table 2.1, whereas the storage modulus of the constraining layers and the complex shear modulus of the viscoelastic core are given in Sections 2.5.1 and 2.5.2, respectively.

First, some criteria for selecting the number of derivatives and the tolerance for the accuracy condition are described for both the proposed iterative and incremental algorithms in order to improve the efficiency.

Then, the complex modal parameters of the beam are determined by the iterative modal strain energy method (IMSE), the iterative complex eigensolution method (ICE), and the proposed iterative algorithm. The results provided by the three methods are discussed, and the proposed one is validated correlating the determined complex modal parameters with those computed by the ICE method.

Table 4.4: Proposed incremental scheme.

1. Solve the undamped real eigenproblem: $\mathbf{K}(0)\phi_{r,0} = \lambda_{r,0}\mathbf{M}\phi_{r,0}$

2. Initialize with $\omega_k = \Delta\omega_{\text{res}}$, and set $\mathit{diff} = 1$, $\mathit{adapt} = 0$

3. Compute the first increment $(\lambda_r^*(\omega_k), \phi_r^*(\omega_k))$ by Eqs. (4.60-4.66) and (4.59)

4. **while** $\omega_k \leq \omega_f$

  if $\mathit{diff} = 1$

    Compute n eigenderivatives at ω_k, and declare $\omega_{\text{last}} = \omega_k$

    if $\Delta\omega = \Delta\omega_{\text{res}}$ infringes Eqs. (4.56) and/or (4.57)

      Adapt $\Delta\omega$ and declare $\Delta\omega_{\text{aux}} = \Delta\omega$, $\omega_{\text{aux}} = \omega_{\text{last}} + \Delta\omega$, and $\mathit{adapt} = 1$

      while $\Delta\omega_{\text{aux}} < \Delta\omega_{\text{res}}$

        Compute $\phi_r^*(\omega_{\text{aux}})$ from $\phi_r^*(\omega_{\text{last}})$ by Taylor's series and normalize

        Compute $\lambda_r^*(\omega_{\text{aux}})$ by Rayleigh

        Compute n eigenderivatives at ω_{aux}, declare $\omega_{\text{last}} = \omega_{\text{aux}}$

        $\Delta\omega = \Delta\omega_{\text{res}} - \Delta\omega_{\text{aux}}$

        Adapt $\Delta\omega$ and compute $\Delta\omega_{\text{aux}} = \Delta\omega_{\text{aux}} + \Delta\omega$

        Update $\omega_{\text{aux}} = \omega_{\text{last}} + \Delta\omega$

    if $\mathit{adapt} = 1$

      Update $\omega_k = \omega_{\text{last}} + \Delta\omega$, and set $\mathit{diff} = 0$

    else

      Update $\omega_k = \omega_{\text{last}} + \Delta\omega_{\text{res}}$, and set $\mathit{diff} = 0$

    Compute $\phi_r^*(\omega_k)$ from $\phi_r^*(\omega_{\text{last}})$ by Taylor's series and normalize

    Compute $\lambda_r^*(\omega_k)$ by Rayleigh

    Update $\omega_k = \omega_k + \Delta\omega_{\text{res}}$

  else

    Compute $\Delta\omega = \omega_k - \omega_{\text{last}}$, and set $\mathit{adapt} = 0$

    if $\Delta\omega$ infringes Eqs. (4.56) and/or (4.57)

      Compute $\omega_k = \omega_k - \Delta\omega_{\text{res}}$, and set $\mathit{diff} = 1$

    else

      Compute $\phi_r^*(\omega_k)$ from $\phi_r^*(\omega_{\text{last}})$ by Taylor's series and normalize

      Compute $\lambda_r^*(\omega_k)$ by Rayleigh

      Update $\omega_k = \omega_k + \Delta\omega_{\text{res}}$

5. Store the computed rth complex and frequency-dependent eigenpair $(\lambda_r^*(\omega), \phi_r^*(\omega))$

After that, three approximated procedures are analyzed for computing the frequency response of the studied beam by modal superposition. The first approach considers the real and non-frequency-dependent modal parameters determined by the IMSE method, the second one the complex and non-frequency-dependent modal parameters determined by the ICE method, and the last one the complex and frequency-dependent modal parameters determined by the proposed incremental scheme. The accuracy of each approximation is discussed by comparing them with the exact dynamic response computed by the direct frequency method. Then, the frequency response obtained by the complex mode superposition method using the complex and frequency-dependent modal parameters determined by the proposed incremental scheme, is validated with the experimental frequency response.

Finally, the analyzed beam is discretized with different element lengths yielding to different system sizes, and the computational requirements demanded by each of the analyzed methods is studied. From this analysis, the efficiency of the proposed algorithms is proved.

4.3.1 Number of derivatives and tolerance

The accuracy of the computed eigenvalues and eigenvectors exclusively depends on the established tolerance in Equation (4.57). The adaptive step-size control scheme implemented in the iterative and the incremental algorithms, preserves the desired accuracy forcing to recalculate the eigenderivatives if a given frequency increment infringes the conditions described by Equations (4.56) and/or (4.57). For the analyzed practical application, tolerances comprised between 1×10^{-4} and 1×10^{-2} provided almost the exact results. By contrast, the efficiency of the algorithms besides the established tolerance, depends on the number of derivatives considered for approximating the eigenvectors.

As mentioned, the major computational cost when determining the first n eigenderivatives, is related to the factorization of the matrix of coefficients $\mathbf{A}_r$ when computing the first order eigenvector derivatives. As this matrix does not change for a given mode and computational frequency, the higher order derivatives are computed faster than the first order ones. In Figure 4.2, the time demanded for computing each of the first 10th eigenderivatives of the beam under study for a given frequency, is shown normalized respect to the time required for computing the first order derivatives.

As can be seen, the second order derivatives required half the time demanded by the first order ones. As well, the time required for computing the higher order derivatives progressively increased since the nth order derivatives contains terms involving $n-1$ and lower order derivatives.

Different strategies are followed when selecting the number of derivatives for the itera-

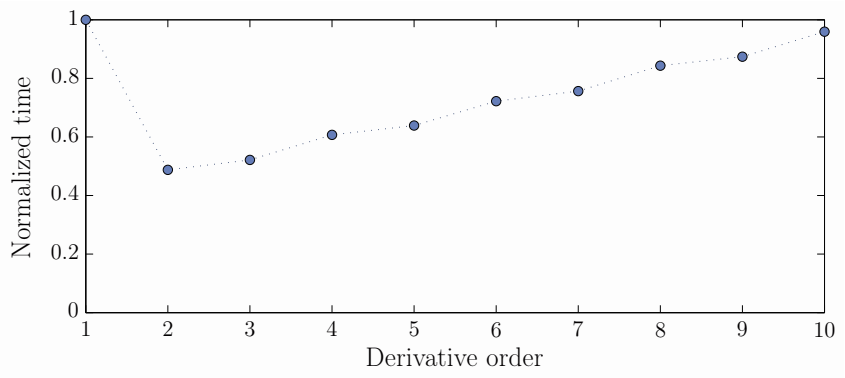

Figure 4.2: Time demanded for computing each of the first 10th eigenderivatives normalized respect to the time required for computing the first order ones.

tive and the incremental schemes. To maximize the efficiency of the iterative algorithm, it must be intended to compute the eigenderivatives just once at $\omega_{r,0}$. As this latter frequency is close to the final converged solution, few derivatives are sufficient to update the complex eigenpair for all the $\omega_{r,j}$ resonance frequencies of the next jth iterations in a single step without infringing the accuracy condition given by Equation (4.57). For the present CLD beam, from three to four derivatives were sufficient for tolerances comprised between 1×10^{-2} and 1×10^{-4}.

When applying the incremental scheme, a compromise must be found when choosing the number of derivatives in order to improve the efficiency [73]. If a small number of derivatives are employed, one of the two conditions is easier violated requiring the recalculation of the eigenderivatives more frequently. As well, using a larger number of derivatives, more frequency steps may be given without infringing the defined accuracy conditions. However, although the eigenderivatives may be computed at fewer frequencies, the required time for computing them is larger. For the analyzed CLD beam, the shorter computational times where obtained with four and five derivatives when the tolerances were between 1×10^{-2} and 1×10^{-4}.

4.3.2 Modal analysis

The modal parameters of the analyzed beam were computed by the IMSE (Table 4.2), by the ICE (Table 4.1) and, by the new iterative algorithm (Table 4.3). The ICE method converges to the exact modal parameters so that it was used as a reference to evaluate the accuracy of the modal parameters determined by the other two iterative methods. Three eigenderivatives were considered for applying the present iterative algorithm and the tolerance for the accuracy condition was set to $\text{Tol} = 1 \times 10^{-3}$. As well, the tolerance related to the convergence of the iterative process was defined using the natural frequencies

as described by Equation (4.8), and its value was set to $\epsilon_r = 1 \times 10^{-4}$ for all the three iterative procedures. In Table 4.5, the modal parameters determined by the three iterative methods are summarized.

Table 4.5: Natural frequency f_r (Hz) and modal loss factor η_r of the first five bending modes determined by the IMSE, ICE and the proposed iterative algorithm.

	Mode 1		Mode 2		Mode 3		Mode 4		Mode 5	
	f_1	η_1	f_2	η_2	f_3	η_3	f_4	η_4	f_5	η_5
IMSE	20.6	0.069	108.6	0.280	280.8	0.392	518.2	0.449	822.8	0.465
ICE	20.8	0.059	114.4	0.213	302.1	0.284	561.1	0.331	888.9	0.356
Present	20.8	0.059	114.4	0.213	302.1	0.284	561.1	0.331	888.9	0.356

As was concluded from the results gathered in Table 4.5, the IMSE method failed to properly determine the modal parameters of the analyzed CLD beam. Important deviations were observed both in natural frequency and modal loss factor estimations, evidencing that the studied CLD beam can not be properly described in terms of normal modes. The largest error when determining the natural frequencies was noticed in the fourth mode being underestimated by 7.7 %, whereas the largest error when calculating the modal loss factors was detected in the third mode being overestimated by 38.3 %. By contrast, with the specified tolerance ($\text{Tol} = 1 \times 10^{-3}$), the proposed iterative algorithm provided almost the same results as the ICE method. All the resonance frequencies were determined with errors $< 1.3 \times 10^{-3}$ %, whereas the modal loss factors were identified with errors $< 1.8 \times 10^{-4}$ %.

As well, the mode shapes determined by the three iterative methods were compared. The correlation degree of the real and the imaginary parts of the eigenvectors was separately correlated by the *Modal Assurance Criterion* (MAC), taking as reference the eigenvectors computed by the ICE method. The MAC indicator is defined as

$$\text{MAC}_r = \frac{\left|\phi_{r_1}^{\text{T}}\, \phi_{r_2}\right|^2}{\left(\phi_{r_1}^{\text{T}}\, \phi_{r_1}\right)\left(\phi_{r_2}^{\text{T}}\, \phi_{r_2}\right)}, \tag{4.67}$$

where ϕ_{r_1} and ϕ_{r_2} refer to the rth eigenvectors computed with two different methods. In Figure 4.3 the complex mode shapes relative to the transverse displacement of the first five bending modes are plotted, and the MAC indicators for the real and imaginary parts of the mode shapes are indicated. Remark that the amplitude of the imaginary part of the complex mode shapes was scaled by a factor of 35, since it was considerably lower than the amplitude of the real part.

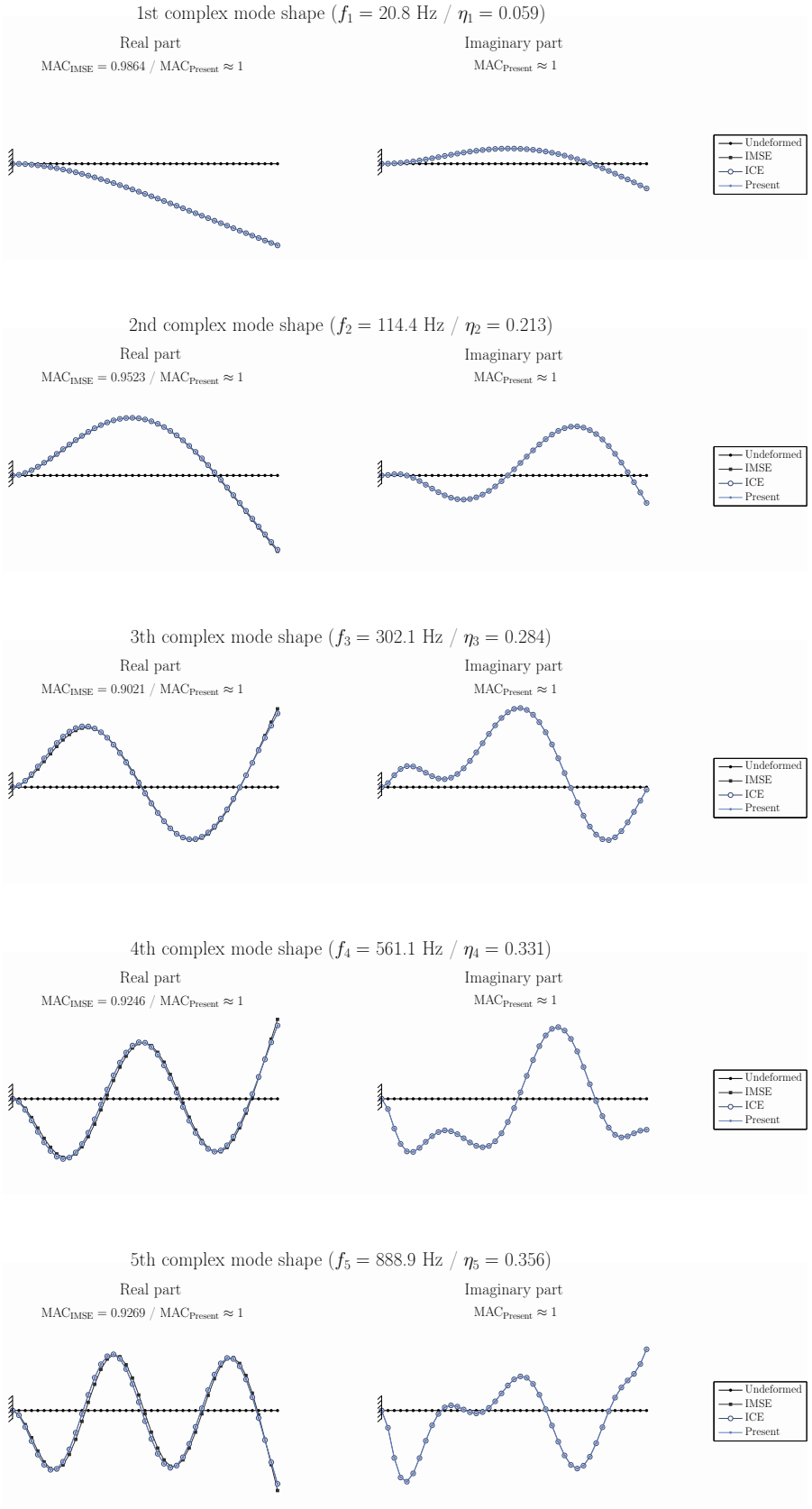

Figure 4.3: Complex mode shapes relative to the transverse displacement of the first five bending modes of the 210 mm long CLD cantilever beam detected below 1 kHz, computed by the IMSE, the ICE and the proposed iterative algorithm.

The normal eigenvectors determined by the IMSE method presented significant differences as was evidenced by the MAC indicator. The major differences were observed in the degree of freedom related to the rotation due to the transverse shear of the core ψ. By contrast, for all the five modes, the MAC index for the real and the imaginary parts of the eigenvectors computed by the proposed iterative scheme was $\text{MAC}_r > 0.999999 \approx 1$. Thus, with the presented results, the effectiveness of the new iterative algorithm was proved.

4.3.3 Frequency response

The computation of the frequency response of the system under study is another common requirement to asses the properness of the designed damping treatment. In the present example, the dynamic response of the 210 mm long CLD cantilever beam was approximated in three different ways.

The first approach consisted in superposing the normal modes determined by the IMSE method. This procedure has been commonly employed for approximating the dynamic response of viscoelastically damped systems [53, 106], but the present analysis aims to highlight its limitations for properly determining the frequency response of non-proportionally damped systems. The second approach superposes the complex modes described by the non-frequency-dependent complex modal parameters computed by the ICE or by the proposed iterative algorithm. The third approach considers the complex and frequency-dependent modal parameters determined by the new incremental scheme.

The complex modal parameters were determined by the incremental scheme within the $0 - 1$ kHz frequency bandwidth with a 1 Hz constant resolution. Four derivatives were considered and the tolerance for the accuracy condition was set to $\text{Tol} = 1 \times 10^{-2}$. With the defined number of derivatives and tolerance, the errors of the approximated eigenpair with respect to the exact ones computed by solving a complex eigenproblem for each computational frequency by IRAM, were determined in order to validate the proposed incremental scheme. The deviations in the eigenvalues of the first five modes detected within the analyzed frequency bandwidth, were smaller than 1×10^{-5} % for both the real and the imaginary parts, whereas the MAC index for the real and the imaginary part of the eigenvectors was greater than $0.999999 \approx 1$. Thus, the effectiveness of the proposed incremental algorithm for approximating the complex eigenpair within a given frequency bandwidth was proved.

The three approximations were correlated with the exact dynamic response computed by the direct frequency method, from where the accuracy and the limitations of each of the approximations were analyzed and discussed. To this end, the transfer functions that relates the transverse displacement of two different points with the transverse displacement applied at the base, were considered. As represented in Figure 4.4, the first response point

R_1, was located 5 mm from the free end, whereas the second point R_2, was selected 20 mm from the clamped end.

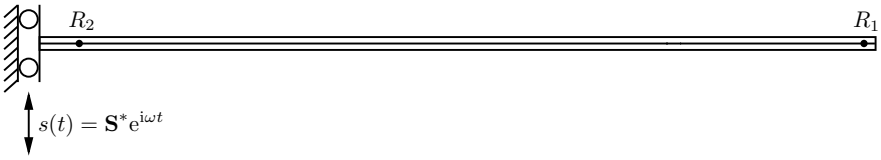

Figure 4.4: Tested 210 mm long CLD cantilever beam subjected to a harmonic transverse base motion $s(t)$; R_1 and R_2 response points located 5 mm from the free end and 20 mm from the clamped end, respectively.

In Figure 4.5, the modulus and the phase of the transfer function relating the transverse displacement of the response point R_1 with that applied at the base, are plotted.

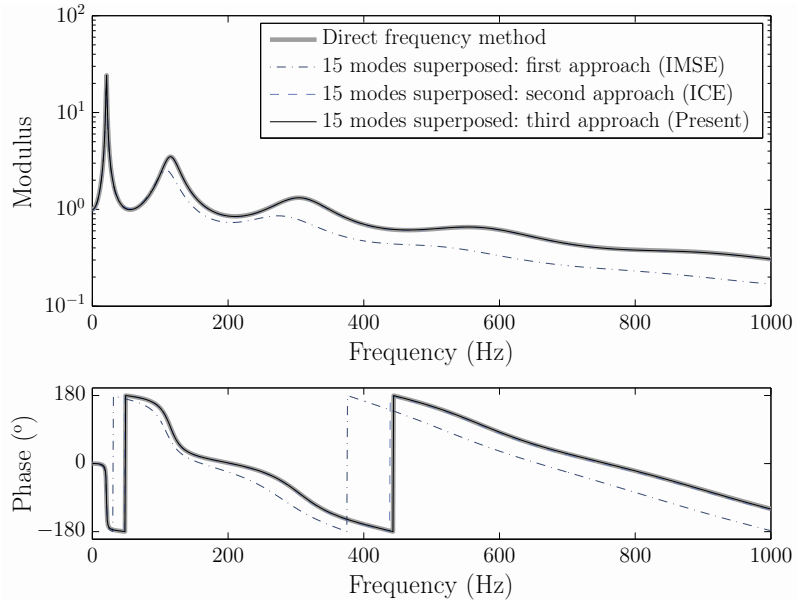

Figure 4.5: Transfer function of the 210 mm long CLD cantilever beam measured at R_1. Exact response computed by the direct frequency method and those determined by superposing the first 15 bending modes assuming three different approaches.

As was evidenced, the first approach did not provide a reliable result evidencing that the normal mode superposition procedure is not suitable for approximating the dynamic response of the analyzed CLD beam. As was also evidenced in the modal parameters summarized in Table 4.5, the IMSE method underestimated the natural frequencies and overestimated the modal loss factor values. By contrast, the second and the third approach provided accurate results. After superposing the first 15 complex bending modes, the largest error committed by the second approach at the resonances, was located at the

third one its amplitude being underestimated by 1 %. Anyway, the largest error was localized at $f = 0$ Hz, where the amplitude resulted underestimated by 3.4 %. The third approach provided more accurate results as the frequency dependence of the complex modal parameters was taken into consideration. With this procedure, the errors resulted smaller than 0.3 % within the analyzed frequency bandwidth. Finally, it should be remarked that a considerable number of modes had to be superposed for obtaining an accurate approximation, evidencing the significant contribution of the higher order modes on the response of the studied frequency bandwidth.

From the transfer functions plotted in Figure 4.5, it was concluded that the superposition of the modes described by complex but non-frequency-dependent modal parameters (second approach) provides accurate results. This suggests that one may obtain an acceptable approximation even if the frequency dependence of the complex modal parameters is omitted. Therefore, the second approach would constitute a more efficient alternative than the third one for approximating the dynamic response of the system. However, the second approach might be valid for determining the dynamic response of certain response points. To better appreciate it, another point closer to the clamped end is considered. In Figure 4.6, the modulus and the phase of the transfer function relating the transverse displacement of the response point R_2 with that applied at the base, can be seen.

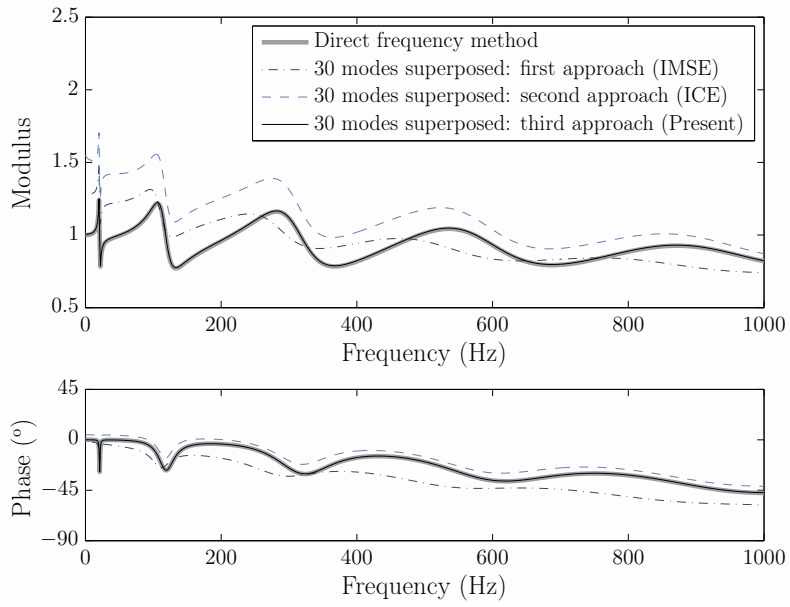

Figure 4.6: Transfer function of the 210 mm long CLD cantilever beam measured at R_2. Exact response computed by the direct frequency method and those determined by superposing the first 30 bending modes assuming three different approaches.

When determining the transfer function of the point R_2, the first 30 bending modes were necessary to be superposed for obtaining a good approximation by the third approach,

which converged to the exact solution. By contrast, the errors of the transfer function approximated by the first and the second approaches were notable after superposing the first 30 modes. These differences were not related to the mode truncation since the error did not decrease after superposing a greater number of modes. This evidenced that omitting the frequency dependence of the complex modal parameters is not an acceptable approach to determine the transfer function of all the response points of the system, showing that the contributions of each of the modes were not properly determined.

The error committed when computing the modal contributions ignoring the variation of the complex modal parameters with the frequency, is clearly appreciated in Figure 4.7. Concretely, the first five modal contributions to the total transfer function of R_1 and R_2 computed with constant (second approach), and frequency-dependent (third approach) complex modal parameters, are represented.

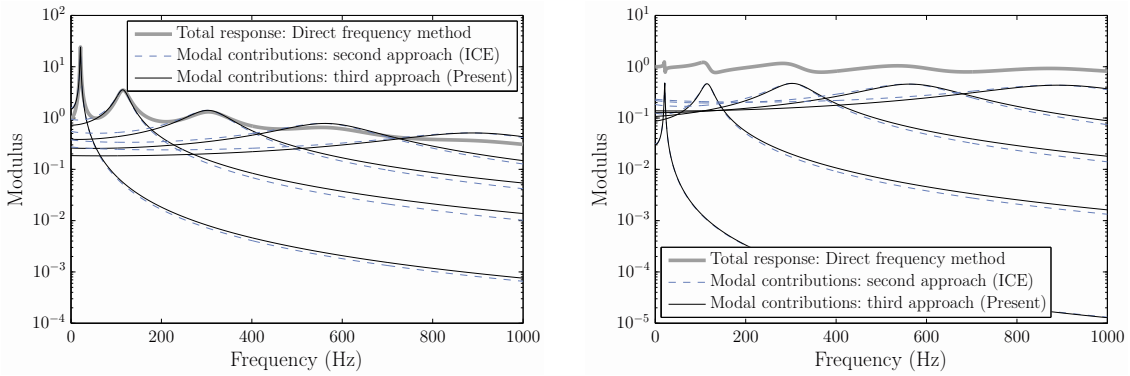

Figure 4.7: Total transfer function (——) and the first five modal contributions of R_1 (a), and R_2 (b), computed with the frequency-dependent complex modal parameters (——) and non-frequency-dependent ones (- - -).

As was expected, the modal contributions computed with both approaches coincided at the resonances but differences were evident for frequencies below and above the resonance frequencies. The errors observed above the resonances did not significantly affect to the total dynamic response, but those located below the resonance frequencies affected notably. Although acceptable approximations can be obtained when the relative contribution of the higher order modes is small (Figure 4.7(a)), special precaution is demanded when this condition is not fulfilled (Figure 4.7(b)). In those cases, the frequency dependence of the modal parameters should be taken into consideration.

In addition, emphasize that the second approach is sensitive to another source of error related to the iterative solution procedure. The limitation is that the accuracy of the modal parameters of the higher order modes can not be assessed as it is not clear whether the material parameters (G_0, G_∞, τ and α) identified up to 1 kHz, correctly describe the

dynamic properties of the viscoelastic core over 1 kHz. By contrast, the third approach is not sensitive to this incertitude as it updates the complex modal parameters from the undamped ones, within the frequency bandwidth where the material properties are known.

Summarizing, the normal mode superposition method has not provided reliable results for the dynamic analysis of the studied CLD beam, evidencing the importance of considering the mode complexity. The second approach results an interesting alternative since the computation of the complex and frequency-dependent modal parameters is avoided, demanding less computational time and memory requirements. Nevertheless, care must be taken when the relative contribution of the higher order modes to the dynamic response of the response point under analysis is significant. As well, special attention is demanded when large number of modes detected over the frequency bandwidth where the material properties have been identified, must be superposed. When one of this conditions is not fulfilled, the complex and frequency-dependent modal parameters should be employed to converge to the exact solution.

To conclude, the frequency response approximated by the superposition of the complex and frequency-dependent modes is compared with the experimental one, in order to validate the performed analysis. In Figures 4.8 and 4.9, the modulus and the phase of the experimental and the approximated transfer functions of the points R_1 and R_2 are plotted, respectively.

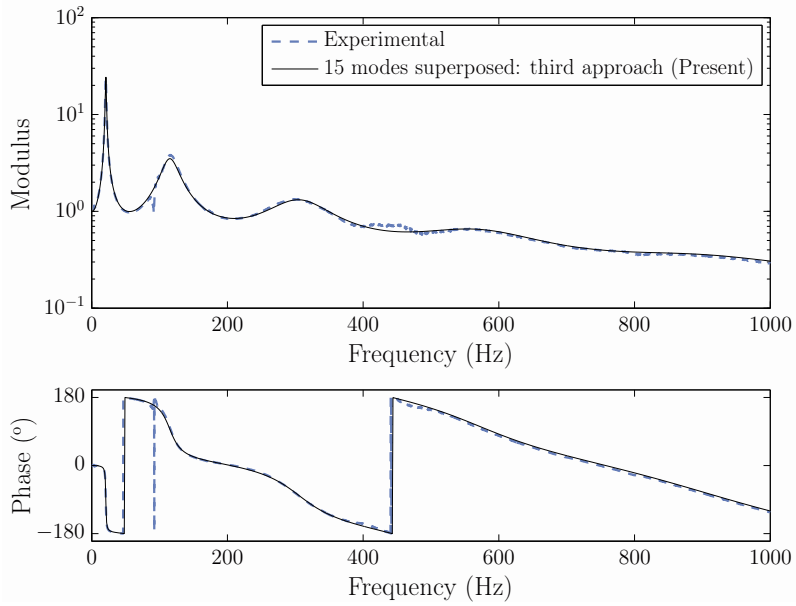

Figure 4.8: Experimental transfer function of the point R_1, and that approximated by superposing the first 15 bending modes described by complex and frequency-dependent modal parameters.

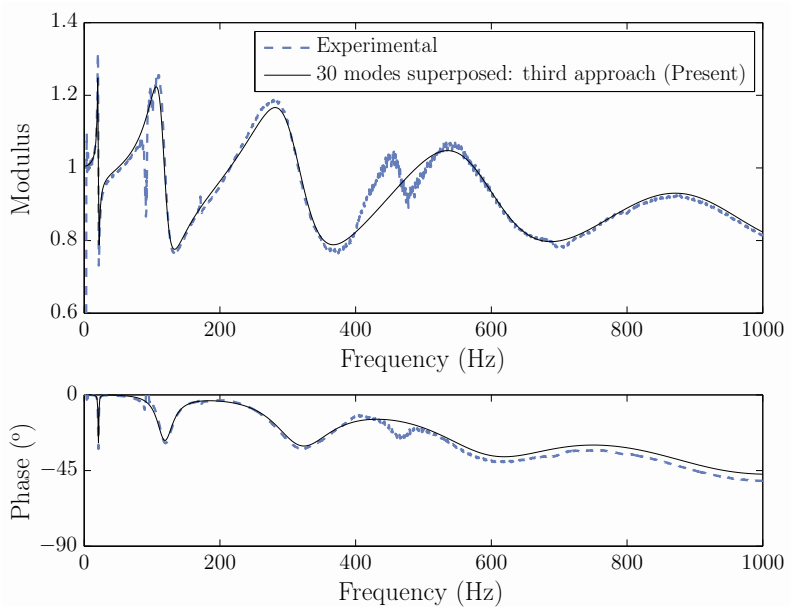

Figure 4.9: Experimental transfer function of the point R_2, and that approximated by superposing the first 30 bending modes described by complex and frequency-dependent modal parameters.

Good correlation is observed between the measured and the approximated transfer functions for both response points. The only remarkable differences observed in both transfer functions between 400 and 500 Hz were originated by the experimental noise.

With this comparison, the validity of three different approaches was analyzed and discussed, concluding that the superposition of modes described by complex and frequency-dependent modal parameters is the only method that converges to the exact solution. The described procedure results of special interest for the design of effective damping treatments, since besides the total dynamic response, the contribution of each mode to the total response is provided.

4.4 Efficiency analysis

For assessing the efficiency of the proposed algorithms, the same 210 mm long CLD beam was discretized with different element lengths yielding to 100, 500, 1000 and 5000 degrees of freedom systems. Both the iterative and the incremental schemes were applied and the computational time † demanded by the proposed algorithms was compared with that of the other considered methods.

†All the CPU times presented in the different tables were obtained running MATLAB® R2010b under Mac OS X 10.6.8 environment with a 2.4 GHz Intel Core i5 processor and 4 GB RAM memory.

First, the time demanded by the three analyzed iterative methods was studied. In Table 4.6, the time required for computing the modal parameters of the first bending mode by the IMSE method, the ICE method, and the proposed iterative algorithm, is summarized. The proposed method considered three derivatives and the tolerance for the accuracy condition was $\text{Tol} = 1 \times 10^{-3}$.

Table 4.6: CPU time demanded by the different iterative methods in ms.

Method	Step	DOF			
		100	500	1000	5000
	Undamped eigensolution, t_0	16	18	21	85
IMSE$^{(1)}$	$t_{\text{iteration}}$ ($n_{\text{iterations}}$)	16 (4)	18 (4)	21 (4)	85 (4)
	t_{Total}	80	90	105	425
ICE$^{(2)}$	$t_{\text{iteration}}$ ($n_{\text{iterations}}$)	20 (4)	25 (4)	42 (4)	180 (4)
	t_{Total}	96	118	189	805
Present$^{(3)}$	$t_{\text{1st Iteration}}$	20	25	42	180
	$t_{\text{differentiation}}$	1.2	2.6	5	30
	$t_{n\text{th Iteration}}$ ($n_{\text{iterations}}$)	0.2 (3)	0.3 (3)	0.5 (3)	1.8 (3)
	t_{Total}	37.8	46.5	69.5	300.4

t_0 : Time for solving the undamped real eigenproblem. Step required for the three methods.

(1) : Algorithm summarized in Table 4.2. A real eigenproblem is solved per iteration.

$$t_{\text{Total}} = t_0 + t_{\text{iteration}} \times n_{\text{iterations}}$$

(2) : Algorithm summarized in Table 4.1. A complex eigenproblem is solved per iteration.

$$t_{\text{Total}} = t_0 + t_{\text{iteration}} \times n_{\text{iterations}}$$

(3) : Algorithm summarized in Table 4.3.

$t_{\text{1st Iteration}}$: Time for solving the complex eigenproblem.

$t_{\text{differentiation}}$: Time for computing the first three eigenderivatives.

$t_{n\text{th iteration}}$: Time for updating the eigenpair from that computed for $\omega_{r,0}$.

$$t_{\text{Total}} = t_0 + t_{\text{1st iteration}} + t_{\text{differentiation}} + t_{n\text{th Iteration}} \times n_{\text{iterations}}$$

From Table 4.6, the efficiency of the proposed iterative scheme was proved. The major computational time was required for solving the complex eigenproblem, then the real undamped eigenproblem, and in a lesser extent, for calculating the first three eigenderivatives. However, the subsequent iterations demanded relatively little computational time. The presented algorithm provided almost the same results as those offered by the ICE method, resulting 60 % faster for all the analyzed systems.

After proving the efficiency of the presented iterative algorithm, the computational requirements demanded by the incremental scheme were analyzed. In Table 4.7, the time required for updating the complex eigenpair of the first bending mode within the studied frequency bandwidth $0-1$ kHz with a 1 Hz resolution, is summarized. The computational time of the proposed incremental scheme is compared with the time demanded for solving the complex eigenproblem at each computational frequency by IRAM. For applying the incremental algorithm four derivatives were considered and the tolerance for the accuracy condition was $\text{Tol} = 1 \times 10^{-2}$. With the defined number of derivatives and tolerance the derivatives were computed 24 times.

Table 4.7: Total time demanded by the proposed incremental scheme and by IRAM for computing the complex modal parameters of the first bending mode within $0-1$ kHz with a 1 Hz resolution.

Method	Step	DOF			
		100	500	1000	5000
IRAM	t_{Total} (s) (1000 increments)	19.8	25.1	41.9*	180.6*
Present(1)	$t_{\text{1st step}}$ (ms)	2.4	3.8	5.7	24.2
	$t_{\text{differentiating}}$ (ms) (24 increments)	4.7	5.6	9.3	49.6
	$t_{\text{without differentiating}}$ (ms) (976 increments)	0.4	0.6	0.8	4.1
	t_{Total} (s) (1000 increments)	0.5	0.7	1.0	5.2
	$t_{\text{IRAM}}/t_{\text{Present}}$	39.1	34.7	41.5	34.6

(1) : Algorithm summarized in Table 4.4.

$t_{\text{1st step}}$: Time for approximating the eigenpair for ω_i by Equations 4.27–4.66.

$t_{\text{differentiating}}$: Time for computing the first four derivatives and updating the next eigenpair.

$t_{\text{without differentiating}}$: Time for updating the next eigenpair without computing any derivative.

$$t_{\text{Total}} = t_{\text{1st step}} + t_{\text{diffrentiating}} \times n_{\text{increments}} + t_{\text{without diffrentiating}} \times n_{\text{increments}}$$

* : All cases used the 25 % of the total CPU capacity, whereas those marked by (*) used the 80 %.

As concluded from the results gathered in Table 4.7, the efficiency of the presented incremental algorithm for computing the complex eigenpair of a given mode within the considered frequency bandwidth, was assessed. For all the analyzed system sizes, the proposed algorithm computed the complex eigenpair of the first mode between 34 and 41 times faster than the IRAM method. As well, mention that the computation of the eigenpair of the first mode was the most time consuming of all the 30 analyzed modes. The higher order modes required to compute the four eigenderivatives between 18 and 20 times instead of 24 times, so that the computation of the complex eigenpair of the higher order modes demanded about 10 % less time. Furthermore, remark that whereas the present method

used the 25 % of the total CPU capacity for all the system sizes, IRAM employed the 80 % of the total capacity for the systems of 1000 and 5000 degrees of freedom.

In Table 4.8, the total time demanded by the proposed method and by IRAM for computing the complex modal parameters of 30 modes within the frequency bandwidth under analysis, and the time required for calculating the exact frequency response by the direct frequency method, are summarized. It should be remarked that one of the major advantage of the IRAM method is that efficiently computes a few number of eigenpairs of large scale systems at once. When applying the IRAM method, took advantage of this characteristic and the eigenpairs of the 30 modes were obtained simultaneously for each computational frequency.

Table 4.8: Total time demanded by the proposed incremental method and by IRAM for computing the complex eigenpairs of the first 30 bending modes within $0-1$ kHz, and total time for computing the exact response by the direct frequency method.

Method	Total time	DOF			
		100	500	1000	5000
Complex mode superposition	t_{IRAM}	79.1*	101.5*	133.5*	481.7*
	t_{Present}	11.8	18.1	26.5	133.1
Direct frequency method	t_{Direct}	0.2	0.5	1.1	6.9

* : All cases used the 25 % of the total CPU capacity, whereas those marked by (*) used the 80 %.

Again, the efficiency of the presented method respect to IRAM was proved. The proposed method computed the eigenpairs of the first 30 modes between 3.6 and 6.7 times faster than IRAM. However, it should be remarked that whereas the proposed incremental method employed the 25 % of the total CPU capacity, the IRAM method used the 80 % of the total capacity for all the analyzed system sizes.

As well, the time demanded by the direct frequency method for computing the exact dynamic response showed that for this specific practical application, it is considerably more efficient than the complex mode superposition method. Nevertheless, it should be also remembered that, whereas the direct frequency method only provides the total frequency response, the computed complex and frequency-dependent modal parameters also allow determining the contribution of each modes to the total frequency response of a given point. Furthermore, with the computed complex eigenpairs additional information is obtained. For example, besides the transfer functions, the frequency response functions (FRF) can also be determined for any excitation and response point without a significant additional computational cost. The complex eigenpairs only must be recalculated when the boundary conditions of the system vary. By contrast, to obtain the frequency response functions of

the analyzed system, the direct frequency method should be applied again, the recalculation being necessary every time that the force vector or the boundary conditions change.

With the presented analysis, the efficiency of the proposed iterative and incremental algorithms for the dynamic analysis of the studied CLD cantilever beam was proved. However, general conclusions can not be drawn in a quantitative sense as the efficiency of the proposed method depends on the analyzed system, and specially on the rate of change of the modal parameters with frequency. Anyway, the studied example was representative as high damping and strong frequency-dependent viscoelastic material was involved, the complexity and the frequency dependence of the modal parameters being remarkable.

4.5 Conclusions

In this chapter, a new numerical method for the dynamic analysis of viscoelastically damped structural systems characterized by a non-proportional and frequency-dependent structural damping matrix, has been presented. The method considers the first and higher order eigenderivatives for computing the complex modal parameters of the system under study.

The first and higher order eigenderivatives with respect to the excitation frequency have been deduced adopting the Nelson's method for the eigenvector derivatives computation. Moreover, it has been demonstrated that the Nelson's method constitutes an efficient way for calculating the higher order eigenvector derivatives.

A fundamental updating procedure that approximates the complex eigenvectors by the Taylor's series, and that computes the complex eigenvalues by the Rayleigh quotient, has been described. The higher order derivatives have been employed for defining a convergence and an accuracy condition for guaranteeing the precision of the updated eigenpair. In this context, an adaptive step-size control scheme has been implemented in order to preserve the established tolerance.

The fundamental updating procedure has been implemented into two different schemes. An iterative algorithm has been proposed for determining the complex modal parameters, and an incremental one for computing the complex eigenpair within the defined frequency bandwidth, in order to compute the frequency response of the system by the complex mode superposition method.

Effective and efficient tools have been provided for the dynamic analysis of viscoelastically damped structural systems. The iterative scheme has shown to be effective and more efficient than the considered classical algorithms. As well, the incremental scheme has proved to be effective demanding less computational time and CPU requirements than

the IRAM method. Still being more time demanding than the direct frequency method, additional information is offered, such as the individual contribution of each mode to the total response. Moreover, with the determined eigenpairs, not only the response to a base motion is obtained, but also the frequency response functions (FRF) for any excitation and response point can be immediately determined without recalculating the eigenpairs while the boundary conditions are not varied. By contrast, the direct frequency method requires to recalculate the dynamic response every time the force vector or the boundary conditions are changed.

The developed numerical method has been published in the *International Journal for Numerical Methods in Engineering* [73].

Chapter 5

Dynamic analysis of press-formed CLD beams

This chapter aims to prove the relevance of the influence of the static prestrain on the dynamic behavior of press-formed CLD parts. Furthermore, all the contributions made in previous chapters are applied to perform this analysis. The nominal dynamic properties identified in Chapter 2 are combined with the frequency-prestrain material model proposed in Chapter 3, and the higher order eigensensitivities-based numerical method developed in Chapter 4 is extended for analyzing the dynamic behavior of press-formed CLD parts.

Several CLD beams are bent into different angles, the static prestrain induced in the viscoelastic core is measured, and the influence of the static prestrain is verified from the experimental frequency responses by the deviations observed in frequency and in amplitude.

After that, the proposed frequency-prestrain material model is applied, proving that the dynamic response is properly determined after including the influence of the static prestrain on the dynamic properties of the viscoelastic core. From this analysis the significance of the influence of the static prestrain on the dynamic behavior of formed CLD beams is assessed.

Finally, the higher order eigensensitivities-based numerical method is extended for the dynamic analysis of press-formed CLD parts. The differences respect to the analysis of straight parts are described, and the effectiveness of the iterative and the incremental algorithms is proved.

From this analysis the relevance of the static prestrain influence on the dynamic behavior of press-formed CLD parts is stated, and the work carried out is validated.

5.1 Introduction

Among the features of the constrained layer damping treatment (CLD), the ability to be formed by classical metal sheet forming processes, is another remarkable characteristic. Unlike the free layer damping (FLD) treatment, where the metallic sheet formed in a previous stage must be further treated with damping materials, the CLD laminated sheets can be press-formed to obtain the final damped part reducing the required manufacturing steps, saving time and costs.

The research works published to date on CLD sheet metal forming, are mainly concerned with the defects and geometrical imperfections derived from the forming process. Nevertheless, how the forming process affects to the dynamic behavior of formed CLD parts remains being an open issue. The influence of the shear modulus variation on the dynamic behavior of press-formed CLD parts was first reported by Balmès and Germès [10]. Concretely, they present a numerical example showing how the natural frequencies and the strain energy density distribution vary when changing the shear modulus of the viscoelastic material located at the bent region. Their preliminary study motivated the work of Kergourlay [48] and Kergourlay *et al.* [49], where the effect of the static prestress is experimentally measured for different temperatures by means of a specially designed test rig. However, the authors do not analyze the dynamic behavior of any press-formed part including the influence of the static prestrain on the dynamic properties of the viscoelastic material. To date, there have not been published further works on this phenomenon, which has motivated the present dissertation. This work aims to asses the relevance of the influence of the static prestrain on the dynamic behavior of press-formed CLD parts.

Next, the published studies on CLD forming are reviewed and the sheet metal forming processes used in these research works are described first. From this revision, the considered experimental forming process and the involved process parameters have been defined.

Sheet metal forming is a grouping of many complementary processes that are combined to form the desired sheet metal parts. The sheet metal operations may be grouped into two categories, cutting and forming operations. Cutting operations such as punching or blanking, consist on applying shear stresses beyond its ultimate strength in order to obtain the desired hole or part, respectively. By contrast, forming operations consist on applying a force to stress the material beyond its yield strength, causing the material to plastically deform. An extensive survey of sheet metal forming technology can be found on the handbook of Kalpakjian and Schmid [47], for example. Combining the wide variety of processes, commonly referred to as stamping, formed CLD parts with complex shapes can be obtained. For example, in Figure 5.1 two press-formed CLD parts are shown.

(a) (b)

Figure 5.1: (a): Rear door of a car; (b): Panel for isolating the passenger compartment of a van from the engine.

Due to the particular construction of this type of laminates, forming CLD parts involves some issues that are not of concern when bending solid sheets. Since this type of laminate is a relatively new material, its manufacturing and forming characteristics have not been fully understood yet. Issues that have been previously addressed for solid sheets, have had to be revisited for this type of laminates. These include, for example, studies on springback, wrinkling, geometrical imperfection or sidewall curl, and delamination. Several authors have analyzed these difficulties manifested when forming laminated sheets. Among the wide variety of existing forming processes, mainly the V-bending, wipe bending and drawing operations have been studied in the different published research works. In Figure 5.2, these forming operations are schematized.

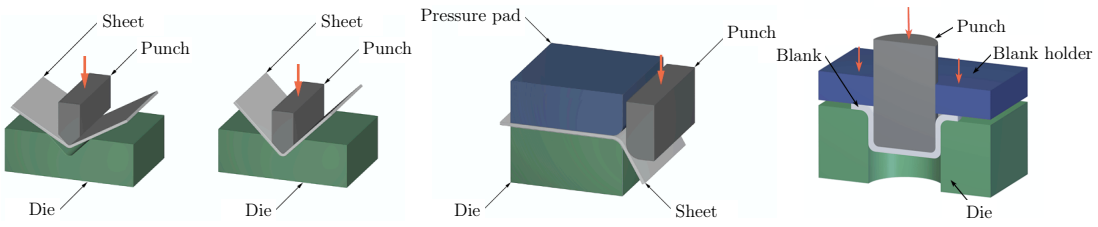

(a) (b) (c) (d)

Figure 5.2: Schemes of metal sheet forming processes. (a): V-bending under air-bending condition; (b): V-bending under die-bending condition; (c): wipe bending; (d): drawing.

The V-bending is the simplest forming operation, where the punch pushes the blank into the die. Depending on the die-sheet contact boundary condition, the air-bending (Figure 5.2(a)) or the die-bending (Figure 5.2(b)), are differentiated. In air-bending, the specimen is always supported by the two die edges; whereas in die-bending, the sheet contacts the die-wall at the final stage. The air-bending and the die-bending condition directly affects to the shear strain of the core as is described by Takiguchi and Yoshida [116]. Concretelly, they analyze the shear strain distribution in the core and its influence on the resultant geometrical imperfection, when performing V-bending operation on partially lapped sheets with both die-sheet boundary conditions.

In wipe bending, also known as edge bending, the sheet is clamped between the die and the pressure pad with a specific clamping force. Then, the punch moves pushing and bending the sheet around the die, as can be seen in Figure 5.2(c). In wipe bending, a dissimilar distribution of the shear strain is obtained in the viscoelastic core of the clamped and the free wings. The shearing in the free wing results larger than in the clamped one, since the pressure pad limits the relative displacement between the face layers at the latter. Eisenhour [32] analyzes the wipe bending of laminated sheets and studies the development of the sidewall curl geometrical inperfection, with the objective of assessing its dependence on bending parameters.

The drawing process shown in Figure 5.2(d), differs from the other described processes because the blank is also in tension during forming. Originated by the significant difference in material properties between the viscoelastic core and the metallic face layers, the laminated sheets are prone to wrinkling during the drawing process. Adjusting the holding force or even using draw beads, besides controlling the degree of stretching of the sheet, the wrinkling may be controlled. Cheng *et al.* [20] analyzed the wrinkling of CLD laminated sheets and compared its behavior with solid homogeneous metallic sheets during the drawing operation.

Most research works on CLD sheets forming, have focused primarily on the analysis of the springback and the sidewall curl phenomena, and in a lesser extent, on the delamination. The springback is originated by the residual stresses in the material which causes to slightly spring-back towards the original position after the bending operation. Due to this elastic recovery, it is necessary to over-bend the sheet a precise amount to achieve the desired bend radius and bend angle. The springback is even more important when bending laminated CLD sheets than solid sheets due to the relaxation phenomenon shown by the viscoelastic core. Moreover, as viscoelastic materials exhibit time dependent behavior, the springback also depends on time, and is referred to as delayed springback. This phenomenon was analyzed by Kim and Thomson [51], and Kleiner and Hellinger [54] showing that the springback can be reduced increasing the forming temperature. By contrast, Liu

and Wang [62] proposed an analytical approach to predict the springback as well as the sidewall curl during the wipe bending of CLD sheets.

The geometric imperfection known as sidewall curl, is another issue related to the bending operation of laminated sheets that has attracted the attention of many researchers. This phenomenon occurs when the wings of a bent part that ideally should remain straight, become curved. While bending of a single layered sheet metal does not exhibit significant sidewall curl, the problem is pronounced when bending CLD laminates. This geometrical imperfection makes subsequent assembly of sheet metal products more difficult and is also a downside in terms of aesthetics is concerned. Takiguchi and Yoshida [116] studied the sidewall curl when performing V-bending operation on partially lapped sheets under air-bending and die-bending conditions. The authors show that the air-bending condition is preferable rather than the die-bending condition as the sidewall curl is minimized. As well, they conclude that when bending under air-bending conditions, increasing the die-span length reduces the undesired sidewall curl. Takiguchi and Yoshida [117] also analyzes the influence of the adhesive strength an its viscoplastic behavior on the resultant shear strain distribution and the consequent sidewall curl.

The last reported defect but not so extensively addressed, is the delamination during the press forming process of laminated CLD sheets. Kim and Thomson [52] analyzes the separation behavior of laminated sheets during the V-bending and deep drawing operations, showing that a tensile separation may occur due to bucking of one of the face layers, or by combined tensile and shear solicitations. In addition, they show that bents close to the free edges performed by the wipe bending process, are prone to originate delamination by shear on the free end. From the tensile lap shear experiments performed by Takiguchi and Yoshida [117], they conclude that increasing the shear strain rate of the adhesive, the maximum achievable shear strain level reduces augmenting the risk of delamination.

The analysis of the state of the art shows that most of the published works, have been concerned with the defects and geometrical imperfections related to the forming process of CLD sheets. In the present chapter, the influence of the forming process on the dynamic behavior of press-formed CLD parts is addressed. For such purpose, beam-type CLD specimens are V-bent with different angles and the influence of the induced static prestrain on their dynamic response is verified with experimental tests. Then, the induced static prestrain distribution in the viscoelastic core is measured, and the proposed frequency-prestrain material model is applied in order to properly predict the dynamic response of the formed CLD beams. As well, the proposed higher order eigensensitivities-based numerical method is extended for the analysis of formed CLD parts. From this analysis the relevance of the static prestrain on the dynamic behavior of press-formed CLD beams is assessed.

Next, the experimental work concerned with the forming process is presented. The employed experimental set-up, the specimens, the parameters of the forming process, and the measurement of the induced prestrain distribution are detailed. Then, the finite element models are defined and the implementation of the frequency-prestrain material constitutive model is described. After that, the influence of the static prestrain on the dynamic behavior of the formed CLD beams is analyzed. The higher order eigensensitivities-based numerical method is applied and validated, and finally the main conclusions derived from the presented analysis are summarized.

5.2 Experimental technique: forming process

For the analysis of the static prestrain influence on the dynamic behavior of formed CLD parts, beam type specimens were considered. The beams were bent into different angles by the V-bending forming process in order to induce different static prestrain levels in the adhesive layer. The specimens were previously marked on one of the sides to allow measuring the slip between the face layers along the beam, thus determining the induced static prestrain distribution in the viscoelastic core.

Next, the experimental work carried out for obtaining the formed CLD beams and for measuring the induced static prestrain in the viscoelastic core, is presented. The experimental set-up employed to form the CLD beams, the considered specimens and the procedure to mark them, are described. The criteria followed for defining the parameters of the forming process are discussed, the technique for measuring the induced static prestrain is detailed, and its distribution along the formed CLD beams is presented.

5.2.1 Experimental set-up

The V-bending process was considered to form the CLD beams because is the most studied metal forming operation in bibliography and also the simplest forming process which parameters can be easily controlled. For performing the V-bending operation, a Schmidt® *ServoPress 420* press shown in Figure 5.3(a) was employed with a regulable die, as can be seen in Figure 5.3(b).

The regulable die-span allowed forming the beams with air-bending or die-bending conditions. As well, the SCHMIDT® *ServoPress 420* press allowed the precise control of the forming process parameters, which are defined in Section 5.2.3.

(a) (b)

Figure 5.3: (a): General view of the press; (b): Detail of the die and the punch, where three specimens are positioned to be formed at once.

5.2.2 Specimens

Two specimen types were considered with different purposes. All the specimens were 10 mm width and 200 mm long, 30 mm were employed for clamping purpose when measuring their dynamic response, so that the effective free length was 170 mm. The geometrical and physical properties of the specimens are those summarized in Table 2.1.

The first type of specimens, were the constraining layers (CL) of the CLD specimens. Their analysis was aimed to validate the employed experimental set-up for measuring the frequency response of formed specimens, and to detect any unexpected influence of the forming process on their dynamic behavior. The beams were bent at midway between the clamp and the free end, i.e., at 85 mm from the free end. The CL specimens were bent into 30°, 60° and 90° nominal bending angles as can be seen in Figure 5.4(a).

After checking that no unexpected factor was affecting to the dynamic behavior of formed metallic specimens and validating the employed experimental set-up, the study was focussed on the dynamic analysis of formed CLD beams. The second type of specimens were V-bent CLD beams, and as the CL specimens, they were bent at midway between the clamp and the free end. The purpose of analyzing these specimens was to analyze the influence of the different induced static prestrain levels on their frequency response. The CLD specimens were bent into 15°, 30°, 45°, 60°, 75° and 90° nominal bending angles, as shown in Figure 5.4(b).

In all cases, three specimens were considered to analyze the repeatability of their frequency response after being formed. In all cases, as shown in Figure 5.3(b), the three specimens were formed simultaneously to guarantee identical forming conditions and therefore, to induce a similar static prestrain distribution to the three CLD specimens.

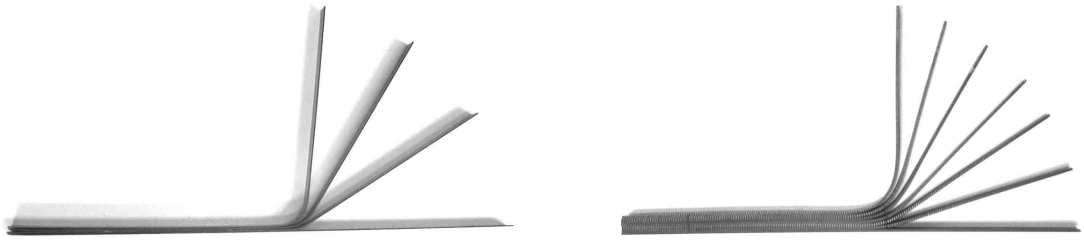

(a) (b)

Figure 5.4: (a): Unformed and formed CL specimens with 30°, 60° and 90° nominal bending angles; (b): Unformed and formed CLD specimens with 15°, 30°, 45°, 60°, 75° and 90° nominal bending angles.

As concluded from Figure 5.4 the sidewall curl was not noticeable, both wings remaining straight after the forming process. Neglecting any geometrical imperfection, the final geometry of the V-bent beams can be defined with just four nodes, as is represented in Figure 5.5.

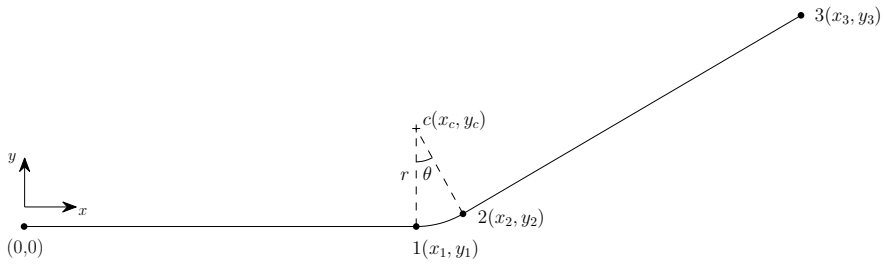

Figure 5.5: Geometrical properties of the formed specimens.

From the coordinates of these nodes the geometry of the formed beams, as well as the bending angle θ, the radius of the arc r, and the coordinates (x_c, y_c) of its center c can be calculated applying trigonometric relations. In Table 5.1, the type and reference, the bending angle, and the coordinates of the nodes are summarized. The specimens were labeled with an *F* for denoting that are formed, followed by the specimen type, the nominal bending angle, and the specimen number. For example, the specimen labeled as "F-CLD-30-2", refers to the second formed CLD specimen with a 30° nominal angle.

For the subsequent dynamic analysis, the static prestrain distribution must be measured after the forming process. For such purpose, before bending the specimens, marks were performed on one of the sides by wire electrical discharge machining (WEDM) process, as is represented in Figure 5.6.

Table 5.1: Type, reference, bending angle, and node coordinates of the formed specimens.

Type	Reference	Angle, θ (°)	Node coordinates (mm)					
			x_1	y_1	x_2	y_2	x_3	y_3
CL	F-CL-30	30.4	80.0	0.0	90.0	3.5	159.0	44.0
	F-CL-60	58.6	75.0	0.0	92.0	10.0	131.0	74.0
	F-CL-90	85.0	75.0	0.0	88.0	13.0	94.5	88.0
CLD	F-CLD-15	16.6	75.0	0.0	96.0	2.5	166.0	24.0
	F-CLD-30	33.8	75.0	0.0	94.5	6.0	156.5	47.5
	F-CLD-45	45.8	75.0	0.0	93.5	8.0	146.0	62.0
	F-CLD-60	59.3	70.0	0.0	95.5	14.0	130.5	73.0
	F-CLD-75	74.7	70.0	0.0	93.0	17.3	111.0	83.0
	F-CLD-90	90.0	65.0	0.0	90.5	25.5	90.5	90.5

The WEDM process offered a precise geometrical and superficial finish enabling measuring the relative displacement between the face layers after the forming operation with certainty.

5.2.3 Forming process parameters

The most important factor to consider when forming the specimens, is that the induced static prestrain distribution does not uniquely depend on the final shape, but also on the tooling and the forming process parameters.

First of all, the parameters related with the tools and their disposition were adjusted. The punch with largest radius (20 mm) was selected. Takiguchi and Yoshida [116] show that the influence of the punch radius on the static prestrain distribution is not significant. By contrast, they prove that the air-bending or die-bending conditions, as well as the used die-span significantly affect to the prestrain distribution. According to their results, the die-span distance was set to the allowed maximum value for minimizing the sidewall curl geometrical imperfection during the V-bending operation. The die-span was set to 115 mm, being the maximum distance for properly bending the specimens with largest bending angle (90°).

After establishing the parameters related with the tooling, the process parameters for controlling the shear strain rate of the adhesive during forming, were defined. The most important aspect that it must be kept in mind, is that the final static prestrain distribution given in the viscoelastic core is not uniform along the beam. Therefore, each

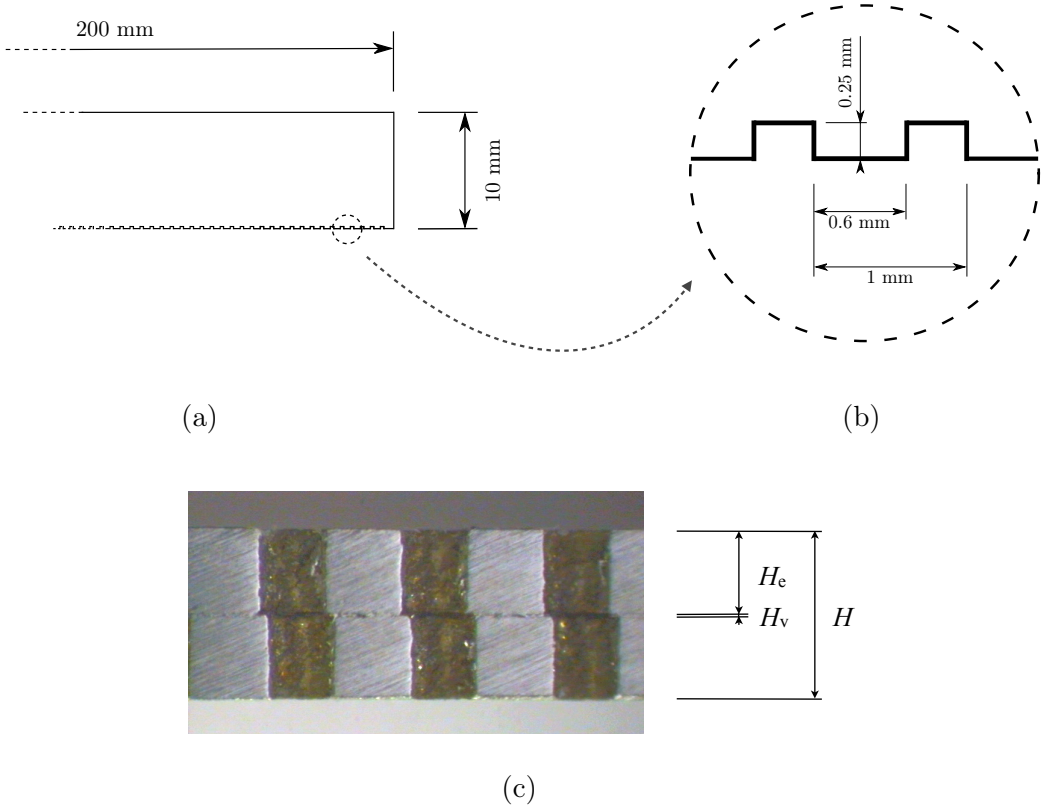

Figure 5.6: (a): Specimen with one of the sides marked; (b): Detail of the marks; (c): Macrograph of the marks evidencing the slip originated between the face layers.

adhesive segment is unequivocally deformed under different shear strain rate conditions. Takiguchi and Yoshida [117] analyzes the viscoplastic behavior of an adhesive, showing that the flow stress and the induced strain strongly depend on the applied strain rate. From this statement, the next question arises: do the dynamic properties of a prestrained viscoelastic material only depend on the prestrain level, or also on the strain rate with which this prestrain is induced? This expands the problematic of the analysis of press-formed CLD parts, since implies that forming under different speeds, similar final shapes could be obtained inducing different static prestrain distributions. Therefore, it suggests that CLD parts with the same shape but with a different dynamic behavior could be obtained. It raises the same reflection in relation to the influence of the temperature with which the part is press-formed. Certainly, this is an open issue that requires further experiments.

According to this reflection, the specimens were intended to be formed shearing the core under similar strain rate conditions. The only way for doing this consisted on forming the beams with very low forming speeds. The punch speed was set to 0.1 mm/s, and therefore, all the finite volumes of the adhesive were deformed with a shear strain rate below $\dot{\gamma} = 5 \times 10^{-3}$ s^{-1}, which is regarded as an quasi-static deformation. The forming

of the CLD beams was performed at room temperature (20 ± 1 °C). In Figure 5.7 the sequence of the V-bending forming process of a CLD beam, can be seen.

Figure 5.7: Sequence of the V-bending forming process of a CLD beam.

Finally, is worthy to mention that all the specimens were over-bent approximately 12° to counterbalance the springback and reach to the nominal bending angle.

5.2.4 Induced prestrain

After forming the CLD specimens, the relative displacement between both constraining layers was measured along the length of the beam. To this end, a Wild® *M420* optical macroscope equipped with a Kappa® *CF 11 DSP* camera was employed. The maximum zoom of the macroscope (32×) was used and the camera provided an extra zoom of 1.5×, so that a total zoom of 48× was used allowing to measure the discrepancies with a ±5 μm incertitude. For example, in Figure 5.8, some macrographs of the F-CLD-60-1 specimen showing the relative displacement between the marks at different points along the length, can be seen.

The relative displacement between the face layers was measured in one of the three specimens. As the three specimens were simultaneously formed in all cases, a similar prestrain distribution was expected for all the specimens. The relative displacement h_0 was measured at 34 points 5mm equispaced along the length of the beam, and the prestrain γ_0 defined in Chapter 3, was determined by

$$\gamma_0 = \frac{|h_0|}{H_\mathrm{v}}. \tag{5.1}$$

where H_v is the thickness of the viscoelastic core.

In Figure 5.9, the relative displacement between the face layers and the resultant prestrain distribution of the V-bent CLD specimens can be seen.

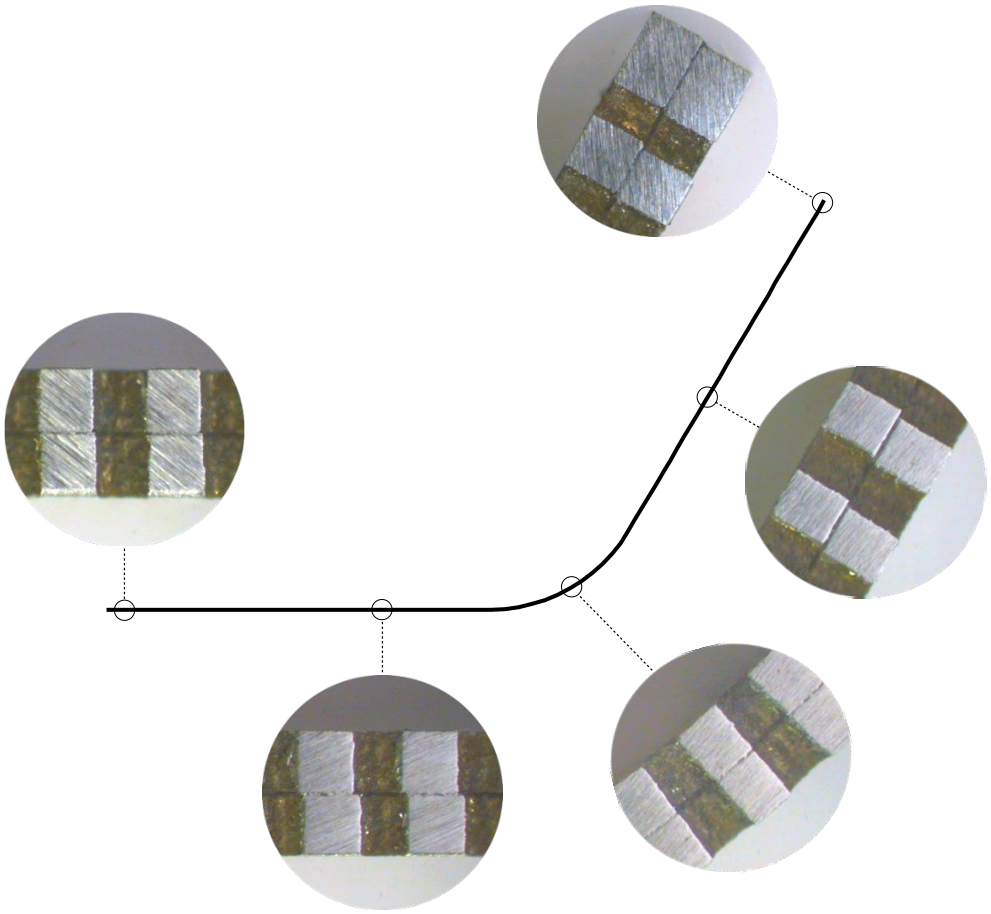

Figure 5.8: Macrographs of the marks showing the relative displacement between the constraining layers at different points of the F-CLD-60-1 specimen.

From Figure 5.9 an important increment of the prestrain level with angles between 15° and 60°, was evidenced. By contrast, the prestrain level increased in a lesser extent between 60° and 90° bending angles. As well, a non-symmetrical distribution of the prestrain was observed because the 200 mm long specimens were not bent just at the middle of the total length. The beams were bent at midway between the clamp and the free end. Therefore, a larger prestrain level was observed in the wing located closer to the free end (shortest wing), as the slip at this side was induced with a lower resistance. The maximum static prestrain level was achieved on the F-CLD-90 specimens resulting about $\gamma_0 = 3$ at the point located 100 mm from the clamp. In all cases, the maximum static prestrain levels were localized at both sides of the bent region.

After determining the forming induced static prestrain distribution in the viscoelastic core, its influence on the frequency response of formed CLD beams is studied. But first, the numerical implementation of the proposed frequency-prestrain material model is described next.

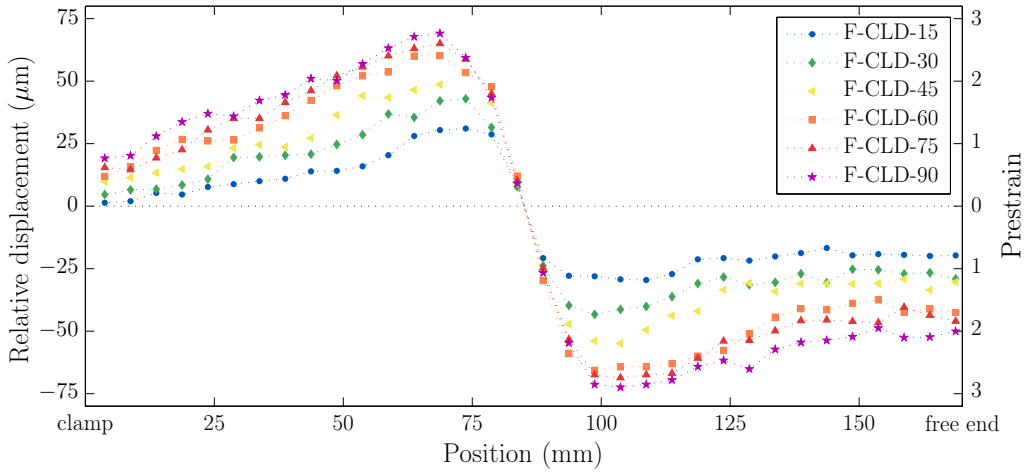

Figure 5.9: Relative displacement between the constraining layers and the resultant prestrain distribution along the length of the V-bent CLD beams.

5.3 FEM implementation of the frequency-prestrain material model

The numerical analysis of the prestrained CLD beams was performed by means of the finite element method (FEM). In this section, the defined FEM models are detailed and some considerations for implementing the proposed frequency-prestrain material model are described.

5.3.1 FEM model

For the numerical analysis of formed CLD beams, a FEM model was defined for each analyzed bending angle (15°, 30°, 45°, 60°, 75° and 90°). The geometries of the V-bent CLD beams were defined with the coordinates summarized in Table 5.1, and the geometrical and physical properties of each layer are gathered in Table 2.1.

The FEM models were defined using the three-layer sandwich finite element already described in Section 2.4.2. This finite element was defined by two nodes with four degrees of freedom per node (u, v, θ_z, ψ_z). The dynamic behavior of curved CLD beams was analyzed using the same planar finite elements, but for properly analyzing them, it was necessary to add five degrees-of-freedom to each of the two nodes (Amichi and Atalla [4]), one displacement and four rotation (w, θ_x, θ_y, ψ_x, ψ_y), resulting in a 9 degrees of freedom per node (u, v, w, θ_x, θ_y, θ_z, ψ_x, ψ_y, ψ_z) finite element. When adding extra degrees of freedom, rank deficiency and ill-conditioning problems emerge when adjacent elements

are coplanar due to the zero stiffness associated with the added degrees of freedom. The assembly is classically stabilized by adding a fictitious stiffness relative to each degree of freedom. To this end, the formulation proposed by Batoz and Dhatt [12] was used to calculate identical fictitious stiffness matrices $\mathbf{K}_w$, $\mathbf{K}_{\theta_x}$, $\mathbf{K}_{\theta_y}$, $\mathbf{K}_{\psi_x}$, $\mathbf{K}_{\psi_y}$ related to the added degrees of freedom. The formulation of the finite element and the details about the fictitious stiffness matrices calculation are detailed in Appendix B.

All the formed CLD beams were discretized into 2.5 mm long 68 finite elements defined by 69 nodes. After applying clamped boundary conditions, the final FEM models yielded to 612 degrees of freedom. Another aspect to be considered when defining the FEM models of the formed CLD beams, was the non-uniform distribution of the static prestrain in the viscoelastic core along the beam. This implied that each elemental stiffness matrix related to the viscoelastic core was different. Therefore, as is discussed next, some considerations were essential when assembling the stiffness matrix related to the viscoelastic material in order to efficiently perform the subsequent numerical analysis.

5.3.2 Frequency–prestrain material model implementation

Next, how the material model presented in Chapter 3 was implemented into the finite element method for the numerical analysis of formed CLD beams, is described. Whereas the plane CLD beams presented a viscoelastic core with equal properties along the length, the viscoelastic core of the formed ones exhibited different dynamic properties throughout the length since each viscoelastic segment was subjected to a different static prestrain level.

As described in Chapters 2 and 4, when analyzing the straight CLD beams the total stiffness matrix $\mathbf{K}^*(\omega)$ was decomposed into a non-frequency-dependent stiffness matrix $\mathbf{K}_\mathrm{e}$ related to the elastic layers, and into a frequency-dependent stiffness matrix $\mathbf{K}^*_\mathrm{v}(\omega)$ related to the viscoelastic core as follows:

$$\mathbf{K}^*(\omega) = \mathbf{K}_\mathrm{e} + \mathbf{K}^*_\mathrm{v}(\omega). \tag{5.2}$$

In the particular case of straight beams, where the viscoelastic material showed the same dynamic properties along the beam, the stiffness matrix related to the viscoelastic core was updated as

$$\mathbf{K}^*_\mathrm{v}(\omega) = \frac{G^*_\mathrm{v}(\omega)}{G_0}\mathbf{K}_{\mathrm{v},0}, \tag{5.3}$$

where $\mathbf{K}_{\mathrm{v},0}$ is the static stiffness matrix related to the viscoelastic core. For the particular case of formed CLD beams, where each finite segment of the viscoelastic material showed a different prestrain level and therefore, different dynamic properties, the complex stiffness

matrix related to the viscoelastic layer could not be updated in such a simple manner. Nevertheless, a similar updating procedure is desirable to avoid reassembling the stiffness matrix related to the viscoelastic core for each computational frequency ω_k, thus allowing to perform the numerical dynamic analysis efficiently. This factor was of special concern when defining the material model for characterizing the viscoelastic material in function of the frequency and the static prestrain.

In Section 3.4, two functions to relate the dynamic properties of the prestrained viscoelastic material with the nominal dynamic properties of the not prestrained viscoelastic material were defined. Such relationship was expressed as,

$$G^*_{\mathrm{v}}(\omega,\gamma_0) = f_R(\omega,\gamma_0)G'_{\mathrm{v}}(\omega) + \mathrm{i}f_I(\omega,\gamma_0)G''_{\mathrm{v}}(\omega), \tag{5.4}$$

where the functions $f_R(\omega,\gamma_0)$ and $f_I(\omega,\gamma_0)$, were defined as

$$f_R(\omega,\gamma_0) = 1 + f_r(\omega)\gamma_0^{n_r} \tag{5.5}$$

and

$$f_I(\omega,\gamma_0) = 1 + f_i(\omega)\gamma_0^{n_i}, \tag{5.6}$$

respectively. Whereas the frequency dependence described by $f_r(\omega)$ and $f_i(\omega)$ is common for all the viscoelastic segments, the functions $f_R(\omega,\gamma_0)$ and $f_I(\omega,\gamma_0)$ differ from segment to segment as each of them exhibited a different static prestrain level γ_0. A closer look to Equations 5.5 and 5.6 evidences that the elastic and dissipative properties of the prestrained viscoelastic material are described as the contribution of the nominal properties and an increment originated by the static prestrain. Therefore, the total stiffness matrix of the prestrained viscoelastic core $\mathbf{K}^*_{\mathrm{v}}$ is defined as a linear combination of three matrices.

The first one is the static stiffness matrix $\mathbf{K}_{\mathrm{v},0}$ evaluated with the nominal static properties G_0 for all the viscoelastic segments. The static stiffness matrix in global coordinates is obtained assembling the elemental static stiffness matrices $\mathbf{K}^e_{\mathrm{v},0}$, given by

$$\mathbf{K}_{\mathrm{v},0} = \sum_{e=1}^{e_{\max}} \mathbf{T}^{\mathrm{T}}\mathbf{K}^e_{\mathrm{v},0}\mathbf{T}, \tag{5.7}$$

where $e_{\max}$ is the total number of elements, $(\bullet)^{\mathrm{T}}$ denotes the transposition operator, and $\mathbf{T}$ is the transformation matrix between the local and global coordinate systems, and $\mathbf{K}^e_{\mathrm{v}}$ is the elemental stiffness matrix, both detailed in Appendix B.

The variation of the dynamic properties is described by two different extra stiffness matrices since the variation of the elastic and the dissipative properties is not identical for a given static prestrain level γ_0. The matrix to account for the variation of the elastic properties $\mathbf{K}_{\mathrm{v},\gamma 0}$ is defined including the static prestrain level of each element during the assembling process as

$$\mathbf{K}_{\mathrm{v},\gamma_0} = \sum_{e=1}^{e_{\max}} \gamma_0^{n_r} \mathbf{T}^{\mathrm{T}} \mathbf{K}_{\mathrm{v}_0}^{e} \mathbf{T}, \tag{5.8}$$

where γ_0 is the static prestrain level exhibited by the eth element. In a similar way, the matrix to account for the variation of the dissipative properties due to the static prestrain $\mathbf{H}_{\mathrm{v},\gamma_0}$, is also defined as

$$\mathbf{H}_{\mathrm{v},\gamma_0} = \sum_{e=1}^{e_{\max}} \gamma_0^{n_i} \mathbf{T}^{\mathrm{T}} \mathbf{K}_{\mathrm{v},0}^{e} \mathbf{T}. \tag{5.9}$$

Including the influence of the static prestrain on the dynamic properties of each element, allows updating the total complex stiffness matrix related to the prestrained viscoelastic core $\mathbf{K}_{\mathrm{v}}^{*}(\omega)$ in a direct way. The latter is decomposed in a stiffness $\mathbf{K}_{\mathrm{v}}(\omega)$ and a structural damping $\mathbf{H}_{\mathrm{v}}(\omega)$ matrices, which are updated separately as follows:

$$\mathbf{K}_{\mathrm{v}}(\omega) = \frac{G'_{\mathrm{v}}(\omega)}{G_0} \left(\mathbf{K}_{\mathrm{v},0} + f_r(\omega) \mathbf{K}_{\mathrm{v},\gamma_0}\right) \tag{5.10}$$

and

$$\mathbf{H}_{\mathrm{v}}(\omega) = \frac{G''_{\mathrm{v}}(\omega)}{G_0} \left(\mathbf{K}_{\mathrm{v},0} + f_i(\omega) \mathbf{H}_{\mathrm{v},\gamma_0}\right), \tag{5.11}$$

respectively. Where $G'_{\mathrm{v}}(\omega)$ and $G''_{\mathrm{v}}(\omega)$ are the nominal storage and loss modulus of the viscoelastic material measured without applying any prestrain level, respectively. This way, the presented frequency-prestrain material constitutive model is combined with the material model considered for characterizing the nominal dynamic properties. Thus, the dynamic properties of the prestrained viscoelastic material are described in terms of the properties of the not prestrained one.

The total complex stiffness matrix of the prestrained viscoelastic layer $\mathbf{K}_{\mathrm{v}}^{*}(\omega)$, is then obtained combining both matrices as

$$\mathbf{K}_{\mathrm{v}}^{*}(\omega) = \mathbf{K}_{\mathrm{v}}(\omega) + \mathrm{i}\mathbf{H}_{\mathrm{v}}(\omega). \tag{5.12}$$

Finally the global frequency-dependent complex stiffness matrix is obtained by

$$\mathbf{K}^*(\omega) = \mathbf{K}_\mathrm{e} + \mathbf{K}_\mathrm{v}^*(\omega). \tag{5.13}$$

This way, including the influence of the static prestrain when assembling the elemental stiffness matrices of the viscoelastic core for the first time, reassembling the complex stiffness matrix $\mathbf{K}_\mathrm{v}^*(\omega)$ is avoided every time the frequency changes. This way, the stiffness matrix updating procedure is performed easily and efficiently.

5.4 Influence of the static prestrain on the dynamic behavior of formed CLD beams

The objective of this analysis is to confirm the influence of the static prestrain on the dynamic response of formed CLD beams by means of experimental tests. The present study has been submitted to the journal *Materials & Design* [76] for publication.

First, CL specimens were tested in order to detect any unexpected influence and verify the validity of the employed experimental set-up for measuring the frequency response of formed specimens. The analysis aimed to verify that the variations observed on the frequency response of the formed CLD beams were exclusively originated by the static prestrain. The plastic deformation of the face layers given when bending the CLD beams should not affect to the storage modulus of the metallic layers, and thus, to the frequency response of the formed CLD specimens. To verify this hypothesis, the frequency response of formed CL beams was numerically computed by means of the finite element method and correlated with the experimental response.

Then, the experimental frequency response measured at 20 °C, was compared with that computed with the nominal dynamic properties identified at the same temperature by the forced vibration test with resonance in Chapter 2. From this comparison, the influence of the static prestrain on the dynamic behavior of formed CLD beams was proved. After that, the frequency-prestrain material model was applied in order to correct the deviations manifested in this first comparison.

The experimental frequency response of the formed beams was measured following exactly the same experimental set-up and procedure described in Section 2.2. A base motion was applied at the clamped end, and the response of the selected points was measured by a laser vibrometer perpendicularly positioned to the surface of the beam. The base motion consisted of a white noise which acceleration amplitude was loopback controlled. The transfer functions were obtained relating the transverse displacement of the response point with that applied at the base. As well, the same linearity analysis detailed in Section 2.2.3 was performed to define the proper excitation acceleration spectrum. After performing

the linearity analysis, the excitation amplitude for the first mode was set to 0.1 m/s^2 and the excitation amplitude for the higher order modes was increased in order to improve the signal-to-noise ratio. Again, the maximum amplitude level to induce deformations within the linear viscoelastic range was determined, resulting of 1.5 m/s^2 up to 1 kHz. After defining the proper excitation acceleration spectrum, the experimental transfer functions of several points were measured up to 1 kHz with a 0.3125 Hz constant resolution. The test temperature was 20 ± 1 °C.

For computing the frequency response of the formed CL beams a FEM model was defined for each of the analyzed bending angles (30°, 60° and 90°). The geometry of the formed beams was defined with the data summarized in Table 5.1. The geometrical and physical properties and the storage modulus of the metallic layers are detailed in Chapter 2, whereas the loss factor was assumed to be $\eta_e = 1 \times 10^{-3}$. The FEM models were defined using two-node beam finite elements with three degrees-of-freedom per node (longitudinal displacement u, transverse displacement v, and rotation θ_z) and cubic shape functions with plane stress hypothesis and assuming Euler–Bernoulli beam theory [61]. The CL beams were discretized into 2.5 mm long 68 finite elements defined by 69 nodes. After applying clamped boundary conditions, the final FEM models yielded to 204 degrees of freedom.

The numerical transfer functions of the CL specimens bent with three different angles were computed by the direct frequency method and correlated with the experimental ones. From this comparison, no significant deviations were observed on the nine tested CL specimens. For example, in Figure 5.10, the modulus and the phase of the experimental and numerical transfer functions of the F-CL-60-1 speciment, can be seen.

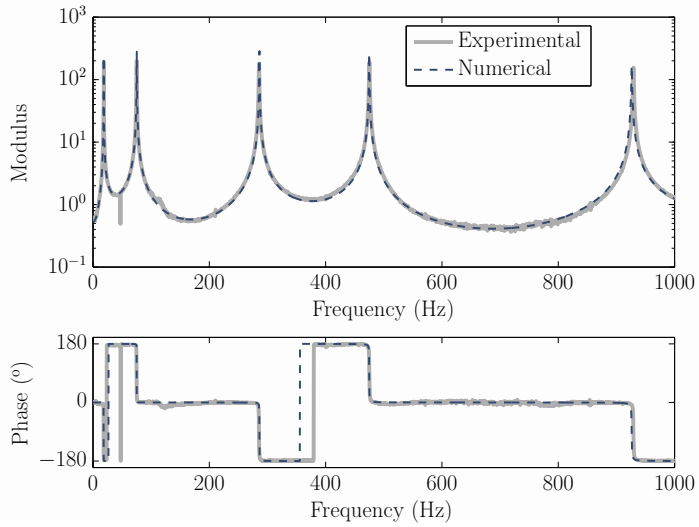

Figure 5.10: Modulus and phase of the experimental and numerical transfer function of the F-CL-60-1 specimen relating the transverse displacement of the free end with that applied at the base.

As concluded, no relevant differences were observed. The largest deviation in frequency was found at the first resonance, where the resonance frequency resulted underestimated by 1.4 %. With this analysis it was verified that the frequency response of the CL specimens does not change because of the forming process. Therefore, the differences observed between the experimental frequency response of formed CLD beams, and the numerical response computed with the nominal properties identified in Chapter 2, were uniquely attributable to the influence of the static prestrain on the dynamic properties of the viscoelastic core.

The experimental transfer functions of the formed CLD specimens were correlated with those computed with the nominal material properties characterized in Chapter 2. Since the nominal properties at 20 °C were identified up to 1 kHz, both responses were correlated within this frequency bandwidth, and how the static prestrain affected to the dynamic response of formed CLD beams, was analyzed. The repeatability of the experimental transfer functions of the three specimens with the same bending angle was verified, and no remarkable differences were observed in frequency nor in amplitude. For example, in Figure 5.11, the modulus and the phase of the experimental and the numerical transfer functions of the F-CLD-60-1 specimen computed with the nominal properties, are compared up to 1 kHz. As well, in order to better appreciate the differences manifested at the first two resonances, in Figure 5.12 the same transfer functions are plotted within $0 - 170$ Hz in linear scale.

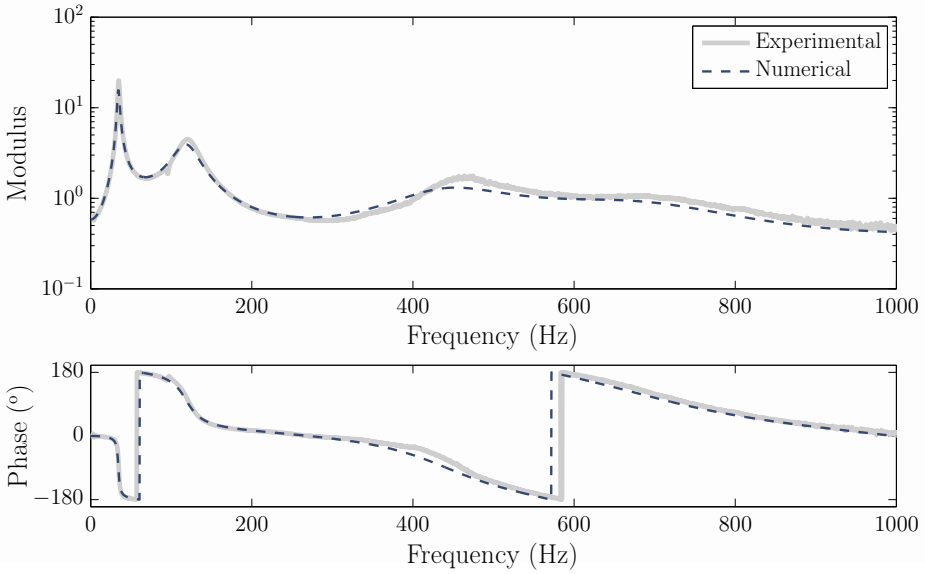

Figure 5.11: Modulus and phase of the transfer function of the F-CLD-60-1 specimen relating the transverse displacement of the free end with that applied at the base. (——) experimental, and (- - -) numerical computed with the nominal dynamic properties.

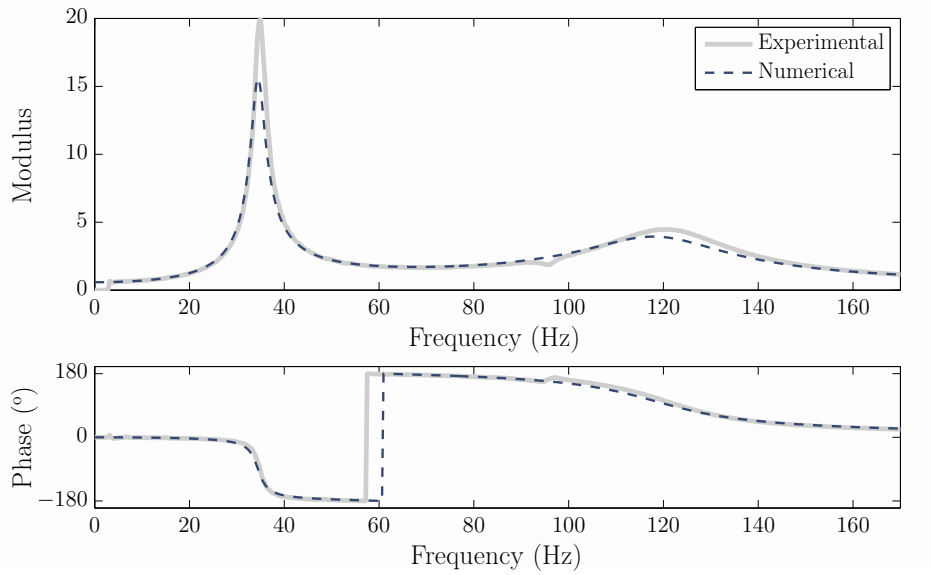

Figure 5.12: Zoom of the first two resonances shown in Figure 5.11 plotted in linear scale. (——) experimental, and (- - -) numerical computed with the nominal dynamic properties.

As was evidenced from Figures 5.11 and 5.12, the two dynamic responses did not correspond precisely. Deviations in amplitude were evident at all the resonances, whereas the differences in frequency were more significant at the higher frequencies. The first and the second resonances showed the largest differences in amplitude being underestimated by 22 % and by 12 %, respectively, whereas the resonance frequencies of both modes resulted underestimated by 2 %. Although with the nominal dynamic properties the frequency response of straight CLD beams was accurately determined, remarkable differences were observed when considering them for computing the dynamic response of formed CLD beams. This comparison highlighted that the static prestrain is another relevant factor to be considered for the correct dynamic analysis of formed CLD parts.

After proving the significance of the static prestrain influence on the dynamic behavior of formed CLD beams with experimental frequency responses, in a next step it was attempted to reduce the observed differences including the frequency-prestrain material model proposed in Chapter 3. It must be remarked the assumed hypothesis related to the temperature when including the static prestrain influence on the dynamic properties of the viscoelastic core. The frequency-prestrain characterization was performed at 30 °C, whereas the forming process and the measurement of the experimental frequency responses were carried out at 20 °C. Despite of the temperature difference, as the measured dynamic properties corresponded with the end of the rubbery and the beginning of the transition regions where the dynamic properties do not significantly vary with temperature (see Figure 3.20), the dependence of the static prestrain effect with the temperature was not ex-

pected to be significant. Thus, the frequency-prestrain material model with the parameters identified at 30 °C and gathered in Tables 3.1 and 3.2, was combined with the fractional derivative model used for describing the nominal dynamic properties with the parameters identified at 20 °C in Chapter 2. Anyway, the validity of this hypothesis was discussed and verified with the results presented next.

In Figures 5.13, the modulus and the phase of the experimental transfer functions relating the transverse displacement of the free end with that applied at the base, of all the analyzed bending angles can be seen. As well, the transfers functions computed with the nominal dynamic properties, and that computed including the effect of the static prestrain, can be seen. In order to better reflect the correlation in amplitude, the Global Amplitude Criterion (GAC) indicator is also provided. The transfer functions are plotted within $0 - 170$ Hz, frequency bandwidth where the influence of the static prestrain on the dynamic properties of the viscoelastic core was characterized.

As was concluded from Figure 5.13, the correlation between the experimental and the numerical transfer function computed with the nominal dynamic properties evidenced again the influence of the static prestrain on the response of the formed CLD specimens. Whereas a good correlation degree was observed when the static prestrain level was small, discrepancies grew as the static prestrain level increased. Its influence was evidenced mainly on the amplitude of the first and the second resonances, which were underestimated when the nominal properties were considered. By contrast, the resonance frequency of both modes slightly differed, the variation being more significant for the second resonance frequency.

By contrast, when including the influence of the static prestrain on the dynamic properties of the viscoelastic core, the numerical frequency response got closer to the experimental one. In general, both resonances were better reproduced, considerably reducing the large differences observed in amplitude. The only remarkable exception was the F-CLD-90 specimen, which frequency response was not predicted as accurately as that of the other specimens after including the influence of the static prestrain. Although the first resonance was reproduced satisfactorily, noticeable differences were observed at the second resonance. Although these specimens were subjected to the largest static prestrain levels, the delamination effect was discarded since the experimental resonance frequency was larger than that numerically predicted. The good correlation observed for the first resonance evidences that the problem is related to the second mode.

In addition to the frequency functions correlation, the discrepancies in frequency and in amplitude observed at the first two resonances were quantified, the results being summarized in Table 5.2.

F-CLD-15

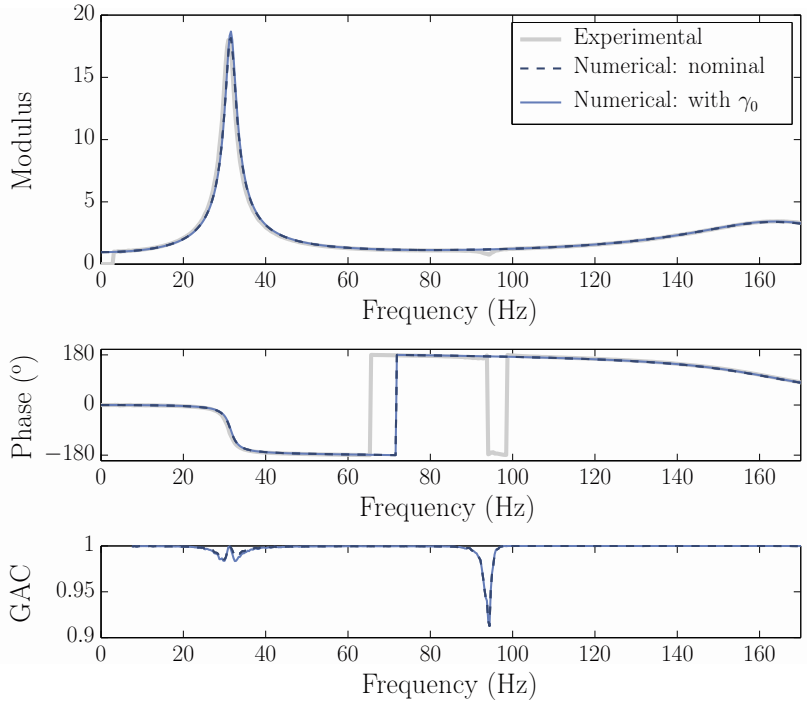

F-CLD-30

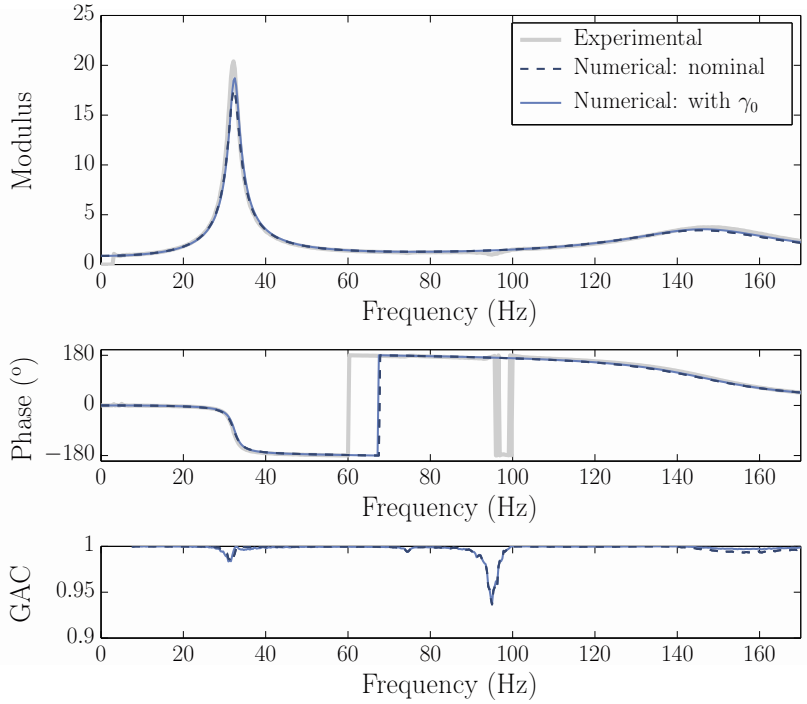

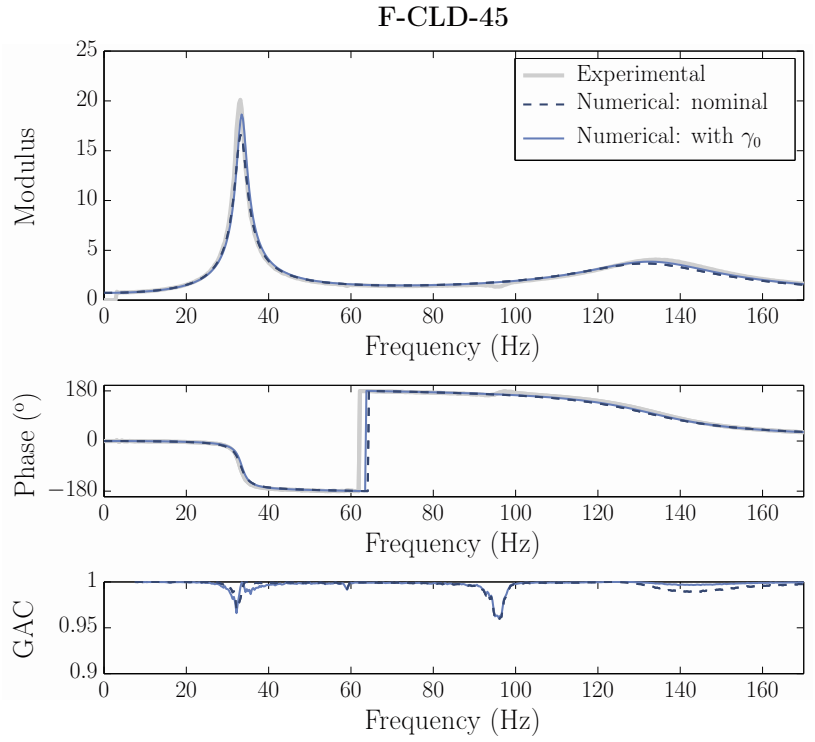
F-CLD-45
Experimental
Numerical: nominal
Numerical: with γ_0
Modulus
Phase (°)
GAC
Frequency (Hz)

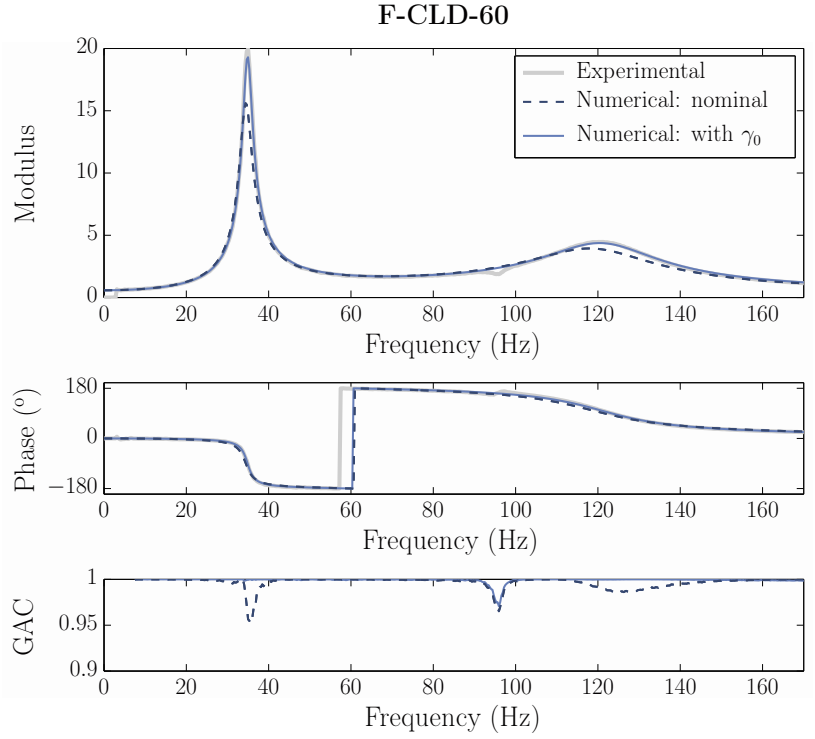
F-CLD-60
Experimental
Numerical: nominal
Numerical: with γ_0
Modulus
Phase (°)
GAC
Frequency (Hz)

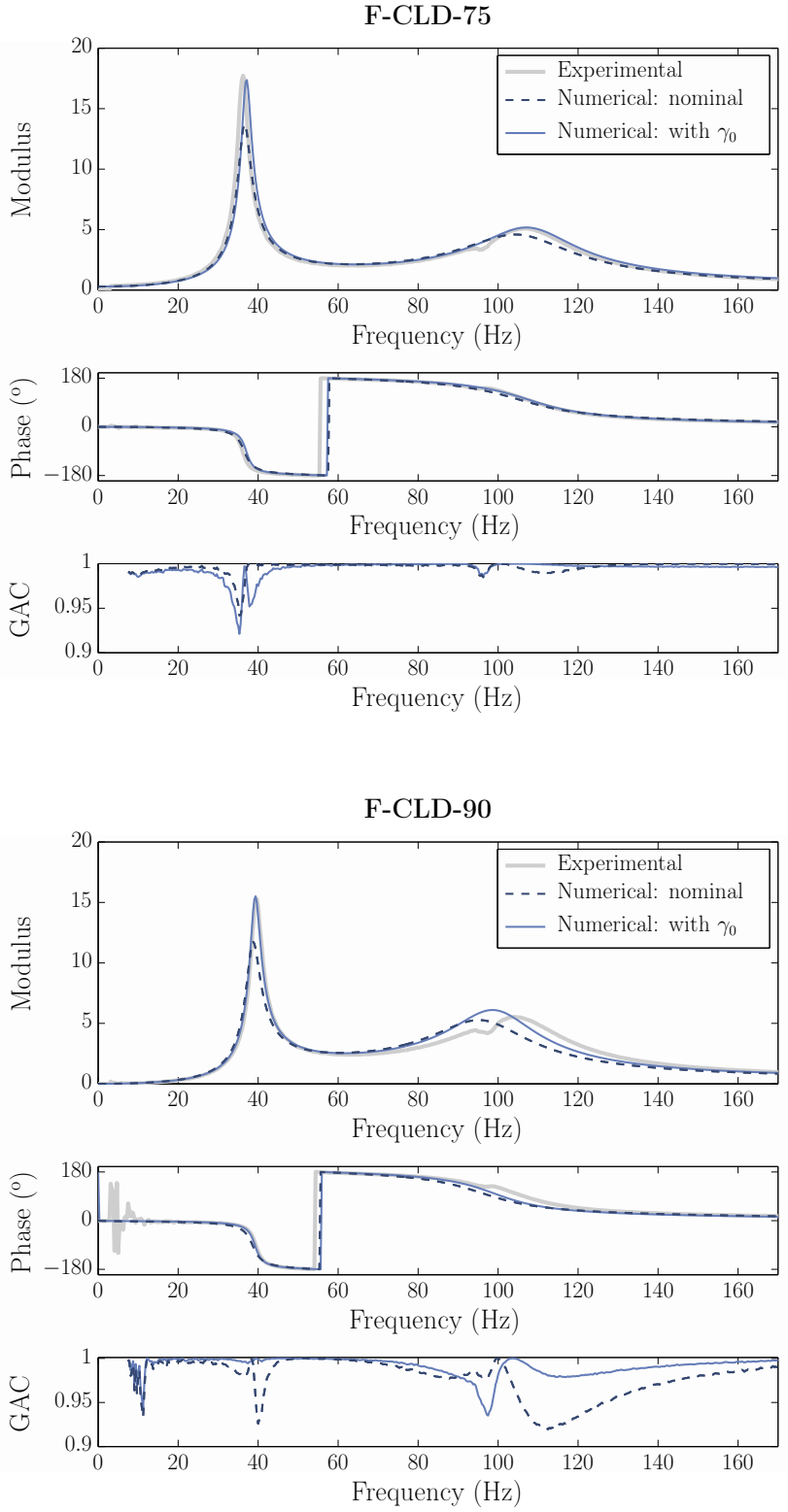

Figure 5.13: Modulus and phase of the transfer functions of formed CLD specimens relating the transverse displacement of the free end with that applied at the base. Experimental (——), computed with the nominal dynamic properties (- - -), and computed accounting for the influence of the static prestrain (——).

Table 5.2: Error in frequency and amplitude of the first two resonances of the numeric responses with and without including the influence of the static prestrain.

Specimen	Frequency response	Mode 1		Mode 2	
		f_1 (Hz)	A_1 (m/m)	f_2 (Hz)	A_2 (m/m)
F-CLD-15	**Experimental**	**31.1**	**18.01**	**164.1**	**3.43**
	Numerical: nominal prop.	31.5 (1.3 %)	18.16 (0.8 %)	162.0 (-1.3 %)	3.39 (-1.2 %)
	Numerical: with prestrain	31.6 (1.6 %)	18.68 (3.7 %)	162.3 (-1.1 %)	3.42 (-0.3 %)
F-CLD-30	**Experimental**	**32.2**	**20.40**	**148.0**	**3.74**
	Numerical: nominal prop.	32.3 (0.3 %)	17.51 (-14.2 %)	144.7 (-2.2 %)	3.45 (-7.8 %)
	Numerical: with prestrain	32.5 (0.9 %)	18.71 (-8.3 %)	145.5 (-1.7 %)	3.55 (-5.1 %)
F-CLD-45	**Experimental**	**33.1**	**20.11**	**134.7**	**4.07**
	Numerical: nominal prop.	33.3 (0.6 %)	16.57 (-17.6 %)	131.1 (-2.7 %)	3.68 (-9.6 %)
	Numerical: with prestrain	33.5 (1.2 %)	18.64 (-7.3 %)	132.3 (-1.8 %)	3.86 (-5.2 %)
F-CLD-60	**Experimental**	**34.9**	**19.96**	**120.4**	**4.46**
	Numerical: nominal prop.	34.5 (-1.1 %)	15.61 (-21.8 %)	117.9 (-2.1 %)	3.94 (-11.7 %)
	Numerical: with prestrain	35.0 (0.3 %)	19.30 (-3.3 %)	120.4 ($\approx$ 0 %)	4.38 (-1.8 %)
F-CLD-75	**Experimental**	**36.3**	**17.73**	**106.9**	**5.09**
	Numerical: nominal prop.	36.7 (1.1 %)	13.70 (-22.7 %)	104.6 (-2.2 %)	4.59 (-9.8 %)
	Numerical: with prestrain	37.2 (2.5 %)	17.37 (-2.0 %)	107.3 (0.4 %)	5.17 (1.6 %)
F-CLD-90	**Experimental**	**39.6**	**15.28**	**102.8**	**5.53**
	Numerical: nominal prop.	38.8 (-2.0 %)	11.74 (-23.2 %)	95.5 (-7.1 %)	5.27 (-4.7 %)
	Numerical: with prestrain	39.4 (-0.5 %)	15.51 (1.5 %)	98.8 (-3.9 %)	6.10 (10.3 %)

As concluded from the data gathered in Table 5.2, and as was also deduced from Figure 5.13, the major differences were related to the amplitude of the first two resonances, where the deviations grew with the static prestrain level. The differences in amplitude for the first mode computed with the nominal properties, were significantly reduced after including the influence of the static prestrain on the dynamic properties of the viscoelastic material. The reduction of the error in amplitude was also noticeable for the second resonance except for the F-CLD-90 specimen, where poor correlation was observed. No significant deviations were observed on the resonance frequencies, and in general better estimates were obtained when including the influence of the static prestrain. Finally, as concluded from the presented results, the static prestrain induced by the metal sheet forming operations negatively affected to the damping performance of the formed CLD parts as long as the amplitude of the resonances became larger.

From the presented results, it should be remarked that although the parameters of the frequency-prestrain material model identified at 30 °C were combined with the nominal dynamic properties measured at 20 °C for correcting the dynamic responses measured at

20 °C, the dynamic responses of the formed CLD beams were satisfactorily predicted. This fact manifested that the influence of the static prestrain on the dynamic properties of the viscoelastic core was similar for both analyzed temperatures. Therefore, the posed hypothesis was verified for this particular case where the temperature difference was relatively small and both corresponded with the end of the rubbery and the beginning of the transition regions were the dynamic properties do not significantly change with temperature.

In the next section, the modal parameters of the formed CLD beams are presented to complete this analysis and to better reflect the influence of the static prestrain on such parameters.

5.5 Application of the higher order eigensensitivities-based numerical method

In this section, the higher order eigensensitivities-based numerical method proposed in Chapter 4 is extended for the dynamic analysis of formed CLD beams. First, the modifications to be introduced when dealing with the analysis of formed CLD parts are described. Then, the iterative algorithm is applied for computing the complex modal parameters of the formed CLD beams and the results are validated by the iterative complex eigensolution (ICE) method. To this end, the same examples used in the previous section are considered. As well, to complete the analysis regarding to the influence of the static prestrain on the dynamic behavior of formed CLD parts, the modal parameters are also computed using the nominal dynamic properties in order to reflect the influence of the static prestrain on such parameters. Finally, the incremental algorithm is applied for computing the complex and frequency-dependent modal parameters in order to obtain the frequency response of the formed CLD beams by the complex mode superposition method. The approximated frequency response is then correlated with the exact one computed by the direct frequency method in order to validate the former.

The only difference respect to the analysis of straight CLD beams is related to the derivatives of the global stiffness matrix, necessary for computing the eigenvalue and eigenvector derivatives. The nth derivative of the global complex stiffness matrix is given by,

$$\frac{\partial^n \mathbf{K}^*}{\partial \omega^n} = \frac{\partial^n \mathbf{K}_\mathrm{e}}{\partial \omega^n} + \frac{\partial^n \mathbf{K}_\mathrm{v}^*}{\partial \omega^n} = \frac{\partial^n \mathbf{K}_\mathrm{v}}{\partial \omega^n} + \mathrm{i}\frac{\partial^n \mathbf{H}_\mathrm{v}}{\partial \omega^n}. \tag{5.14}$$

Attending to the frequency-prestrain material model implementation detailed in Section 5.3.2, where the stiffness matrix related to the viscoelastic core has been defined as a linear combination of three different constant matrices as described by Equations (5.10-5.13), the derivatives of the global stiffness and structural damping matrices, are obtained

differentiating Equations 5.10 and 5.11, yielding to

$$\frac{\partial^n \mathbf{K}}{\partial \omega^n} = \frac{1}{G_0}\left[\mathbf{K}_{\mathrm{v},0}\frac{\partial^n G'_{\mathrm{v}}}{\partial \omega^n} + \mathbf{K}_{\mathrm{v},\gamma_0}\left(\frac{\partial^n G'_{\mathrm{v}}}{\partial \omega^n} f_r + G'_{\mathrm{v}}\frac{\partial^n f_r}{\partial \omega^n} + \sum_{p=1}^{n-1}\binom{n}{p}\frac{\partial^p G'_{\mathrm{v}}}{\partial \omega^p}\frac{\partial^{n-p} f_r}{\partial \omega^{n-p}}\right)\right] \quad (5.15)$$

and

$$\frac{\partial^n \mathbf{H}}{\partial \omega^n} = \frac{1}{G_0}\left[\mathbf{K}_{\mathrm{v},0}\frac{\partial^n G''_{\mathrm{v}}}{\partial \omega^n} + \mathbf{H}_{\mathrm{v},\gamma_0}\left(\frac{\partial^n G''_{\mathrm{v}}}{\partial \omega^n} f_i + G''_{\mathrm{v}}\frac{\partial^n f_i}{\partial \omega^n} + \sum_{p=1}^{n-1}\binom{n}{p}\frac{\partial^p G''_{\mathrm{v}}}{\partial \omega^p}\frac{\partial^{n-p} f_i}{\partial \omega^{n-p}}\right)\right] \quad (5.16)$$

respectively. Once the first nth derivatives of the global stiffness matrix are computed, the process to be followed is exactly the same to that described in Chapter 4. The nth eigenderivatives are computed, the eigenvectors updated by the Taylor's series and the eigenvalues calculated by the Rayleigh quotient. The proposed iterative algorithm outlined in Section 4.2.3 may then be applied for computing the complex modal parameters of the system, and the incremental algorithm detailed in Section 4.2.4 for computing the complex and frequency-dependent modal parameters in order to obtain the frequency response by the complex mode superposition method.

5.5.1 Modal parameters

Next, the complex modal parameters of the formed CLD beams are determined with two main objectives. First, the proposed iterative scheme is validated by correlating the determined modal parameters with those computed by the ICE method. After that, the influence of the static prestrain on the modal parameters of the formed CLD specimens is further analyzed to complete the results presented in the previous section. To this end, the modal parameters were computed considering the nominal dynamic properties of the viscoelastic material, and accounting for the influence of the static prestrain originated by the forming process.

For applying the iterative algorithm the first three eigenderivatives were considered and the tolerance for the accuracy condition given by Equation (4.57) was set to $\mathrm{Tol} = 1 \times 10^{-3}$. The convergence criterion for the iterative process was that given by Equation (4.8), and the tolerance was set to $\epsilon = 1 \times 10^{-4}$. The complex modal parameters determined by the proposed higher order eigensensitivities-based iterative algorithm were validated with those determined by solving the non-linear complex eigenproblem by the iterative complex eigensolution method (ICE). The resonance frequencies of the first two modes were determined with errors $< 5.6 \times 10^{-4}$ %, whereas the modal loss factors were identified with errors $< 6.4 \times 10^{-4}$ %. As well, the correlation degree between the eigenvectors computed by both methods was evaluated by the Modal Assurance Criterion (MAC) indicator,

resulting $\mathrm{MAC}_r > 0.999999 \approx 1$ for both the real and the imaginary parts. Thus, the effectiveness of the proposed iterative algorithm for determining the complex modal parameters of press-formed CLD parts was proved.

After validating the iterative algorithm, the modal parameters were computed using the nominal dynamic properties and taking into consideration the static prestrain influence, the results being those gathered in Table 5.3.

Table 5.3: Natural frequency f_r and modal loss factor η_r of the first two modes determined by the proposed iterative algorithm considering the nominal dynamic properties and including the influence of the static prestrain.

Specimen	Properties	Mode 1				Mode 2			
		f_1 (Hz)	η_1	$\mathrm{MAC}_{\mathrm{Re}}$	$\mathrm{MAC}_{\mathrm{Im}}$	f_2 (Hz)	η_2	$\mathrm{MAC}_{\mathrm{Re}}$	$\mathrm{MAC}_{\mathrm{Im}}$
F-CLD-15	Nominal	31.5	0.083			162.0	0.245		
	With γ_0	31.6	0.081			162.3	0.243		
	Difference (%)	-0.2	2.6	0.99995	0.99997	-0.16	0.9	0.99999	0.99995
F-CLD-30	Nominal	32.3	0.084			144.7	0.245		
	With γ_0	32.5	0.078			145.5	0.239		
	Difference (%)	-0.4	6.6	0.99976	0.99984	-0.5	2.7	0.99993	0.99977
F-CLD-45	Nominal	33.3	0.084			131.1	0.244		
	With γ_0	33.5	0.075			132.3	0.233		
	Difference (%)	-0.7	11.9	0.99917	0.99948	-0.9	4.6	0.99974	0.99942
F-CLD-60	Nominal	34.5	0.084			117.9	0.242		
	With γ_0	35.0	0.068			120.4	0.219		
	Difference (%)	-1.3	23.4	0.99745	0.99871	-2.0	10.6	0.99881	0.99734
F-CLD-75	Nominal	36.7	0.085			104.6	0.238		
	With γ_0	37.2	0.068			107.3	0.212		
	Difference (%)	-1.4	26.5	0.99719	0.99874	-2.5	12.3	0.99883	0.99800
F-CLD-90	Nominal	38.8	0.086			95.5	0.235		
	With γ_0	39.4	0.066			98.8	0.203		
	Difference (%)	-1.5	31.5	0.99615	0.99844	-3.3	15.6	0.99846	0.99730

As concluded from the data summarized in Table 5.3, the natural frequencies were not significantly affected by the static prestrain, being its influence larger for the natural frequency of the second mode. By contrast, the modal loss factor manifested large differences, and specially that of the first mode. The modal loss factor was overestimated when the influence of the static prestrain was not taken into consideration, leading to the underestimation of the amplitude of the resonances observed in Figure 5.13. Furthermore, the influence of the static prestrain on the eigenvectors was also reflected by the the MAC indi-

cator. The correlation degree decreased as the static prestrain level increased. The static prestrain affected more to the real part of the first eigenvectors, whereas its influence resulted greater for the imaginary part of the second eigenvectors.

5.5.2 Frequency response

Next, the frequency response of the F-CLD-60 beam is computed by the complex mode superposition method using the complex and frequency-dependent modal parameters determined by the proposed incremental algorithm. In order to validate the presented incremental algorithm, the computed modal parameters are correlated with those computed by IRAM, and the approximated total frequency response with that calculated by the direct frequency method.

The incremental algorithm was applied with four derivatives and the tolerance for the accuracy condition described by Equation (4.57) was set to $\text{Tol} = 1 \times 10^{-2}$. The complex and frequency-dependent modal parameters computed by the incremental algorithm were correlated with those determined by IRAM. The complex eigenpair of all the six modes superposed for approximating the total frequency response, were computed with errors smaller than 6.3×10^{-4} % and 2.1×10^{-3} % for the real and the imaginary parts of the eigenvalues, respectively. As well, the correlation degree between the eigenvectors computed by both methods was evaluated resulting $\text{MAC}_r > 0.999999 \approx 1$ for both the real and the imaginary parts. Thus, the effectiveness of the proposed incremental algorithm for computing the complex and frequency-dependent modal parameters of formed CLD beams was verified.

After that, the individual contributions to the total transfer function ${}_rT^*_{ij}(\omega)$ of the first six modes were computed, and the total transfer function $T^*_{ij}(\omega)$ was approximated by superposing them. The approximated total response was correlated with that provided by the direct frequency method in order to validate the former. In Figure 5.14, the modulus and the phase of the transfer function computed by the direct frequency method and that approximated by the superposition of the first six complex modes can be seen.

As concluded, the superposition of the first six modes provided almost the exact result, so that the frequency response computed by the complex mode superposition method was validated. The largest difference at the resonances was localized at the second one, which amplitude was overestimated by 0.1 %. This difference may be reduced by superposing a larger number of modes. The major advantage of the complex mode superposition method respect to the direct frequency method, is that besides the total frequency response, the individual participation of each mode to the total is provided. This information is of special interest for engineers concerned with the design of effective damping treatments involving viscoelastic materials.

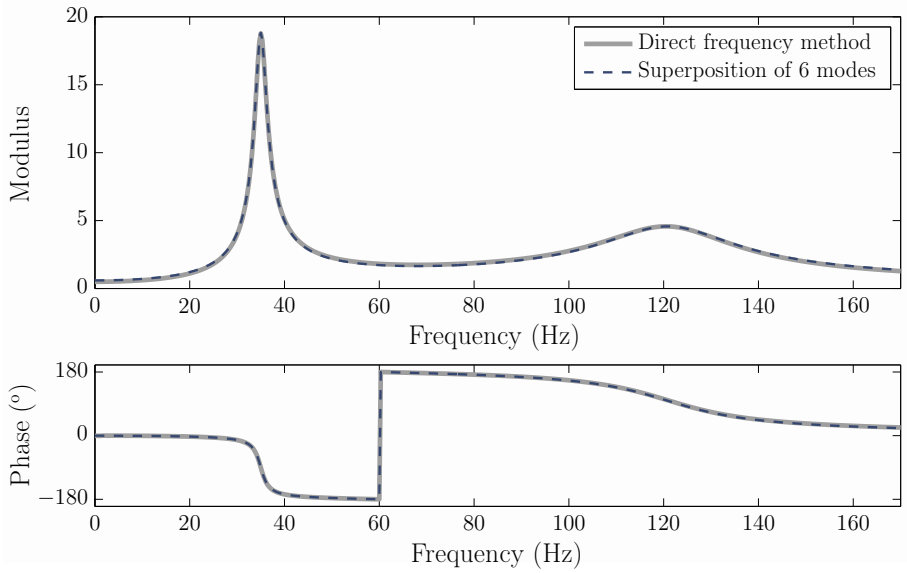

Figure 5.14: Transfer function of the free end of the F-CLD-60 beam computed by the direct frequency method and by the superposition of the first six complex modes.

With the presented analysis, the iterative and the incremental algorithms based on the use of the higher order eigensensitivities were validated for the dynamic analysis of press-formed CLD parts.

5.6 Conclusions

In the present chapter, the influence of the static prestrain on the dynamic behavior of press-formed CLD parts, has been analyzed. To this end, CLD beams have been bent into different angles, the static prestrain distribution has been determined, and their dynamic response has been measured.

The influence of the static prestrain on the dynamic behavior of press-formed CLD beams has been verified by experimental tests, showing that its influence is non-negligible. The amplitudes of all the resonances have been underestimated when the influence of the static prestrain has been omitted. By contrast, the influence on the resonance frequencies has been more significant for the higher order modes.

Once proving the relevance of the influence of the static prestrain on the dynamic response of the formed beams, the proposed frequency-prestrain material model has been applied in order to correct the observed deviations. The finite element implementation of the material model for updating the global complex stiffness matrix avoiding the re-

assembly has been detailed. The numerical responses computed with the nominal dynamic properties and including the influence of the static prestrain, have been compared with the experimental responses. The major differences have been observed on the amplitude of the first resonance, whereas the resonance frequencies have not significantly varied. The observed differences have been notably reduced after including the influence of the static prestrain on the dynamic properties of the viscoelastic core.

In addition, the proposed higher order eigensensitivities-based numerical method has been extended for the dynamic analysis of formed CLD parts. To this end, the nth derivatives of the stiffness and the structural damping matrices, necessary for computing the eigenvalue and eigenvector derivatives, have been presented.

The iterative algorithm has been applied for computing the complex modal parameters of the formed CLD beams, and validated with the results provided by the iterative complex eigensolution (ICE) method. As well, the modal parameters have been computed with the nominal dynamic properties, from where further conclusions regarding the influence of the static prestrain have been drawn. The static prestrain has mainly affected to the modal loss factor.

Similarly, the incremental algorithm has been applied for computing the complex and frequency-dependent modal parameters, and validated with the results provided by IRAM. The total frequency response has been approximated by the complex mode superposition method and its accuracy has been checked by correlating it with the exact response computed by the direct frequency method. Unlike the latter, the complex mode superposition method has determined the contribution of each mode to the total response of the selected point, providing practical information for engineers.

The influence of the static prestrain has been analyzed proving that it is a relevant factor that should be taken into consideration for properly determining the dynamic behavior of press-formed CLD parts. The presented results have evidenced that the forming process negatively affects to the damping performance of the CLD laminates.

The presented study has been submitted to the journal *Materials & Design* [76] for publication.

Appendix A

RKU Homogenization theory

The Ross, Kerwin and Ungar [107] model has been the most widely used to describe the behavior of different types of surface damping treatments [87]. Ross, Kerwin and Ungar derived the expression for the complex stiffness of FLD and CLD beams. For the particular case of a symmetric CLD beam, and considering that the storage modulus of the viscoelastic core is some orders of magnitude smaller than that of the constraining layers, the homogenized complex flexural stiffness, $EI(1+\mathrm{i}\eta)$, yields

$$EI\left(1+\mathrm{i}\eta\right)=\frac{E_{\mathrm{e}}I_{\mathrm{e}}}{6}+E_{\mathrm{e}}H_{\mathrm{e}}\left(H_{\mathrm{e}}+H_{\mathrm{v}}\right)^{2}\frac{g\left(1+\mathrm{i}\eta_{\mathrm{v}}\right)}{1+2g\left(1+\mathrm{i}\eta_{\mathrm{v}}\right)}, \tag{A.1}$$

where g is the shear parameter given by

$$g=\frac{G_{\mathrm{v}}}{E_{\mathrm{e}}H_{\mathrm{e}}H_{\mathrm{v}}p^{2}}, \tag{A.2}$$

and

$$p=\xi_{r}/L \tag{A.3}$$

is the wave number, where ξ_r is a coefficient for the rth mode. E, I, and η are the storage modulus, the second moment of area, and the loss factor of the homogenized beam, respectively; E_{e}, I_{e} and H_{e} are the storage modulus, the second moment and the thickness of area of the constraining layer, respectively; G_{v}, H_{v} and η_{v} are the shear modulus, the thickness and the loss factor of the viscoelastic core, respectively.

Although the RKU model has been developed to predict the response of damped three-layer systems assuming that the properties of the damping material are known, it has been commonly applied also in reverse. In such cases, the dynamic properties of the viscoelastic

material are identified from the damped response of the system.

For identifying the complex shear modulus of the viscoelastic material constrained between two elastic layers, first the homogenized dynamic properties of the whole CLD structure are determined. From the homogenized complex modulus the complex shear modulus of the viscoelastic core can be determined. The shear modulus is determined from

$$G_{\mathrm{v}} = \left[A - B - 2\left(A - B\right)^2 - 2\left(A\eta\right)^2\right]\left[\frac{\left(\frac{2\pi C_r E_{\mathrm{e}} H_{\mathrm{e}} H_{\mathrm{v}}}{L^2}\right)}{\left(1 - 2A + 2B\right)^2 + 4\left(A\eta\right)^2}\right], \tag{A.4}$$

and the loss factor is determined by

$$\eta_{\mathrm{v}} = \frac{A\eta}{A - B - 2\left(A - B\right)^2 - 2\left(A\eta\right)^2}, \tag{A.5}$$

where

$$A = \frac{\omega_s^2\left(2 + DT\right)B}{2\omega_r^2}, \tag{A.6}$$

$$B = \frac{1}{6\left(1 + T\right)^2}, \tag{A.7}$$

with ω_s and ω_r being the resonance frequencies of the CLD and CL specimens, respectively; with $D = \rho_{\mathrm{v}}/\rho_{\mathrm{e}}$ and $T = H_{\mathrm{v}}/H_{\mathrm{e}}$ being the ratios of the corresponding densities and thicknesses of the viscoelastic core and constraining layers, respectively.

Since the RKU equation was developed using sinusoidal expansion for the mode shapes of vibration, the data of the first mode is ignored in practice since this assumption is acceptable only for the higher order modes. Therefore, the RKU equation is directly applicable for pinned-pinned beams, but correction factors may be used for other boundary conditions [104].

Appendix B

Two-node three-layer sandwich beam finite element

In the second and the fourth chapters, a two-node three-layer sandwich beam finite element has been employed with four degrees of freedom per node. As well, in the fifth chapter a similar beam-type finite element has been used for the dynamic analysis of formed CLD beams. This latter finite element is based on the first one, where five degrees of freedom are added yielding to a finite element with nine degrees of freedom per node. The displacement field assumed by the finite element has also been used by Trindade *et al.* [123], Sainsbury and Zhang [109], Galucio *et al.* [39], or Amichi and Atalla [4].

In Figure B.1 the assumed displacement field is represented.

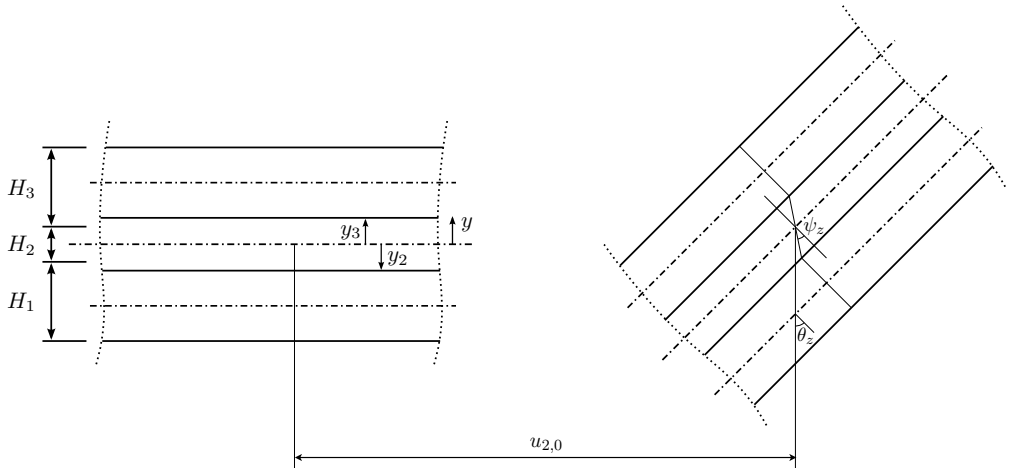

Figure B.1: Displacement field of the beam-type sandwich finite element.

where H_i is the thickness of the ith layer, $\theta_z = \partial v/\partial x$ is the rotation of the face layers, and $u_{2,0}$ and ψ_z are the axial displacement of the center line and the shear strain of the viscoelastic core, respectively. The present finite element assumes Euler-Bernoulli theory for the elastic face layers and the Timoshenko theory for the viscoelastic core. All layers are assumed incompressible through the thickness, perfectly bonded, and in plane stress state.

The displacement fields of each of the three layers are given by

$$\begin{aligned} u_1 &= u_{2,0} - y\theta_z + y_2\psi_z, \\ u_2 &= u_{2,0} - y\left(\theta_z - \psi_z\right), \\ u_3 &= u_{2,0} - y\theta_z + y_3\psi_z, \\ v_1 &= v_2 = v_3 = v. \end{aligned} \tag{B.1}$$

All the layers are assumed to be perfectly bonded, so the continuity conditions with $y_2 = -H_\mathrm{v}/2$ and $y_3 = H_\mathrm{v}/2$, are defined as follows:

$$\begin{aligned} u_1(x, y_2, t) &= u_2(x, y_2, t), \\ u_3(x, y_3, t) &= u_2(x, y_3, t). \end{aligned} \tag{B.2}$$

The finite element is defined by two nodes with four degrees of freedom per node. The generalized displacements $\mathbf{u} = [u_{2,0}\ v\ \psi_z]^\mathrm{T}$ are discretized with linear shape functions for the displacement $u_{2,0}$ and the rotation ψ_z, and cubic shape functions for the transverse displacement v. The vector of the generalized displacements $\mathbf{u}$ is related to the elementary degrees of freedom vector $\mathbf{q} = [u_1\ v_1\ \theta_{z1}\ \psi_{z1}\ u_2\ v_2\ \theta_{z2}\ \psi_{z2}]^\mathrm{T}$ by the interpolation matrix $\mathbf{N}$, given by

$$\mathbf{u} = \mathbf{N}\mathbf{q}, \tag{B.3}$$

where the interpolation matrix $\mathbf{N}$ is defined as

$$\mathbf{N} = \begin{bmatrix} N_1 & 0 & 0 & 0 & N_2 & 0 & 0 & 0 \\ 0 & N_3 & N_4 & 0 & 0 & N_5 & N_6 & 0 \\ 0 & 0 & 0 & N_1 & 0 & 0 & 0 & N_2 \end{bmatrix}, \tag{B.4}$$

the interpolation functions being given by,

$$
\begin{aligned}
N_1 &= 1 - \frac{x}{l_e}, \\
N_2 &= \frac{x}{l_e}, \\
N_3 &= 1 - 3\left(\frac{x}{l_e}\right)^2 + 2\left(\frac{x}{l_e}\right)^3, \\
N_4 &= x - 2x\frac{x}{l_e} + x\left(\frac{x}{l_e}\right)^2, \\
N_5 &= 3\left(\frac{x}{l_e}\right)^2 - 2\left(\frac{x}{l_e}\right)^3, \\
N_6 &= x\left(\frac{x}{l_e}\right)^2 - x\left(\frac{x}{l_e}\right),
\end{aligned}
\tag{B.5}
$$

where l_e is the length of the element.

The mass matrix for the sandwich element $\mathbf{M}^e$ is obtained from the kinetic energy of the finite element, and is composed of inertia terms, of translation in x and y directions and rotation around z, as well as coupling terms of translation-rotation, such as

$$
\begin{aligned}
\mathbf{M}^e = \sum_{i=1}^{3} \int_L \Bigg(& bH_i \mathbf{N}_{xi}^{\mathrm{T}} \rho_i \mathbf{N}_{xi} - b\left(\frac{y_{i+1}^2 - y_i^2}{2}\right)\left(\mathbf{N}_{ri}^{\mathrm{T}} \rho_i \mathbf{N}_{xi} + \mathbf{N}_{xi}^{\mathrm{T}} \rho_i \mathbf{N}_{ri}\right) + \\
& + b\left(\frac{y_{i+1}^3 - y_i^3}{3}\right) \mathbf{N}_{ri}^{\mathrm{T}} \rho_i \mathbf{N}_{ri} + bH_i \mathbf{N}_y^{\mathrm{T}} \rho_i \mathbf{N}_y \Bigg) \mathrm{d}x,
\end{aligned}
\tag{B.6}
$$

where b is the width, ρ_i is the density of the ith layer, and $\mathbf{N}_x$, $\mathbf{N}_r$ and $\mathbf{N}_y$ are the interpolation vectors related to the axial displacements, to the rotation, and to the transverse displacements defined for each of the ith layer as

$$
\begin{aligned}
\mathbf{N}_{x1} &= \begin{bmatrix} N_1 & 0 & y_2 N_1 & 0 & N_2 & 0 & y_2 N_2 & 0 \end{bmatrix}, \\
\mathbf{N}_{x2} &= \begin{bmatrix} N_1 & 0 & 0 & 0 & N_2 & 0 & 0 & 0 \end{bmatrix}, \\
\mathbf{N}_{x3} &= \begin{bmatrix} N_1 & 0 & y_3 N_1 & 0 & N_2 & 0 & y_3 N_2 & 0 \end{bmatrix}, \\
N_{r1} &= \begin{bmatrix} 0 & N_3' & N_4' & 0 & 0 & N_5' & N_6' & 0 \end{bmatrix}, \\
\mathbf{N}_{r2} &= \begin{bmatrix} 0 & N_3' & N_4' & -N_1 & 0 & N_5' & N_6' & -N_2 \end{bmatrix}, \\
\mathbf{N}_{r3} &= \begin{bmatrix} 0 & N_3' & N_4' & 0 & 0 & N_5' & N_6' & 0 \end{bmatrix}, \\
\mathbf{N}_y &= \begin{bmatrix} 0 & N_3 & N_4 & 0 & 0 & N_5 & N_6 & 0 \end{bmatrix},
\end{aligned}
\tag{B.7}
$$

The stiffness matrix for the sandwich element $\mathbf{K}^e$ is obtained from the strain energy of the finite element, and is written including the membrane, bending, coupling membrane-bending, and shear terms, yielding to

$$\begin{aligned}\mathbf{K}^e = &\sum_{i=1}^{3}\int_L \Bigg(bH_i\mathbf{B}_{mi}^{\mathrm{T}}E_i\mathbf{B}_{mi} + b\left(\frac{y_{i+1}^3 - y_i^3}{3}\right)\mathbf{B}_{fi}^{\mathrm{T}}E_i\mathbf{B}_{fi} + \\ &+ b\left(\frac{y_{i+1}^2 - y_i^2}{2}\right)\left(\mathbf{B}_{mi}^{\mathrm{T}}E_i\mathbf{B}_{fi} + \mathbf{B}_{fi}^{\mathrm{T}}E_i\mathbf{B}_{mi}\right) + bH_2\mathbf{B}_c^{\mathrm{T}}G_2\mathbf{B}_c\Bigg)\mathrm{d}x,\end{aligned} \tag{B.8}$$

where $\mathbf{B}_{mi}$, $\mathbf{B}_{fi}$, and $\mathbf{B}_c$ are the membrane, bending and shear strain operators, respectively, being defined as

$$\begin{aligned}\mathbf{B}_{m1} &= \left[\frac{\partial}{\partial x} \quad 0 \quad y_2\frac{\partial}{\partial x}\right]\mathbf{N},\\ \mathbf{B}_{m2} &= \left[\frac{\partial}{\partial x} \quad 0 \quad 0\right]\mathbf{N},\\ \mathbf{B}_{m3} &= \left[\frac{\partial}{\partial x} \quad 0 \quad y_3\frac{\partial}{\partial x}\right]\mathbf{N},\\ \mathbf{B}_{f1} &= \left[0 \quad \frac{\partial^2}{\partial x^2} \quad 0\right]\mathbf{N},\\ \mathbf{B}_{f2} &= \left[0 \quad \frac{\partial^2}{\partial x^2} \quad -\frac{\partial}{\partial x}\right]\mathbf{N},\\ \mathbf{B}_{f3} &= \left[0 \quad \frac{\partial^2}{\partial x^2} \quad 0\right]\mathbf{N},\\ \mathbf{B}_c &= \left[0 \quad 0 \quad 1\right]\mathbf{N},\end{aligned} \tag{B.9}$$

which relates the membrane strain β_{xi} and the curvature χ_{xi} of the ith layer, and the shear strain of the core γ_{xy}, with the vector of displacements $\mathbf{q}$, respectively, such that

$$\begin{aligned}\beta_{xi} &= \mathbf{B}_{mi}\mathbf{q},\\ \chi_{xi} &= \mathbf{B}_{fi}\mathbf{q},\\ \gamma_{xy} &= \mathbf{B}_c\mathbf{q},\end{aligned} \tag{B.10}$$

where assuming the hypothesis of plane stress state, the axial strain $\epsilon_{xx,i}$ of the ith layer and the shear strain γ_{xy} of the viscoelastic core are given by,

$$\begin{aligned}\epsilon_{xx,i} &= \beta_{xi} - y\chi_{xi},\\ \epsilon_{yy,i} &= \epsilon_{zz,i} = 0,\\ \gamma_{xy} &= \psi_z,\\ \gamma_{xz} &= \gamma_{yz} = 0,\end{aligned} \tag{B.11}$$

For analyzing curved CLD beams, the same planar finite element is used but five degrees of freedom are added ($w\ \theta_x\ \theta_y\ \psi_x\ \psi_y$), resulting in a 9 degrees of freedom per node (u, v, w, θ_x, θ_y, θ_z, ψ_x, ψ_y, ψ_z) finite element. When adding extra degrees of freedom, rank deficiency and ill-conditioning problems emerge when adjacent elements are coplanar due to the zero stiffness associated with the added degrees of freedom. The assembly is stabilized by adding identical fictitious stiffness matrices relative to each degree of freedom $\mathbf{K}_w$, $\mathbf{K}_{\theta_x}$, $\mathbf{K}_{\theta_y}$, $\mathbf{K}_{\psi_x}$, and $\mathbf{K}_{\psi_y}$, by the formulation proposed by Batoz and Dhatt [12], such that

$$\mathbf{K}_{\text{fictitious}} = \alpha \sum_{i=1}^{3} \int_L bH_i \mathbf{B}_z^{\mathrm{T}} E_i \mathbf{B}_z \mathrm{d}x \tag{B.12}$$

where α is a scaling factor, commonly being $\alpha \approx 10^{-4}$; and where $\mathbf{B}_z$ is a 1×18 vector of zeros, and the element relative to a given added degree of freedom and node is set to N_1' and N_2', respectively. For example, the fictitious stiffness matrix related to the w displacment $\mathbf{K}_w$, is defined by including N_1' and N_2' in the third and the 12th position of the $\mathbf{B}_z$ zero vector, respectively.

In addition, when formed CLD beams are analyzed the coordinate transformation matrix must be defined for assembling the mass and stiffness matrices in the global coordinate system. The displacement vector based on the global coordinate system XYZ, is obtained by transforming the displacement vector based on the local coordinate system xyz, given by

$$\begin{Bmatrix} u \\ v \\ w \end{Bmatrix} = \mathbf{Q} \begin{Bmatrix} U \\ V \\ W \end{Bmatrix}, \quad \begin{Bmatrix} \theta_x \\ \theta_y \\ \theta_z \end{Bmatrix} = \mathbf{Q} \begin{Bmatrix} \theta_X \\ \theta_Y \\ \theta_Z \end{Bmatrix}, \quad \begin{Bmatrix} \psi_x \\ \psi_y \\ \psi_z \end{Bmatrix} = \mathbf{Q} \begin{Bmatrix} \psi_X \\ \psi_Y \\ \psi_Z \end{Bmatrix}, \tag{B.13}$$

where $\mathbf{Q}$ is the transformation matrix for the displacements and rotations [4]. For the particular case of systems defined in the XY plane where $w = W = 0$ [135], $\mathbf{Q}$ results

$$\mathbf{Q} = \begin{bmatrix} \cos\theta & \sin\theta & 0 \\ -\sin\theta & \cos\theta & 0 \\ 0 & 0 & 1 \end{bmatrix}, \tag{B.14}$$

from where the total transformation matrix $\mathbf{T}$ is determined as

$$\mathbf{A}_{9\times 9} = \begin{bmatrix} \mathbf{Q} & [0] & [0] \\ [0] & \mathbf{Q} & [0] \\ [0] & [0] & \mathbf{Q} \end{bmatrix}, \tag{B.15}$$

$$\mathbf{T}_{18\times18} = \begin{bmatrix} \mathbf{A} & [0] \\ [0] & \mathbf{A} \end{bmatrix}. \tag{B.16}$$

Before assembling the total mass $\mathbf{M}$ and stiffness $\mathbf{K}$ matrices, the mass $\mathbf{M}^e$ and stiffness $\mathbf{K}^e$ matrices of the element defined in the local coordinate system, are transformed into the global coordinate system using the transformation matrix $\mathbf{T}$, such that

$$\mathbf{M} = \mathbf{T}^{\mathrm{T}}\mathbf{M}^e\mathbf{T} \tag{B.17}$$

and

$$\mathbf{K} = \mathbf{T}^{\mathrm{T}}\mathbf{K}^e\mathbf{T}, \tag{B.18}$$

where $(\bullet)^{\mathrm{T}}$ denotes the transposition operator.

Bibliography

[1] ASTM E 756-05. *Standard test method for measuring vibration-damping properties of materials*. American Society for Testing and Materials, 2005.

[2] H.M. Adelman and R.T. Haftka. Sensitivity analysis of discrete structural systems. *AIAA journal*, 24(5):823–832, 1986.

[3] S. Adhikari and J. Woodhouse. Quantification of non-viscous damping in discrete linear systems. *Journal of sound and vibration*, 260(3):499–518, 2003.

[4] K. Amichi and N. Atalla. A New 3D Finite Element for Sandwich Beams With a Viscoelastic Core. *Journal of Vibration and Acoustics*, 131:021010 (9 pp.), 2009.

[5] W.E. Arnoldi. The principle of minimized iterations in the solution of the matrix eigenvalue problem. *Quaterly of Applied Mathematics*, 9(17):17–29, 1951.

[6] R.L. Bagley and P.J. Torvik. Fractional calculus - a different approach to the analysis of viscoelastically damped structures. *AIAA Journal*, 21(5):741–748, 1983.

[7] R.L. Bagley and P.J. Torvik. A theoretical basis for the application of fractional calculus to viscoelasticity. *Journal of Rheology*, 27(3):201–210, 1983.

[8] R.L. Bagley and P.J. Torvik. Fractional calculus in the transient analysis of viscoelastically damped structures. *American Institute of Aeronautics and Astronautics*, 23(6):918–925, 1985.

[9] R.L. Bagley and P.J. Torvik. On the fractional calculus model of viscoelastic behavior. *Journal of Rheology*, 30(1):133–155, 1986.

[10] E. Balmès and S. Germès. Design strategies for viscoelastic damping treatment applied to automotive components. In *22nd International Modal Analysis Conference (IMAC-XXII)*, Dearborn, Michigan, US, 2004.

[11] E. Barkanov, E. Skukis, and B. Petitjean. Characterisation of viscoelastic layers in sandwich panels via an inverse technique. *Journal of Sound and Vibration*, 327(3-5):402–412, 2009.

[12] J.L. Batoz and G. Dhatt. *Modélisation des structures par éléments finis: volume 2: poutres et plaques*. Hermès, Paris, 1990.

[13] C.W. Bert. Material damping: An introductory review of mathematical models, measures and experimental techniques. *Journal of Sound and Vibration*, 29(2):129–153, 1973.

[14] M.A. Biot. Variational principles in irreversible thermodynamics with application to viscoelasticity. *Physical Review*, 97(6):1463–1469, 1955.

[15] L. Boltzmann. Zur theorie der elastischen nachwirkung. *Annalen der Physik*, 241(11):430–432, 1878.

[16] D.I. Bower. *An Introduction to Polymer Physics*. Cambridge University Press, Cambridge, UK, 2002.

[17] H.F. Brinson and L.C. Brinson. *Polymer engineering science and viscoelasticity: An introduction*. Springer, 2008.

[18] T.K. Caughey and M.E.J. O'Kelly. Classical normal modes in damped linear dynamic systems. *ASME Journal of Applied Mechanics*, 32:583–588, 1965.

[19] G. Chen. *FE model validation for structural dynamics*. University of London, 2001.

[20] H.S. Cheng, J. Cao, H. Yao, S.D. Liu, and B. Kinsey. Wrinkling behavior of laminated steel sheets. *Journal of Materials Processing Technology*, 151(1–3):133–140, 2004.

[21] R.M. Christensen. *Theory of viscoelasticity: an introduction*. Academic Press, New York, US, 2nd edition, 1982.

[22] F. Cortés. *Análisis dinámico de sistemas estructurales con amortiguamiento viscoelástico*. PhD thesis, Mondragon Unibertsitatea, 2006.

[23] F. Cortés and M.J. Elejabarrieta. Complex modes superposition in non-classically damped structures. In *6th International Conference on Structural Dynamics*, Paris, France, 2005.

[24] F. Cortés and M.J. Elejabarrieta. An approximate numerical method for the complex eigenproblem in systems characterised by a structural damping matrix. *Journal of Sound and Vibration*, 296(1-2):166–182, 2006.

[25] F. Cortés and M.J. Elejabarrieta. Finite element formulations for transient dynamic analysis in structural systems with viscoelastic treatments containing fractional derivative models. *International Journal for Numerical Methods in Engineering*, 69(10):2173–2195, 2007.

[26] F. Cortés and M.J. Elejabarrieta. Viscoelastic materials characterisation using the seismic response. *Materials and Design*, 28(7):2054–2062, 2007.

[27] F. Cortés and M.J. Elejabarrieta. Forced response of a viscoelastically damped rod using the superposition of modal contribution functions. *Journal of Sound and Vibration*, 315(1-2):58–64, 2008.

[28] F. Cortés, M. Martinez, and M.J. Elejabarrieta. *Mechanical vibrations: measurements, effects and control*, chapter On mechanical vibration control using viscoelastic surface treatments. Nova Science Publishers, Inc, 2009.

[29] F. Cortés, M. Martinez, and M.J. Elejabarrieta. *Mechanical Vibrations: Types, Testing and Analysis*, chapter On mechanical vibration control using viscoelastic surface treatments. Nova Science Publishers, Inc, 2010.

[30] F. Cortés, M. Martinez, and M.J. Elejabarrieta. *Viscoelastic Surface Treatments for Passive Control of Structural Vibration*. Nova Science Publishers Inc, 2011.

[31] J.J. de Espíndola, J.M. da Silva Neto, and E.M.O. Lopes. A generalised fractional derivative approach to viscoelastic material properties measurement. *Applied Mathematics and Computation*, 164(2):493–506, 2005.

[32] T.A. Eisenhour. *Experimental and numerical investigations of the bending characteristics of laminated steel*. PhD thesis, University of Notre Dame, Notre Dame, Indiana, 2007.

[33] I. Emri, B.S. von Bernstorff, R. Cvelbar, and A. Nikonov. Re-examination of the approximate methods for interconversion between frequency- and time-dependent material functions. *Journal of Non-Newtonian Fluid Mechanics*, 129(2):75–84, 2005.

[34] D.J. Ewins. *Modal testing* (2^{nd} Edition). Baldock, Hertfordshire, Great Britain: Research Studies Press, 2000.

[35] J.D. Ferry. *Viscoelastic properties of polymers*. John Wiley & sons, New York, US, 3rd edition, 1980.

[36] RL Fox and MP Kapoor. Rates of change of eigenvalues and eigenvectors. *AIAA Journal*, 6(12):2426–2429, 1968.

[37] M.I. Friswell. Calculation of second and higher order eigenvector derivatives. *Journal of Guidance, Control, and Dynamics*, 18(4):919–921, 1995.

[38] M.I. Friswell and D.J. Inman. Reduced-order models of structures with viscoelastic components. *AIAA Journal*, 37(10):1318–1325, 1999.

[39] A.C. Galucio, J.F. Deü, and R. Ohayon. Finite element formulation of viscoelastic sandwich beams using fractional derivative operators. *Computational Mechanics*, 33(4):282–291, 2004.

[40] D.F. Golla and P.C. Hughes. Dynamics of viscoelastic structures–a time-domain, finite element formulation. *Journal of Applied Mechanics*, 52(12):897–906, 1985.

[41] TA Instruments. http://www.tainstruments.com.

[42] K. Jahani and A.S. Nobari. Identification of dynamic (youngs and shear) moduli of a structural adhesive using modal based direct model updating method. *Experimental Mechanics*, 48(5):599–611, 2008.

[43] C.D. Johnson and D.A. Kienholz. Finite element prediction of damping in structures with constrained viscoelastic layers. *AIAA Journal*, 20(9):1284–1290, 1982.

[44] C.D. Johnson, D.A. Kienholz, and L.C. Rogers. Finite element prediction of damping in beams with constrained viscoelastic layers. *Shock and Vibration Bulletin*, 50(1):71–81, 1980.

[45] D.I.G. Jones. Reflections on damping technology at the end of the twentieth century. *Journal of Sound and Vibration*, 190(3):449–462, 1996.

[46] D.I.G. Jones. *Handbook of viscoelastic vibration damping*. John Wiley & sons, Chichester, UK, 2001.

[47] S. Kalpakjian and S.R. Schmid. *Manufacturing Processes for Engineering Materials*. Prentice-Hall, Englewood Cliffs, New Jersey, 5th edition, 2003.

[48] G. Kergourlay. *Mesure et prèdiction de structures viscoèlastiques - Application à une enceinte acoustique*. PhD thesis, Ecole Centrale de Paris, 2004.

[49] G. Kergourlay, E. Balmès, and G. Legal. A characterization of frequency–temperature–prestress effects in viscoelastic films. *Journal of Sound and Vibration*, 297(1-2):391–407, 2006.

[50] E.M. Jr. Kerwin. Damping of flexural waves by a constrainded viscoelastic layer. *Journal of the Acoustical Society of America*, 31(7):952–962, 1959.

[51] J.K. Kim and P.F. Thomson. Forming behaviour of sheet steel laminate. *Journal of Materials Processing Technology*, 22(1):45–64, 1990.

[52] J.K. Kim and P.F. Thomson. Separation behaviour of sheet steel laminate during forming. *Journal of Materials Processing Technology*, 22(2):147–161, 1990.

[53] S.Y. Kim and D.H. Lee. Identification of fractional-derivative-model parameters of viscoelastic materials from measured FRFs. *Journal of Sound and Vibration*, 324(3-5):570–586, 2009.

[54] M. Kleiner and V. Hellinger. New possibilities for improved bending of vibration damping laminated sheets. *CIRP Annals - Manufacturing Technology*, 48(1):217–220, 1999.

[55] R.S. Lakes. Viscoelastic measurement techniques. *Review of scientific instruments*, 75(4):797–810, 2004.

[56] C. Lanczos. An iteration method for the solution of the eigenvalue problem of linear differential and integral operators. *Journal of Research of the National Bureau of Standards*, 45(4):255–282, 1950.

[57] R.B. Lehoucq, D.C. Sorensen, and C. Yang. *ARPACK users' guide: solution of large-scale eigenvalue problems with implicitly restarted Arnoldi methods*. Philadelphia: SIAM, 1998.

[58] G.A. Lesieutre and E. Bianchini. Time domain modeling of linear viscoelasticity using anelastic displacement fields. *Journal of Vibration and Acoustics*, 117(4):424–430, 1995.

[59] G.A. Lesieutre and D.L. Mingori. Finite element modeling of frequency-dependent material properties using augmented thermodynamic fields. *AIAA Journal of Guidance, Control and Dynamics*, 13(6):1040–1050, 1990.

[60] Z. Li and M.J. Crocker. A review on vibration damping in sandwich composite structures. *International Journal of Acoustics and Vibrations*, 10(4):159–169, 2005.

[61] G.R. Liu and S.S. Quek. *The finite element method: a practical course*. Butterworth-Heinemann, Oxford, UK, 2003.

[62] L. Liu and J. Wang. Modeling springback of metal-polymer-metal laminates. *Transactions of the ASME, Journal of Manufacturing Science and Engineering*, 126(3):599–604, 2004.

[63] Z.S. Liu, S.H. Chen, and Y.Q. Zhao. An accurate method for computing eigenvector derivatives for free-free structures. *Computers and Structures*, 52(6):1135–1143, 1994.

[64] Y.C. Lu. Fractional derivative viscoelastic model for frequency-dependent complex moduli of automotive elastomers. *International Journal of Mechanics and Materials in Design*, 3(4):329–336, 2006.

[65] J.E. Mark, editor. *Polymer Data Handbook*. Oxford University Press, 1999.

[66] M. Martinez, F. Cortés, and M.J. Elejabarrieta. Experimental and numerical analysis of vibroacoustic attenuation in sandwich structures. In *Proceedings of the 19th International Congress on Acoustics*, Madrid, Spain, 2007.

[67] M. Martinez and M.J. Elejabarrieta. Caracterización dinámica de estructuras CLD con alto amortiguamiento. In *Proceedings of 40th Congreso Nacional de Acústica*, Cádiz, Spain, 2009.

[68] M. Martinez and M.J. Elejabarrieta. Complex modes superposition applied to beams with constrained layer damping. In *Proceedings of Noise and Vibration: Emerging Methods*, Oxford, UK, 2009.

[69] M. Martinez-Agirre and M.J. Elejabarrieta. Aplicación de adhesivos en el transporte para la mejora del confort vibroacústico. In *Proceedings of 11th Congreso de Adhesión y Adhesivos*, Madrid, Spain, 2010.

[70] M. Martinez-Agirre and M.J. Elejabarrieta. Characterisation and modelling of viscoelastically damped sandwich structures. *International Journal of Mechanical Sciences*, 52(9):1225–1233, 2010.

[71] M. Martinez-Agirre and M.J. Elejabarrieta. Dynamic characterization of high damping viscoelastic materials from vibration test data. *Journal of Sound and Vibration*, 330(16):3930–3943, 2011.

[72] M. Martinez-Agirre and M.J. Elejabarrieta. Effectiveness of different surface damping treatments for structural vibration reduction. In *10th Conference on Mechanics*, Oujda, Morocco, 2011.

[73] M. Martinez-Agirre and M.J. Elejabarrieta. Higher order eigensensitivities-based numerical method for the harmonic analysis of viscoelastically damped structures. *International Journal for Numerical Methods in Engineering*, 88(12):1280–1296, 2011.

[74] M. Martinez-Agirre and M.J. Elejabarrieta. Method for the identification of constitutive model parameters of high damping viscoelastic materials. In *8th International Conference on Structural Dynamics*, Leuven, Belgium, 2011.

[75] M. Martinez-Agirre, S. Illescas, and M.J. Elejabarrieta. Dynamic characterization of prestrained viscoelastic films. *International Journal of Adhesion and Adhesives*, (submitted).

[76] M. Martinez-Agirre, S. Illescas, and M.J. Elejabarrieta. Static prestrain influence on the dynamic behavior of press-formed viscoelastic sandwich beams. *Materials & Design*, (submitted).

[77] *MATLAB Version R2010b.* The Math Works Inc., Natick, US, 2010.

[78] D.J. McTavish and P.C. Hughes. Modeling of linear viscoelastic space structures. *Journal of Vibration and Acoustics*, 115(1):103–110, 1993.

[79] M.E.R. Melo, C.A.G. Salazar, U.O. Méndez, and J.J.M. Vega. Aplicación del cálculo fraccional en el modelado de la viscoelasticidad en polímeros. Parte I: Manifestación mecánica de la viscoelasticidad. *Ingenierías*, 8(27):7–15, 2005.

[80] K.P. Menard. *Dynamic Mechanical Analysis: A Practical Introduction.* CRC Press, Boca Raton, Florida, US, 1999.

[81] J.D. Menczel and R.B. Prime. *Thermal analysis of polymers: fundamentals and applications.* Wiley Online Library, 2009.

[82] R. Moreira and J.D. Rodrigues. Constrained damping layer treatments: finite element modeling. *Journal of Vibration and Control*, 10:575–595, 2004.

[83] R.A.S. Moreira and R. de Carvalho. Inverse method for dynamic characterisation of cork compounds. *International Journal of Materials Engineering Innovation*, 1(2):254–275, 2009.

[84] R.A.S. Moreira, F.J.Q. de Melo, and J.F. Dias Rodrigues. Static and dynamic characterization of composition cork for sandwich beam cores. *Journal of Material Science*, 45(12):3350–3366, 2010.

[85] R.A.S. Moreira, J. Dias Rodrigues, and A.J.M. Ferreira. A generalized layerwise finite element for multi-layer damping treatments. *Computational Mechanics*, 37(5):426–444, 2006.

[86] D.V. Murthy and R.T. Haftka. Derivatives of eigenvalues and eigenvectors of a general complex matrix. *International Journal for Numerical Methods in Engineering*, 26(2):293–311, 1988.

[87] A.D. Nashif, D.I.G. Jones, and J.P. Henderson. *Vibration damping.* New York: John Wiley & sons, 1985.

[88] JA Nelder and R. Mead. A simplex method for function minimization. *The computer journal*, 7(4):308–313, 1965.

[89] R.B. Nelson. Simplified calculation of eigenvector derivatives. *AIAA journal*, 14(9):1201–1205, 1976.

[90] H. Oberst and K. Frankenfeld. Über die Dämpfung der Biegeschwigungen dünner Bleche durch fest haftende Beläge. *Acustica*, 4:184–194, 1952.

[91] G.M. Odegard, T.S. Gates, and H.M. Herring. Characterization of viscoelastic properties of polymeric materials through nanoindentation. *Experimental Mechanics*, 45(2):130–136, 2005.

[92] D. Ouis. Combination of a standard viscoelastic model and fractional derivate calculus to the characterization of polymers. *Materials Research Innovations*, 7(1):42–46, 2003.

[93] J. Padovan. Computational algorithms for fe formulations involving fractional operators. *Computational Mechanics*, 2(4):271–287, 1987.

[94] C.H. Park, D.J. Inman, and M.J. Lam. Model reduction of viscoelastic finite element models. *Journal of Sound and Vibration*, 219(4):619–637, 1999.

[95] S.W. Park and R.A. Schapery. Methods of interconversion between linear viscoelastic material functions. part i–a numerical method based on prony series. *International Journal of Solids and Structures*, 36(11):1653–1675, 1999.

[96] T.S. Plagianakos and D.A. Saravanos. High-order layerwise mechanics and finite element for the damped dynamic characteristics of sandwich composite beams. *International Journal of Solids and Structures*, 41(24–25):6853–6871, 2004.

[97] T.S. Plagianakos and D.A. Saravanos. High-order layerwise finite element for the damped free-vibration response of thick composite and sandwich composite plates. *International Journal for Numerical Methods in Engineering*, 77(11):1593–1626, 2009.

[98] A. Plouin and E. Balmès. Steel/viscoelastic/steel sandwich shells computational methods and experimental validations. In *International Modal Analysis Conference*, pages 384–390, 2000.

[99] T. Pritz. Analysis of four-parameter fractional derivative model of real solid materials. *Journal of Sound and Vibration*, 195(1):103–115, 1996.

[100] T. Pritz. Frequency dependences of complex moduli and complex poisson's ratio of real solid materials. *Journal of Sound and Vibration*, 214(1):83–104, 1998.

[101] T. Pritz. Loss factor peak of viscoelastic materials: magnitude to width relations. *Journal of Sound and Vibration*, 246(2):265–280, 2001.

[102] T. Pritz. Five-parameter fractional derivative model for polymeric damping materials. *Journal of Sound and Vibration*, 265(3):935–952, 2003.

[103] G.L. Qian, S.V. Hoa, and X. Xiao. A vibration method for measuring mechanical properties of composite, theory and experiment. *Composite structures*, 39(1-2):31–38, 1997.

[104] D.K. Rao. Frequency and loss factors of sandwich beams under various boundary conditions. *Journal of Mechanical Engineering Science*, 20(5):271–282, 1978.

[105] M.D. Rao. Recent applications of viscoelastic damping for noise control in automobiles and commercial airplanes. *Journal of Sound and Vibration*, 262(3):457–474, 2003.

[106] Z. Ren, N. Atalla, and S. Ghinet. Optimization based identification of the dynamic properties of linearly viscoelastic materials using vibrating beam technique. *Journal of Vibration and Acoustics*, 133(4):041012 (12 pp.), 2011.

[107] D. Ross, E.E. Ungar, and E.M. Jr. Kerwin. Damping of plate flexural vibrations by means of viscoelastic laminae. *Structural Damping*, pages 49–87, 1959.

[108] Y. Saad. *Iterative methods for sparse linear systems*. Society for Industrial Mathematics. Disponible en: http://www.stanford.edu/class/cme324/saad.pdf, 2003.

[109] M.G. Sainsbury and Q.J. Zhang. The Galerkin element method applied to the vibration of damped sandwich beams. *Computers & structures*, 71(3):239–256, 1999.

[110] R.A. Schapery and S.W. Park. Methods of interconversion between linear viscoelastic material functions. part ii–an approximate analytical method. *International Journal of Solids and Structures*, 36(11):1677–1699, 1999.

[111] A. Schmidt and L. Gaul. Application of fractional calculus to viscoelastically damped structures in the finite element method. In *Proceedings of the International Conference on Structural Dynamics Modelling*, pages 297–306, 2002.

[112] F.A. Settle. *Handbook of Instrumental Techniques for Analytical Chemistry*. Prentice Hall PTR, Upper Saddle River, New Jersey, US, 1997.

[113] Y. Shi, H. Sol, and H. Hua. Material parameter identification of sandwich beams by an inverse method. *Journal of Sound and Vibration*, 290(3-5):1234–1255, 2006.

[114] D.C. Sorensen. Numerical methods for large eigenvalue problems. *Acta Numerica*, 11:519 – 84, 2002.

[115] C.T. Sun and Y.P. Lu. *Vibration damping of structural elements*. Prentice Hall, New Jersey, US, 1995.

[116] M. Takiguchi and F. Yoshida. Plastic bending of adhesive-bonded sheet metals. *Journal of Materials Processing Technology*, 113(1–3):743–748, 2001.

[117] M. Takiguchi and F. Yoshida. Effect of forming speed on plastic bending of adhesively bonded sheet metals. *JSME International Journal Series A*, 47(1):47–53, 2004.

[118] T.L. Teng and N.K. Hu. Analysis of damping characteristics for viscoelastic laminated beams. *Computer methods in applied mechanics and engineering*, 190(29-30):3881–3892, 2001.

[119] G.R. Tomlinson. *Structural Dynamics @ 2000: current status and future directions*, chapter State of the art review: damping. Philadelphia: Research Studies Press, 2001.

[120] M.A. Trindade. Reduced-order finite element models of viscoelastically damped beams through internal variables projection. *Journal of Vibration and Acoustics*, 128(4):501–508, 2006.

[121] M.A. Trindade and A. Benjeddou. Hybrid active-passive damping treatments using viscoelastic and piezoelectric materials: review and assessment. *Journal of Vibration and Control*, 8(6):699–745, 2002.

[122] M.A. Trindade, A. Benjeddou, and R. Ohayon. Modeling of frequency-dependent viscoelastic materials for active-passive vibration damping. *Journal of vibration and acoustics*, 122(2):169–174, 2000.

[123] M.A. Trindade, A. Benjeddou, and R. Ohayon. Finite element modelling of hybrid active–passive vibration damping of multilayer piezoelectric sandwich beams–part I: Formulation. *International Journal for Numerical Methods in Engineering*, 51(7):835–854, 2001.

[124] N. Trišović. Eigenvalue Sensitivity Analysis in Structural Dynamics. *FME Transactions*, 35:149–156, 2007.

[125] N.W. Tschoegl, W.G. Knauss, and I. Emri. Poisson's ratio in linear viscoelasticity–a critical review. *Mechanics of Time Dependent Materials*, 6(1):3–51, 2002.

[126] E.E. Ungar and E.M. Kerwin Jr. Loss factors of viscoelastic systems in terms of energy concepts. *The Journal of the Acoustical Society of America*, 34:741, 1962.

[127] C.M.A. Vasques, R.A.S. Moreira, and J.D. Rodrigues. Viscoelastic damping technologies–Part I: Modeling and finite element implementation. *Journal of Advanced Research in Mechanical Engineering*, 1(2):76–95, 2010.

[128] C.M.A. Vasques, R.A.S. Moreira, and J.D. Rodrigues. Viscoelastic damping technologies–Part II: Experimental identification procedure and validation. *Journal of Advanced Research in Mechanical Engineering*, 1(2):96–110, 2010.

[129] B.P. Wang. Improved approximate methods for computing eigenvector derivatives in structural dynamics. *AIAA journal*, 29:1018–1020, 1991.

[130] I.M. Ward and J. Sweeney. *An introduction to the mechanical properties of solid polymers*. John Wiley & sons Inc, 2004.

[131] M.L. Williams. Structural analysis of viscoelastic materials. *AIAA journal*, 2(5):785–808, 1964.

[132] W. Williams, R. Landel, and J. Ferry. The temperature dependence of relaxation mechanisms in amorphous polymers and other glass-forming liquids. *Journal of the American Chemical Society*, 77:3701–3707, 1955.

[133] C. Zang, H. Grafe, and M. Imregun. Frequency-domain criteria for correlating and updating dynamic finite element models. *Mechanical Systems and Signal Processing*, 15(1):139–155, 2001.

[134] O. Zhang and A. Zerva. Iterative method for calculating derivatives of eigenvectors. *AIAA journal*, 34(5):1088–1090, 1996.

[135] O.C. Zienkiewicz, R.L. Taylor, and J.Z. Zhu. *The finite element method: Its basis and fundamentals*. Butterworth-Heinemann, 6th edition, 2005.